

**DOCTORAL THESIS**

# The Electrochemical Reduction of Oxygen on Noble Metal Free and Biomass-based Carbon Nanomaterials

Kätlin Kaare

TALLINN UNIVERSITY OF TECHNOLOGY  
DOCTORAL THESIS  
48/2022

# **The Electrochemical Reduction of Oxygen on Noble Metal Free and Biomass-based Carbon Nanomaterials**

KÄTLIN KAARE



TALLINN UNIVERSITY OF TECHNOLOGY

School of Engineering

Department of Mechanical and Industrial Engineering

This dissertation was accepted for the defence of the degree 25/07/2022

**Supervisor:** Dr. Ivar Kruusenberg  
National Institute of Chemical Physics and Biophysics  
Tallinn, Estonia

**Co-supervisor:** Prof Jakob Kübarsepp  
Department of Mechanical and Industrial Engineering  
Tallinn University of Technology  
Tallinn, Estonia

**Opponents:** Prof Drew C. Higgins  
Department of Chemical Engineering  
McMaster University  
Hamilton, Ontario, Canada

Dr. Tim-Patrick Fellingner  
BAM Federal Institute for Materials Research and Testing  
Berlin, Germany

**Defence of the thesis:** 31/08/2022, Tallinn

**Declaration:**

Hereby I declare that this doctoral thesis, my original investigation and achievement, submitted for the doctoral degree at Tallinn University of Technology has not been submitted for doctoral or equivalent academic degree.

Kätlin Kaare

-----  
signature



European Union  
European Regional  
Development Fund



Investing  
in your future

Copyright: Kätlin Kaare, 2022

ISSN 2585-6898 (publication)

ISBN 978-9949-83-877-6 (publication)

ISSN 2585-6901 (PDF)

ISBN 978-9949-83-878-3 (PDF)

Printed by Koopia Niini & Rauam

TALLINNA TEHNIKAÜLIKOOL  
DOKTORITÖÖ  
48/2022

# **Hapniku elektrokeemiline redutseerumine väärismetalli-vabadel ja biomassil põhinevatel süsiniku nanomaterjalidel**

KÄTLIN KAARE





# Contents

List of publications .....	7
Author's contribution to the publications .....	8
Introduction .....	9
Abbreviations and symbols .....	10
1 Literature overview .....	12
1.1 Oxygen reduction reaction.....	12
1.2 Transition to low-carbon energy and fuel cells.....	13
1.3 Carbon nanomaterials and ORR.....	14
1.4 Heteroatom-doped carbon nanomaterials and ORR .....	15
1.5 Biomass-based carbon nanomaterial synthesis and ORR .....	18
1.6 Heteroatom-doped biomass-based carbon nanomaterials and ORR .....	23
1.7 Non-precious metal-carbon catalysts for the ORR.....	24
2 Aims of the study .....	27
3 Experimental .....	28
3.1 Purification of MWCNTs.....	28
3.2 Synthesis of GO .....	28
3.3 Synthesis of N, S-co-doped catalysts.....	28
3.4 Synthesis of N-doped biomass-based catalysts .....	29
3.5 Synthesis of M-N-C catalysts.....	29
3.6 Preparation of electrodes and electrochemical measurements.....	29
3.7 Physical characterisation methods .....	31
3.8 Theoretical calculations .....	31
4 Results and discussion.....	33
4.1 Oxygen electroreduction on heteroatom co-doped composite .....	33
4.2 Oxygen electroreduction on N-doped biomass-based carbons.....	41
4.2.1 Oxygen electroreduction on N-doped wood-based carbon.....	41
4.2.2 Oxygen electroreduction on N-doped wood-based graphene-like carbon .....	47
4.3 Oxygen electroreduction on M-N-C catalysts .....	53
4.3.1 Oxygen electroreduction on Mn- and CuPc-based MWCNT catalysts .....	53
4.3.2 Oxygen electroreduction on Zn- and Li <sub>2</sub> Pc-based MWCNT catalysts.....	59
5 Conclusions .....	68
6 Novelty and further research .....	70
References .....	71
Acknowledgements.....	93
Abstract.....	94
Lühikokkuvõte.....	95
Appendix 1 .....	97
Appendix 2 .....	109
Appendix 3 .....	119

Appendix 4 .....	131
Appendix 5 .....	143
Curriculum vitae .....	152
Elulookirjeldus.....	154

## List of publications

The list of author's publications, based on which the thesis has been prepared:

- I **K. Kaare**, I. Kruusenberg, M. Merisalu, L. Matisen, V. Sammelselg, K. Tammeveski, Electrocatalysis of oxygen reduction on multi-walled carbon nanotube supported copper and manganese phthalocyanines in alkaline media, *J. Solid State Electrochem.* 20 (2016) 921–929 (previously covered in my BSc thesis).
- II K.-K. Türk, **K. Kaare**, I. Kruusenberg, M. Merisalu, U. Joost, L. Matisen, V. Sammelselg, J.H. Zagal, K. Tammeveski, Oxygen Electroreduction on Zinc and Dilithium Phthalocyanine Modified Multiwalled Carbon Nanotubes in Alkaline Media, *J. Electrochem. Soc.* 164 (2017) H338–H344 (partially covered in my BSc thesis).
- III K.M. Villemson, **K. Kaare**, R. Raudsepp, T. Käämbre, K. Šmits, P. Wang, A. V. Kuzmin, A. Šutka, B.A. Shainyan, I. Kruusenberg, Identification of Active Sites for Oxygen Reduction Reaction on Nitrogen- and Sulfur-Codoped Carbon Catalysts, *J. Phys. Chem. C.* 123 (2019) 16065–16074.
- IV **K. Kaare**, E. Yu, A. Volperts, G. Dobeles, A. Zhurinsh, A. Dyck, G. Niaura, L. Tamasauskaite-Tamasiunaite, E. Norkus, M. Andrulevičius, M. Danilson, I. Kruusenberg, Highly Active Wood-Derived Nitrogen-Doped Carbon Catalyst for the Oxygen Reduction Reaction, *ACS Omega.* 5 (2020) 23578–23587.
- V **K. Kaare**, E. Yu, T. Käämbre, A. Volperts, G. Dobeles, A. Zhurinsh, G. Niaura, L. Tamasauskaite-Tamasiunaite, E. Norkus, I. Kruusenberg, Biomass-derived Graphene-like Catalyst Material for Oxygen Reduction Reaction, *ChemNanoMat.* 7 (2021) 307–313.

## **Author's contribution to the publications**

Contribution to the papers in this thesis are:

- I The author was responsible for carrying out the catalyst materials synthesis and performing all the electrochemical measurements analysing the data. The author interpreted the electrochemical testing data and participated in the writing of the manuscript.
- II The author was responsible for carrying out the catalyst materials synthesis, performing half of the electrochemical measurements and analysing the data. The author interpreted the electrochemical testing data and participated in the writing of the manuscript.
- III The author was responsible for electrochemical measurements and analysing the data. The author interpreted the electrochemical testing data and participated in the writing of the manuscript.
- IV The author was responsible for carrying out the catalyst materials synthesis, performing all the electrochemical measurements and analysing the data. The author interpreted the electrochemical testing data and participated in the writing of the manuscript.
- V The author was responsible for carrying out the catalyst materials synthesis, performing all the electrochemical measurements, and analysing the data. The author interpreted the electrochemical testing data and participated in the writing of the manuscript.

## Introduction

It has been estimated that the world's population will rise to 9.77 billion in the year 2050 [1]. Next to that, it has been projected that the energy demand will rise by 50% in the next 30 years [2]. Since the growing energy demand, depletion of fossil fuels, and the rising levels of CO<sub>2</sub> in the atmosphere are very urgent problems in today's society, there is a great need to find more sustainable ways to produce electricity and take a new route that leads away from fossil fuel-based energy technologies. Hydrogen is a clean energy carrier and the most abundant element in the universe [3].

In a fuel cell, hydrogen is oxidised and as a result, only pure water is produced. This has led to the rapid development of this type of technologies. Fuel cells convert chemical energy into electricity and are very attractive for portable applications [4], including transportation [5]. Therefore, the research carried out in this field has grown enormously. Today, the most popular choice of catalyst for fuel cells is platinum [6], which is expensive and suffers from many drawbacks (stability, agglomeration, etc.). So, various directions for reducing the platinum loading or employing non-platinum catalysts are being developed.

Since Jasinski [7] discovered the electrocatalytic activity of metal macrocycles towards the oxygen reduction reaction, this type of transition-metal macrocyclic compounds have been widely investigated. In addition to that, non-metal heteroatom doped catalysts have gained a lot of interest, since they show even better stability and have no problems with active site blockage due to metal nanoparticle agglomeration. Biomass-based nanocarbons are also becoming a hot topic due to the fact that they can also be employed in fuel cells. The valorisation of different (waste) biomass is a very important topic in the circular economy, where it is of utmost importance to find feasible ways to valorise materials, which otherwise would be disregarded at landfills or treated as low-value materials that are just burned in order to get heat/electricity.

In this thesis, different routes were studied to produce nanocarbon-based materials that were employed as potential electrocatalysts for the oxygen reduction reaction, which is taking place at the cathode of fuel cells. In the first section, heteroatom co-doped carbon composite was studied [III], followed by biomass-based nitrogen-doped carbons [IV, V]. In the final part of the thesis, less-studied metal-based macrocycles were used for modifying carbon nanotubes [I, II].

## Abbreviations and symbols

$A$	Geometric surface area of GC electrode
AC	Activated carbon
AEMFC	Anion-exchange fuel cell
at.%	Atomic percent
AWC	Alder wood char
BET	Brunauer-Emmet-Teller
CNTs	Carbon nanotubes
CoPc	Cobalt(II)phthalocyanine
CuPc	Copper(II)phthalocyanine
CV	Cyclic voltammetry
CVD	Chemical vapor deposition
$C_{O_2}^b$	Oxygen concentration in the bulk solution
DCDA	Dicyandiamide
DFT	Density functional theory
$D_{O_2}$	Diffusion coefficient of oxygen molecule
$E$	Electrode potential
$e$	Electron charge
$E^0$	Electrode standard potential
$E_{1/2}$	Half-wave potential
EDX	Energy dispersive X-ray spectroscopy
$E_{onset}$	Onset potential
$\Delta E$	Energy difference between the products and reactants
$F$	Faraday constant
FC	Fuel cells
FCV	Fuel cell vehicle
FePc	Iron(II)phthalocyanine
FWHM	Full width half maximum
GC	Glassy carbon
GO	Graphene oxide
$\Delta G$	Change in free energy
HER	Hydrogen evolution reaction
HTC	Hydrothermal carbonisation
$j$	Current density
$j_d$	Diffusion-limited current density
$j_k$	Kinetic current density
$k_B$	Boltzmann constant
K-L	Koutecky-Lecvich
LDVs	Light duty vehicles
Li <sub>2</sub> Pc	Dilithiumphthalocyanine

LIB	Li-ion battery
LSV	Linear sweep voltammogram
MAB	Metal-air battery
M-N-C	Metal-nitrogen-carbon
MnPc	Manganese(II)phthalocyanine
MPcs	Metal phthalocyanines
MWCNTs	Multi-walled carbon nanotubes
$N$	Number of electrons transferred per oxygen molecule
N-C	Nitrogen-carbon
OER	Oxygen evolution reaction
OMCs	Ordered mesoporous carbons
oMUS	<i>o</i> -methylisourea bisulfate
ORR	Oxygen reduction reaction
PGE	Platinum group element
PVP	Polyvinylpyrrolidone
QSDFt	Quenched solid density functional theory
RDE	Rotating disk electrode
rGO	Reduced graphene oxide
RHE	Reversible hydrogen electrode
SC	Supercapacitor
SCE	Saturated calomel electrode
SDG	Sustainable development goals
SEM	Scanning electron microscopy
SHE	Standard hydrogen electrode
SSA	Specific surface area
SWCNTs	Single-walled carbon nanotubes
$\Delta S$	Zero-point corrections to the entropy
$T$	Temperature
TEM	Transmission electron microscopy
$U$	Electrode overpotential
XPS	X-ray photoelectron spectroscopy
ZnPc	Zinc phthalocyanine
$\Delta ZPE$	Zero-point corrections to the total
$v$	Potential scan rate
$\omega$	Electrode rotation rate

# 1 Literature overview

## 1.1 Oxygen reduction reaction

The oxygen reduction reaction (ORR) is one of the most important processes in electrochemical energy conversion devices, such as fuel cells (FCs) [8,9] and metal-air batteries (MABs) [10]. It can be used to produce hydrogen peroxide industrially as well [11]. The ORR is quite complicated process, depending on the electrode material and electrolyte, it can produce different intermediates. In alkaline medium, the ORR can proceed via two pathways [8]:

4- electron pathway:



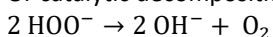
or 2-electron pathway:



Which is followed by reduction:



Or catalytic decomposition:



All the potentials are shown as standard potentials regarding standard hydrogen electrode (SHE) at 25 °C.

Simplified schematic representation of the ORR in alkaline media is shown in Figure 1 [12]:

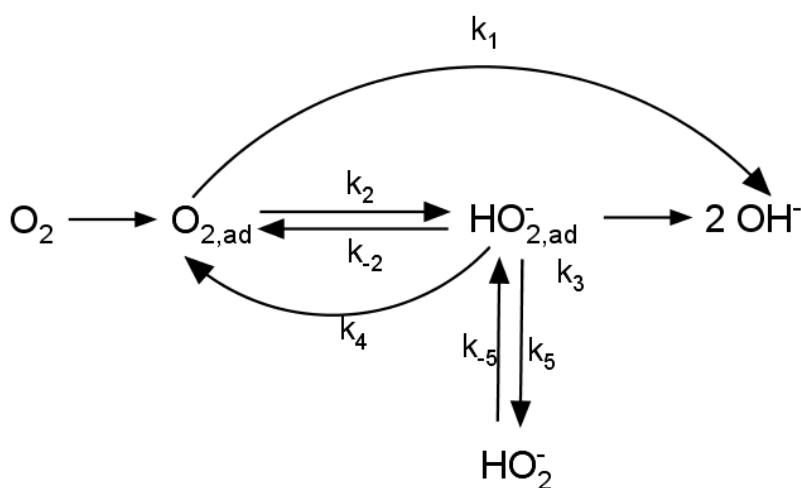


**Figure 1.** ORR reduction in alkaline media,  $k_i$  denotes the rate constants of different steps and (ad) denotes adsorbed species [12].

In case of fuel FCs and MABs, the direct 4-electron reduction is preferred, because the  $\text{HOO}^-$  anions can cause corrosion to the FC components if they do not get reduced further. The formation of  $\text{HOO}^-$  decreases the efficiency of the FCs as well. The 2-electron process could be used as an alternative to the industrial process to produce  $\text{H}_2\text{O}_2$  [13].

## 1.2 Transition to low-carbon energy and fuel cells

Low-carbon energy transition is essential to achieve the UN 2030 Sustainable Development Goals (SDGs) [14]. Intense research has been put into developing highly efficient electrode materials that could promote the ORR. As this is the key process that takes place in FC and MAB cathodes. Up to know, platinum group element (PGE) catalysts are the most widely used catalysts, but the high cost, scarcity, poor stability and the intolerance to fuel crossover have restricted the large-scale application of PGEs in energy conversion systems [15–17]. The further development of the fuel cell vehicles (FCVs) will rise the demand for PGEs [16,18]. Most of the studies are oriented towards the cost of FCs rather than the availability of the Pt itself [16], but Bodreau *et al.* [19] have found that if the global FCVs market develops, a maximum of 15% penetration of FCVs on the automotive market is probable. By combining historical data and scenario for Pt recycling, Sun *et al.* have found in 2011 that if FCVs reach 40% of light-duty vehicles (LDVs) by the year 2050, the increase in Pt price would be around 70% over the current one [20]. Today, the Pt-loading on the anode side is around  $0.05 \text{ mg cm}^{-2}$ , but at the cathode side the loading is almost 10x higher, mainly due to the low ORR rate, meaning that  $\sim 90\%$  of the Pt in the FC is located at the cathode [21].

Anion exchange membrane fuel cell (AEMFC) is a device that converts electrochemical energy into electricity [8]. The main difference between batteries is the fact that the production of electricity is possible until there is fuel supplied and there is no need to recharge, but to refuel. Since in the alkaline media the ORR proceeds more easily, it is possible to use non-PGE catalysts [22]. The schematic representation of AEMFC is shown on Figure 2 [23]. The main drawback of AEMFCs is their durability [24–27]. It is important to find or create a thin membrane, which can create good conductivity ( $>100 \text{ mS cm}^{-1}$ ), deliver sufficient current density ( $>0.5 \text{ A cm}^{-2}$ ), while also achieving the target stable operation time (5000 h at  $80 \text{ }^\circ\text{C}$ ) [26].

In this work, different non-PGM and metal-free catalysts are studied as potential catalyst materials for the AEMFC. Both these topics are important in order to finally achieve breakthrough in non-PGM catalysts in the field of electrocatalysis.

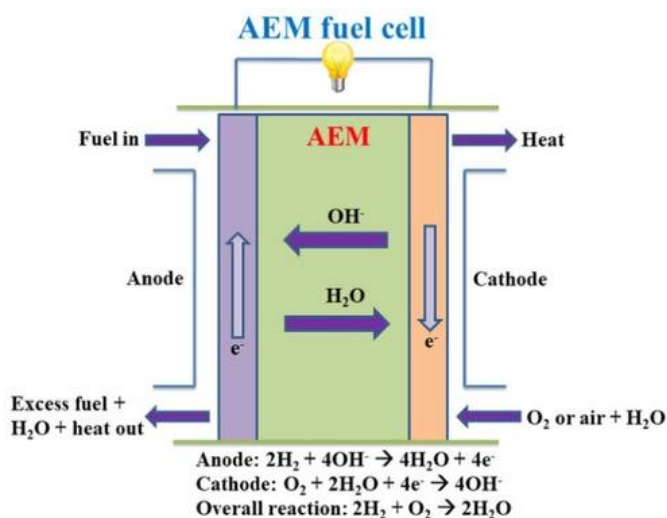


**Figure 2.** Schematic representation of AEMFC and reactions taking place at anode and cathode [23].

### 1.3 Carbon nanomaterials and ORR

Due to their variety of microstructures and morphologies, exceptional properties and wide potential applications, the carbon nanomaterials have been the focus of research in the past 30 years. Carbon nanomaterials have high specific surface area (SSA), pore distribution, high mechanical strength and conductivity (electrical, thermal), which makes them attractive materials for energy conversion and storage systems [28–30]. Carbon-based nanomaterials have been used as catalyst carriers and electrocatalysts [9,31]. In alkaline media the electrocatalytic activity towards the ORR is connected to the quinone groups that are on the surface of the catalyst [32], but at lower pH values, the activity of these groups decreases notably [33].

Graphene was discovered by Geim *et al.* in 2004 [34]. It has the thickness of one carbon atom and consists of carbon atoms in  $sp^2$  hybridisation in a six-member honeycomb lattice [35]. Graphene has various desirable properties, such as excellent electronic conductivity, high SSA and mechanical properties, high chemical stability [17,36]. Without defects in the honeycomb lattice, the oxygen content is very low or even non-existent [37]. Graphene oxide (GO) is the exfoliated structure of graphite oxide and the reduced graphene oxide (rGO) is achieved by reducing the GO thermally, chemically or hydro/solvothermally [31]. Although these above-mentioned properties should have a positive effect for achieving high electrocatalytic activity, in practice, due to Van der Waals interactions and  $\pi$ - $\pi$  stacking between layers, graphene sheets can easily restack and aggregate, which in turn lowers the SSA and hinders the oxygen transport [38]. This is the main reason, why the research has rather shifted to functionalised and/or heteroatom-doped graphene and its composites [38–40]. The doping will alter the electronic structure and conductivity of the material, which helps to improve catalytic activity, and the functionalisation will aid the solubility, which helps against restacking [36,41]. Heteroatom-doped graphene-based catalysts have shown outstanding electrocatalytic activity towards the ORR in alkaline media [40,42,43].

Since the first observation of carbon nanotubes (CNTs) by S. Iijima in 1991 [44], the research carried out by employing carbon nanomaterials in various applications has grown enormously. CNTs are, in essence, six-membered carbon-based sheets rolled up to form tubes. Due to the hollow geometry and conjugated  $\pi$ -electron structure, CNTs possess many exceptional mechanical, thermal, optical, electrical and chemical properties, making them ideal for various applications [37]. Depending on the number of sheets, CNTs are classified into two different types: (a) single-wall carbon nanotubes (SWCNTs) and multi-wall carbon nanotubes (MWCNTs) [35]. A SWCNT is a single sheet of honeycomb lattice rolled-up, with a diameter ranging from 0.4 to 2 nm. A MWCNT consists of at least two or more layers of graphene sheets and the diameter can range between 5 to 20 nm. The lengths range from 100 nm to even several centimetres for both [45]. As CNTs are synthesised by employing metal catalysts, traces of catalysts remaining in the tubes after synthesis is a common problem [30]. This is especially relevant for the purpose of electrocatalysis, because the metals (Fe, Co or Ni) that are used as common catalysts are very active towards the ORR as well [46]. To remove these impurities, acid-treatment is carried out by employing concentrated acids (mixture of  $H_2SO_4$  and  $HNO_3$ , mainly) that helps to dissolve residual metal particles and dissolve impurities [30]. Treatment with oxidising agents improves the effectiveness of doping as the oxidation introduces oxygen-containing groups, which will increase the solubility [37] (CNTs are quite difficult to disperse in many solvents without functionalisation) and which are quite easy to substitute with heteroatoms [17,47] and desired dopant metals

[37]. The oxidative treatment must be carried out carefully, as the acid treatment is quite harsh (high temperature, concentrated acids). Thus, the defective sites at the surface of CNTs could be oxidised, which will in turn shorten or even destruct the CNTs [30], as a result the catalytic activity decreases.

Most of the extensively used nanocarbons for the ORR are synthesised by employing fossil fuels (e.g. phenol, methane, ethylene) and/or relatively harmful (large CO<sub>2</sub> footprint) and not easily scalable methods [40,48]. Research has been carried out in order to study the environmental effects etc. on the production of carbon nanomaterials [49]. But the laboratory scale and industrial scale production are not comparable [50]. For example, the state-of-the-art catalyst carrier for FCs, carbon black, is synthesised by using the incomplete combustion of liquid and gaseous carbonaceous fuels (mainly aromatic hydrocarbons) [45,46]. Since carbon black is amorphous, it has problems with oxidation at higher potentials when employed in FCs [51]. On a large scale, graphene that is very important in battery manufacturing and electrocatalysis overall, is synthesised by chemical vapor deposition (CVD) method [40,47]. But CVD is more expensive than top-down methods [38,47] and produces toxic by-products, which are removed from the chamber with the gas flow [38]. The mass production of high-quality graphene is rather challenging. CNTs are most commonly produced by arc discharge technique or CVD method [17,39], latter is preferred for the mass production [38]. It is possible to synthesise CNTs on a large scale by employing arc discharge method as well, but the operation temperatures are above 1700 °C, it produces unwanted carbon side products and contains metal catalysts, so the synthesised CNTs must be purified [17,39,40]. CVD method has many advantages over arc discharge method, but the nanotubes produced vary greatly in the quality of the structure [17]. Despite all this, carbon nanomaterials owing to their morphology and porosity, offer advantages for the electrocatalysis. For example, the high SSA offers channels that help to boost O<sub>2</sub> transfer and mass diffusion, the high SSA also increases the number of active sites [52].

#### **1.4 Heteroatom-doped carbon nanomaterials and ORR**

Since Gong *et al.* [53] discovered the electrocatalytic activity of N-doped carbon nanotube arrays towards the ORR in alkaline media, an enormous amount of research on metal-free carbon-based electrocatalysts has been published [54]. Different heteroatoms, such as nitrogen [55–57], boron [58–60], phosphorus [61–63], sulfur [64–66] have been used for doping. Despite that, N-doped carbon nanomaterials are still the most studied and applied as catalysts for the ORR [67,68]. Due to similar atomic radii of nitrogen and carbon (74 pm and 77 pm, respectively) the N-doping has achieved the most interest, since it possesses easy doping process and greater stability than of other heteroatoms [69]. The above-mentioned heteroatoms have different electronegativity values and atomic sizes in comparison to carbon, and as a result, doping will lead to a change in their charge distribution and electronic properties [70]. The fact that nitrogen is next to carbon in the periodic table makes it relatively easy to incorporate it into the carbon skeleton without too much distortion (similar atomic sizes, number of valence electrons) [67]. The formation of N-functionalities will introduce additional electrocatalytically active sites [15,71]. Nitrogen is able to create chemically stable species in the carbon framework, which makes carbons durable under electrochemical operation [21]. The electronegativity of N (3.04) is higher than of C (2.55) [67,70], so, the N-doping creates defects into the carbon structure since N atoms change their configuration [70,72]. The defects can increase the electrical conductivity, wettability and the surface

polarity of carbons, thereby enhancing electrocatalytic activity towards the ORR [15,73]. Of course, other types of defects, e.g. unsaturated C atoms, vacancies or additional structural defects are relevant in electrocatalytic activity [21]. The effect of defects is positive only as long as the conductivity of the catalysts remains high enough, to ensure efficient electron transport to the active sites [21]. Due to different electronegativities, the electron withdrawing ability of nitrogen atoms will induce a net positive charge in nearby carbon atoms and this charge delocalisation facilitates the adsorption of O<sub>2</sub> and further reduction [70,72].

Although there are great disagreements if the bulk content of the nitrogen plays even a very important role in the electrochemical activity, some studies have found that the catalytic activity is related to N content [70,74,75]. Meanwhile other studies have found that the relationship between doping sites and catalytic activity is more important than the amount of N [15,21,70,76]. Pyridinic-N is mainly named to be responsible for the high ORR activity [21]. Pyridinic-N is important because due to lone pair of electrons in the carbon structure, it can increase the carbon's electron donor properties, as a result facilitating the reductive O<sub>2</sub> adsorption [70]. So the active sites are not exactly nitrogen atoms, but the neighbouring carbon atoms, where O<sub>2</sub> is first attracted, chemisorbed and finally reduced [21].

Boron forms electron-deficient compounds and the doping of B into the carbon network will give a partial positive charge on B atoms (electronegativity of B is 2.04), thus the partially positively charged B atoms serve as active sites for the ORR [77]. P has bigger atomic radius (110 pm) and lower electronegativity than carbon (2.19), so P-doping will create defect sites and modify the electronic properties, induces greater electron conductivity than of N-doping [78], and therefore has a positive effect on electrocatalytic activity as well [79].

As the atomic radius of S (102 pm) is larger than that of N (77 pm) or C (75 pm), the doping of carbon lattice with S is more difficult [77,80]. Although, it is predicted that S-doping will create positively charged catalytic centres for the ORR [81], the change of charge distribution in case of S-doped carbon is rather small due to similar electronegativities (2.58 for S vs 2.55 for C) [64]. The main effect will rise due to the spin density changes as suggested by Yang *et al.* [64]. The replacement of C atoms with S atoms will create more vacancies and defects due to different atomic radii [80]. Other authors have found that the presence of sulfur in the carbon is responsible for defects in the C framework, which in turn are responsible for the increased catalytic activity towards the ORR [82]. But most of the research carried out with doping of carbons with boron or sulfur is rather concentrating on co-doping with nitrogen and their synergistic effects. Thus, the exact mechanism of improvement of the ORR regarding S-doping is not so clear [21].

The nitrogen doping of carbon nanomaterials can be achieved by carrying out high temperature treatment with N-rich chemicals, such as melamine [83–85], urea [72,83,86] or dicyandiamide (DCDA) [87,88]. These N-rich precursors decompose at less than 800 °C, first forming graphitic carbon nitride (g-C<sub>3</sub>N<sub>4</sub>), which decomposes at temperatures higher than 700 °C and then forms NH<sub>3</sub> and carbon nitride gases, such as C<sub>2</sub>N<sub>2</sub><sup>+</sup>, C<sub>3</sub>N<sub>2</sub><sup>+</sup> or C<sub>3</sub>N<sub>3</sub><sup>+</sup> [89–91]. The N-doping will create four main nitrogen configurations: pyridinic-N, pyrrolic-N, pyridine-N-oxide and quaternary-N (or graphitic-N) [67,71]. In pyridinic-N the nitrogen atom is connected to two carbon atoms at the edge of graphene plane (donating one p-electron to the π-system); in pyrrolic-N the N atoms are bonded to two C atoms (giving two p-electrons); in pyridine-N-oxide the N atoms are bonded to two

carbons and one oxygen; in quaternary-N the substituted N atom is connected to three carbon atoms [68,70]. All these different nitrogen configurations are shown in Figure 6 [80]. It has been found that pyridinic-N is the most active species towards the ORR, mainly due to the lone pair of electrons that are easily accessible to oxygen [68,92,93]. Rao *et al.* have prepared vertically aligned N-doped CNTs by varying polymer precursors [94]. They found that the catalytic activity of the materials was connected with the increase of at.% of pyridinic-N – the higher the pyridinic-N at.%, the higher electrocatalytic activity towards the ORR was achieved. Miao *et al.* prepared N-doped reduced graphene oxide (rGO) catalysts by employing hydrothermal method that was followed by annealing at different temperatures (from 600–800 °C) [95]. The content of pyridinic-N increased with the higher annealing temperature as well as the electrocatalytic performance, suggesting that pyridinic-N is the active site responsible for ORR activity in N-doped carbons. Combining experiments (ORR, high-resolution XPS) and DFT calculations, the ORR activity of different nitrogen configurations is found to be as follows: pyridinic-N > pyrrolic-N > graphitic-N > oxidised-N [21,68]. Of course, there is still ongoing a huge debate about the active sites and nitrogen species that contribute to the ORR in carbon materials, because it is very difficult to dope carbon with only one specific nitrogen species [21]. In addition to creating nitrogen active sites, surface hydrophilicity of the material is increased with N-doping, because N functional groups are hydrophilic, which in turn will make the contact between the electrolyte and catalyst material more efficient [80]. Although, the outstanding catalytic activities of N-doped nanocarbons are usually measured in alkaline media and the activity is much lower in acidic media [21]. Since the stability of metal-free catalysts is much better than metal-based carbons and their structure is tuneable due to rich surface chemistries, the non-metal catalysts do not suffer from metal dissolution and poisoning [96].

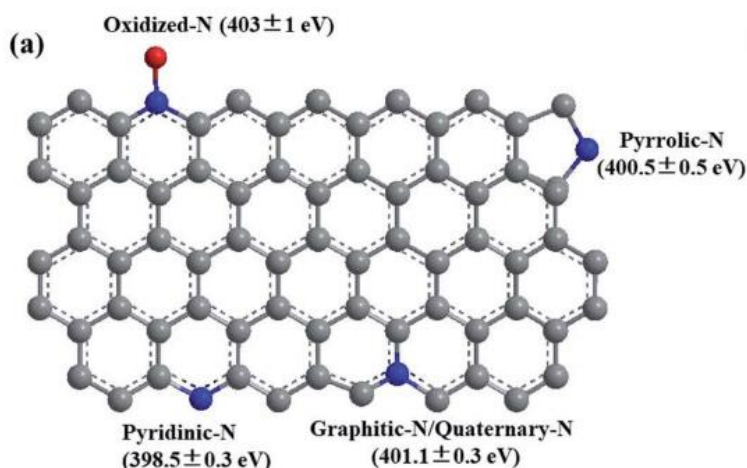


**Figure 6.** Main N-species on N-doped carbon [80].

Next to mono-doped carbon catalysts, the co-doping of carbon nanomaterials with two or more heteroatoms can enhance the catalytic activity even further, by increasing the number of active sites and possible synergistic effects [77]. The co-doping is mainly carried out by doping with N and a second element, such as B [97,98], S [99,100] or P [101,102]. Liang *et al.* have produced N and S co-doped graphene catalysts by using

melamine and benzyl disulfide as N and S precursors, respectively [100]. The resulting N-S-G catalyst showed N content of 4.5 at.% and S content of 2.0 at.% and the onset potential ( $E_{\text{onset}}$ ) of  $-60$  mV (vs Ag/AgCl reference electrode) which is close to that of commercial Pt/C and much more positive than of just N-G, S-G or G, indicating to the synergistic effect to co-doping as well [100]. Actually, a lot of attention has been paid to co-doping of N along with S, due to fact that it has been found that it is easier to replace C with S when N is doped together with sulfur [93]. Compared to mono-doped N-graphene, theoretical calculations showed that the difference in charge density around nitrogen atoms before and after doping with sulfur is similar, so the electrocatalytic activity enhancement is not connected with the change of electron charge density [103]. The differences in spin density in co-doped materials is more important, meaning that a number of C atoms could serve as electrocatalytically active sites as well [103]. Most of the studies show that co-doping will lead to higher catalytic activity than of mono-doping [37,98,104]. Hu *et al.* have showed that not all B and N co-doped carbons show higher electrocatalytic activity [104]. Combining theoretical and experimental results, they showed that when B and N are bonded, they cannot activate CNTs, but separated B and N can. Additionally, the co-doping definitely has an effect on the defects by the example of ordered mesoporous carbons (OMCs). For example, Ye *et al.* have compared the intensity ratio of D and G bands in Raman spectra ( $I_D/I_G$ ), which is widely used to evaluate structural defects in carbon nanomaterials [105]. The corresponding  $I_D/I_G$  values for undoped OMC, N-doped OMC and N,S co-doped OMC were 1.0, 1.01, 1.08, respectively. Deng *et al.* have shown that the  $I_D/I_G$  ratio of N,P co-doped OMC was higher (0.95) than of just N-doped OMC (0.92) or P-doped OMC (0.86) [101]. Zeng *et al.* found that the highest  $I_D/I_G$  was achieved with N,B co-doped OMC (1.31) and the value was much higher compared to N-doped OMC (1.20), B-doped OMC (1.25) and undoped OMC (1.16) [106]. This indicates that the co-doping will indeed create a synergetic effect of different heteroatoms, and this may provide more active sites towards the ORR. Co-doping gives rise to bi- or even multifunctional catalysts that can be used for different reactions [96]. Zhang and Dai [107] have prepared even tri-doped graphene that was employed as a trifunctional electrocatalyst for the ORR, OER and HER. Although there are many reports on co-doping [77,93,96–102,105–109], the challenges still lay behind the fact that it is hard to control the content, location and distribution of dopants, which in turn has an effect on the electrochemical activity [96].

In this work, heteroatom doping is carried out to produce oxygen electrocatalysts for the ORR. Since up to now, there are not commercial heteroatom-doped catalysts developed for the AEMFCs, the research in this field is utmost important.

## 1.5 Biomass-based carbon nanomaterial synthesis and ORR

Because of the growing concern on global warming and the depletion of fossil fuels, there is a great urge to find more environmentally friendly and economically feasible ways to produce carbon nanomaterials. The number of articles in WoS Core Collection that contain “biomass” and “carbon” in all the fields, restricted to “synthesis” has been growing every year, the bar chart can be seen on Figure 3, the number of articles since the year 2013 has grown around five times (331 records in the year 2013 vs 1491 records in the year 2021). Compared with the traditional carbon nanomaterials synthesis methods, the utilisation of biomass as a precursor for the production of porous carbons has several advantages: (1) precursor materials are cheap, sustainable and widely available; (2) valorisation and utilisation of waste materials (promotes circular economy) [15].



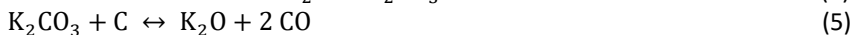
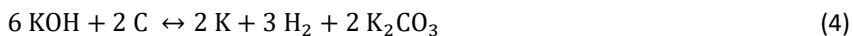
**Figure 3.** Number of records from WoS Core Collection of articles consisting of “biomass”, “carbon” in all fields, restricted to “synthesis”.

Biomass resources can be roughly classified as plant (lignocellulosic) or animal. Plant biomass consists mainly of agricultural residues and animal biomass is the waste (feathers, shells etc.), that mainly consists of proteins and minerals [108]. More precisely, biomass is classified into 7 categories: (1) fungus-based biomass; (2) bacteria-based biomass; (3) marine algae and plants-based biomass; (4) herbaceous and agriculture-based biomass; (5) human-waste-based biomass; (6) industrial-waste-based biomass; (7) animal-based biomass [70]. Around 200 billion metric tons of lignocellulose is produced around the world every year [109], it is composed of natural polymers, such as phenolic polymer, cellulose (40–50 wt.%), lignin (15–30 wt.%) and hemicellulose (25–30 wt.%) [110], but the distribution of different components can vary depending on the source [111]. Lignin has a higher carbon content (up to 60 wt.%) than cellulose or hemicellulose and it contributes to ~30% of organic carbon in the biosphere [112]. It is one of the main by-products of the pulp and paper industry and biorefineries [113].

Since all these polymers consist mainly of carbon, lignocellulosic biomass is a good precursor to synthesise carbon nanomaterials [70,114]. Lignocellulosic biomass is easily obtained from various and widely available agricultural products and by-products [111]. To produce carbon, the first and inevitable step is carbonisation, which is carried out at relatively low temperatures (<800 °C), the achieved biochar is quite dense and the pores are filled with tarry residues, resulting in a low surface area [114,115]. At the first stage (<100 °C), mainly moisture volatilises, but when the temperature is around 220–315 °C, hemicellulose degrades, cellulose degradation happens around 315–400 °C, but lignin covers even wider temperature ranges (up to 1000 °C) [109,116]. In the second step, an activation process is needed to create an activated porous carbon network [15,71,111]. Porous carbons can have micropores (diameter is less than 2 nm), macropores (diameter more than 50 nm), and mesopores (diameter between 2 to 50 nm) [17,68]. Micropores are needed to reach high surface areas and increase the number of active sites, macropores are needed for the fast mass transfer and mesopores are needed so electrolytes and reactants could enter the active sites that are buried deeper under the surface of catalyst (mainly in micropores) [17,21]. The ORR activity is connected to the pore structure and SSA, so in order to achieve better mass diffusion and kinetics of the

reaction, the pore structure optimisation is needed [17]. The fast transfer of oxygen from solution to active sites is a key step in achieving high current density.

Besides pyrolysis, other methods, such as hydrothermal carbonisation (HTC) and microwave heating, have also been developed [111]. Sometimes the carbonisation and activation processes are carried out subsequently [111]. Activation is divided into physical and chemical activation [115]. In physical activation the activation is carried out by employing oxidising gas (steam, air, CO<sub>2</sub> or their mixtures) at temperatures ranging from 800 to 1100 °C [15,70,110]. In chemical activation, activating agents (e.g. alkali hydroxides) are used and it is carried out at lower activation temperatures [117]. Zhang *et al.* [118] have employed CO<sub>2</sub> activation of biomass-based carbons from different types of forest and agricultural residues. As a result, microporous carbons were produced, with the SSA ranging from 400 to 1000 m<sup>2</sup> g<sup>-1</sup>, but they concluded that higher activation temperature results in a larger SSA and micropore volumes. Chemical activation is carried out by utilising corrosive chemicals that are called activating agents (e.g. KOH, ZnCl<sub>2</sub> and H<sub>3</sub>PO<sub>4</sub>) [15]. The activating agent is mixed with carbon and then heat treated at a high temperature under inert gas atmosphere. KOH is the most extensively used activating agent and the mechanism is as follows [15,117,119]:



As KOH melts around 360 °C, the reactions take place at a solid-liquid interface. The carbon oxidation by KOH Eq. (4) starts around 400 °C as metallic K, H<sub>2</sub> and K<sub>2</sub>CO<sub>3</sub> form and above 700 °C carbon reacts further with K<sub>2</sub>CO<sub>3</sub> Eqs (5)–(7). In addition to chemical etching of both KOH and K<sub>2</sub>CO<sub>3</sub>, the release of gaseous products (H<sub>2</sub>, CO<sub>2</sub> and CO) facilitates the formation of pores in the carbon. The metallic K can intercalate into the carbon lattice and that produces micropores through a physical effect [117].

There are several works, where different activating agents have been compared. For example, Li *et al.* have prepared hierarchical porous active carbons by using fallen leaves as the carbon source [119]. They tried the activation with KOH and K<sub>2</sub>CO<sub>3</sub>, the SSA was much lower when using K<sub>2</sub>CO<sub>3</sub> instead of KOH (1003 m<sup>2</sup> g<sup>-1</sup> vs 2869 m<sup>2</sup> g<sup>-1</sup>). Kwiatkowski and Broniek have compared the activation of carbon with CO<sub>2</sub>, H<sub>2</sub>O, K<sub>2</sub>CO<sub>3</sub>, KOH, H<sub>3</sub>PO<sub>4</sub> and ZnCl<sub>2</sub>, the SSA values were as follows: 968, 1057, 912, 2031, 1333 and 1643 m<sup>2</sup> g<sup>-1</sup> [110]. Comparing physical and chemical activation, the latter is more favourable, as it produces activated carbons (ACs) with higher quality (high carbon yield, higher pore volume and SSA) and the activation process is more efficient (lower heating temperature and shorter time) [70,111,115,117]. The advantages of chemical activation are shown in Figure 4 [114]. It has been found that chemical activation removes selectively non-graphitic parts, whereas the physical activation does not [120]. Although, since chemical activation uses corrosive chemicals, the utilisation of the waste products must be considered, otherwise it could cause environmental effects if hazardous and toxic substances are not managed properly.

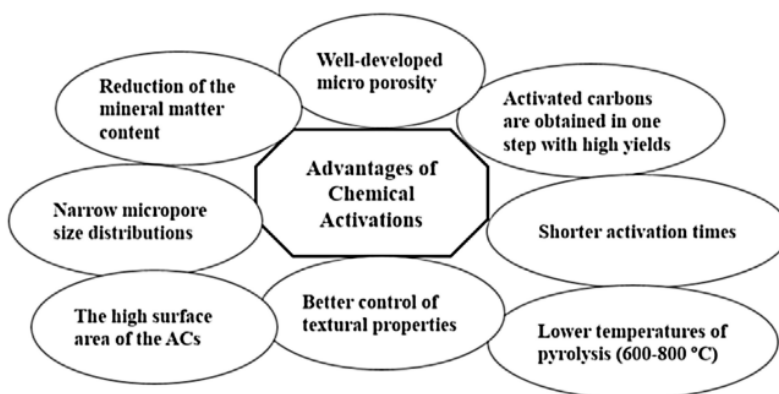


**Figure 4.** The advantages of chemical activation [110].

Microwave-induced activation has also been used in order to create ACs [121,122]. Wu *et al.* [121] prepared microwave assisted KOH activation of peanut shell and achieved carbons with SSA of  $1277 \text{ m}^2 \text{ g}^{-1}$ . Microwave activation is much faster than the conventional pyrolysis, but the number of research articles in the field of energy storage devices discussing this method is rather low, possibly because this method creates noticeable reduction in micropore volume and size [123].

The characteristics (carbon content, ash content, SSA, porosity) of the prepared carbons highly depend on the precursor material and the activating agent and synthesis conditions (temperature/heating rate/residence time of the pyrolysis, etc.) [15,111]. And the choice of carbon sources depends highly on cost, availability and quality (low inorganic and volatile contents, high C content) [117]. The achieved ACs can be used in various applications: water and wastewater treatment (heavy metals, dyes, organic compounds, pesticides removal) [124,125], supercapacitors (SCs) [15,71,126], FCs [108,127,128], lithium-/sodium- ion batteries [129,130], etc. Different activation and modification steps of biomass-based carbons and the possible applications are shown in Figure 5 [115,131,132]. Although for FC applications, most of the authors concentrate on heteroatom and/or metal-doping [133], there are some reports, where activated biomass-based carbons have been used as a cathode catalyst in the ORR [134–136]. For example, Nunes *et al.* have prepared activated carbons using sucrose as the biomass precursor and employing HTC and chemical activation [134]. They used  $\text{K}_2\text{CO}_3$  or KOH as activator. Physical and electrochemical characterisation revealed that the KOH activated sample had a SSA of  $2431 \text{ m}^2 \text{ g}^{-1}$  and the micropores on average had wider diameter. Sucrose-derived hydrochar activated with KOH showed higher current densities and higher stability in methanol tolerance testing than commercial Pt/C, but the ORR proceeded via a 2-electron process (selectivity to  $\text{H}_2\text{O}_2$ ) [134]. Thus, the generation of highly porous networks and/or defects could help to create more active sites for the ORR, but it is important to select the suitable activation reagents in order to fabricate biomass-based carbon nanomaterials that could possess ORR activity even without doping [136]. Biomass-derived carbons can serve as efficient catalyst carriers for Pt nanoparticles. Guilminot *et al.* have demonstrated a carbonised aerocellulose as a support for depositing Pt nanoparticles [137]. The mass activity was smaller than of commercial Pt/C, but the research showed that it is possible to find green and low-cost

methods to prepare supports for Pt catalysts. Rooke *et al.* have used carbonised aerocellulose as a support for Pt and achieved comparable results with the available state-of-the-art Pt catalyst [138].

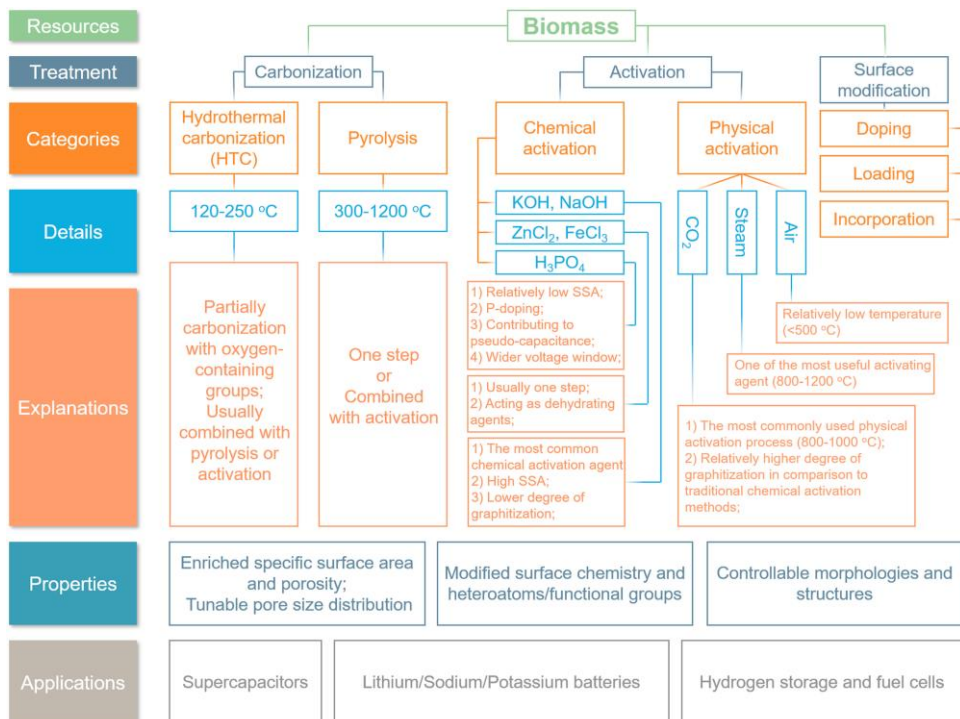


**Figure 5.** Different biomass treatment methods and end applications [115].

It is possible to synthesise different carbonaceous structures out of biomass, with the porosity and SSA depending highly on the activation method. By varying the synthesis conditions (temperature, time, activating agents) it is possible to tune the final product quality (yield, porosity, etc.) [12]. There are reports of converting biomass into different carbon structures, such as graphene [54,139], amorphous high SSA carbons, carbon nanotubes/nanofibers [140,141]. As already mentioned, using biomass as a precursor is an attractive way how to contribute to the circular economy and find alternative ways for carbon nanomaterial synthesis. The challenges for full commercialisation of biomass-derived carbon include [128]:

- 1) Finding cost-effective ways for the synthesis to prepare high-performance biomass-based carbons for electrochemical energy conversion systems
- 2) Better fundamental understanding by combining experiments and theoretical calculations about the degradation mechanisms – this gives a better understanding about synergetic effects of different components and helps to perform further optimisations
- 3) Optimisation different important parameters (combination of porous structure, SSA, defects and active sites) in order to reach better electrochemical performance
- 4) Exploration of possible application to produce flexible and portable electrode materials (for flexible Li-ion batteries (LIBs) and SCs)

- 5) Progress in scalable synthesis strategies to produce biomass-based carbon nanomaterials for practical and commercial materials for electrochemical energy systems (LIBs, SCs and FCs)

## 1.6 Heteroatom-doped biomass-based carbon nanomaterials and ORR

Since the cost of energy conversion and storage systems (FCs, supercapacitors) is too high to be deployed on a large scale, the conversion of biomass into carbon and the heteroatom doping has gained a lot of interest in the scientific world [115]. The performance of these above-mentioned electrochemical energy conversion devices depends strongly on the properties of electrode and electrolyte materials, so the cost-effective and environmentally friendly synthesis routes are needed to gain satisfactory properties that match the energy devices requirements [128].

Compared with other widely employed carbon nanomaterials, such as graphene, CNTs, the biomass-based carbon nanomaterials are more sustainable, cost effective and relatively easy to prepare. As the professor Donald Sadoway said in his TED talk "The missing link to renewable energy": "... if you want to make something dirt cheap, make it out of dirt – preferably dirt that's locally sourced." [142]. As already discussed above, to produce porous carbon nanomaterials out of biomass, the activation step is inevitable. It has been found that all biomass material treated with alkali metal hydroxide will produce carbons with high SSA, N-content and good stability and electrocatalytic performance [70]. Since huge amount of biomass (e.g. agricultural residues, forest by-products) is simply burnt and this has very low efficiency and causes air pollution [116], there is a great need to valorise this type of waste materials.

Different biomass precursors have been used to synthesise heteroatom-doped carbon nanomaterials and there are practically two popular ways to prepare heteroatom-doped biomass-based nanocarbons: (1) 'in situ doping', where direct pyrolysis of biomass precursors is carried out to achieve self-doped biomass-based carbon nanomaterials [79,116] or (2) 'post doping', where pyrolysis in the presence of heteroatom-containing organic compounds is performed [79]. The self-doping comes into play when the precursor biomass consists of the heteroatoms needed. The examples that contain nitrogen in addition to carbon are chitosan [143], collagen [144], pomelo peel [145], protein-rich biomass (horns, bones, chicken feathers) [146], fungi [146], etc. Precursors that lack N or other heteroatoms commonly require doping with a doping agent to achieve electrocatalytic activity relevant in FCs. These precursors include lignocellulosic biomass (consists of cellulose, hemicellulose, lignin) [70,109]. The content of N in different biomasses will decrease in the following order: 1) animal-derived biomass; 2) fungus biomass; 3) food biomass; 4) contaminated/industrial-based biomass; 5) bacterial biomass; 6) marine algae and plants biomass; 7) human-waste biomass; 8) herbaceous and agricultural biomass [70]. Sometimes the precursor materials can already contain heteroatoms, and it is possible to carry out self-doping. For example, Demir *et al.* have produced sulfur self-doped biomass-based carbon by using a calcium lignosulfonate (lignin derivative) as a precursor [147]. So, it is possible to employ simple synthesis routes to prepare electrocatalysts from the industrially produced waste materials.

The nitrogen content in the final N-doped biomass-based nanocarbons can vary greatly depending on the procedure and dopants. For example, there is a report where glucose has been used as a precursor and thiourea as a N source and the final N content is between 9.53 to 18.50 atomic percent (at.%) [148].

Biomass is a good precursor to synthesise carbon catalysts that possess high SSA and tuneable porosity, both which are important in order to achieve high electrochemical activity [116], since they promote the electrolyte penetration and shorten the diffusion distance of the ions [115].

Chen *et al.* [149] have prepared N-doped porous carbon nanosheets using *Typha Orientalis* as a precursor, the SSA was found to be  $898 \text{ m}^2 \text{ g}^{-1}$  and the N content 9.1%. The electrochemical activity was very similar to Pt/C catalyst and the cycling performance was even better. There are reports on preparing the N-doped graphene-like materials from biomass. For example, Guo *et al.* [150] have used fungus and melamine as a nitrogen source and produced graphene-like sheets, which showed good electrocatalytic activity ( $E_{\text{onset}} = 970 \text{ mV vs RHE}$ ) and excellent stability and resistance to methanol in comparison to Pt/C. In addition, pomelo fruit [145] or banana peels [151] have been used to synthesise highly active electrocatalysts.

Practically it is possible to use very wide range of biomass to produce catalysts for fuel cells. The production methods vary depending on the source, but the preparation methods and the achieved properties are highly tuneable and by optimising different parameters, therefore, it is possible to synthesise wide range of doped carbon nanomaterials.

In this work, wood has been used as a precursor for synthesising carbon nanomaterials that are studied as potential ORR catalysts in the alkaline media. The waste valorisation is an important topic and the research carried out within this thesis strives to show the potential value of wood-based waste materials for energy conversion devices.

## 1.7 Non-precious metal-carbon catalysts for the ORR

There are numerous research papers on seeking replacements for platinum-based catalysts, but today, Pt and Pt-based catalysts are still superior. The research is mainly directing in two ways: 1) the research on non-precious metal catalyst materials and 2) the development of metal-free catalysts [21]. Different non-precious metal catalysts that are widely studied are mainly transition metal-based, such as Fe or Co [152]. M-N<sub>x</sub>-C catalysts have achieved a lot of attention, because the binding strength between metal and nitrogen atoms is quite strong, due to the strong hybridisation between 2p orbitals of N and the d-orbitals of transition metals [37]. M-N<sub>x</sub>-C catalysts can be prepared by mixing metal salts, nitrogen source and different carbon carriers [153–155].

In 1964 Jasinski *et al.* discovered the electrocatalytic activity of metal phthalocyanines (MPcs) [7], which initiated the research in this field. Later it was found that the pyrolysis of metal macrocycles increased the catalytic activity and durability even further [156–158].

Pcs consist of four isoindole subunits (Figure 7), connected via meso-positioned N atoms, by varying central ion, the structure allows diverse functionalities – the ligands bound at the axial positions of the metal center, substituents can be bound at the  $\alpha$ - or  $\beta$ -positions (peripheral or non-peripheral) [157]. Almost all elements from different groups in the periodic table can interact with the N atoms in the Pc macrocycle, so there are more than 70 types of metal or metalloid macrocycle complexes and the central metal cation affects the physical properties of the Pc strongly [51, 55, 52]. In case the oxidation state of the central metal cation is +1, nitrogen atoms ligate two ions, typical example is dilithium phthalocyanine ( $\text{Li}_2\text{Pc}$ ) [56,57].

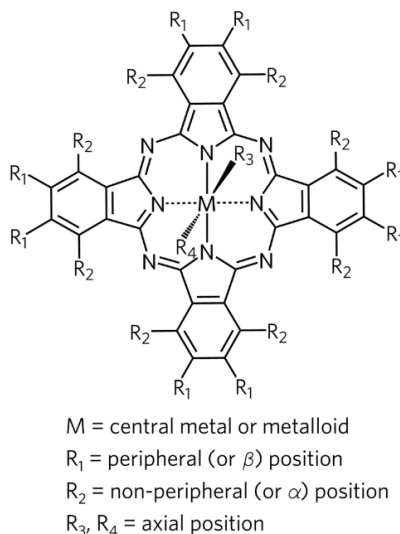


**Figure 7.** Overall structure of Pc [157].

As mentioned above, the thermal treatment of MPc improves their electrocatalytic activity and stability [157]. In terms of heat treatment parameters, most attention has been devoted to the temperature, as this has the significant influence on the structure of Pcs. Very high temperature may be accompanied by the degradation of the Pc and causes metal agglomeration [110]. The best synthesis temperature depends on the Pc and the central metal, of course. And there are some contradictory results in the literature as well, however, it is clear that heating to temperatures above 700 °C leads to formation of a metal- $N_x$ -C structure [157]. Very high synthesis temperature causes the full degradation of the macrocycle, which is followed by the agglomeration of metal nanoparticles [159].

Among macrocycle-based catalysts, FePc- and CoPc-based electrocatalysts are the most extensively researched and could possibly replace Pt-based catalysts in the FC applications [157]. Central metal atoms of the Pc ring have a great influence on the catalytic activity of unpyrolysed macrocycles, by comparing the onset ( $E_{\text{onset}}$ ) and half-wave potential ( $E_{1/2}$ ), the sequence in case of Pc is as follows:  $\text{Fe}^{2+} > \text{Co}^{2+} > \text{Mn}^{2+} > \text{Cu}^{2+} > \text{Ni}^{2+} > \text{Zn}^{2+}$  [158].

Thus far, atomically dispersed M- $N_x$  sites are known as the most active species towards the ORR after PGMs. Mukerjee *et al.* have carried out in-situ XANES measurements to identify the changes of Fe- $N_x$  structure upon  $\text{O}_2$  exposure [160]. The Fe(II)/Fe(III) redox couple in the Fe- $N_x$  centre was found to be responsible in the ORR activity. Some of the studies have shown that M- $N_2$  and M- $N_{2+2}$  could also be the active sites for the ORR, therefore, the structure of the active sites of non-noble metal catalysts could be as follows: M/ $N_x$ /C ( $x = 2$  or 4 or 2+2) [17]. Of course, there are some disagreements on the active sites, other types of active sites proposed are: encapsulated metal-containing species and N-C moieties (without metal) [158].

Although, there are reports of potential application of non-precious metal and N-doped carbon nanomaterials in acidic media and even commercialised product by Ballard Power Systems [161], their performance in acidic media is still rather poor [162]. The mechanisms of the low stability are not known with full certainty, but main

hypotheses include: 1) dissolution/leaching of the metal, 2) oxidative attack by peroxide (or the free radicals that are produced), 3) protonation of the active site or N species near the active site, followed by anion adsorption [163].

The MPc carrier (support) material plays an important role in the preparation of MPc-based catalysts. One of the first used carbonaceous support for loading MPcs was carbon black, since it is widely available, has good distribution of mesoporosity and low cost [164,165]. However, graphitised carbon black, graphene and CNTs are more stable than conventional carbon blacks and possess higher SSA and electrical conductivity, which makes them more desirable support materials for MPcs [166–169].

In this work, first MWCNTs modified with transition metals are studied as electrocatalysts for the ORR. The less studied MPcs are studied as well, and the goal is to show that not only transition metal Pcs are active towards the ORR. The results are important input to the further studies carried out with Pc-modified MWCNTs.

## 2 Aims of the study

The aim of this PhD project was to study different novel electrocatalysts for the ORR, the practical work was divided into three parts:

- 1) The effect of co-doping of carbon composite with sulfur and nitrogen was studied. The aim was to vary dopant ratios and study also different synthesis temperatures in order to find optimal synthesis process for preparing ORR electrocatalyst in alkaline media [III].
- 2) The potential application of biomass as an electrocatalyst was studied. The aim was to employ widely available wood as a precursor to synthesise N-doped carbon catalyst and study the potential application as a metal-free electrocatalyst in alkaline media [IV–V].
- 3) Modification of MWCNTs with different metal phthalocyanines was investigated (MnPc, CuPc, ZnPc, Li<sub>2</sub>Pc). The aim was to use transition metal phthalocyanines, also less studied metal phthalocyanines and evaluate their electrochemical activity towards the ORR in alkaline media [I–II]. Since the MPc has been and still is the topic of interest in my research since my bachelor's studies, a part of this work is also previously covered in my BSc thesis.

## 3 Experimental

### 3.1 Purification of MWCNTs

The purification of MWCNTs was carried out by using method developed earlier [170]. 0.5 g of MWCNTs (purity >95%, diameter  $30 \pm 10$  nm, length 5–20  $\mu\text{m}$  from NanoLab Inc., USA) [I–III] were weighed into a standard 0.5 L three neck cell and then 25 mL of concentrated  $\text{H}_2\text{SO}_4$  and 25 mL of concentrated  $\text{HNO}_3$  was added to the cell. The mixture was then first heated on a magnetic stirrer for 2 h at 55  $^\circ\text{C}$  and then for 3 h at 80  $^\circ\text{C}$ . Afterwards the mixture was cooled to room temperature, washed with Milli-Q water on a vacuum filter until neutral pH was achieved. Finally, the MWCNTs were dried overnight at 60  $^\circ\text{C}$ .

### 3.2 Synthesis of GO

To synthesise GO, graphene powder (Graphene Trading Company) was oxidised by employing modified Hummer's method [55,171] [III]. To start 2.0 grams of graphite weighed into a beaker and mixed with 50 mL of concentrated  $\text{H}_2\text{SO}_4$  and the mixture was sonicated for 1 h. Then 2.0 grams of  $\text{NaNO}_3$  and 6.0 grams of  $\text{KMnO}_4$  were slowly added in a sequence to the mixture (in smaller portions) while magnetic stirring as well. The mixture was then heated at 35  $^\circ\text{C}$  for 18 hours. Once the heating was finished, the beaker was put into ice bath and then 80 mL of deionised water was added and after few minutes 20 mL of  $\text{H}_2\text{O}_2$  (30%, Merck). The mixture was then washed with 10% HCl solution and with Milli-Q water on a vacuum filter. The resulting GO was dried in a vacuum at 75  $^\circ\text{C}$ .

### 3.3 Synthesis of N, S-co-doped catalysts

To synthesise the catalyst materials, first MWCNTs from NanoLab were purified by the method explained in the section 3.1 and GO was synthesised as described in the section 3.2. To synthesise the catalyst material, first GO and MWCNTs were weighed into a vial, the weight of MWCNTs corresponded to the weight of GO. To improve the catalytic performance, the mixture of GO and MWCNTs was doped with N- and S-precursor *o*-methylisourea bisulfate (oMUS) (Sigma Aldrich). First, the mixture of GO and MWCNTs was blended ultrasonically in the presence of polyvinylpyrrolidone (PVP) and isopropanol (Honeywell). Next, the dopant was added with a mass ratio of 1 [1:1 MWCNT/graphene oxide (GO)]/5 (oMUS), the dispersion was sonicated for 1 h in order to achieve homogenous mixture that was later dried in the oven at 65  $^\circ\text{C}$ . The material was then collected into a quartz boat and pyrolysed for 2 h at 800  $^\circ\text{C}$  in flowing nitrogen atmosphere. Afterwards the oven was slowly cooled down and the resulting catalyst material was collected and weighed. The catalyst prepared in the presence of oMUS is denoted as C/oMUS [III]. The oMUS structure is shown on Figure 8:

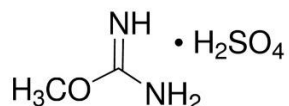


**Figure 8.** Chemical structure of oMUS.

### 3.4 Synthesis of N-doped biomass-based catalysts

Alder wood charcoal with 82% non-volatile carbon content was used as a precursor (SIA Fille 2000, Latvia) [IV–V]. Charcoal was processed in a planetary mill Pulverizette Classic 5 (Fritch, Germany) by employing mortar and beads made from zirconium oxide to reach fraction size of  $\sim 10^{-6}$ . The mass was then impregnated with a 50% of NaOH (Chempur, Pekary Slaskie, Poland) solution (mass ratio of activator-to-carbon was 3 to 1). The mixture was then activated in flowing Ar ( $100 \text{ L h}^{-1}$ ) at  $700 \text{ }^\circ\text{C}$  [IV] or  $800 \text{ }^\circ\text{C}$  [V] for 2 h (Nabertherm 40 L muffle oven, Lilienthal, Germany). The produced AC was then washed with deionized water and 10% HCl solution and again deionized water until the pH reached 5. AC was then dried overnight at  $105 \text{ }^\circ\text{C}$ .

The AC was further doped with nitrogen by using DCDA (Sigma-Aldrich, Germany) solution in dimethylformamide (DMF, Lachner, Czech Republic), with mass ratio of AC:DCDA = 1:20. DMF was then removed in a rotary evaporator and the doping was carried out at  $800 \text{ }^\circ\text{C}$  for 1 h in flowing Ar atmosphere; the sample achieved is denoted as N-AC [IV] or N-AWC [V]. The sample [IV] was later ball-milled once again using  $\text{ZrO}_2$  beads and secondary pyrolysis was performed in the tube furnace at  $800 \text{ }^\circ\text{C}$  in the flowing  $\text{N}_2$  atmosphere, the resulting final catalyst was denoted as N-AC-1. The structure of DCDA is shown on Figure 9:

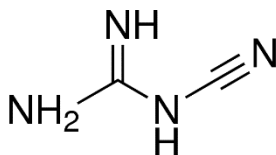


*Figure 9. Chemical structure of DCDA.*

### 3.5 Synthesis of M-N-C catalysts

In order to prepare MWCNT/MPc catalysts, different mixtures of MPc (M = Mn, Cu, Zn, Li) and MWCNTs were prepared in isopropanol by varying the mass ratio (1:3; 1:1 and 3:1) [I–II]. The mixture was sonicated for 30 min (or 1 h [II]) and then left on a magnetic stirrer for an hour [I]. The homogenous mass was then placed into a ceramic boat and pyrolysed at different temperatures ( $400, 600, 800, 1000 \text{ }^\circ\text{C}$ ) in flowing Ar/ $\text{N}_2$  atmosphere. The final loading of MPcs on the MWCNTs was not ascertained. The resulting catalyst powder was collected and weighed.

### 3.6 Preparation of electrodes and electrochemical measurements

To prepare glassy carbon (GC, GC-20SS, Tokai Carbon) electrodes to conduct rotating disc electrode (RDE) measurements, the electrodes were first polished with  $1 \mu\text{m}$  and  $0.5 \mu\text{m}$  aluminium oxide ( $\text{Al}_2\text{O}_3$ ) powders (Buehler). After the surface was very smooth and shiny, the electrodes were sonicated for 5 min in isopropanol and 5 min in Milli-Q water in order to remove any polishing residues left. The catalyst ink was prepared in isopropanol (Sigma-Aldrich) and sonicated for 1 h. The concentration of the coating suspension was  $1 \text{ mg mL}^{-1}$  [I] or  $4 \text{ mg mL}^{-1}$  [II–V] and the ink consisted of 0.25 wt.% of Tokuyama ionomer (Tokuyama Corp., Japan). The electrode was coated total of 4 times by pipetting  $5 \mu\text{l}$  of catalyst ink onto the surface of the cleaned electrode. Electrodes were dried in vacuum at  $60 \text{ }^\circ\text{C}$ . Resulting loading on the electrodes was  $100 \mu\text{g cm}^{-2}$  [I] or  $400 \mu\text{g cm}^{-2}$  [III–V].

RDE method was used for determining the electrochemical activity of the prepared catalyst materials towards the ORR. For controlling and regulating the rotation speed, a controlling unit CTV202 (Radiometer) [I–III] or Pine AFMSRCE (Pine, USA) was used. The experiments itself were controlled by General Purpose Electrochemical System (GPES) [I–II] or Nova 2.1.2 (Metrohm Autolab P.V, The Netherlands) [III–V] and the potential was applied by employing potentiostat/galvanostat Autolab PGSTAT30 (Metrohm Autolab P.V., The Netherlands) [I–II] or PGSTAT 128 N (Metrohm Autolab P.V., The Netherlands) [III–V]. The rotation rates ( $\omega$ ) were varied from 4600 to 360 rpm. Electrochemical measurements were performed at room temperature ( $23 \pm 1$  °C) in a conventional 5-neck electrochemical cell. Testing was carried out with three electrodes: Pt foil [I–IV] or graphite rod [V] served as a counter electrode, saturated calomel electrode (SCE) as a reference and the working electrode was the polished GC electrode (geometric surface area ( $A$ )  $0.2 \text{ cm}^2$ ) covered with the catalyst material in interest. To measure the ORR, the electrolyte was saturated with  $\text{O}_2$  (99.999 %, AGA) [I–II] or (6.0) [III–V]. To measure the background current, the electrolyte was saturated with Ar (99.999 %, AGA) [I–II] or Ar (5.0) [III–V]. The flow of gases was maintained over the solution during the measurements. In this work,  $E_{\text{onset}}$  is defined as the potential value when the current density reaches  $0.1 \text{ mA cm}^{-2}$ . Koutecky-Levich (K-L) equation [172] was used to calculate the number of electrons transferred per  $\text{O}_2$  molecule ( $n$ ) and to construct K-L plots:

$$\frac{1}{j} = \frac{1}{j_k} + \frac{1}{j_d} = -\frac{1}{nFkc_{\text{O}_2}^b} - \frac{1}{0.62nFD_{\text{O}_2}^{2/3}\nu^{-1/6}c_{\text{O}_2}^b\omega^{1/2}} \quad (8)$$

where  $j$  is the experimental current density (background current has been subtracted),  $j_k$  and  $j_d$  are the kinetic and diffusion limited current densities, respectively,  $k$  is the electrochemical rate constant for  $\text{O}_2$  reduction,  $c_{\text{O}_2}^b$  is the concentration of oxygen in the bulk ( $1.2 \times 10^{-6} \text{ mol cm}^{-3}$ ) [173],  $F$  is the Faraday constant ( $96,485 \text{ C mol}^{-1}$ )  $D_{\text{O}_2}$  is the diffusion coefficient of  $\text{O}_2$  in  $0.1 \text{ M KOH}$  ( $1.9 \times 10^{-5} \text{ cm}^2 \text{ s}^{-1}$ ) [173],  $\nu$  is the kinematic viscosity of the solution ( $0.01 \text{ cm}^2 \text{ s}^{-1}$ ), and  $\omega$  is the rotation rate of the electrode ( $\text{rad s}^{-1}$ ) [174].

To make the research data obtained more easily comparable with the literature and with different materials that are presented in this work, the electrode potentials that were recorded vs. SCE were calculated to the reversible hydrogen electrode (RHE) scale by employing Nernst equation:

$$E_{\text{RHE}} = E_{\text{SCE}} + 0.059 \cdot \text{pH} + E_{\text{SCE}}^0 \quad (9)$$

where  $E_{\text{SCE}}$  is the potential value recorded vs. SCE, and  $E_{\text{SCE}}^0 = 0.242 \text{ V}$  at  $25$  °C. All the potential values are stated against RHE, unless noted otherwise.

The stability of the prepared catalysts was evaluated by carrying out 1000 potential cycles at a scan rate of  $100 \text{ mV s}^{-1}$  while the rotation rate was set to 960 rpm. After every 100 cycles the linear sweep voltammograms (LSVs) were recorded at  $10 \text{ mV s}^{-1}$  [IV]. The chronoamperometry test was carried out for 20 h at  $0.6 \text{ V}$  and the rotation speed of 610 rpm [V]. Methanol tolerance tests were carried out at  $0.6 \text{ V}$  and at 1900 rpm,  $3 \text{ M MeOH}$  was added at 300 s [IV–V].

### 3.7 Physical characterisation methods

The porosity was evaluated from N<sub>2</sub> sorption/desorption isotherms that were obtained in a sorptometer Quantachrome NOVA 4000 (USA) by using NovaWin 11.03 software. Degassing was performed at 300 °C for 2 h. The results were analysed using Brunauer-Emmet-Teller (BET, in a P/P<sub>0</sub> range of 0.05–0.35), Dubinin-Radushkevich (DR, P/P<sub>0</sub> range of 10<sup>-5</sup>–0.35) and quenched solid density functional theory (QSDFT, in a whole P/P<sub>0</sub> range) [IV].

High-resolution scanning electron microscope (HR-SEM) Helios 600 (FEI) [I, II] or Helios Nanolab 650 (FEI) [IV] was used to study the surface morphology of the as-prepared catalysts. A high-resolution elemental mapping was carried out with scanning transmission electron microscopy (STEM, JEM-ARM200CF, JEOL, Japan) with energy dispersion spectroscopy (EDS) using accelerating voltage of 200 kV [III]. The powder was dispersed in ethanol and dropped onto a 200 mesh Cu TEM grid (contained a 20 nm thick amorphous C supporting film [III]). Transmission electron microscopy (TEM) images were obtained by employing Tecnai G2 F20 (FEI) [III, IV] and a fast Fourier transform (FFT) analysis was conducted by using a DigitalMicrograph (Gatan) [III].

The surface composition was studied with employing X-ray photoelectron spectroscopy [I–V]. The catalyst materials were dispersed in alcohol and deposited on a GC plate, the solvent was allowed to evaporate [I, II, IV] or pressing catalyst powder into metallic indium ingot [III]. The XPS measurements were carried out with SCIENTA SES100 spectrometer that used a non-monochromated Mg K $\alpha$  X-ray source (1253.6 eV [I, II] or 1486.6 eV [IV]), take off angle of 90° and a source power of 300 W, the pressure in the analysis chamber was set below 10<sup>-9</sup> Torr. Overview spectra was collected using energy range from 1000 to 0 eV, pass energy of 200 eV, step size of 0.5 eV. For the high-resolution scan, the corresponding values were for energy range 410 to 390 eV (N 1s); 660 to 635 (Mn 2p); 975 to 920 eV (Cu 2p) [I]; 60 to 50 eV (Li 1s); 1030 to 1015 (Zn 2p) [II] pass energy of 200 eV and step size of 0.1 eV [I, II].

The Raman spectra were collected by using an InVia Raman (Renishaw, UK) spectrometer that was equipped with a thermoelectrically cooled (-70 °C) CCD camera and microscope. The spectra were excited by diode-pumped solid state (DPSS) laser (Renishaw, UK) (excitation energy 532 nm). For recording the spectra, 20x/0.40 NA objective lens together with 1800 lines/grating were employed. To avoid the potential damage to the sample, the power of the laser was restricted to 0.6 mW and the accumulation time was 40 s. The Raman frequencies were calibrated by employing the polystyrene standard, the band parameters were determined by carrying out the fitting of the experimental spectra with Gaussian–Lorentzian shape components and GRAMS/A1 8.0 (Thermo Scientific) software [IV–V].

### 3.8 Theoretical calculations

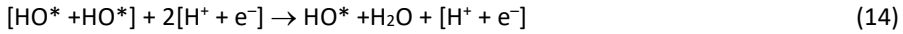
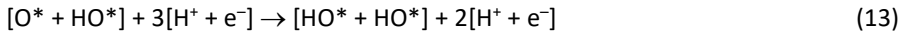
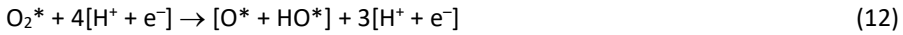
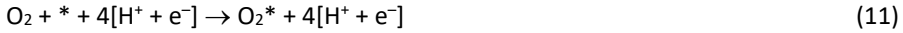
For the theoretical calculations at the DFT level, Becke's three-parameter exchange potential and Lee–Yang–Parr correlation functional was used. All of the calculations were carried out with full geometry optimisation using 6-31+G(D) basis set or 6-311G(d) basis set for calculating frequencies, utilising Gaussian09 program suite [175] and visualised with ChemCraft program [176]. Due to the oxidative conditions of the process investigated, different oxidised forms were computed, energetically the most favourable one (pyridine-N-oxide) was used to carry out further calculations. In the next step,

N,S,O-doped graphene with O<sub>2</sub> in different position was calculated and energetically the most favourable form was chosen.

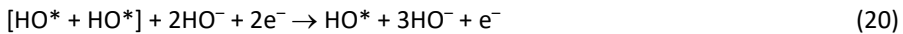
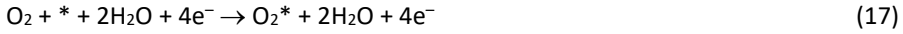
The stability of the different O<sub>2</sub> adsorbates together with protonated species that are involved in the ORR on the N,S-co-doped GO, the adsorption energy ( $E_{\text{ads}}$ ) was found as follows:

$$E_{\text{ads}} = E_{\text{adsorbate/GrO-NS}} - E_{\text{adsorbate}} - E_{\text{GrO-NS}} \quad (10)$$

where  $E_{\text{adsorbate/GrO-NS}}$ ,  $E_{\text{adsorbate}}$ ,  $E_{\text{GrO-NS}}$ , correspond to the gas-phase total energies of the adsorbate together with GrO-NS, the isolated adsorbate, and to the GrO-NS. Since the value of  $E_{\text{ads}}$  is negative, the adsorption process is exothermic. The 4-electron ORR pathways were investigated on the GrO-NS catalyst in the present study. In the acidic medium, the ORR steps are defined as follows (where \* = GrO-NS) [177]:



In the alkaline media, the steps are defined as follows:



The energy diagrams for the ORR were estimated according to the method proposed by Nørskov *et al.* [178]:

$$\Delta G = \Delta E + \Delta ZPE - T\Delta S + \Delta G_U + \Delta G_{\text{pH}} \quad (23)$$

where  $\Delta E$  corresponds to the energy difference between the products and the reactants (Eqs 11–22);  $\Delta ZPE$  and  $\Delta S$  are the zero-point corrections to the total and entropy, respectively;  $T$  is the temperature (298.15 K);  $\Delta G_U = -neU$  ( $n$  – number of electrons,  $e$  – electron charge,  $U$  – electrode overpotential (vs SHE));  $\Delta G_{\text{pH}} = k_B T \ln 10 \cdot \text{pH}$  ( $k_B$  – Boltzmann constant). In this work,  $\text{pH} = 0$  ( $\Delta G_{\text{pH}} = 0$ ) or  $\text{pH} = 13$  ( $\Delta G_{\text{pH}} = 0.77$  eV). The free energy of water molecule in bulk was calculated in the gas phase ( $P = 0.035$  bar, which is the equilibrium vapor pressure of water at 298.15 K). The total and free energy of  $[\text{H}^+ + \text{e}^-]$ , was estimated as the energy of  $1/2\text{H}_2$  (under standard conditions).  $\text{HO}^-$  free energy was received from the reaction in equilibrium in the  $\text{H}_2\text{O}$  solution ( $\text{H}^+ + \text{HO}^- = \text{H}_2\text{O}$ ). The entropy values for the molecules in the gas phase were taken from the NIST [179]. The ZPE corrections were achieved from vibrational frequencies (excluding GrO-NS).

Herein, we consider the S-oxidised form in a view of low oxygen content (2.4 at.%), since this issue deserves special analysis and a separate study.

## 4 Results and discussion

### 4.1 Oxygen electroreduction on heteroatom co-doped composite

The co-doping of carbon nanomaterials is widely used in order to prepare non-precious metal electrocatalysts for the ORR [100,148,180]. Herein, GO and MWCNTs composite was modified with a precursor *o*-methylisourea bisulfate, that consists both of S and N, the mixture was then heat-treated to prepare co-doped catalyst material for the ORR in alkaline media. The exact preparation methods are explained in the section 3.3 and the physical/electrochemical characterisation methods are written in more detail in section 3.7 and 3.6, respectively.

The catalyst that showed best electrocatalytic activity towards the ORR (C/oMUS 1:5) was first studied by employing XPS and TEM. The surface chemical composition fitting was performed with SPANCF curve-fitting macropackage [181,182]. The overview spectrum is shown in Figure 10a; high-resolution spectra are shown in Figure 10b-e (O 1s, N 1s, C 1s, and S 2p). The Figure 10a shows dominating carbon peak (C content 93.5 at.%), O 1s (2.4 at.%), N 1s (3.1 at.%) and S 2p (1.0 at.%). In 3d peak can be seen because indium was used as a substrate. XPS results confirm that both nitrogen and sulfur have been successfully incorporated into the carbon structure and it is possible to use oMUS as a precursor for co-doping. The O 1s peak (Figure 10b) shows broad (full width at half maximum (FWHM)  $\sim 3.5$  eV) peak, with a maximum at 531.9 eV, indicating that C-O single bonds are mainly dominant. The asymmetry at the higher binding energies may come from double bonded carbon, but the asymmetry of O 1s spectra may have several origins (e.g. proximity to a carboxyl radical) [183]. C 1s spectra on Figure 10c shows strong peak with the maximum at 284.3 eV (FWHM  $\sim 1.4$  eV). The asymmetric shape is characteristic to  $sp^2$ -carbon in (nonoxidised) graphene. To avoid overestimating contributions from oxidised components, the C 1s peak was fitted mainly with an asymmetric Doniach-Sunjić line profile that is suitable for peaks that have metallic characteristics. Two minor contributions were introduced as well, one that relates to the shake-up (i.e., loss in kinetic energy) that is related to graphene itself, this feature is broad and centred  $\sim 6$  eV above the main C 1s peak. Second minor contribution is related to single bonded oxygen (at the level of 4 to 5% of the total peak intensity). The N 1s spectra with two peaks at 398.3 eV (pyridinic-N) and 400.7 eV (pyrrolic-N) is shown in Figure 10d. The broader spectral feature with a maximum around 403.2 eV belongs to graphitic-N. The contents of different nitrogen species are as follows: 43% of pyridinic-N, 40% of pyrrolic-N and 17% of graphitic-N. Deconvoluted S 2p peak can be seen on Figure 10e. The leading peak belongs to  $2p_{3/2}$  at 163.9 eV, that correspond to C-S-C bonds, the more diffuse and broader feature (a bit below 168 eV) corresponds to sulfur oxides that exist at the edges of the carbon skeleton [99].

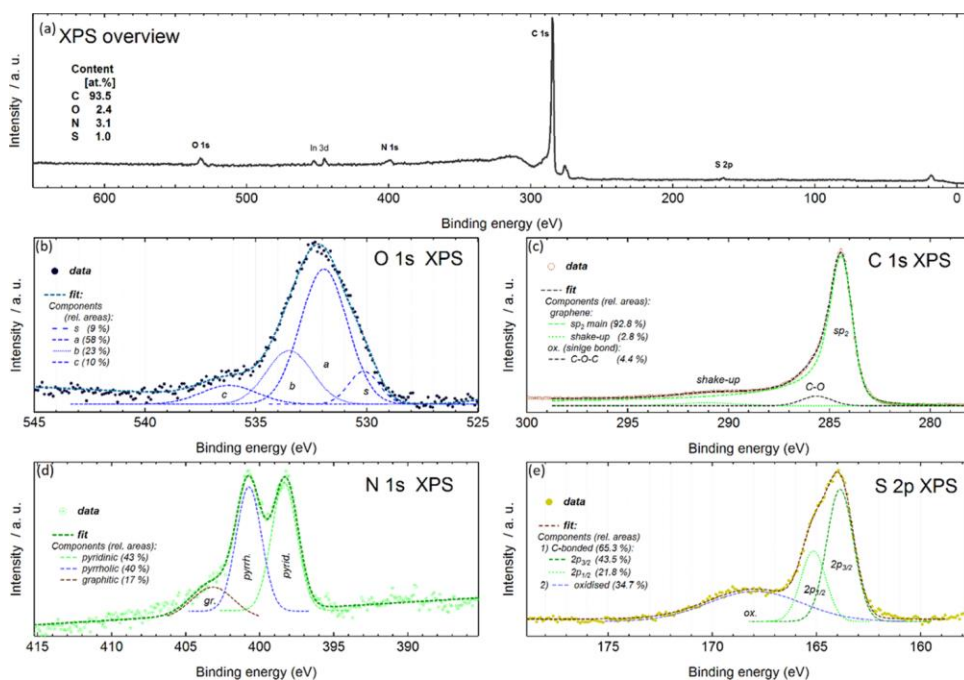


**Figure 10.** (a) XPS overview spectrum; high resolution (b) O 1s; (c) C 1s; (d) N 1s and (e) S 2p spectra of C/oMUS 1:5.

TEM images are shown in Figure 11a,b. The sample consists of typical MWCNTs and graphene/GO layers (Figure 11a). One layer or multilayer GO agglomerations with MWCNTs were observed all over the sample. HR-TEM images of areas 1 and 2 and typical hexagonal Fast Fourier Transform (FFT) images that originate from two-layer GO are shown in Figure 11b.

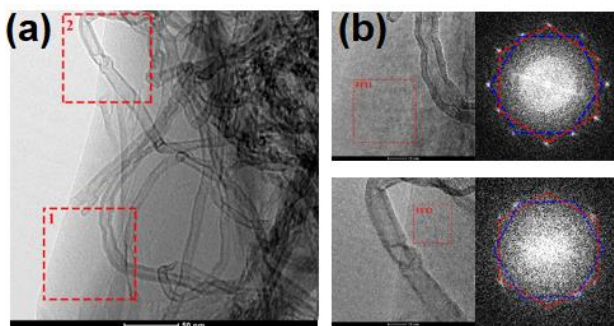


**Figure 11.** TEM microphotos of C/oMUS 1:5.

STEM-EDS elemental mapping is shown in Figure 12. Both nitrogen and sulfur can be seen from the STEM-EDS mapping, meaning that both elements are successfully doped into the carbon lattice. The results obtained are in good agreement with the XPS results.

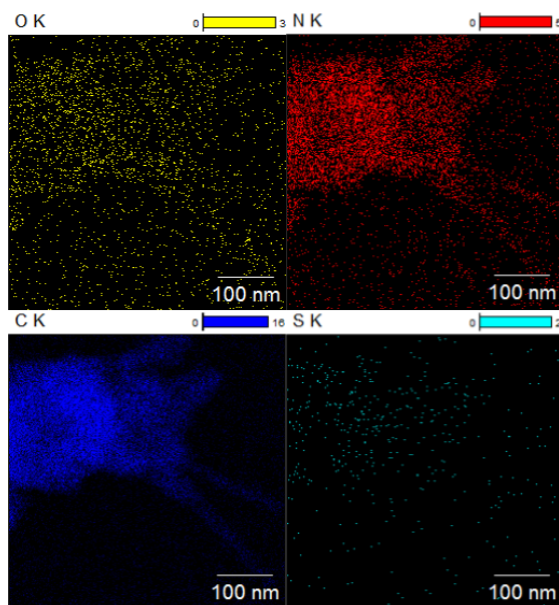


**Figure 12.** EDX elemental mappings of oxygen, nitrogen, carbon and sulfur in the C/oMUS 1:5 catalyst.

The ORR was studied on C/oMUS catalyst in 0.1 M KOH at room temperature. In the first step, the ratio of carbon composite (GO/MWCNT) and oMUS was varied (more detailed explanation in section 3.3). The results are shown in Figure 13. The best ratio of C/oMUS was 1:5, although the differences between the ratios of 1:5 and 1:2.5 are not that significant, the increase in the oMUS amount has an effect on the ORR  $E_{\text{onset}}$  and  $E_{1/2}$  values. If the ratio of the precursor gets too high (1:7.5) the effects on both onset and half-wave potentials are quite drastic, as the overall performance drops notably. This may be due to the minor and hardly recognisable change in the structure and porosity of the catalyst, which is related to the concentration of the doping agent [184]. The change of the doping agent to C ratio can have effects on electrocatalytic activity in case of graphene-type materials, as the graphene lattice will change and this in turn will result in lower number of edge defects and active sites [185]. Higher amounts of doping agent will create more defects to the  $sp^2$ -carbon structure, this in turn will reduce the electrical conductivity of the carbon skeleton [186].

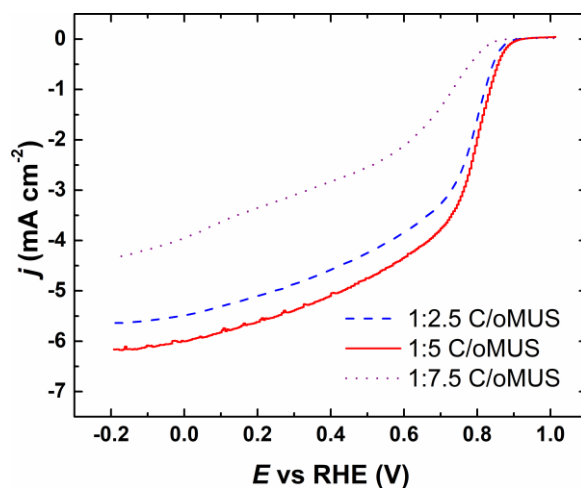


**Figure 13.** RDE polarisation curves for ORR on GC electrodes modified with different ratios of C/oMUS in O<sub>2</sub>-saturated 0.1 M KOH.  $\nu = 10 \text{ mV s}^{-1}$ ;  $\omega = 1900 \text{ rpm}$ .

The 1:5 C/oMUS catalyst was heat-treated at various temperatures in order to study the effects of the change in pyrolysis temperature. The results are shown in Figure 14. The best electrocatalytic activity was achieved when the temperature was 800 °C. For the sample pyrolysed at 900 °C the  $E_{\text{onset}}$  and  $E_{1/2}$  values are even a bit higher, but the limiting current density values decrease notably. This could be caused by the carbon reconstruction to heal the defects and the damage to the active sites, which occurs at 900 °C and higher [187]. Previous research carried out have shown that the low heat-treatment temperature can result in lower limiting current densities and poor conductivity, but if the pyrolysis temperature is too high, the number of structural defects is low, and this has an effect on the limiting current densities [188,189]. Due to previous research carried out, we assume that the pyrolysis of C in the presence of oMUS at 800 °C can provide number of defects and exposed edges that are active towards the ORR, but this is rather speculative. The exact reason in the change of catalytic activity and the nature and number of active sites for the ORR on this type of materials are still under discussion. There are reports that have found that doping of carbon below 800 °C can give lower carbonisation degree of the material, whereas higher heat-treatment temperatures will lead to decomposition of the heteroatom species, therefore, the electrochemical activity will decrease [190,191]. Different pyrolysis temperatures will have an effect of different N species contents, especially on the pyridinic-N content, which is accepted as one of the main factors in achieving high electrocatalytic activity [95].

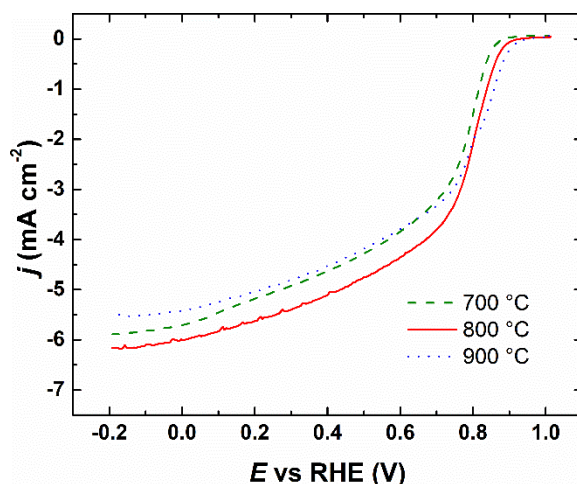


**Figure 14.** RDE polarisation curves for ORR on GC electrodes modified with C/oMUS 1:5 pyrolysed at different temperatures in  $O_2$ -saturated 0.1 M KOH.  $v = 10 \text{ mV s}^{-1}$ ;  $\omega = 1900 \text{ rpm}$ .

The ORR results for the 1:5 C/oMUS catalyst are shown in Figure 15a. The onset potential for this material is 926 mV and the current density values are increasing with the increase in the rotation speed, meaning that the process is under diffusion control. The K-L plots are shown in Figure 15b, from the experimental data shown in previous figure. K-L plots are linear and the extrapolation to the y-axis gives the intercept value near to zero, meaning that in the studied potential range, the process is limited by diffusion. The  $n$  value was 4 at more negative potentials, but at higher positive potential values, it drops a bit. The limiting current density at 1900 rpm is  $-6.16 \text{ mA cm}^{-2}$ , which is very similar to the expected value that is obtained from K-L equation ( $-6.21 \text{ mA cm}^{-2}$ ).

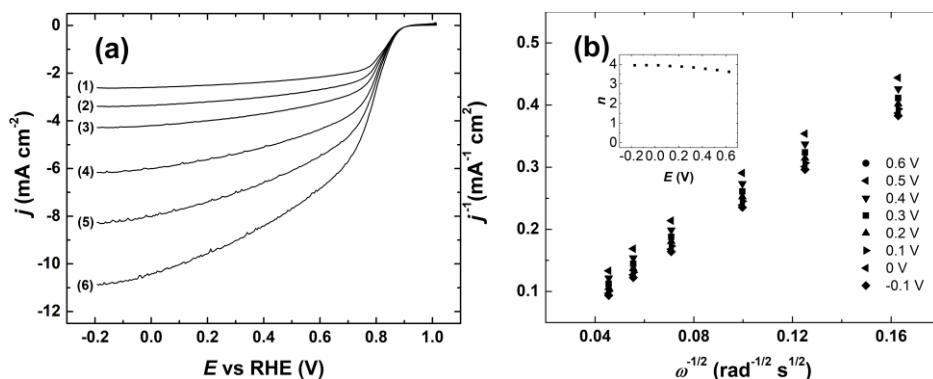


**Figure 15.** (a) RDE polarisation curves for ORR on GC electrodes modified with C/oMUS 1:5 in  $O_2$ -saturated 0.1 M KOH.  $v = 10 \text{ mV s}^{-1}$ ;  $\omega =$  (1) 360; (2) 610; (3) 960; (4) 1900; (5) 3100; (6) 4600 rpm. (b) K-L plots for the ORR on the C/oMUS 1:5 in 0.1 M KOH at different potentials; the inset figure shows the  $n$  dependence on potential.

The enhanced activity towards the ORR was achieved due to co-doping carbon with nitrogen and sulfur. The difference in electronegativity values between carbon (2.55) and nitrogen (3.04) are quite big, so the N-doping will create favourable sites for the surface adsorption of  $O_2$  [95]. The bond in oxygen molecule gets weakened and 4-electron

reduction is happening on the electrode. The difference in electronegativity values between carbon (2.55) and sulfur (2.58) are marginal, but the two lone pairs of electrons on sulfur can have an effect on the oxygen interaction, as sulfur can easily donate electrons, therefore, 4-electron reduction may happen. Due to the large atomic radius of sulfur (110 ppm), the doping can cause defects in the carbon skeleton, which in turn will create a charge difference that facilitates the oxygen chemisorption [192,193].

The comparison of the RDE data for C/oMUS and other commercial carbon materials is shown in Figure 16. The  $E_{\text{onset}}$  is almost 80 mV higher than of the MWCNTs and around 150 mV higher than of the GC. The low limiting current densities in case of the rGO are most possibly connected to the restacking effects and effects that come from ionomer. The typical two-wave polarisation curve is lost in case of C/oMUS, indicating that both the ORR pathway and mechanism have changed due to the N,S-co-doping. For further comparison, the mass activity of C/oMUS was calculated, the mass activity of 1:5 C/oMUS at 0.8 V is  $4.89 \text{ A g}^{-1}$ . This is better than for the doped materials investigated by Pašti *et al.*, they calculated the mass activities to the doped materials and the values varied between 0.5 to  $3.5 \text{ A g}^{-1}$  [194].

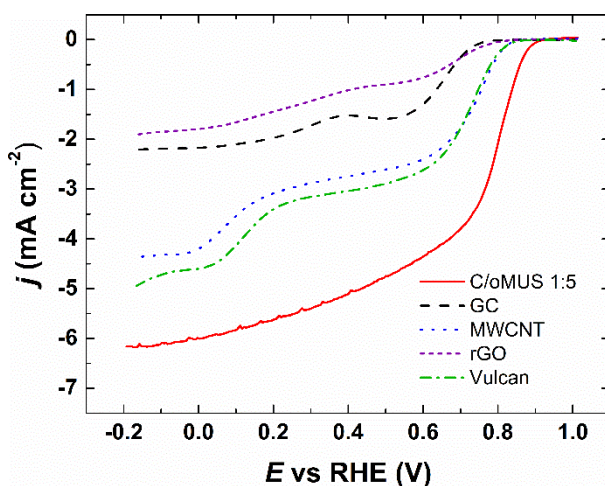


**Figure 16.** RDE polarisation curves for ORR on unmodified GC, MWCNTs, rGO, commercial Vulcan and C/oMUS 1:5 modified GC electrodes in  $\text{O}_2$ -saturated 0.1 M KOH.  $v = 10 \text{ mV s}^{-1}$ ;  $\omega = 1900 \text{ rpm}$ .

DFT calculations were carried out by employing the structures shown in Figure 17. Graphene sheet ( $\text{C}_{54}\text{H}_{18}$ ) on 1a was doped with nitrogen and sulfur ( $\text{C}_{49}\text{H}_{15}\text{N}_3\text{S}$ ) (1b), which correlates to the composition achieved from the XPS. Since the catalyst was partially oxidised (rGO), the testing of different C-oxidised isomers of the epoxide and pyridine-N-oxide structures was done. Structure  $\text{C}_{49}\text{H}_{15}\text{N}_3\text{SO}$  (1c) was chosen for the ORR simulation, because the pyridine-N-oxide form corresponds to the global minimum (energy of formation  $\sim 0.87 \text{ eV}$ ).

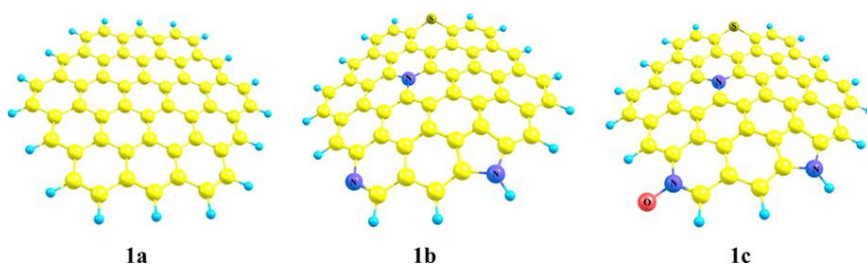


**Figure 17. (1a)** Undoped  $C_{54}H_{18}$ ; **(1b)**  $N,S$ -co-doped  $C_{49}H_{15}N_3S$ ; **(1c)**  $N,S$ -co-doped oxidised  $C_{49}H_{15}N_3SO$  graphene sheets.

The structure 1c was tested to find the most favourable active site for oxygen adsorption, this was done using Mulliken positive charges on C atoms. The structure 2a, where oxygen is adsorbed over the  $C_{\alpha}-C_{\beta}$  bond at the graphitic-N, is most favourable energetically ( $E_{ads} = -1.14$  eV) and corresponds to the global minimum as well. The oxygen bond distance in structure 2a increases compared to free  $O_2$  molecule and equals to 1.478 Å.

The protonation by  $[H^+ + e^-]$  of the O–O occurs in  $O_2^*$  with the rupture of the oxygen bond and  $[O^* HO^*]$  forms (3), thus the 2-electron ORR pathway is prevented. When the cationic or anionic form of (3) was protonated, the oxygen bond breakage occurred. The  $E_{ads} = -1.41$  of adduct (3) is 0.27 eV lower than that of  $O_2^*$  (2a). Further protonation of the adduct (3) with  $[H^+ + e^-]$  in direction to  $O^*$  or  $HO^*$  gives the formation of adduct (4) (diol  $[HO^* HO^*]$ ), with small exothermic effect and the  $E_{ads} = -0.01$  with respect to adduct (3). The protonation of the adduct (4) with  $[H^+ + e^-]$  produces water molecule and adduct (5)  $[HO^*]$ , which is the most stable species in this series (2 to 5),  $E_{ads} = -1.51$  eV.

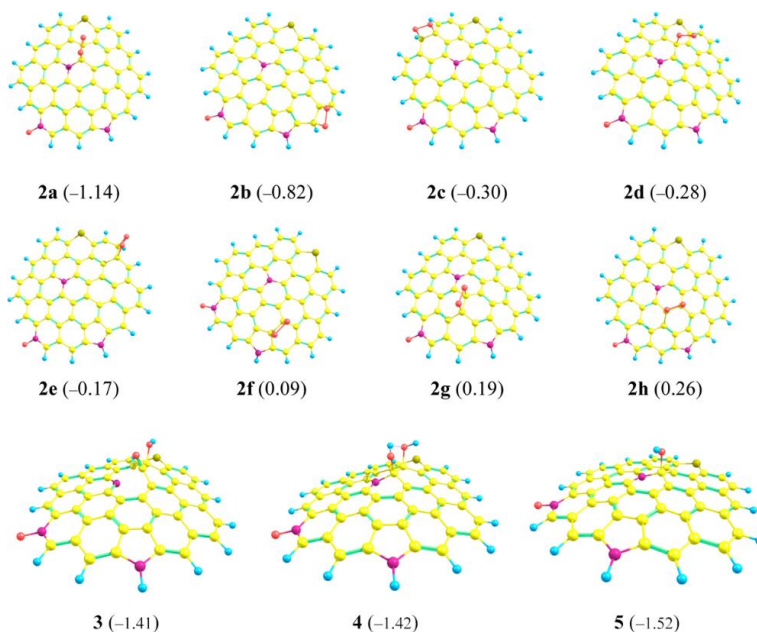


**Figure 18. (2a–h)** Structures of  $O_2^*$ ; reduced forms of (3)  $[O^*HO^*]$ ; (4)  $[HO^*HO^*]$  and (5)  $HO^*$  adsorbed on rGO- $N,S$  (1c in Figure 17). In brackets:  $E_{ads}$  in eV with respect to non-reacting molecules:  $O_2$ ,  $OOH$ ,  $H_2O_2$ ,  $OH$ . Carbon – yellow; hydrogen – blue; oxygen – red, nitrogen – magenta; sulfur – olive.

According to Equations 11–23 (in section 3.8), the free-energy diagrams were constructed for  $O_2$  reduction on rGO-N,S (structure 1c) at different electrode overpotentials ( $U$ ) in both acidic and alkaline media (Figure 19a,b). In both media the oxygen adsorption on the catalyst surface expectedly gives rise to the increase in the free energy by 0.81 eV due to the entropy losses upon adsorption. When the free energies of  $3[H^+ + e^-] + O^* + HO^*$  and  $2[H^+ + e^-] + 2HO^*$  become equal, the free energy in acidic media decreases down to 0.85 eV. When the equilibrium is reached in the system ( $2H_2 + O_2 \rightleftharpoons 2H_2O$ ) and the increase of  $U$  value to 1.23, results with all intermediates lying in the diagram above the initial or the final level of the system, meaning that all  $O_2$  species are ablated from the catalyst surface. Excluding the  $O_2$  adsorption on the active site from consideration, the rate determining step in the acidic solution (at  $U > 0.85$  V) is the second protonation, which leads to the formation of  $2HO^*$ .

In the alkaline, the  $O_2^*$  reduction proceeds in a barrierless way, with monotonous decrease in free energy (at small negative  $U$  values). When  $U = 0.0$  V, the free energy of  $HO^*$  is lower than that of the reaction product ( $-0.04$  eV) and, thus, the final step of the ORR is rate-determining. This trend is maintained for positive  $U$  values and up to the equilibrium overpotential ( $0 \text{ V} < U < 0.46$  V). When the  $U = 0.46$  V is applied, the most favourable structure corresponds to  $2HO^*$ , for which the free energy is  $-0.51$  eV.

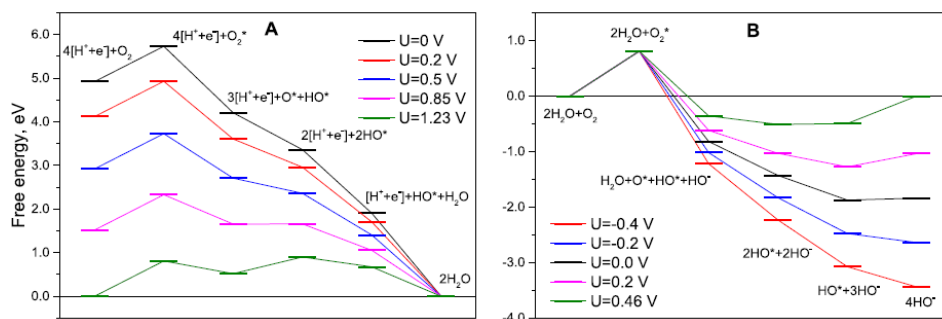


**Figure 19.** Free energy diagrams of the ORR on rGO-N,S (1c in Figure 17) at different electrode overpotentials in (A) acidic and (B) alkaline media.

But in a real system, the increase in free energy in the adsorption step must be much smaller, or the free energy values may even decrease. As the oxygen is supplied to the cathode either in the dissolved form or through porous membranes, meaning that it already interacts with other species. Then, the entropy losses will be much smaller than those that calculated for the pure gaseous  $O_2$  on the catalyst material and may even be outweighed by the gain of energy due to adsorption.

In this work, *o*-methylisourea bisulfate was successfully used as a precursor to synthesise metal-free electrocatalyst for the ORR in alkaline media. Co-doping is an effective way to produce electrocatalysts that could be further applied in metal-air batteries or fuel cells. Since the detection of catalytic sites and the ORR mechanism only by electrochemical measurements is impossible, the DFT calculations carried out showed that the electrocatalytically active  $C_\alpha$  and  $C_\beta$  that are at the graphitic-N and close to the sulfur atom, show the global minimum value and could act as active sites.

## 4.2 Oxygen electroreduction on N-doped biomass-based carbons

### 4.2.1 Oxygen electroreduction on N-doped wood-based carbon

As the Baltic region is known for wood industry and as most of the by-products that get produced are simply just burnt [116], there is a tremendous need for finding more feasible ways to valorise different by-products from wood. The same waste products could be used to substitute traditional fossil-based nanocarbons that are used in different energy conversion systems. Herein, alder wood char was used as a precursor to produce the final N-doped biomass-based catalyst (N-AC-1). The catalyst preparation is explained in more detail in section 3.4. Since one of the main problems with wood-based materials is the heterogeneity [195], the N-doped N-AC sample was once again ball-milled and secondary pyrolysis was carried out at 800 °C to see the effects on physical characteristics and electrochemical performance. The final sample that had gone through secondary treatment is denoted N-AC-1. Physical characterisation methods are described in more detail in the section 3.7 and electrochemical characterisation in the section 3.6.

The samples were first studied by using nitrogen adsorption at 77 K (Figure 20). Both samples show characteristic isotherms belonging to the type I, meaning samples are highly microporous [196].

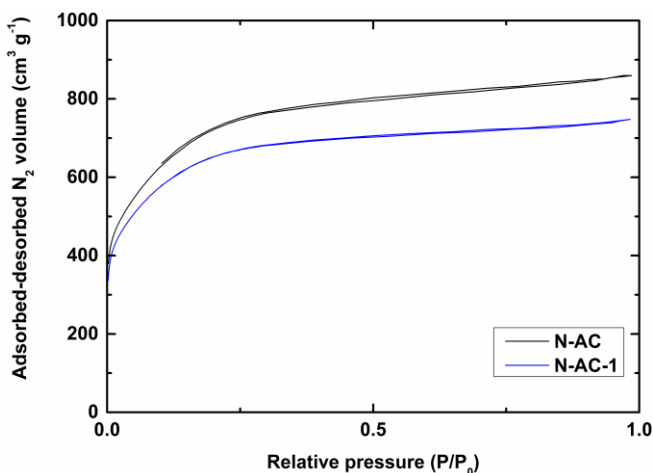


**Figure 20.** Nitrogen sorption isotherms at 77 K of wood-based N-doped nanocarbon before (N-AC) and after secondary pyrolysis (N-AC-1).

The changes in BET surface area, total volume of pores ( $V_{\text{total}}$ ) and the average pore diameter value ( $L$ ) are shown in Table 1. The BET surface area decreased a bit after the second heat-treatment, but the  $V_{\text{total}}$  and the average pore diameter increased.

**Table 1.** Porosity data of wood-based N-doped carbon before (N-AC) and after secondary pyrolysis (N-AC-1).

Samples	$S_{\text{BET}}$ ( $\text{m}^2 \text{g}^{-1}$ )	$S_{\text{DFT}}$ ( $\text{m}^2 \text{g}^{-1}$ )	$V_{\text{total}}$ ( $\text{cm}^3 \text{g}^{-1}$ )	$V_{\text{micro(DR)}}$ ( $\text{cm}^3 \text{g}^{-1}$ )	$L$ (nm)
N-AC	2435	1763	1.27	0.86	1.36
N-AC-1 (after second pyrolysis)	2245	1594	1.34	0.82	1.63

The morphology and microstructure of the sample N-AC-1 was further evaluated with SEM and TEM. The N-AC-1 mainly consists of amorphous carbon and exhibits rough surface structure (Figure 21a,c), but some parts of the catalyst show typical structure that is characteristic to carbon nanoplatelets (Figure 21b).

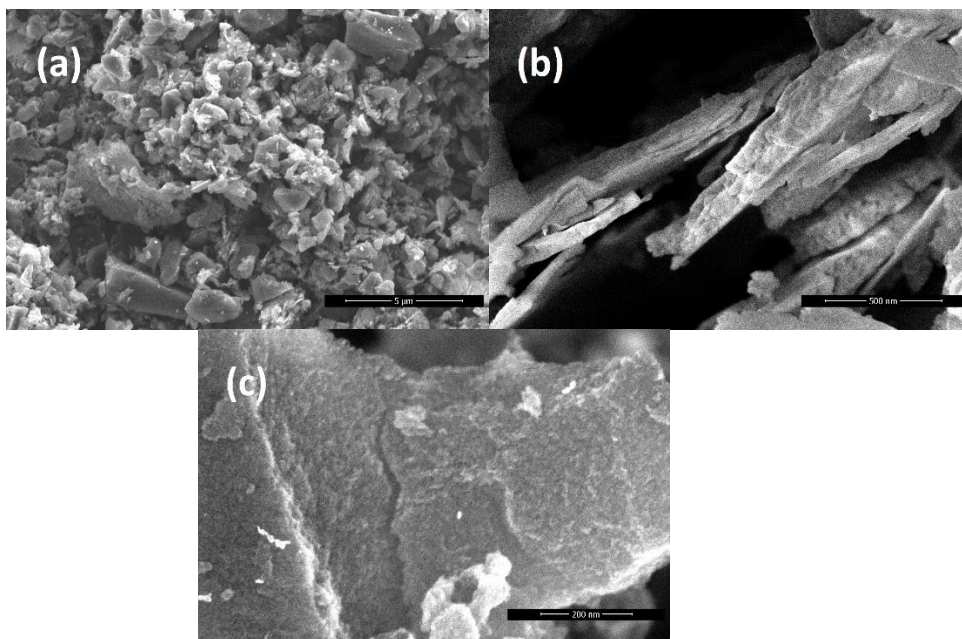


**Figure 21.** SEM microphotos of N-AC-1.

TEM microphotos show the graphitic lattice fringes (most likely corresponding to the same platelets that are also seen from the SEM images) (Figure 22b), but areas of porous amorphous carbon (Figure 22c,d). The 10x thickness of the catalyst particle is around 3.55 nm, which gives the interlayer spacing between two carbon layers  $\sim 0.35$  nm. The interlayer spacing of few layered graphene is around 0.35 nm, indicating that some parts of the catalyst possess a graphene-like structure [197]. SEM microphotos confirmed the existence of nanoplatelets in some parts of the catalyst material and the presence of nanoplatelets was further confirmed by TEM microphotos.

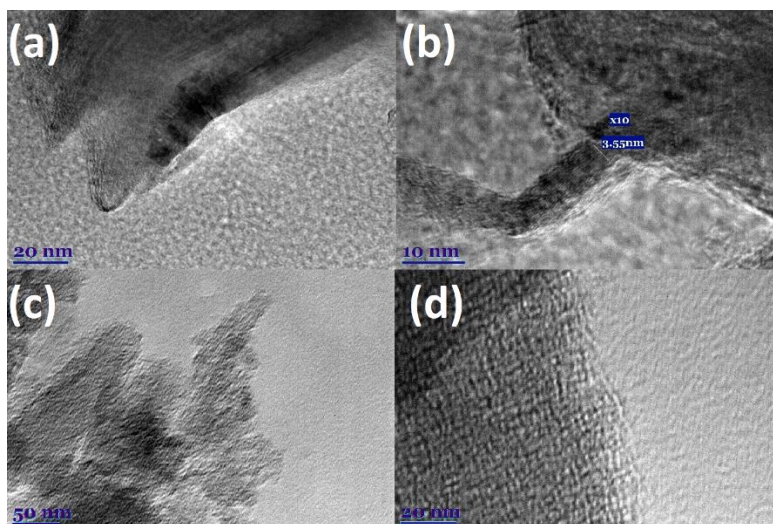


**Figure 22.** TEM microphotos of N-AC-1.

The surface composition of the N-AC-1 was evaluated by XPS. The survey spectrum showed the characteristic peaks of C 1s, O 1s and N 1s. The high resolution XPS spectra of C 1s and N 1s are presented in Figure 23a,b. The C 1s peak consists mainly of  $sp^2$  hybridised carbon atoms [198]. As the nitrogen content on the surface of catalyst material N-AC-1 is rather low, the intensity of the peak is comparatively low, but the N 1s peak can be deconvoluted into different nitrogen species (explained in section 1.4). It is commonly believed that the electrocatalytic activity is rather related to various nitrogen surface groups than to the overall nitrogen content [199,200]. The N 1s peak was deconvoluted and it is possible to distinguish between 4 different N-groups: pyridinic-N (398.3 eV), pyrrolic-N (399.7 eV), graphitic-N (400.8 eV) and oxidised-N (N-O, 402.3 eV) [201,202]. The contents of different N forms were as follows: 59% of pyridinic-N, 53% of graphitic-N, 21% of pyrrolic-N and 23% of N-O. Lai *et al.* have found that pyridinic-N has an effect on the onset potential of the ORR [203] and graphitic-N is the active site for the ORR and this helps to achieve higher diffusion limiting current densities, pyrrolic-N and N-O show no significant effect on the electrochemical activity towards the ORR [203,204].

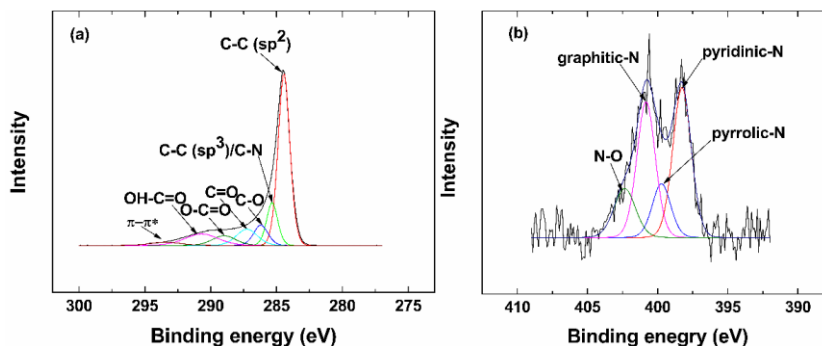


**Figure 23.** (a) Deconvoluted C 1s spectrum and (b) deconvoluted N 1s spectrum of N-AC-1.

Raman spectroscopy is widely used to describe the structure and disorder in carbon-based materials [205–207]. Raman spectrum of N-AC and N-AC-1 in the spectral region of 400–3200  $\text{cm}^{-1}$  (excited at 532 nm) is shown in Figure 24. The intense bands near 1345 and 1594  $\text{cm}^{-1}$  belong to D and G modes that are characteristic to carbon network [206–208]. The G band ( $E_{2g}$  symmetry) is connected to the in-plane relative motion of carbon atom pairs in  $sp^2$  hybridisation [207] and this mode is always allowed in carbonaceous nanomaterials. The D band ( $A_{1g}$  symmetry) is associated with breathing vibrations of aromatic rings and therefore indicates to the presence of defects that is needed in order to activate this mode [205–208]. The band parameters were estimated by fitting experimental data with four Gaussian–Lorentzian form components (in the frequency range of 900–1800  $\text{cm}^{-1}$ ). The widths of the D and G bands for the sample N-AC were determined as full width at half maximum (FWHM) and the values were 204 and 79  $\text{cm}^{-1}$ , respectively. High width of both bands and high relative integrated intensity ( $A(D)/A(G) \sim 3.6$ ) indicates that there is considerable disorder in the N-AC material. The FWHM value for the G band for undoped pristine graphene is found to be 15  $\text{cm}^{-1}$ . After the secondary pyrolysis, the sample N-AC-1 shows a considerable decrease in the integrated intensities ( $A(D)/A(G) \sim 2.2$ ) and a little decrease in the D band width (FWHM = 196  $\text{cm}^{-1}$ ). Considering the peak intensity ratios for D and G bands, the  $I(D)/I(G)$  decreases from 1.02 to 0.93 after the secondary heat-treatment of the sample. The differences between integrated and peak intensity ratios are connected to the change in widths of D and G bands as the G band FWHM is considerably lower. So to conclude, both integrated and peak intensity ratios decrease after the secondary pyrolysis is carried out and these changes indicate to the fact that there is a slight decrease in the number of defects in graphene layer [199]. The peak intensity ratio probes the occurrence of point-like defects that are related to the modifications in the carbon network due to the destruction of  $sp^2$  hybridisation. As the formation of oxygen-containing functionalities boosts the development of  $sp^3$  defect sites [206]; the decrease in the  $I(D)/I(G)$  ratio may be connected to the deoxygenation of the carbon lattice due to high temperature and the recovery of the  $sp^2$  structure of graphene.

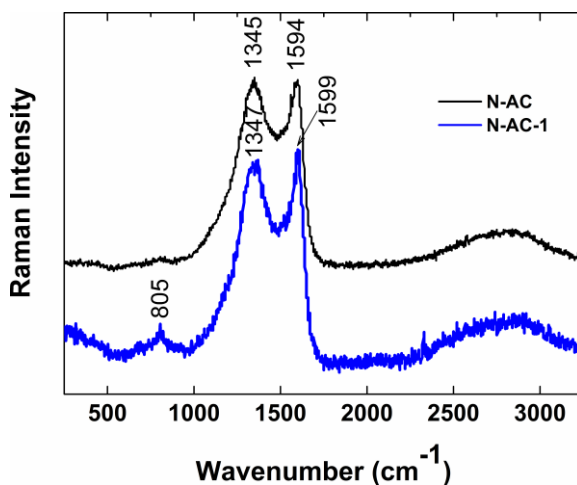


**Figure 24.** Raman spectra of wood-based N-doped carbon before (N-AC) and after second heat treatment (N-AC-1). The excitation wavelength is set to 532 nm (0.6 mW).

The electrochemical activity towards the ORR in alkaline media was studied on GC electrodes by employing RDE method (explained in more detail in section 3.6). The results of oxygen electroreduction on N-AC-1 by varying the rotation rates is shown in Figure 25a. The onset potential is an important criterion for evaluating the ORR activity of the catalyst material, the  $E_{\text{onset}}$  for N-AC-1 is approximately 920 mV vs RHE. By varying the rotation rate, the onset potential remains the same, indicating that the N-AC-1 is at least stable on the short term. The Koutecky-Levich (K-L) plots were constructed (Figure 25b) by employing the K-L equation (explained in more detail in section 3.6) and by using the polarisation data shown in Figure 25a. The K-L lines are almost linear, the intercepts of the extrapolated lines are close to zero, indicating that the ORR that takes place on the electrode is diffusion limited within the studied potential range. The electrons transferred per oxygen molecule ( $n$ ) was calculated at different potential values and the  $n$  value is shown in the inset of Figure 25b. The  $n$  value is close to 4 throughout the whole potential range studied, meaning that oxygen is directly reduced to water. Although, it is impossible to determine through K-L analysis if the process is a direct four electron process or  $\text{O}_2$  reduction via  $\text{HO}_2^-$  intermediate (so called  $2 e^- + 2 e^-$  reduction) pathway.

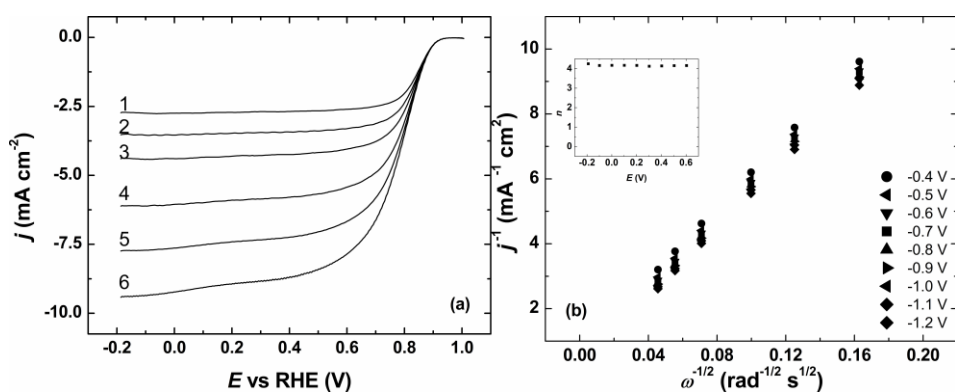


**Figure 25.** (a) RDE polarisation curves for ORR on GC electrodes modified with N-AC-1 in  $\text{O}_2$ -saturated 0.1 M KOH.  $v = 10 \text{ mV s}^{-1}$ ;  $\omega = (1) 360$ ; (2) 610; (3) 960; (4) 1900; (5) 3100; (6) 4600 rpm. (b) K-L plots for ORR on the N-AC-1 in 0.1 M KOH at different potentials; the inset figure shows the changes in  $n$  depending on the potentials studied.

Similar tendencies have been previously observed by Hu *et al.* [87], who studied N-doped carbon prepared from hydroxypropyl methylcellulose as the ORR catalyst in alkaline media. Although, the electrocatalytic performance was similar to the catalyst presented herein ( $E_{\text{onset}}$  920 mV vs 910 mV vs RHE), the catalyst loading was higher than used in this work ( $500 \mu\text{g cm}^{-2}$ ). Han *et al.* [209] have synthesised nitrogen-doped mesoporous hollow-core nanospheres with the BET surface area of  $770 \text{ m}^2 \text{ g}^{-1}$  and quite high nitrogen content (4.4–6.7 wt.%), but the catalyst loading was once again higher than reported in this work ( $460 \mu\text{g cm}^{-2}$ ). So, the electrochemical activity towards the ORR presented in this work is comparable or even higher than for other similar catalyst materials.

Stability is very important factor in potential practical applications in fuel cells and metal-air batteries. Stability test results for the N-AC-1 are shown in Figure 26a. 1000 potential cycles between 1 to  $-0.2 \text{ V}$  were carried out, the onset and half-wave potentials only changed very slightly during the 1000 cycles in alkaline media. However, a slight decrease in the diffusion limited current values can be observed, meaning that the

morphology of the catalyst material on the electrode changes a bit, but it has no effect on the active sites. More likely cause of that is that a very small amount of the catalyst material detaches from the electrode during these 1000 potential cycles. Methanol tolerance tests were conducted to compare commercial Pt/C catalyst and the N-AC-1 and further study the catalyst's durability for potential utilisation in direct methanol fuel cells. The results of methanol tolerance tests are shown in Figure 26b, methanol was added at 300 s, and it is possible to see that in case of commercial Pt/C the relative current drops to around 30%. In case of N-AC-1 the current drop is not as drastic, the value of relative current decreases slightly, but stabilises quite well and shows no significant change after that.

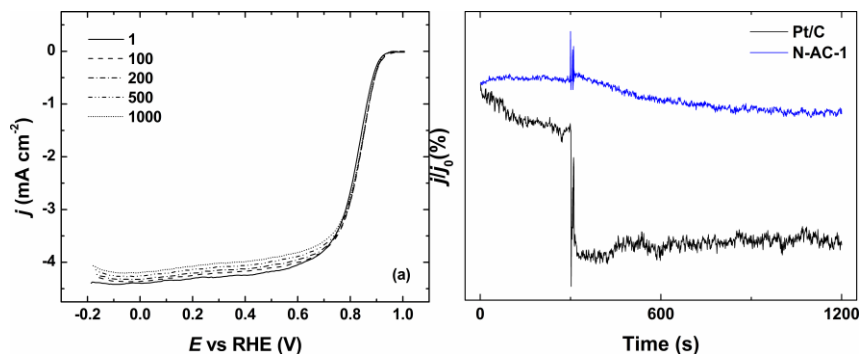


**Figure 26.** (a) Stability of GC electrodes modified with N-AC-1 in 0.1 M KOH,  $v = 10 \text{ mV s}^{-1}$ ;  $\omega = 960 \text{ rpm}$ . (b) Methanol tolerance test carried out at 0.6 V with the addition of 3 M MeOH comparing N-AC-1 and commercial Pt/C.

The comparison between N-AC-1 and different commercial catalysts is shown in Figure 27. The onset and half-wave potential for the N-AC-1 is much more positive comparing to N-AC and the most commonly used metal-free catalyst support Vulcan XC 72R. In comparison with the commercial 20% Pt/C, the onset potential is slightly more negative, but the diffusion-limited current density values are reaching much higher values at 1900 rpm compared to the commercial 20% Pt/C catalyst.

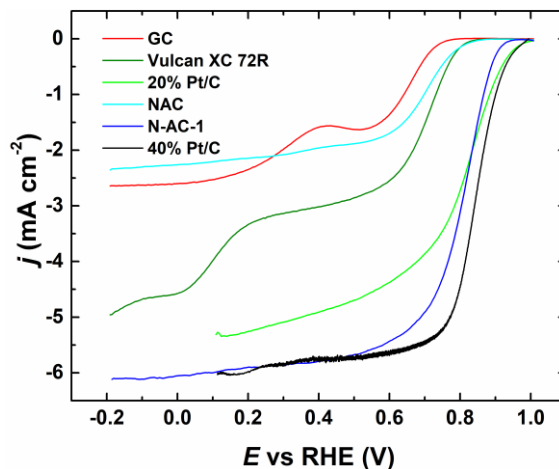


**Figure 27.** RDE voltammetry curves for ORR on GC electrodes modified with N-AC, N-AC-1 and different commercial catalyst materials in  $\text{O}_2$ -saturated 0.1 M KOH.  $v = 10 \text{ mV s}^{-1}$ ;  $\omega = 1900 \text{ rpm}$ .

Wu *et al.* have synthesised N-doped graphitic carbon nanoribbons [210] that exhibit higher onset potential than presented in this work, but the catalyst loading was  $2.3 \text{ mg cm}^{-2}$ , which is more than five times higher than the loading of N-AC-1 ( $400 \text{ } \mu\text{g cm}^{-2}$ ). Wu *et al.* have also used ferrous chloride in the synthesis process and this may have a great impact on the electrochemical activity, as Fe-based catalysts are one of the most active towards the ORR [211].

There are many research articles that have used biomass as a precursor to produce carbon [212–217], and some of these exceed the electrochemical activity presented herein, but the goal of this work was to employ and valorise easily available precursor in Europe.

Good electrochemical activity of the N-AC-1 has been achieved due to very high SSA and enlarged pore volume of the catalyst, that increases after the second pyrolysis step, that has a positive effect towards the oxygen transport etc. The N-AC-1 showed high amount of pyridinic-N and the synergy of the above-mentioned factors should be responsible for the high electrocatalytic activity towards the ORR. The work carried out shows that there is a great potential to develop highly effective, cheap, sustainable, and active wood-based nanocarbon materials for energy storage applications.

The work carried out herein shows that there is a great potential to prepare wood-based nanocarbons that can further be employed as catalysts for the ORR. Further optimisation of the synthesis is needed to carry out in order to make it even more efficient and sustainable.

#### **4.2.2 Oxygen electroreduction on N-doped wood-based graphene-like carbon**

Wood was used as a precursor to synthesise graphene-like catalyst material for the ORR. The graphene-like structure was achieved by varying the synthesis parameters. The graphene and graphene-like materials are very attractive for various clean energy technology applications, including fuel cells [31,39] and batteries [218]. So, the probability of producing graphene from biomass is fascinating, because right now, the graphene is mainly produced through top-bottom [219] bottom-up methods [220], employing fossil-based and environmentally hazardous or not easily scalable methods.

In this work, graphene-like catalyst material was produced by using alder wood char as a precursor and the exact preparation mechanism is described in more detail in section 3.4. The electrochemical characterisation is described in section 3.6 and physical characterisation in 3.7, respectively.

Textural properties of the precursor wood char (WC), activated wood char (AWC) and doped wood char-based (N-AWC) catalyst material were studied by employing  $\text{N}_2$  physisorption. The isotherms are shown in Figure 28a and the pore size distributions calculated by employing the quenched solid density functional theory (QSDFT) are shown in Figure 28b. The isotherms for the AWC and N-AWC belong to the type IV [221], which is characteristic to mesoporous materials, but the isotherm for precursor WC belongs to typical type I [196].

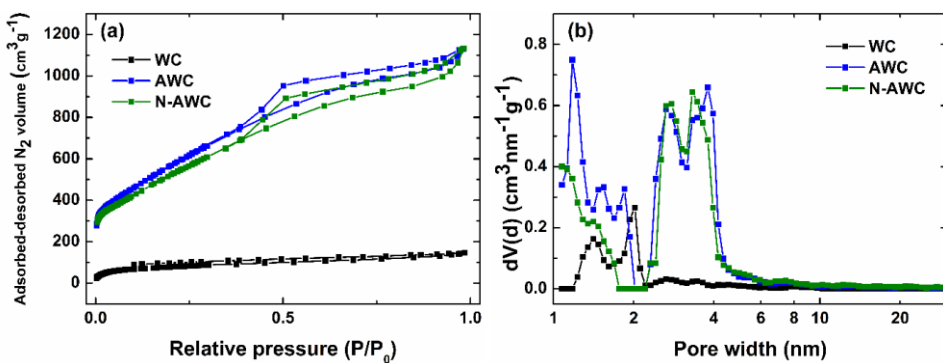


**Figure 28.** (a) Nitrogen adsorption-desorption isotherms for precursor WC, AWC, and N-AWC; (b) pore distribution for WC, AWC and N-AWC.

The SSAs calculated by Brunauer-Emmet-Teller (BET) and QSDFT are shown in Table 2. Before activation, the SSA of WC is very low, but after the activation process is carried out (explained in more detailed in section 1.3 and 3.4) the SSA values have grown enormously (280 vs 2088  $\text{m}^2 \text{g}^{-1}$ ). Activation gives a lot of surface to react with the N-containing dopant DCDA and the final SSA does not change significantly after the doping. The total ( $V_{\text{total}}$ ) and micropore volume ( $V_{\text{micro(DR)}}$ ), calculated by employing Dubinin-Radushkevich theory) values and the average pore diameter ( $L$ ) values in Table 2 show that the activation introduced micro- and mesoporosity to the catalyst material. Although, the microporosity decreases slightly due to a closure of some of the micropores present in the material, because the carbon structure becomes more ordered during the heating.

**Table 2.** Textural properties of the wood-based materials as determined by BET and QSDFT.

Material	$S_{\text{BET}}$ , $\text{m}^2 \text{g}^{-1}$	$S_{\text{DFT}}$ , $\text{m}^2 \text{g}^{-1}$	$V_{\text{total}}$ , $\text{cm}^3 \text{g}^{-1}$	$V_{\text{micro(DR)}}$ , $\text{cm}^3 \text{g}^{-1}$	$L$ , nm
WC	280	180	0.20	0.11	2.02
AWC	2088	1419	1.61	0.44	2.26
N-AWC	1924	1383	1.60	0.35	2.31

The microstructure of the N-AWC was further studied by employing TEM and the microphotos are shown in Figure 29a,b. The morphology of typical translucent, wrinkled and wavy layered graphene can be seen in Figure 29a. Such appearance of N-doped graphene is confirmed by previous researchers [86,222–224]. Figure 29b shows that the distance between two layers is 0.34 nm and this matches with the distance between two sheets in graphene-like materials [225].

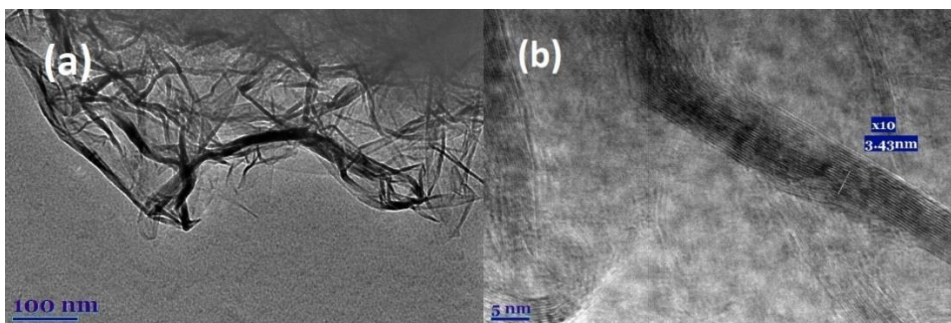


**Figure 29.** TEM microphotos of the N-AWC catalyst material.

The surface elemental composition was further studied by XPS, and the overview spectrum is shown in Figure 30a. O 1s, N 1s and C 1s are clearly visible from the overview spectrum. Due to the limited statistics, particularly for the nitrogen peak in the overview, their relative content (at.%) in the legend was verified by comparing with the corresponding region spectra and normalised to acquisition time, estimated escape depth at their respective kinetic energies, photoionisation cross section and instrument transmission function. The surface content of N is relatively low (0.9%) compared to other findings in the literature [204,226,227]. The C 1s peak corresponding to carbon in  $sp^2$  hybridisation is very intense and can be seen near 284.5 eV (Figure 30b). 95.7% of C 1s intensity corresponds to the characteristic asymmetric (Doniach-Sunjjic) line shape of metallic (graphene) specimen and the remaining contributions come from valence shake-up (around 290 eV, 3.1%) and very minor component (1.2%) corresponds to the typical single-bonded oxygen (C–O). The fitting of O 1s yielded components around 530.1 eV, 531.6 eV, 532.9 eV and 535 eV. The indium peak can be seen from the overview spectrum (Figure 30a), because the sample was pressed into metallic indium prior to the measurement. As the indium was not fully covered with the sample, it had implications on the O 1s spectrum interpretation (Figure 30c). The peak at 530.1 eV could be attributed to the fully oxidised indium within the probe depth of XPS, but this is not fully plausible, more likely the contribution comes from the quinone moiety that is present in the sample [228,229]. The peak at 531.6 eV could correspond to the double bonded carbon or as well as to surface hydroxyl groups. The contribution from the surface hydroxyl groups is rather plausible, as no feature of C=O can be seen in the C 1s spectrum (should be around 288.5 eV), but it could be buried by the onset of the shake-up features of the very abundant  $sp^2$  carbon. The peak at 532.9 eV corresponds to single bonded carbon (C–O).

Theories around the ORR activity on N-doped materials is still very controversial, as some of the research groups have found that the high surface content of nitrogen is the main source of achieving high electrocatalytic activity towards the ORR [94,200,230]. At the same time, some other researchers have not found any correlation between the higher nitrogen content and enhanced electrocatalytic activity [199,203,231]. The N 1s peak was deconvoluted into 4 different N-containing groups. The most abundant component was of course pyridinic-N (398.2 eV, 42%), followed by pyrrolic-N (400.2 eV, 30.5%) and graphitic-N (402.4 eV, 14%) and N–O (405 eV, 13.5%). Both experimental data of catalysts consisting almost only of pyridinic-N [92] and theoretical calculations [184] have shown that pyridinic-N is regarded as the most active nitrogen moiety. In case of N-AWC, almost half of the nitrogen was in pyridinic form, and this effect could be significant even though the surface content of nitrogen might be low.

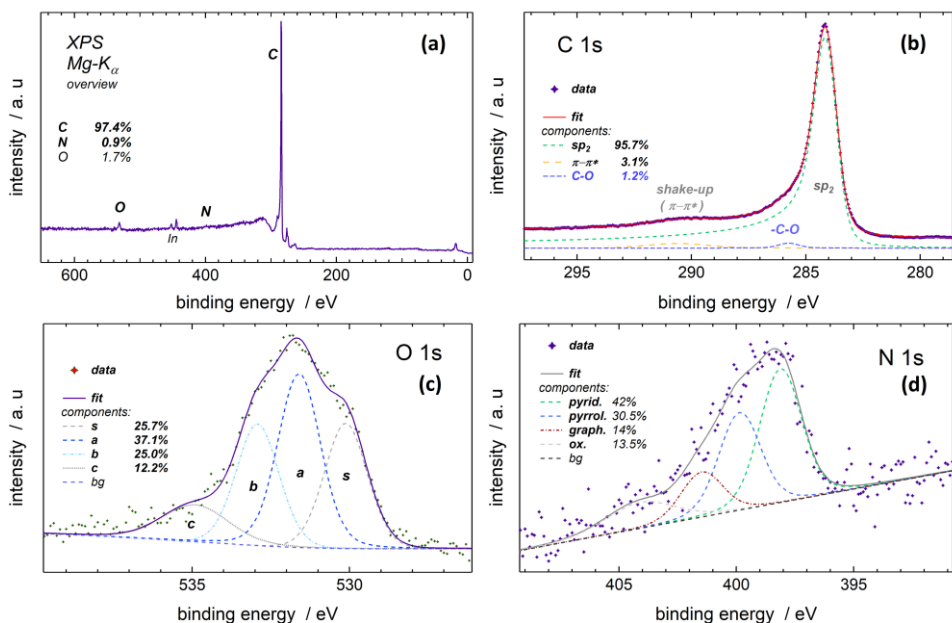


**Figure 30.** (a) XPS overview spectrum of N-AWC; high resolution spectra of (b) C 1s; (c) O 1s and (d) N 1s.

To study the catalyst molecular structure, Raman spectroscopy was employed, and Figure 31 compares N-AWC with AWC and with the starting material WC. Main bands for characterising the carbon nanomaterials are D, G and 2D and the corresponding wavenumbers for 532 nm excited spectrum are as follows: around  $1350\text{ cm}^{-1}$  for D,  $\sim 1580\text{ cm}^{-1}$  for G and  $\sim 2695\text{ cm}^{-1}$  for 2D. The low intensity shoulder around  $1619\text{ cm}^{-1}$  belongs to D' mode, both D and D' modes are connected with the defects that are present in materials as well as  $\text{sp}^3$  hybridised carbons [232]. G band indicates to the existence of  $\text{sp}^2$  carbon, mainly C-C and C-N [209,233]. Before activation the Raman spectrum of pristine WC shows broad D and G bands around  $1362$  and  $1595\text{ cm}^{-1}$ , respectively. The 2D band, which is characteristic to graphene-like materials is not visible at all, instead, broad feature that is composed of many bands appears in the higher frequency region. The G band width value at FWHM(G) was found to be  $78.3\text{ cm}^{-1}$ . Hence, the Raman spectrum of precursor WC shows highly disordered carbon skeleton [208,234]. Noticeable changes were observed in the Raman spectrum after the activation and N-doping. The spectra of AWC and N-AWC resemble a graphene-like material, as well-defined 2D band and narrow G and D bands occur in the spectra [208,234]. As mentioned below the ratio of  $I_D/I_G$  describes the defects or irregularities in carbon nanomaterials, smaller ratio indicates that there are less defects present in the material [232]. The N-AWC material showed graphene-like structure and Raman spectra (Figure 31) shows that D band intensity is lower than of G band intensity in case of both materials.  $I_D/I_G$  ratio for N-AWC is 0.43 and for AWC the ratio is 0.36, indicating that there are more defects in N-doped sample. The FWHM(G) for N-AWC was  $30\text{ cm}^{-1}$  and the corresponding value for AWC was  $27.5\text{ cm}^{-1}$ . Hence, both values indicate that the doping induces negligible disordering in the graphene plane. The broad feature between  $1450\text{--}1500\text{ cm}^{-1}$  is clearly visible after fitting the experimental data with Lorentzian-Gaussian form components. This band indicates the amorphisation of the carbon [208,234] and the intensity in the case of N-doped sample is higher comparing to activated sample.

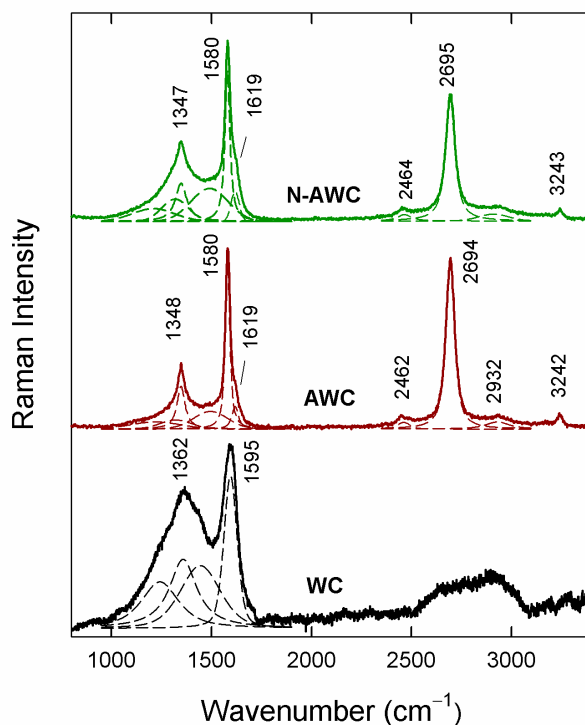


**Figure 31.** Raman spectra of N-AWC, AWC and precursor WC. The Lorentzian-Gaussian form components that were fitted are shown. The excitation wavelength is 532 nm.

The electrochemical properties towards the ORR were evaluated by carrying out RDE measurements in 0.1 M KOH solution. The electrode and catalyst ink preparation are described in more detail in section 3.6. The onset and half-wave potentials of the wood-based graphene-like material are 921 mV and 791 mV, respectively. The RDE polarisation curves measured at different rotating speeds (from 4600 to 360 rpm) are shown in Figure 32a. The current density increases with higher rotation speeds as the diffusion distance gets shorter. The  $E_{\text{onset}}$  does not change during the measurement, indicating that the material does not detach from the electrode and the material is stable during the ORR measurement. The K-L (explained in more detail in section 3.6) plot (Figure 32b) derived from data shown in Figure 32a shows that the process is almost completely diffusion limited, because the intercept is close to zero. The inset of Figure 32b shows that the  $n$  value is 4 within the studied potential range, suggesting that the ORR proceeds via 4-electron pathway. Figure 32c shows the CV curves recorded in oxygen or in nitrogen saturated 0.1 M KOH solution ( $\nu = 10 \text{ mVs}^{-1}$ ). The N-AWC shows no noticeable cathodic ORR peak for the curve recorded in  $\text{N}_2$ -saturated 0.1 M KOH, but in  $\text{O}_2$ -saturated solution, the cathodic ORR peak is clearly visible. Finally, the comparison with undoped graphene (G) and commercial N-doped graphene (N-G) and commercial 40% Pt/C is shown in Figure 32d. The  $E_{\text{onset}}$  and  $E_{1/2}$  values for commercial N-doped graphene are 851 mV and 552 mV, respectively. So, the corresponding values for N-AWC are both more positive than of the commercial catalyst ( $E_{\text{onset}} = 921 \text{ mV}$ ;  $E_{1/2} = 791 \text{ mV}$ ). Compared to a commercial Pt catalyst the onset and half-wave potential values are

slightly more negative for our catalyst N-AWC, but the goal of this work was to synthesise sustainable biomass-based N-doped carbon catalyst, that has higher electrocatalytic activity towards the ORR than of commercial materials. The further modification could include Pt on biomass-based carbon carrier, but this is out of the scope of the work carried out within this research, as the main goal is still to prepare metal-free catalysts for the ORR. The N-AWC is metal-free and consists of different surface nitrogen groups, the most abundant nitrogen group is pyridinic-N. Since the debate about the N-groups and their activity is still ongoing, it is hard to make definitive conclusions, but different research groups have found that pyridinic-N is mainly responsible for the electrocatalytic activity [203,235–237]. Lai *et al.* [203] have shown that pyridinic-N is essential for lowering the onset potential for the ORR polarisation curve.

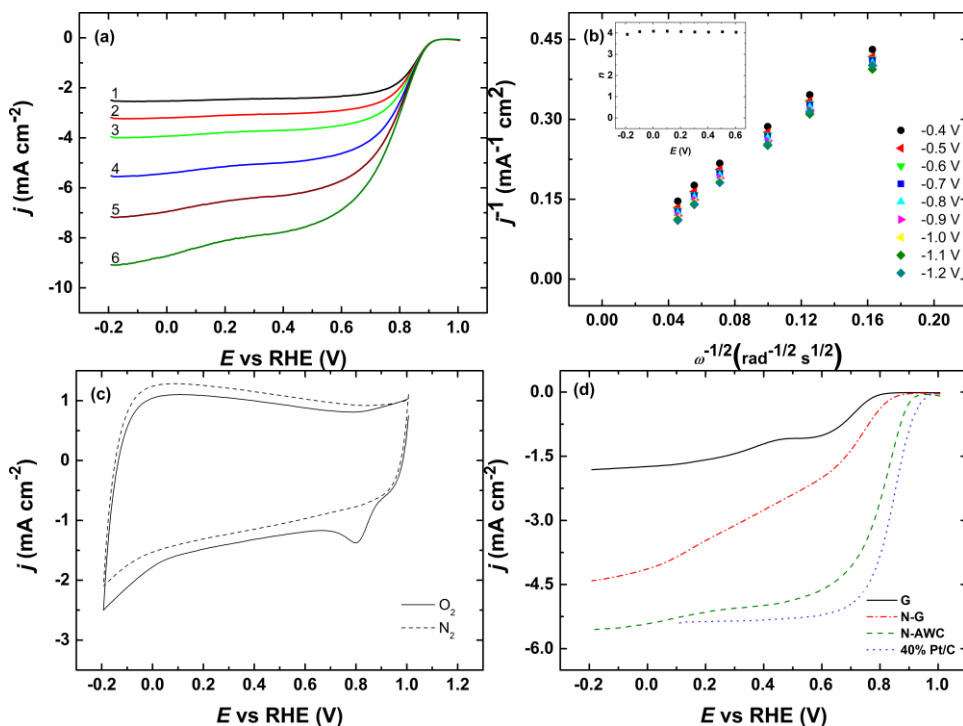


**Figure 32.** (a) RDE polarisation curves of GC electrodes modified with N-AWC in  $O_2$ -saturated 0.1 M KOH.  $v = 10 \text{ mV s}^{-1}$ ;  $\omega =$  (1) 360; (2) 610; (3) 960; (4) 1900; (5) 3100; (6) 4600 rpm; (b) K-L plots derived on the data shown on Figure 32a, inset shows the change of  $n$  values at different potentials; (c) CV in  $O_2$  or  $N_2$  saturated 0.1 M KOH; (d) comparison of polarisation curves for ORR on N-AWC and commercial catalyst materials.  $v = 10 \text{ mV s}^{-1}$ ;  $\omega = 1900 \text{ rpm}$ .

Since stability is an important factor to be considered in potential applications, chronoamperometry and methanol tolerance tests were carried out at 0.6 V (explained in more detail in section 3.6). The chronoamperometry results of commercial 40% Pt/C and N-AWC can be seen in Figure 33a. The current drops about 23% for commercial Pt catalyst after 20 hours, but the relative current density value of catalyst synthesised from alder wood char stays around 93% after 1200 minutes. This demonstrates the better durability of the wood-based carbon catalyst than of the commercial 40% Pt/C. Methanol tolerance testing proved the better durability even more, as the current drops drastically

and stabilises around 35% in case of Pt/C (Figure 33b), but in case of N-AWC the injection of methanol does not show any significant change in the relative current density values, since it remains around 100%.

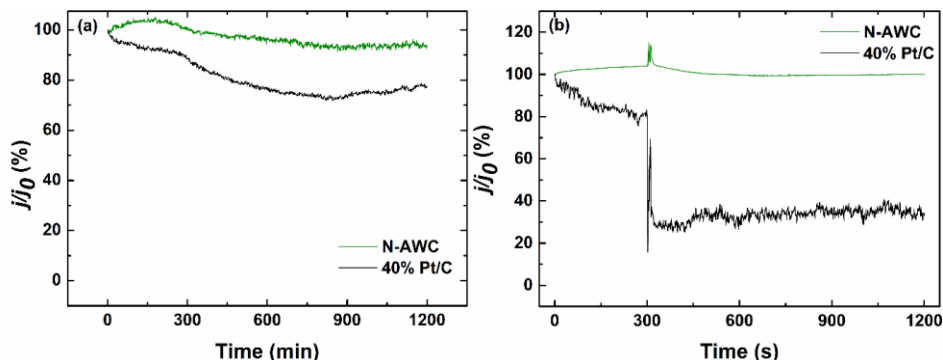


**Figure 33.** (a) Chronoamperometric responses for the N-AWC and commercial Pt catalyst; (b) methanol tolerance testing results for the N-AWC and commercial Pt catalyst.  $U = 0.6$  V,  $\omega = 1900$  rpm.

As a result, we have prepared graphene-like electrocatalyst for the ORR. The graphene-like material was achieved by easy pyrolysis procedure that could be easily upscaled and used on a larger scale. Herein the material was tested for the ORR, but this type of material could be used in other energy conversion systems, such as batteries.

### 4.3 Oxygen electroreduction on M-N-C catalysts

Since different transition metal-based phthalocyanines are thoroughly studied, the goal of this work was to employ different phthalocyanines for modifying MWCNTs and study them as potential catalysts for the ORR in alkaline media. The work in this field began with manganese and copper phthalocyanine (MnPc and CuPc) and was later continued with even less studied zinc and dilithium phthalocyanine (ZnPc and Li<sub>2</sub>Pc).

#### 4.3.1 Oxygen electroreduction on Mn- and CuPc-based MWCNT catalysts

The ORR catalysts were prepared by modifying MWCNTs with MnPc or CuPc. In this work, at first, different ratios were varied and once the best ratio was confirmed, the best ratio was pyrolysed at various temperatures in order to see the effects of heat-treatment temperature as well. The more detailed catalyst preparation process is explained in the section 3.5. And the electrochemical and physical characterisation methods are described in more detail in the section 3.6 and 3.7, respectively.

First the best ratios were evaluated by employing SEM. In case of MnPc the best ratio was found to be 1:1 (MnPc-to-MWCNT), but in case of copper, the best ratio was 3:1 (CuPc-to-MWCNT). The SEM microphotos of the catalysts are presented in Figure 34a,b, respectively. In case of MnPc the metal phthalocyanine is more uniformly dispersed on the surface of MWCNTs and no bigger agglomerations of possible metal particles cannot be seen, only small nanoparticles on the MWCNTs walls. In case of CuPc, the MWCNT surface is possibly covered with larger copper metal particles, that could influence the electrochemical activity of the catalyst.

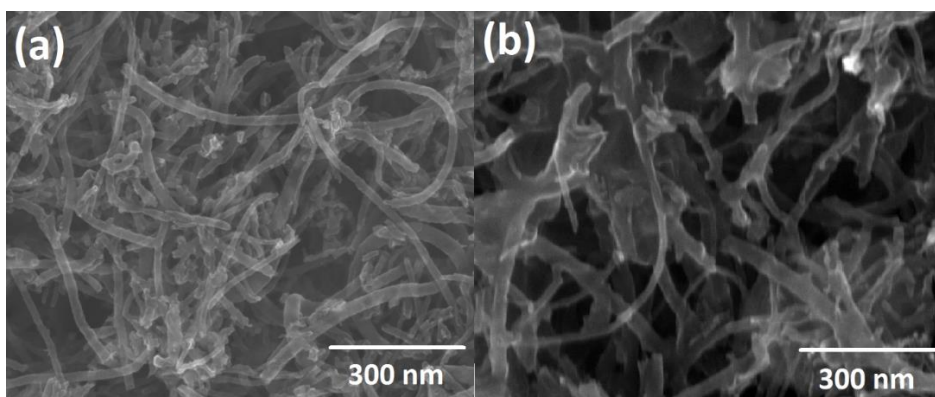


**Figure 34.** HR-SEM photos of (a) MnPc/MWCNTs (1:1) and (b) CuPc/MWCNT (3:1).

Surface composition and the existence of different elements in the sample was further studied by XPS. Figure 35a, b shows the overview and high-resolution spectra of metal and nitrogen as well. For both samples, four XPS peaks are clearly visible in the spectra – Cu 2p or Mn 2p, C 1s, O 1s and N 1s. The oxygen peak is related to the support material MWCNTs and is coming from different carbon-oxygen functionalities that exist on the surface of MWCNTs. Due to very close binding energies, the identification of oxygen functionalities in the catalyst material is very difficult, although, different studies have shown that main groups that are present on the MWCNTs surface are quinone and carboxyl groups [238,239]. In case of MnPc-based catalyst, the N 1s peak can be deconvoluted into three different peaks – pyridinic-N emerges around 398.6 eV, second hump at bit higher binding energies corresponds to pyrrolic-N (around 400 eV) and the third one belongs to graphitic-N (around 401 eV). These results are in good agreement with the conclusions made by Dominguez *et al.* [240]. For the CuPc/MWCNT catalyst the N 1s region shows two peaks, the peak around 398.7 eV could belong to pyridinic-N and the peak around 401.3 eV could be assigned to graphitic-N. It is clearly visible, that pyrrolic-N and pyridine-N-oxide contribute to these N peaks, but similarly to the oxygen peak, the definition of the exact surface species is rather difficult and under debate. Although, similar results are achieved by Ding *et al.* [241]. Both samples showed evident metal peaks – the inset of Figure 35a shows a wide manganese peak in the range of 640.9–641.6 eV. This peak is connected to different manganese oxides and Mn 2p<sub>3/2</sub>, which appears around 640 eV. Very small peak of Mn 2p<sub>3/2</sub> and wide peak of Mn 2p<sub>1/2</sub> are clearly recognisable at 645 eV and 654 eV, respectively. The inset of Figure 35b shows the Cu 2p XPS peaks around 932.6 eV belongs to Cu 2p<sub>3/2</sub> and is most probably connected to the decomposition of CuPc ring and the reduction to Cu(I) in the pyrolysis process [242]. The small peak around 934.6 eV belongs to Cu(II)hydroxide that forms if exposed to air. The wide peak in the range of 946 to 940 eV corresponds to the Cu(II) satellite peak and the peak around 952.3 belongs to Cu 2p<sub>1/2</sub>.

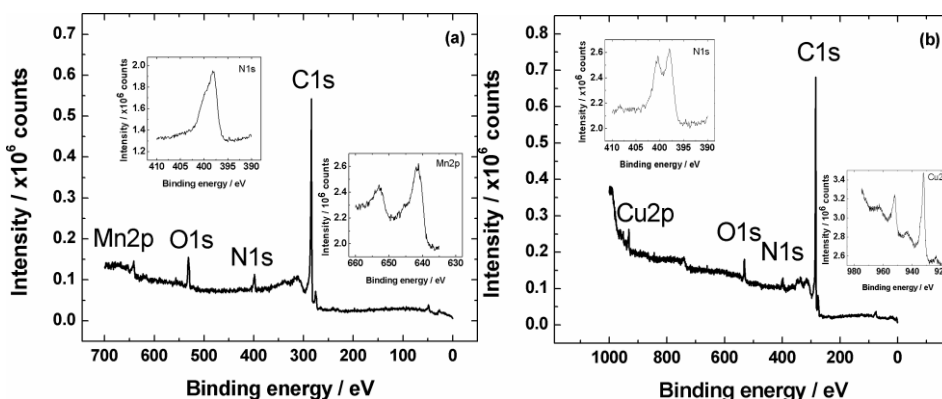


**Figure 35.** XPS overview spectra of (a) MnPc/MWCNT (1:1) and (b) CuPc/MWCNT (3:1). The inset shows N 1s and Mn 2p and Cu 2p, respectively.

Oxygen electroreduction was investigated by RDE method in 0.1 M KOH. The measurement parameters, electrode and catalyst ink preparation are written in more detail in section 3.6. First, different ratios of MPcs-to-MWCNTs were synthesised at 800 °C and the results are shown in Figure 36a,b. The optimal ratio for MnPc/MWCNT was 1:1 and for CuPc/MWCNT the ratio was 3:1. The best ratios synthesised at different temperatures are shown in Figure 36c,d. For both catalyst materials, the favourable heat-treatment temperature was 800 °C. The catalyst activity increases with rising the temperature until 800 °C, as the half-wave potential shifts to more positive more than 100 mV for both catalysts. In case of CuPc/MWCNT this shift is observed for onset potential as well. The electrochemical activity of MPcs pyrolysed at this temperature is usually attributed to both, the M-N<sub>x</sub> moieties and pyridinic-N groups forming at 800 °C [243,244]. The nitrogen surface group activity towards the ORR is proved by N-doping of carbon nanomaterials [245,246]. When the heat-treatment temperature was increased to 1000 °C, a decrease in the ORR activity was observed. This is most probably connected to the decomposition of the electrocatalytically active sites into metallic Mn and Cu or metal carbides, which are less active in alkaline media and the amount of pyridinic-N groups decreases at higher temperatures [241].

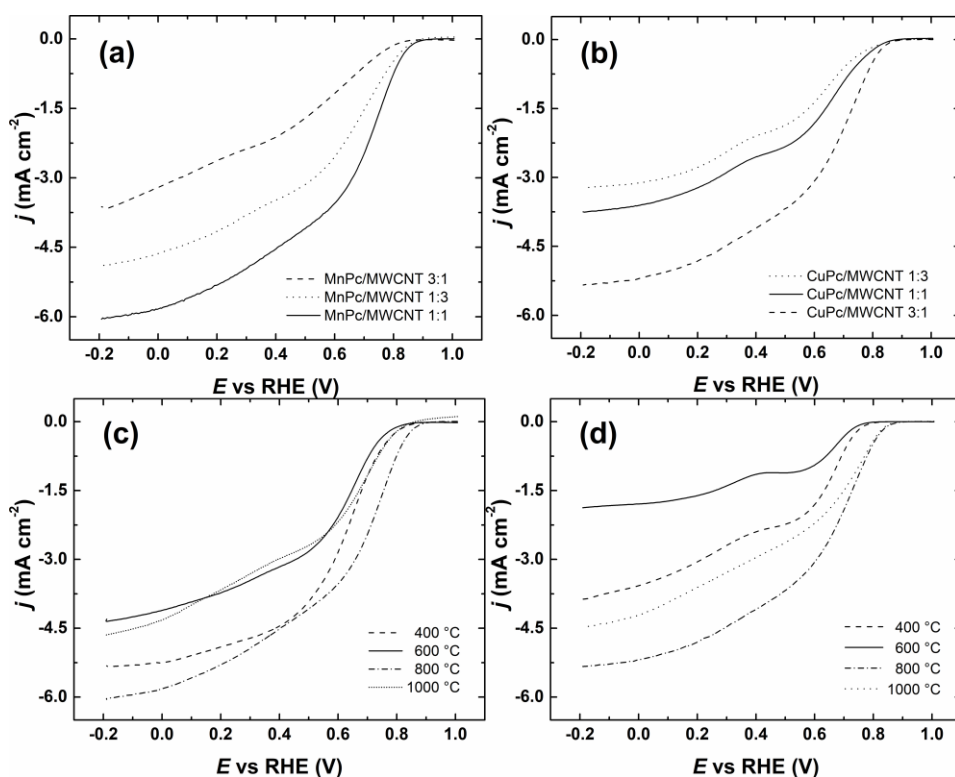


**Figure 36.** RDE voltammetry curves for ORR on GC electrodes modified with (a) MnPc/MWCNT and (b) CuPc/MWCNT, synthesised at 800 °C by varying ratios; (c) MnPc/MWCNT (1:1) synthesised at different temperatures; (d) CuPc/MWCNT (3:1) synthesised at different temperatures.  $\nu = 10 \text{ mV s}^{-1}$ ,  $\omega = 1900 \text{ rpm}$ .

A set of the ORR polarisation curves for the best catalysts (MnPc/MWCNT 1:1 800 °C and CuPc/MWCNT 3:1 800 °C) are shown in Figure 37a,b. As expected, the limiting current densities in the hydrodynamic mode increase with increasing the rotation rate and the onset potential shows no significant change. This means that no material has left from the electrode and no significant changes are taking place during the electrochemical measurements. The onset potential for MnPc/MWCNT 1:1 is 926 mV and for CuPc/MWCNT 3:1, it is 896 mV, which are quite similar or even slight better compared to the values achieved by other research carried out with MnPc and CuPc catalysts on Vulcan XC-72R [240,247,248]. The electrocatalytic activity of MnPc-based catalyst is even somewhat better than for the previously investigated CoPc and FePc-based catalysts [249]. The small second reduction wave for the CuPc/MWCNT catalyst (Figure 37b) is observable, notably at higher rotation speeds and negative potentials ( $\sim 356 \text{ mV}$ ), this is quite common and in great agreement with previous reports [250]. The pre-wave is connected to the oxygen-containing groups on the surface for undoped nanocarbons, especially quinone groups [251]. Similar  $\text{O}_2$  reduction results have been achieved with GO- and for the non-pyrolysed MPc/GO electrodes [252,253]. The high reduction current densities for both catalyst materials (especially MnPc/MWCNT) were observed probably due to the generation of electrocatalytic active sites that usually form between temperatures 700–950 °C. Ladoeur *et al.* have found that the electrocatalytic activity of heat-treated CoPc/Vulcan XC-72 (annealed at 800 °C) was twice as high compared to

non-pyrolysed catalyst [159,254]. The number of electrons and K-L plots were constructed based on the Koutecky-Levich equation that is written in section 3.6. Figure 37c,d show the K-L plots derived from the data shown in Figure 37a,b. The intercepts for both catalysts are close to zero at negative potentials, indicating that the O<sub>2</sub> reduction process is almost completely under diffusion control at negative potentials, but at more positive potentials, the process is dominated by mixed kinetics-diffusion control. The insets of Figure 37c,d show the *n* values, which vary from 3.5 to 4, indicating that rather mixed 2 e<sup>-</sup> and 4 e<sup>-</sup> process is taking place at more positive potentials, whereas at more negative potentials the *n* value reaches 4 and it can be predicted that mostly OH<sup>-</sup> ions are produced at the potentials that are more negative than 0.4 V. This is in good agreement with the previous research carried out on MnPc/C catalysts, which found that the ORR proceeds primarily via 4-electron pathway in alkaline media [247,255]. Inset of Figure 37d shows the *n* values in case of CuPc/MWCNT and similar tendency can be observed, only the value of *n* reaches 4 at *E* < 0.2 V.

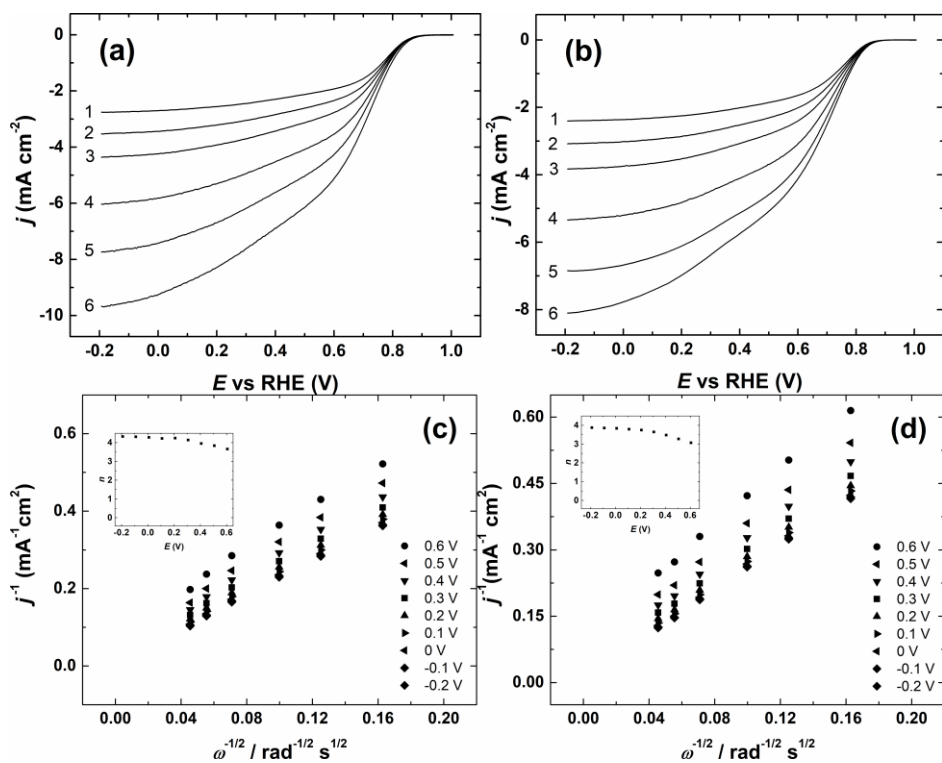


**Figure 37.** RDE polarisation curves of GC electrodes modified with (a) MnPc/MWCNT (1:3) and (b) CuPc/MWCNT (3:1) in O<sub>2</sub>-saturated 0.1 M KOH.  $v = 10 \text{ mV s}^{-1}$ ;  $\omega = (1) 360$ ; (2) 610; (3) 960; (4) 1900; (5) 3100; (6) 4600 rpm; (c) and (d) K-L plots derived on the data showed on Figure 37a,b, respectively; inset shows the change of *n* values at different potentials.

Figure 38 presents the comparison of GC electrodes modified with the most active catalyst materials studied (MnPc/MWCNT 1:1 800 °C and CuPc/MWCNT 3:1 800 °C). The voltammetry curve of O<sub>2</sub> reduction on pure MWCNTs has been added for comparison purposes. As shown in the Figure 38 the onset potential on unmodified MWCNTs is more negative than of MnPc- or CuPc-modified MWCNTs. The onset potential for MnPc-based

catalyst shifted more than 100 mV and the reduction current densities at 1900 rpm were almost  $4 \text{ mA cm}^{-2}$  higher as compared to unmodified nanotubes. CuPc-based catalyst differs only slightly from MnPc-based catalyst, since the onset potential is a bit more negative and current density values are  $0.75 \text{ mA cm}^{-2}$  lower at 1900 rpm. All this indicates that the ORR activity is connected to the catalytically active sites that are formed during pyrolysis, when metal phthalocyanines decompose and get attached on the surface of MWCNTs. The visible differences in MnPc- and CuPc-based catalyst activities could be connected to the difference in the central metal atom of the Pc ring and the existence of better  $\pi$ - $\pi$  interactions between MPc and MWCNTs [256]. The interaction of MnPc/MWCNT with  $\text{O}_2$  is more favourable compared to that of CuPc/MWCNT due to energy differences of the metal d-orbitals. Zagal has reported that high electrocatalytic activity is expected when the relative energies of the central metal d-orbitals in the MPc is with similar energy as the catalysed species. Therefore, the highest electrochemical activity towards the ORR is expected for the MPcs that contain a central metal ion that can reversibly bind both  $\text{HO}^-$  and  $\text{O}_2$  [257].

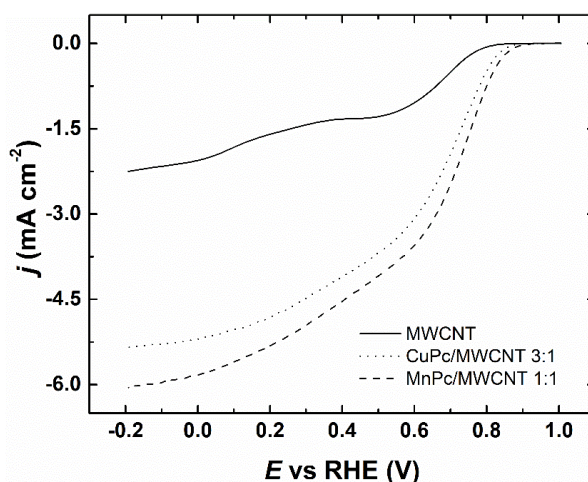


**Figure 38.** RDE polarisation curves for ORR on GC electrodes modified with different catalyst materials or pure MWCNTs in 0.1 M KOH.  $v = 10 \text{ mV s}^{-1}$ ;  $\omega = 1900 \text{ rpm}$ .

The RDE results show that the best heat-treatment temperature regarding the ORR activity for both catalysts is  $800 \text{ }^\circ\text{C}$ . Previously, it has been found that the electrocatalytic activity could be connected to pyridinic-type nitrogen that is formed at  $800 \text{ }^\circ\text{C}$  [258]. It is proved that the catalytic activity is not only related to the central metal, because the central metal atoms do not play major role towards the ORR in alkaline media [259]. Even though the metal nanoparticles on carbon supports are sometimes not reported to be related to the ORR activity and the nitrogen is not reported being part of the catalytically active sites, these two species can form highly active catalyst centre for the ORR, and this is demonstrated in this study. The importance of MnPc- and CuPc-based catalysts have been recognised earlier [248,260], but the results obtained in this research give further insights into their electrochemical properties.

#### 4.3.2 Oxygen electroreduction on Zn- and Li<sub>2</sub>Pc-based MWCNT catalysts

ZnPc and Li<sub>2</sub>Pc-based catalysts were prepared by using the MWCNTs as a support. At first, different MPc-to-MWCNTs ratios were altered and after the best ratio was determined at 800 °C, the best ratio was heat-treated at different temperatures in order to see the effects of pyrolysis to the catalyst material as well. The MPc/MWCNTs preparation process is written in more detail in the section 3.5. Electrochemical and physical characterisation methods are explained in the sections 3.6 and 3.7, respectively.

The surface morphology of ZnPc/MWCNT (1:3 800 °C) and Li<sub>2</sub>Pc/MWCNT (1:1 1000 °C) deposited onto a GC disc was evaluated with HR-SEM and the images are presented in Figures 39a,b. From Figure 39a it can be seen that there are no agglomerates of nanotubes on the surface of the sample and there is no evidence of larger ZnPc particles. From Figure 39b it can be seen that the HR-SEM image is quite similar than of ZnPc-based catalyst and for both of the materials the MWCNTs are well dispersed and there are some solid residues on the surface of MWCNTs.

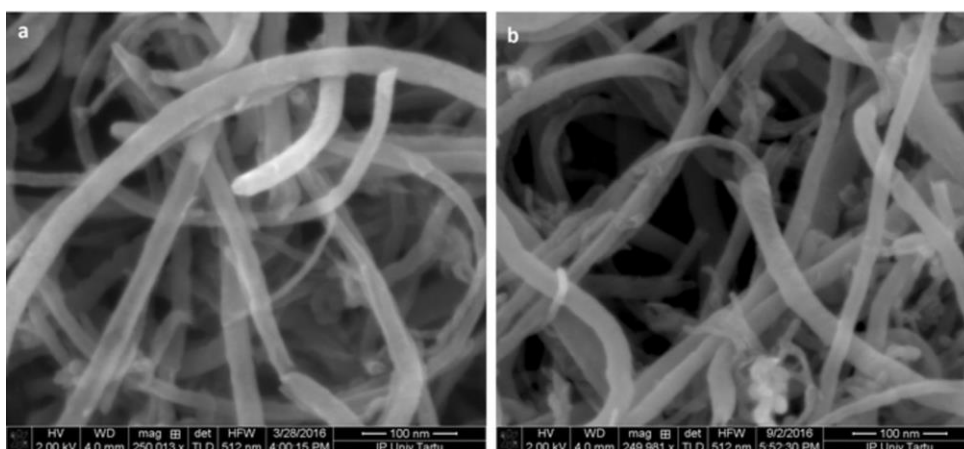


**Figure 39.** HR-SEM images of (a) ZnPc/MWCNT (1:3) and (b) Li<sub>2</sub>Pc/MWCNT (1:1).

The surface composition of the Pc-based catalysts was evaluated by XPS. Figure 40a,b presents the overview spectra of ZnPc/MWCNT (1:3 800 °C) and Li<sub>2</sub>Pc/MWCNT (1:1 800 °C). Four different peaks can be seen from the wide-scan spectra – C 1s, N 1s, O 1s and Zn 2p or Li 1s. N 1s XPS spectra in high-resolution show four different peaks that belong to pyridinic-N (398 eV), pyrrolic-N (400 eV), graphitic-N (401 eV) and pyridine-N-oxide (403 eV). The XPS analysis of N-doped carbon nanomaterials have been investigated more thoroughly by Atanassov *et al.* [261,262]. The total nitrogen content on the surface was 2.8 at.% for ZnPc/MWCNT (1:3 800 °C) and 3.2 at.% for Li<sub>2</sub>Pc/MWCNT (1:1 800 °C).

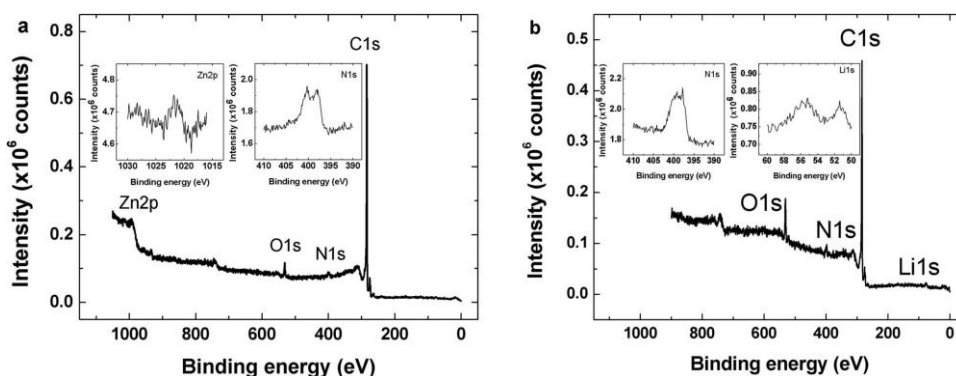


**Figure 40.** XPS overview spectra of (a) ZnPc/MWCNT (1:3) and (b) Li<sub>2</sub>Pc/MWCNT (3:1). The inset shows N 1s and Zn 2p and Li 1s, respectively.

Deconvolution results of different N-forms is shown in Table 3.

**Table 3.** The % of different N-forms on the surface of catalysts.

Catalyst	Pyridinic-N	Pyrrolic-N	Graphitic-N	Pyridine-N-oxide
ZnPc/MWCNT (1:3)	40	31	14	15
Li <sub>2</sub> Pc/MWCNT (1:1)	56	31	12	1

Two of these nitrogen forms, pyridinic and graphitic have been proposed as active sites for the ORR in alkaline media [263,264]. The origin of the N 1s peaks lies behind the decomposition of the macrocyclic complexes at high pyrolysis temperatures, since these complexes are the only possible sources of nitrogen. The O 1s peak is connected to different carbon-oxygen functionalities on the surface of MWCNTs [170]. The inset of Figure 40a shows the high-resolution Zn 2p spectrum, the total content of Zn is 0.7 at.% and the peak belongs to metallic Zn or ZnO (~1022 eV). The inset of Figure 40b shows the high-resolution spectrum of Li 1s and there are different states of Li, the peak at 55.6 eV belongs to Li in Li<sub>2</sub>O and the peak at 55.1 eV belongs to pure metallic Li. The overall content of Li is 3.4 at. %. Since the appearance of the pure metal particles on the catalyst surface is highly unlikely, we propose that the metal particles may be located between the MWCNTs or incorporated into the graphitic carbon skeleton and thereby are connected additionally to the nitrogen species. Usually, the presence of transition metals is necessary in order to synthesise highly active electrocatalysts, but it is unclear what is the role of transition metals in the formation of active sites that are non-redox-active [240].

The additional XPS measurements were carried out to determine the surface elemental contents of the catalysts pyrolysed at different temperatures. ZnPc/MWCNT 1:3 and Li<sub>2</sub>Pc/MWCNT 1:1 XPS spectra pyrolysed at different temperatures are shown in Figure 41a-d and Figure 42a-d, respectively. And the corresponding surface compositions are shown in Table 4. In case of ZnPc/MWCNT 1:3 samples pyrolysed at different temperatures, the surface content at 400 °C is relatively high (4.9 at.%), possibly due to the fact that the macrocyclic Pc structure has not yet fully been decomposed. With raising the temperature, the nitrogen content decreases and at 1000 °C no Zn is detected at the surface.

**Table 4.** Surface composition (at.%) of the catalyst materials evaluated by XPS.

Catalyst	N	C	O	Li/Zn
ZnPc/MWCNT (1:3, 400 °C)	4.9	89.9	4.3	0.9
ZnPc/MWCNT (1:3, 600 °C)	3.3	93.6	2.6	0.5
ZnPc/MWCNT (1:3, 800 °C)	2.8	91.1	5.4	0.7
ZnPc/MWCNT (1:3, 1000 °C)	1.6	95.0	3.4	0.0
Li <sub>2</sub> Pc/MWCNT (1:1, 400 °C)	3.5	92.6	2.5	1.4
Li <sub>2</sub> Pc/MWCNT (1:1, 600 °C)	0.9	91.4	5.0	2.7
Li <sub>2</sub> Pc/MWCNT (1:1, 800 °C)	3.2	84.2	9.2	3.4
Li <sub>2</sub> Pc/MWCNT (1:1, 1000 °C)	1.1	95.1	3.8	0.0

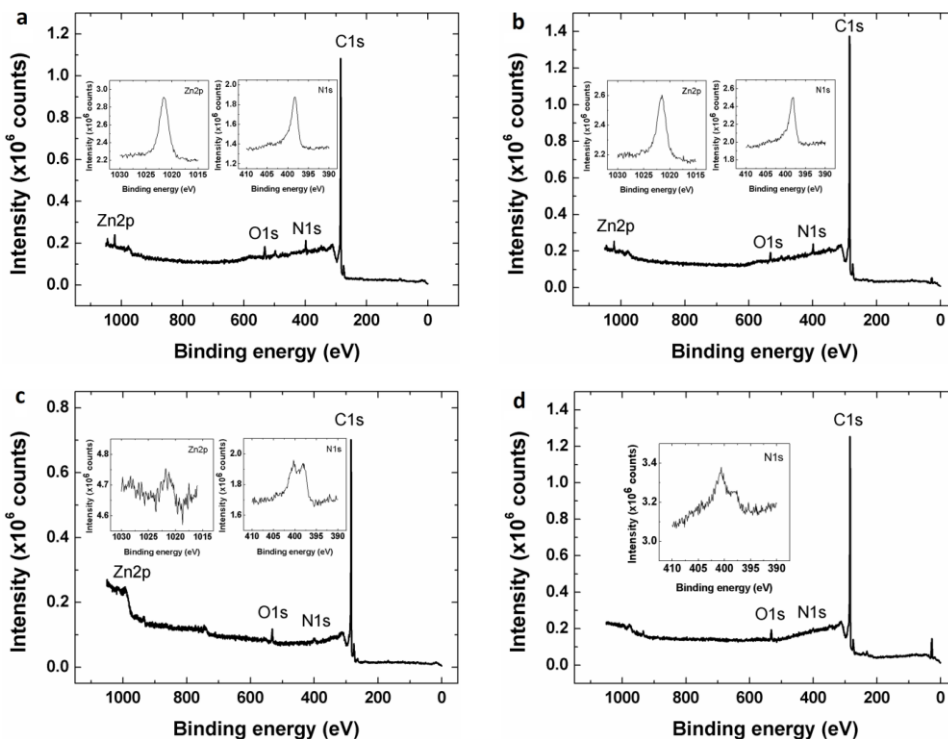


**Figure 41.** XPS survey spectra of the ZnPc/MWCNT (1:3) synthesised at (a) 400 °C; (b) 600 °C; (c) 800 °C and 1000 °C. The insets show N 1s and Zn 2p, respectively.

The same trend is visible in case of Li<sub>2</sub>Pc/MWCNT 1:1, at 400 °C the N content is 3.5 at.% and then at higher temperatures, the content decreases, but the optimum surface content is achieved at 800 °C. At 1000 °C no Li is detected (Table 4).

The comparison between relative content of different nitrogen species on catalysts synthesised at different temperatures and between the onset potential was done. The results are shown in Table 5. In case of ZnPc/MWCNT 1:3 the best onset potential was achieved with the catalyst pyrolysed at 800 °C, the Zn content is highest at this temperature (0.7 at.%) and the dominating N species is pyridinic-N. In case of Li<sub>2</sub>Pc/MWCNT 1:1, the highest metal content is achieved at 800 °C and most of the nitrogen on the surface is in pyridinic form. The synergy between the metal content and pyridinic-N content will definitely have an effect on the electrocatalytic activity of these catalysts.

**Table 5.** Relative content (%) of different N-forms and the  $E_{onset}$  values in 0.1 M KOH.

Catalyst	Pyridinic-N	Pyrrolic-N	Quaternary-N	Pyridine-N-oxide	$E_{onset}$ (mV vs RHE)
ZnPc/MWCNT (1:3, 400 °C)	61	11	19	9	816
ZnPc/MWCNT (1:3, 600 °C)	58	11	13	18	816
ZnPc/MWCNT (1:3, 800 °C)	40	31	14	15	936
ZnPc/MWCNT (1:3, 1000 °C)	19	18	36	27	776
Li <sub>2</sub> Pc/MWCNT (1:1, 400 °C)	58	22	5	15	856
Li <sub>2</sub> Pc/MWCNT (1:1, 600 °C)	41	34	10	15	906
Li <sub>2</sub> Pc/MWCNT (1:1 800 °C)	56	31	12	1	886
Li <sub>2</sub> Pc/MWCNT (1:1 1000 °C)	27	31	25	17	886

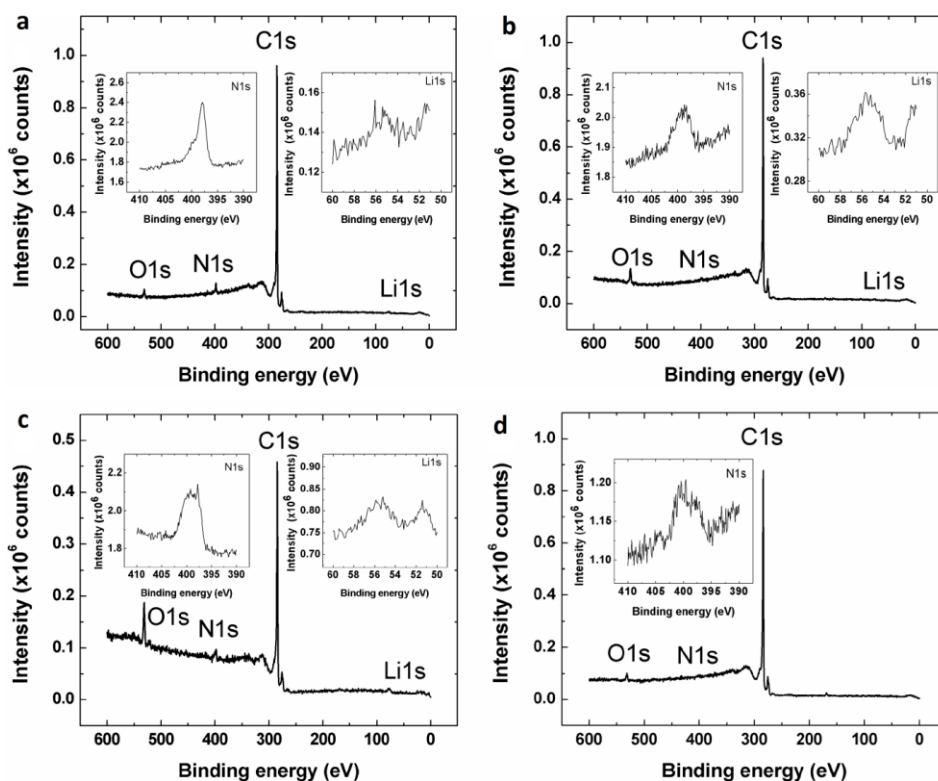


**Figure 42.** XPS survey spectra of the  $\text{Li}_2\text{Pc}/\text{MWCNT}$  (1:1) synthesised at (a) 400 °C; (b) 600 °C; (c) 800 °C and 1000 °C. The insets show N 1s and Li 1s, respectively.

Electrochemical measurements were carried out in 0.1 M KOH. Figure 43a,b shows the RDE polarisation curves for the ORR on ZnPc/MWCNT and  $\text{Li}_2\text{Pc}/\text{MWCNT}$ , the MPC-to-MWCNTs ratio was varied: 3:1, 1:1, 1:3. For comparison, unmodified MWCNTs are also shown. The MPC/MWCNT catalysts were all synthesised at 800 °C and the polarisation curves are shown at 1900 rpm. Figure 43a shows that the most active material in case of ZnPc/MWCNT is obtained when the mass ratio is 1:3, the  $E_{\text{onset}}$  is 936 mV, which is around 100 mV higher than the second-best catalyst material (ZnPc-to-MWCNT ratio 1:1). The  $E_{1/2}$  for the most active material is approximately 756 mV. The electrochemical activity increases as follows: pure MWCNTs < ZnPc/MWCNT (3:1) < ZnPc/MWCNT (1:1) < ZnPc/MWCNT (1:3), indicating that only little amounts of ZnPc is needed in order to improve the electrocatalytic activity towards the ORR. In case of  $\text{Li}_2\text{Pc}/\text{MWCNT}$  the best ratio is 1:1 (Figure 43b). The activity of different MPC-to-MWCNT increases in the following order: pure MWCNTs <  $\text{Li}_2\text{Pc}/\text{MWCNT}$  (3:1) <  $\text{Li}_2\text{Pc}/\text{MWCNT}$  (1:3) <  $\text{Li}_2\text{Pc}/\text{MWCNT}$  (1:1). Although the mass ratio of 1:3 shows a bit higher reduction current density, the  $E_{\text{onset}}$  and  $E_{1/2}$  values are still not as good as for the  $\text{Li}_2\text{Pc}/\text{MWCNT}$  (1:1). The  $E_{\text{onset}}$  for the most active  $\text{Li}_2\text{Pc}$ -based catalyst is around 886 mV and  $E_{1/2}$  is ca 806 mV. So, to compare ZnPc/ $\text{Li}_2\text{Pc}$ -based catalysts, the onset potential is higher in case of  $\text{Li}_2\text{Pc}$ -based, but half-wave potential is higher in case of ZnPc-based material.

The pyrolysis temperature was therefore optimised for the catalyst ratios of ZnPc-to-MWCNT (1:3) and  $\text{Li}_2\text{Pc}$ -to-MWCNT (1:1). The heat-treatment temperatures were varied from 400 to 1000 °C and the results are shown in Figure 43c,d. The ORR

curves are recorded at 1900 rpm in 0.1 M KOH. The optimum pyrolysis temperature for ZnPc/MWCNT (1:3) was 800 °C, as there is remarkable increase in the electrocatalytic activity for the material pyrolysed at this temperature compared to the materials annealed at other temperatures. The onset potential is clearly better than of materials pyrolysed at other temperatures and the current density achieves higher values, this is in good agreement with the previous studies carried out on MPc modified CNT materials [170,252,265].

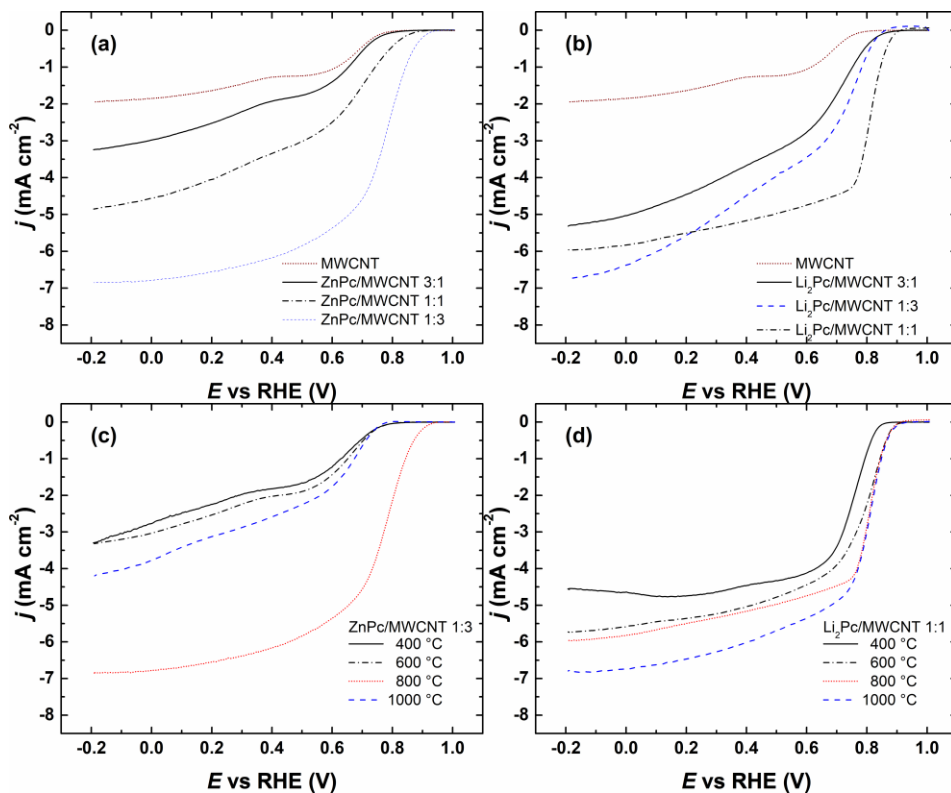


**Figure 43.** RDE voltammetry curves for ORR on GC electrodes modified with (a) ZnPc/MWCNT and (b) Li<sub>2</sub>Pc/MWCNT, synthesised at 800 °C by varying ratios; (c) ZnPc/MWCNT (1:3) synthesised at different temperatures; (d) Li<sub>2</sub>Pc/MWCNT (1:1) synthesised at different temperatures.  $v = 10 \text{ mV s}^{-1}$ ,  $\omega = 1900 \text{ rpm}$ .

Yeager *et al.* have found that heat-treated M-N<sub>x</sub> moieties act more as active species than of untreated M-N<sub>4</sub> moieties [266]. In addition, Zagal [267–270] and Mukerjee [160,271] have found that the electrocatalytic activity after pyrolysis increases due to increasing electron-withdrawing characteristics of the surrounding environment around the M-N<sub>4</sub> moiety, which is apparent in the shift in the M(III)/M(II) redox potential to more positive values (pyrolysed vs intact M-N<sub>4</sub> moieties). Fundamentally, this means that more positive redox potential values favour the electrochemical reduction of oxygen [160, 267–273]. The experiments carried out within this work show that the complexes studied herein do not show any visible redox activity on the metal, so the higher ORR activity cannot be attributed to the redox potential shifts. Other possible reason for that the redox changes are not clearly visible in the CVs. Although, both Zn and Li are known to

be able to form coordination complexes and coordinate with electron pairs. So, the metals can form Zn-/Li- and N-species on the catalyst surface through this type of interactions. The formation of different N-species is apparently conducting in achieving high electrocatalytic activity [274]. The four different types of nitrogen that has been doped into the carbon lattice are the most widely studied: pyridinic-N, graphitic-N, pyrrolic-N and pyridine-N-oxide, from which pyridinic-N and graphitic-N are usually considered as active towards the ORR in alkaline solution and pyrrolic-N and pyridine-N-oxide are considered inactive [53,275,276]. Since there are still no ways to obtain only one type of nitrogen species into a catalyst structure, it is rather difficult to determine the contribution of different N-species to the overall ORR activity.

In case of Li<sub>2</sub>Pc/MWCNT catalysts that are synthesised at different temperatures (400, 600, 800 °C), there are not many differences, since the onset potential is around the same value and the  $E_{1/2}$  values are rather similar (the only exception is the material heat-treated at 400 °C). The Li<sub>2</sub>Pc/MWCNT (1:1) material synthesised at 1000 °C shows the highest current density values and similar effects on heat-treatment has been observed before [277]. The heat-treatment at higher temperatures than of 800 °C will lead to the increase in the number of graphitic-N groups among the nitrogen surface groups as well the carbon structure will get more graphitised, and this in turn will lead to higher electrical conductivity of the carbon-based catalyst materials [278].

Figures 44a,b illustrate the polarisation curves for the most active catalysts: ZnPc/MWCNT (1:3) and Li<sub>2</sub>Pc/MWCNT (1:1). For both of the catalysts the  $E_{\text{onset}}$  stays the same even and no catalyst material wears off from the electrode or undergoes major changes during the experiment. It has been found that active MPC catalysts consist of central metal ions that have half-filled d-orbitals, e.g. Fe, Co or Mn [267,273,279]. Since the ORR activity of these catalysts cannot be attributed to that (Li is an s-block metal and Zn has its d-orbitals filled), the electrocatalytic activity can mainly be explained by the formation of different N-species during the pyrolysis and these sites act as active sites for the ORR [264].

The K-L plots derived from the data shown in Figure 44a,b are shown in Figure 44c,d. The intercepts are close to zero at negative potentials and the lines are parallel, indicating that the process is limited by mass-transfer. The inset figures show the  $n$  values, for both of the catalyst the  $n$  value is close to 4 throughout all the potential ranges studied.

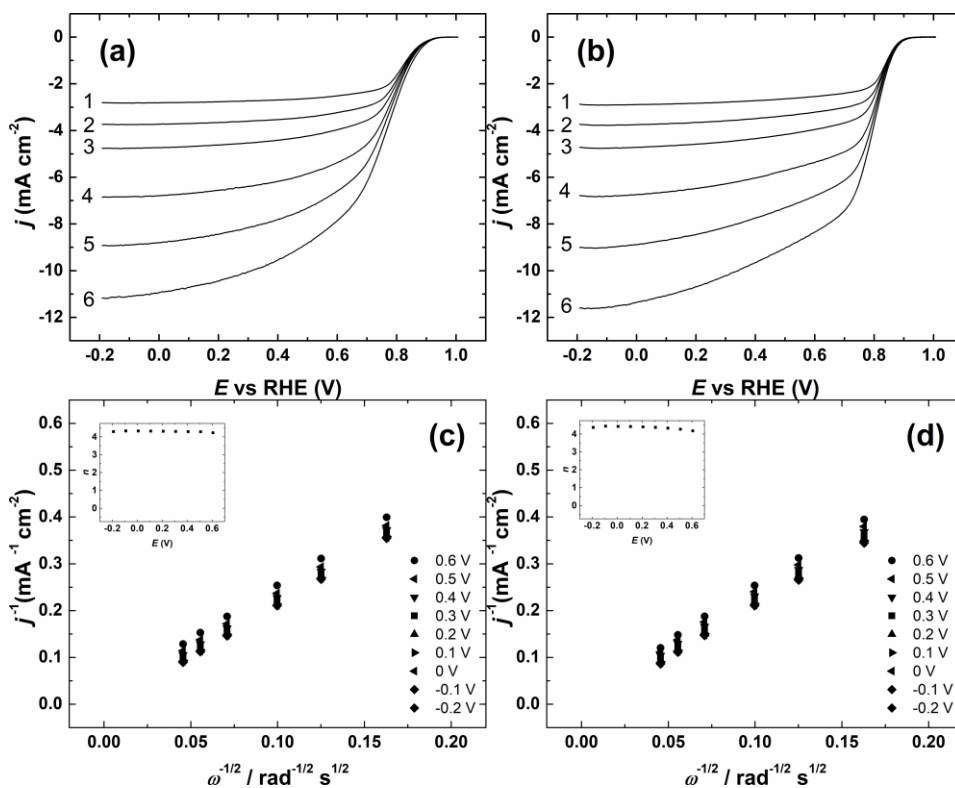


**Figure 44.** RDE polarisation curves of GC electrodes modified with (a) ZnPc/MWCNT (1:3) and (b) Li<sub>2</sub>Pc/MWCNT (3:1) in O<sub>2</sub>-saturated 0.1 M KOH.  $\nu = 10 \text{ mV s}^{-1}$ ;  $\omega = (1) 360$ ; (2) 610; (3) 960; (4) 1900; (5) 3100; (6) 4600 rpm; (c) and (d) K-L plots derived on the data showed on Figure 44a,b, respectively; inset shows the change of  $n$  values at different potentials.

Both catalyst materials are rather unique, since they exhibit the 4-electron oxygen reduction and similar ORR activity than of other MPC-based catalyst materials [169,244,249]. Osmieri *et al.* have studied ZnPc as an electrocatalyst synthesised with SBA-15 [280]. The  $E_{\text{onset}}$  value at similar rotation speeds (900 rpm for Zn-N-CNT and 960 for ZnPc/MWCNT (1:3)) is 866 mV for the Zn-N-CNT, but for the catalyst studied herein, the  $E_{\text{onset}}$  is 936 mV, which is 70 mV better. The  $E_{1/2}$  value is slightly more negative (766 mV vs 768 mV, respectively). The loading of Zn-N-CNT in the work carried out by Osmieri *et al.* [280] is higher (0.673 mg cm<sup>-2</sup>) than in this work (0.4 mg cm<sup>-2</sup>), so the material studied herein shows better electrocatalytic activity towards the ORR with even smaller loading. Morozan *et al.* [169] have studied Co- and Fe-based phthalocyanines and porphyrins supported on MWCNTs and have achieved similar results that are presented herein, but these Pcs are widely known to be active in the alkaline media.

Figure 45 presents the comparison between the ORR polarisation curves with CoPc/MWCNT(1:3, pyrolysed at 800 °C) that was previously synthesised and tested in the same conditions as LiPc and ZnPc catalysts, one can see that the catalyst exhibit comparable performance to the state of the art CoPc-based catalyst material in the alkaline media.

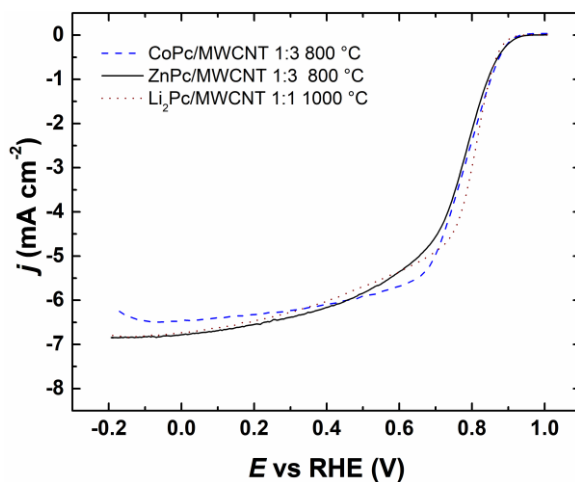


**Figure 45.** RDE polarisation curves for ORR on GC electrodes modified with different catalyst materials in 0.1 M KOH.  $\nu = 10 \text{ mV s}^{-1}$ ;  $\omega = 1900 \text{ rpm}$ .

In this work, zinc and dilithium phthalocyanine were used to prepare catalysts for the ORR. These novel materials showed extraordinary activity towards the ORR, since the electrochemical activity of these materials in alkaline media was comparable with the state-of-the-art FePc catalyst. Since previously, it has been suggested that the redox transition on the central metal ion is important in order to achieve electrochemical activity, but since these elements do not possess any redox transitions, the electrocatalytic reaction schemes for this type of catalyst are not suitable. Since the effect of central metal ion is indistinct, the importance of surface N-species that are formed during the pyrolysis is highlighted.

## 5 Conclusions

In this thesis, three different routes were explored in order to prepare oxygen reduction reaction catalysts for the alkaline media. In the first part, the mixture of graphene oxide and multi-walled carbon nanotubes were modified with two different heteroatoms – nitrogen and sulfur to evaluate the effect of co-doping towards the oxygen reduction reaction [III]. The mass ratio of dopant and carbon material was optimised, and the best results were achieved, when the C/oMUS ratio was 1:5. If the dopant ratio got too high (1:7.5), a drastic reduction in electrocatalytic activity was observed. This could be caused by the change in catalyst structure and porosity by excessive doping. The synthesis temperature yielding the catalyst with the highest activity was 800 °C and the density functional theory calculations showed that the C<sub>α</sub> and C<sub>β</sub> carbon atoms at the graphitic-N close to sulfur atom are energetically most favourable towards the ORR. X-ray photoelectron spectroscopy and transmission electron microscopy results showed the successful incorporation of both nitrogen and sulfur to the carbon matrix. The onset potential of the best performing catalyst material was 926 mV vs RHE.

In the second part of the thesis, wood was used as a precursor to produce highly active electrocatalysts towards the oxygen reduction reaction [IV,V]. Because wood lacks nitrogen functionalities, after the carbonisation and activation processes, additional doping was carried out to achieve an efficient metal-free electrocatalyst. Two different wood-based materials were prepared: the first one required secondary ball milling followed by pyrolysis to reduce the size of primary particles for proper suspension and electrode casting as well as increase the ORR activity, while the second material was prepared without any post-synthesis treatment. This catalyst material showed structure of graphene-like material, which was confirmed by transmission electron microscopy. The onset potentials were quite similar for both wood-based materials: for nitrogen-doped wood-based material the onset potential was 920 mV vs RHE and for nitrogen-doped wood-based graphene-like material the value was 921 mV vs RHE. However, the synthesis process for the latter was less complex and it had more desirable properties for further applications in fuel cells. The results showed that by employing simple pyrolysis process, it is possible to produce nitrogen-doped biomass-based carbon nanomaterials that demonstrate good activity and stability. Compared to a commercial Pt catalyst, which lost 23% of its activity, the wood-derived catalyst retained 93% of its activity after 20 hours. Thus, this work proves that it is possible to use a widely available resource – wood – to produce biomass-based carbonaceous materials that can be doped with nitrogen to gain highly active catalysts. These types of materials are considered as metal-free and show very good stability compared to the commercial platinum-based catalyst materials. Physical characterisation of biomass-based materials revealed that it is possible to produce materials with variable porosity and specific surface areas, which are both important parameters in practical applications. As proven here, various structures can be achieved by optimising the synthesis parameters.

In the third part of the thesis, MWCNTs were modified with different metal phthalocyanines [I-II]. All the MPc/MWCNT catalysts were heat-treated first in different mass ratios (1:3, 1:1 and 3:1), by varying the amount of MPc and carbon carrier MWCNTs. The ratio that showed best electrocatalytic activity towards the ORR, was then heat-treated at different temperatures: 400, 600, 1000 °C. For all of the catalysts except Li<sub>2</sub>Pc/MWCNT (1:1), the optimum heat-treatment temperature was 800 °C. For different central metal ions, the optimal ratio of MPc-to-MWCNTs differed as well. The best ratios were as

follows: MnPc/MWCNT 1:1 (onset potential 926 mV vs RHE), CuPc/MWCNT 3:1 (onset potential 896 mV vs RHE), ZnPc/MWCNT 1:3 (onset potential 936 mV) and Li<sub>2</sub>Pc/MWCNT 1:1 (onset potential 886 mV vs RHE). Most of the MPc/MWCNT catalysts showed even distribution of nanotubes and no visible metal nanoparticles were seen, but in the case of CuPcMWCNT (3:1), larger copper particles were seen on the surface of MWCNTs. This could have a negative effect regarding electrochemical activity.

## 6 Novelty and further research

- Not only transition-metal based catalysts are active towards the ORR, since the electrochemical activity of ZnPc/Li<sub>2</sub>Pc is also comparable to transition-metal based carbon catalysts
- It is possible to use widely available wood as a precursor to synthesise carbon nanomaterials that are active towards the ORR
- Since all the materials showed good electrocatalytic activity and stability on a small-scale experiments (RDE), actual fuel cell tests must also be carried out in order to see the materials' performance in larger systems
- In order to produce larger quantities that are relevant in the industrial applications, the upscaling of the synthesis process must be investigated
- The relationship between different nitrogen types and different metals in the phthalocyanine-based catalysts is further studied by employing synchrotron radiation

## References

- [1] World Population Prospects - Population Division - United Nations, (n.d.). <https://population.un.org/wpp/> (accessed May 20, 2022).
- [2] Z. Hua, Z. Zheng, E. Pahon, M.C. Péra, F. Gao, A review on lifetime prediction of proton exchange membrane fuel cells system, *J. Power Sources*. 529 (2022) 231256. <https://doi.org/10.1016/J.JPOWSOUR.2022.231256>.
- [3] L. Fan, Z. Tu, S.H. Chan, Recent development of hydrogen and fuel cell technologies: A review, *Energy Reports*. 7 (2021) 8421–8446. <https://doi.org/10.1016/J.EGYR.2021.08.003>.
- [4] Ş. Neaţu, F. Neaţu, I.M. Chirica, I. Borbáth, E. Tálas, A. Tompos, S. Somacescu, P. Osiceanu, M.A. Folgado, A.M. Chaparro, M. Florea, Recent progress in electrocatalysts and electrodes for portable fuel cells, *J. Mater. Chem. A*. 9 (2021) 17065–17128. <https://doi.org/10.1039/D1TA03644K>.
- [5] S. Li, N. Djilali, M.A. Rosen, C. Crawford, P.-C. Sui, Transition of heavy-duty trucks from diesel to hydrogen fuel cells: Opportunities, challenges, and recommendations, *Int. J. Energy Res.* (2022). <https://doi.org/10.1002/ER.8066>.
- [6] D. Banham, S. Ye, Current status and future development of catalyst materials and catalyst layers for proton exchange membrane fuel cells: An industrial perspective, *ACS Energy Lett.* 2 (2017) 629–638. <https://doi.org/10.1021/acsenergylett.6b00644>.
- [7] R. Jasinski, A new fuel cell cathode catalyst, *Nature*. 201 (1964) 1212–1213. <https://doi.org/10.1038/2011212a0>.
- [8] L. Carrette, K.A. Friedrich, U. Stimming, Fuel cells: Principles, types, fuels, and applications, *ChemPhysChem*. 1 (2000) 162–193. [https://doi.org/10.1002/1439-7641\(20001215\)1:4<162::AID-CPHC162>3.0.CO;2-Z](https://doi.org/10.1002/1439-7641(20001215)1:4<162::AID-CPHC162>3.0.CO;2-Z).
- [9] M. Shao, Q. Chang, J.-P. Dodelet, R. Chenitz, Recent advances in electrocatalysts for oxygen reduction reaction, *Chem. Rev.* 116 (2016) 3594–3657. <https://doi.org/10.1021/acs.chemrev.5b00462>.
- [10] B. Chi, X. Zhang, M. Liu, S. Jiang, S. Liao, Applications of M/N/C analogue catalysts in PEM fuel cells and metal-air/oxygen batteries: Status quo, challenges and perspectives, *Prog. Nat. Sci. Mater. Int.* 30 (2020) 807–814. <https://doi.org/10.1016/J.PNSC.2020.10.014>.
- [11] Y. Ding, W. Zhou, J. Gao, F. Sun, G. Zhao, Y. Ding, W. Zhou, J. Gao, F. Sun, G. Zhao, H<sub>2</sub>O<sub>2</sub> Electrogeneration from O<sub>2</sub> Electroreduction by N-Doped Carbon Materials: A Mini-Review on Preparation Methods, Selectivity of N Sites, and Prospects, *Adv. Mater. Interfaces*. 8 (2021) 2002091. <https://doi.org/10.1002/ADMI.202002091>.
- [12] M.R. Tarasevich, A. Sadkowsky, E. Yeager, Oxygen Electrochemistry, in: *Compr. Treatise Electrochem.*, Springer US, Boston, MA, 1983: pp. 301–398. [https://doi.org/10.1007/978-1-4613-3584-9\\_6](https://doi.org/10.1007/978-1-4613-3584-9_6).
- [13] Z.Y. Sang, F. Hou, S.H. Wang, J. Liang, Research progress on carbon-based non-metallic nanomaterials as catalysts for the two-electron oxygen reduction for hydrogen peroxide production, *New Carbon Mater.* 37 (2022) 136–151. [https://doi.org/10.1016/S1872-5805\(22\)60583-3](https://doi.org/10.1016/S1872-5805(22)60583-3).
- [14] R.B. Johnston, Arsenic and the 2030 Agenda for sustainable development, *Arsen. Res. Glob. Sustain. - Proc. 6th Int. Congr. Arsen. Environ. AS 2016.* (2016) 12–14. <https://doi.org/10.1201/B20466-7>.

- [15] X.L. Zhou, H. Zhang, L.M. Shao, F. Lü, P.J. He, Preparation and Application of Hierarchical Porous Carbon Materials from Waste and Biomass: A Review, *Waste Biomass Valorization* 2020 124. 12 (2020) 1699–1724. <https://doi.org/10.1007/S12649-020-01109-Y>.
- [16] G. Reverdiau, A. Le Duigou, T. Alleau, T. Aribart, C. Dugast, T. Priem, Will there be enough platinum for a large deployment of fuel cell electric vehicles?, *Int. J. Hydrogen Energy*. 46 (2021) 39195–39207. <https://doi.org/10.1016/J.IJHYDENE.2021.09.149>.
- [17] Z. Li, B. Li, Y. Hu, S. Wang, C. Yu, Highly-dispersed and high-metal-density electrocatalysts on carbon supports for the oxygen reduction reaction: From nanoparticles to atomic-level architectures, *Mater. Adv.* 3 (2022) 779–809. <https://doi.org/10.1039/d1ma00858g>.
- [18] Y. Liang, R. Kleijn, A. Tukker, E. van der Voet, Material requirements for low-carbon energy technologies: A quantitative review, *Renew. Sustain. Energy Rev.* 161 (2022) 112334. <https://doi.org/10.1016/J.RSER.2022.112334>.
- [19] (PDF) Platinum Supply and the Growth of Fuel Cell Vehicles | Khalid Saeed - Academia.edu, (n.d.). [https://www.academia.edu/28312654/Platinum\\_Supply\\_and\\_the\\_Growth\\_of\\_Fuel\\_Cell\\_Vehicles](https://www.academia.edu/28312654/Platinum_Supply_and_the_Growth_of_Fuel_Cell_Vehicles) (accessed April 12, 2022).
- [20] Y. Sun, M. Delucchi, J. Ogden, The impact of widespread deployment of fuel cell vehicles on platinum demand and price, *Int. J. Hydrogen Energy*. 36 (2011) 11116–11127. <https://doi.org/10.1016/J.IJHYDENE.2011.05.157>.
- [21] J. Quílez-Bermejo, E. Morallón, D. Cazorla-Amorós, Metal-free heteroatom-doped carbon-based catalysts for ORR. A critical assessment about the role of heteroatoms, *Carbon N. Y.* 165 (2020) 434–454. <https://doi.org/10.1016/j.carbon.2020.04.068>.
- [22] J. Zhang, W. Zhu, T. Huang, C. Zheng, Y. Pei, G. Shen, Z. Nie, D. Xiao, Y. Yin, M.D. Guiver, Recent Insights on Catalyst Layers for Anion Exchange Membrane Fuel Cells, *Adv. Sci.* 8 (2021) 2100284. <https://doi.org/10.1002/ADVS.202100284>.
- [23] M. Mandal, Recent Advancement on Anion Exchange Membranes for Fuel Cell and Water Electrolysis, *ChemElectroChem*. 8 (2021) 36–45. <https://doi.org/10.1002/CELC.202001329>.
- [24] D.R. Dekel, Review of cell performance in anion exchange membrane fuel cells, *J. Power Sources*. 375 (2018) 158–169. <https://doi.org/10.1016/J.JPOWSOUR.2017.07.117>.
- [25] G. Das, J.H. Choi, P.K.T. Nguyen, D.J. Kim, Y.S. Yoon, Anion Exchange Membranes for Fuel Cell Application: A Review, *Polymers (Basel)*. 14 (2022). <https://doi.org/10.3390/POLYM14061197>.
- [26] T.B. Ferriday, P.H. Middleton, Alkaline fuel cell technology - A review, *Int. J. Hydrogen Energy*. 46 (2021) 18489–18510. <https://doi.org/10.1016/J.IJHYDENE.2021.02.203>.
- [27] W.E. Mustain, M. Chatenet, M. Page, Y.S. Kim, Durability challenges of anion exchange membrane fuel cells, *Energy Environ. Sci.* 13 (2020) 2805–2838. <https://doi.org/10.1039/D0EE01133A>.
- [28] N. Gupta, S.M. Gupta, S.K. Sharma, Carbon nanotubes: synthesis, properties and engineering applications, *Carbon Lett.* 29 (2019) 419–447. <https://doi.org/10.1007/S42823-019-00068-2/FIGURES/14>.

- [29] Y.M. Manawi, Ihsanullah, A. Samara, T. Al-Ansari, M.A. Atieh, A Review of Carbon Nanomaterials' Synthesis via the Chemical Vapor Deposition (CVD) Method, *Mater.* 2018, Vol. 11, Page 822. 11 (2018) 822. <https://doi.org/10.3390/MA11050822>.
- [30] S. Rathinavel, K. Priyadarshini, D. Panda, A review on carbon nanotube: An overview of synthesis, properties, functionalization, characterization, and the application, *Mater. Sci. Eng. B.* 268 (2021) 115095. <https://doi.org/10.1016/J.MSEB.2021.115095>.
- [31] D. Higgins, P. Zamani, A. Yu, Z. Chen, The application of graphene and its composites in oxygen reduction electrocatalysis: a perspective and review of recent progress, *Energy Environ. Sci.* 9 (2016) 357–390. <https://doi.org/10.1039/C5EE02474A>.
- [32] K. Honda, Y. Waki, A. Matsumoto, B. Kondo, Y. Shimai, Amorphous carbon having higher catalytic activity toward oxygen reduction reaction: Quinone and carboxy groups introduced onto its surface, *Diam. Relat. Mater.* 107 (2020) 107900. <https://doi.org/10.1016/J.DIAMOND.2020.107900>.
- [33] G. Jürmann, D.J. Schiffrin, K. Tammeveski, The pH-dependence of oxygen reduction on quinone-modified glassy carbon electrodes, *Electrochim. Acta.* 53 (2007) 390–399. <https://doi.org/10.1016/J.ELECTACTA.2007.03.053>.
- [34] K.S. Novoselov, A.K. Geim, S. V Morozov, D. Jiang, Y. Zhang, S. V Dubonos, I. V Grigorieva, A.A. Firsov, Electric field effect in atomically thin carbon films, *Science.* 306 (2004) 666–9. <https://doi.org/10.1126/science.1102896>.
- [35] M. Li, B. Mu, Effect of different dimensional carbon materials on the properties and application of phase change materials: A review, *Appl. Energy.* 242 (2019) 695–715. <https://doi.org/10.1016/J.APENERGY.2019.03.085>.
- [36] X. Zhang, J. Gao, Y. Xiao, J. Wang, G. Sun, Y. Zhao, L. Qu, Regulation of 2D Graphene Materials for Electrocatalysis, *Chem. – An Asian J.* 15 (2020) 2271–2281. <https://doi.org/10.1002/ASIA.202000249>.
- [37] L.-H. Zhang, Y. Shi, Y. Wang, N.R. Shiju, L.-H. Zhang, Y. Shi, N.R. Shiju, Y. Wang, Nanocarbon Catalysts: Recent Understanding Regarding the Active Sites, *Adv. Sci.* 7 (2020) 1902126. <https://doi.org/10.1002/ADVS.201902126>.
- [38] X. Tong, Q. Wei, X. Zhan, G. Zhang, S. Sun, The New Graphene Family Materials: Synthesis and Applications in Oxygen Reduction Reaction, *Catal.* 2017, Vol. 7, Page 1. 7 (2016) 1. <https://doi.org/10.3390/CATAL7010001>.
- [39] L.M. Rivera, G. García, E. Pastor, Novel graphene materials for the oxygen reduction reaction, *Curr. Opin. Electrochem.* 9 (2018) 233–239. <https://doi.org/10.1016/J.COEELEC.2018.05.009>.
- [40] P. Hu, K. Liu, C.P. Deming, S. Chen, Multifunctional graphene-based nanostructures for efficient electrocatalytic reduction of oxygen, *J. Chem. Technol. Biotechnol.* 90 (2015) 2132–2151. <https://doi.org/10.1002/JCTB.4797>.
- [41] J. Liu, J. Tang, J.J. Gooding, Strategies for chemical modification of graphene and applications of chemically modified graphene, *J. Mater. Chem.* 22 (2012) 12435–12452. <https://doi.org/10.1039/C2JM31218B>.
- [42] Q. Lv, W. Si, J. He, L. Sun, C. Zhang, N. Wang, Z. Yang, X. Li, X. Wang, W. Deng, Y. Long, C. Huang, Y. Li, Selectively nitrogen-doped carbon materials as superior metal-free catalysts for oxygen reduction, *Nat. Commun.* 9 (2018) 1–11. <https://doi.org/10.1038/s41467-018-05878-y>.

- [43] H. Kim, K. Lee, S.I. Woo, Y. Jung, On the mechanism of enhanced oxygen reduction reaction in nitrogen-doped graphene nanoribbons, *Phys. Chem. Chem. Phys.* 13 (2011) 17505. <https://doi.org/10.1039/c1cp21665a>.
- [44] S. Iijima, Helical microtubules of graphitic carbon, *Nature*. 354 (1991) 56–58. <https://doi.org/10.1038/354056a0>.
- [45] R. Khare, S. Bose, Carbon Nanotube Based Composites-A Review, *J. Miner. Mater. Charact. Eng.* 4 (2005) 31–46.
- [46] M.M. Mohideen, Y. Liu, S. Ramakrishna, Recent progress of carbon dots and carbon nanotubes applied in oxygen reduction reaction of fuel cell for transportation, *Appl. Energy*. 257 (2020) 114027. <https://doi.org/10.1016/J.APENERGY.2019.114027>.
- [47] L.M. Esteves, H.A. Oliveira, F.B. Passos, Carbon nanotubes as catalyst support in chemical vapor deposition reaction: A review, *J. Ind. Eng. Chem.* 65 (2018) 1–12. <https://doi.org/10.1016/J.JIEC.2018.04.012>.
- [48] E.T. Thostenson, Z. Ren, T.-W. Chou, Advances in the science and technology of carbon nanotubes and their composites: a review, (n.d.).
- [49] R. Das, Z. Shahnavaz, M.E. Ali, M.M. Islam, S.B. Abd Hamid, Can We Optimize Arc Discharge and Laser Ablation for Well-Controlled Carbon Nanotube Synthesis?, *Nanoscale Res. Lett.* 2016 111. 11 (2016) 1–23. <https://doi.org/10.1186/S11671-016-1730-0>.
- [50] S. Temizel-Sekeryan, F. Wu, A.L. Hicks, Global scale life cycle environmental impacts of single- and multi-walled carbon nanotube synthesis processes, *Int. J. Life Cycle Assess.* 26 (2021) 656–672. <https://doi.org/10.1007/S11367-020-01862-1/FIGURES/7>.
- [51] S. Patowary, R. Chetry, C. Goswami, B. Chutia, P. Bharali, Oxygen Reduction Reaction Catalysed by Supported Nanoparticles: Advancements and Challenges, *ChemCatChem*. 14 (2022) e202101472. <https://doi.org/10.1002/CCTC.202101472>.
- [52] W. Cheng, L. Sun, X. He, L. Tian, Recent advances in fuel cell reaction electrocatalysis based on porous noble metal nanocatalysts, *Dalt. Trans.* (2022). <https://doi.org/10.1039/D2DT00841F>.
- [53] K. Gong, F. Du, Z. Xia, M. Durstock, L. Dai, Nitrogen-doped carbon nanotube arrays with high electrocatalytic activity for oxygen reduction, *Science* (80-. ). 323 (2009) 760–764. <https://doi.org/10.1126/science.1168049>.
- [54] X. Kong, Y. Zhu, H. Lei, C. Wang, Y. Zhao, E. Huo, X. Lin, Q. Zhang, M. Qian, W. Mateo, R. Zou, Z. Fang, R. Ruan, Synthesis of graphene-like carbon from biomass pyrolysis and its applications, *Chem. Eng. J.* 399 (2020) 125808. <https://doi.org/10.1016/J.CEJ.2020.125808>.
- [55] L. Sun, L. Wang, C. Tian, T. Tan, Y. Xie, K. Shi, M. Li, H. Fu, Nitrogen-doped graphene with high nitrogen level via a one-step hydrothermal reaction of graphene oxide with urea for superior capacitive energy storage, *RSC Adv.* 2 (2012) 4498. <https://doi.org/10.1039/c2ra01367c>.
- [56] D. Yu, Q. Zhang, L. Dai, Highly efficient metal-free growth of nitrogen-doped single-walled carbon nanotubes on plasma-etched substrates for oxygen reduction, *J. Am. Chem. Soc.* 132 (2010) 15127–15129. <https://doi.org/10.1021/ja105617z>.
- [57] N. Zhou, N. Wang, Z. Wu, L. Li, Probing Active Sites on Metal-Free, Nitrogen-Doped Carbons for Oxygen Electroreduction: A Review, *Catalysts*. 8 (2018) 509. <https://doi.org/10.3390/catal8110509>.

- [58] Z.-H.H. Sheng, H.-L.L. Gao, W.-J.J. Bao, F.-B. Bin Wang, X.-H.H. Xia, Synthesis of boron doped graphene for oxygen reduction reaction in fuel cells, *J. Mater. Chem.* 22 (2012) 390–395. <https://doi.org/10.1039/c1jm14694g>.
- [59] A.R. Jang, Y.W. Lee, S.S. Lee, J. Hong, S.H. Beak, S. Pak, J. Lee, H.S. Shin, D. Ahn, W.K. Hong, S. Cha, J.I. Sohn, I.K. Park, Electrochemical and electrocatalytic reaction characteristics of boron-incorporated graphene: Via a simple spin-on dopant process, *J. Mater. Chem. A.* 6 (2018) 7351–7356. <https://doi.org/10.1039/C7TA09517A>.
- [60] X. Bo, L. Guo, Ordered mesoporous boron-doped carbons as metal-free electrocatalysts for the oxygen reduction reaction in alkaline solution, *Phys. Chem. Chem. Phys.* 15 (2013) 2459–2465. <https://doi.org/10.1039/C2CP43541A>.
- [61] D.-S. Yang, D. Bhattacharjya, S. Inamdar, J. Park, J.-S. Yu, Phosphorus-Doped Ordered Mesoporous Carbons with Different Lengths as Efficient Metal-Free Electrocatalysts for Oxygen Reduction Reaction in Alkaline Media, *J. Am. Chem. Soc.* 134 (2012) 16127–16130. <https://doi.org/10.1021/ja306376s>.
- [62] J. Wu, Z. Yang, X. Li, Q. Sun, C. Jin, P. Strasser, R. Yang, Phosphorus-doped porous carbons as efficient electrocatalysts for oxygen reduction, *J. Mater. Chem. A.* 1 (2013) 9889. <https://doi.org/10.1039/c3ta11849e>.
- [63] Y.-P. Zhu, Y. Liu, Y.-P. Liu, T.-Z. Ren, T. Chen, Z.-Y. Yuan, Direct Synthesis of Phosphorus-Doped Mesoporous Carbon Materials for Efficient Electrocatalytic Oxygen Reduction, *ChemCatChem.* 7 (2015) 2903–2909. <https://doi.org/10.1002/cctc.201500148>.
- [64] Z. Yang, Z. Yao, G. Li, G. Fang, H. Nie, Z. Liu, X. Zhou, X.X. Chen, S. Huang, Sulfur-doped graphene as an efficient metal-free cathode catalyst for oxygen reduction, *ACS Nano.* 6 (2012) 205–211. <https://doi.org/10.1021/nn203393d>.
- [65] M. Klingele, C. Pham, K.R. Vuyyuru, B. Britton, S. Holdcroft, A. Fischer, S. Thiele, Sulfur doped reduced graphene oxide as metal-free catalyst for the oxygen reduction reaction in anion and proton exchange fuel cells, *Electrochem. Commun.* 77 (2017) 71–75. <https://doi.org/10.1016/j.elecom.2017.02.015>.
- [66] M. Seredych, K. László, T.J. Bandoz, Sulfur-Doped Carbon Aerogel as a Metal-Free Oxygen Reduction Catalyst, *ChemCatChem.* 7 (2015) 2924–2931. <https://doi.org/10.1002/cctc.201500192>.
- [67] I.Y. Jeon, H.J. Noh, J.B. Baek, Nitrogen-Doped Carbon Nanomaterials: Synthesis, Characteristics and Applications, *Chem. – An Asian J.* 15 (2020) 2282–2293. <https://doi.org/10.1002/ASIA.201901318>.
- [68] J. Wang, J. Kim, S. Choi, H. Wang, J. Lim, A Review of Carbon-Supported Nonprecious Metals as Energy-Related Electrocatalysts, *Small Methods.* 4 (2020) 1–22. <https://doi.org/10.1002/smt.202000621>.
- [69] S. Nagappan, M. Duraivel, S.A. Hira, K. Prabakar, C.S. Ha, S.H. Joo, K.M. Nam, K.H. Park, Heteroatom-doped nanomaterials/core–shell nanostructure based electrocatalysts for the oxygen reduction reaction, *J. Mater. Chem. A.* 10 (2022) 987–1021. <https://doi.org/10.1039/D1TA09861F>.
- [70] P. Kaur, G. Verma, S.S.S. Sekhon, Biomass derived hierarchical porous carbon materials as oxygen reduction reaction electrocatalysts in fuel cells, *Prog. Mater. Sci.* 102 (2019) 1–71. <https://doi.org/10.1016/J.PMATSCI.2018.12.002>.

- [71] L. Qian, F. Guo, X. Jia, Y. Zhan, H. Zhou, X. Jiang, C. Tao, Recent development in the synthesis of agricultural and forestry biomass-derived porous carbons for supercapacitor applications: a review, *Ionics* 2020 268. 26 (2020) 3705–3723. <https://doi.org/10.1007/S11581-020-03626-1>.
- [72] S.S. Sekhon, J.S. Park, Biomass-derived N-doped porous carbon nanosheets for energy technologies, *Chem. Eng. J.* 425 (2021) 129017. <https://doi.org/10.1016/J.CEJ.2021.129017>.
- [73] W. Shen, W. Fan, Nitrogen-containing porous carbons: synthesis and application, 1 999–1013. <https://doi.org/10.1039/C2TA00028H>.
- [74] Y. Li, D. Wang, H. Xie, C. Zhang, Electrocatalytic Activity and Stability of 3D Ordered N-doped Hierarchically Porous Carbon Supported Pt Catalyst for Methanol Oxidation and Oxygen Reduction Reactions, *ChemistrySelect*. 4 (2019) 12601–12607. <https://doi.org/10.1002/SLCT.201903610>.
- [75] H. Liu, Y. Cao, F. Wang, Y. Huang, Nitrogen-doped hierarchical lamellar porous carbon synthesized from the fish scale as support material for platinum nanoparticle electrocatalyst toward the oxygen reduction reaction, *ACS Appl. Mater. Interfaces*. 6 (2014) 819–825. [https://doi.org/10.1021/AM403432H/ASSET/IMAGES/AM403432H.SOCIAL.JPEG\\_V03](https://doi.org/10.1021/AM403432H/ASSET/IMAGES/AM403432H.SOCIAL.JPEG_V03).
- [76] H. Zhou, J. Zhang, J. Zhu, Z. Liu, C. Zhang, S. Mu, A self-template and KOH activation co-coupling strategy to synthesize ultrahigh surface area nitrogen-doped porous graphene for oxygen reduction, *RSC Adv.* 6 (2016) 73292–73300. <https://doi.org/10.1039/C6RA16703A>.
- [77] B. Wang, B. Liu, L. Dai, Non-N-Doped Carbons as Metal-Free Electrocatalysts, *Adv. Sustain. Syst.* 5 (2021) 2000134. <https://doi.org/10.1002/ADSU.202000134>.
- [78] M. Kaur, M.K. Ubhi, J.K. Grewal, V.K. Sharma, Boron- and phosphorous-doped graphene nanosheets and quantum dots as sensors and catalysts in environmental applications: a review, *Environ. Chem. Lett.* 19 (2021) 4375–4392. <https://doi.org/10.1007/S10311-021-01281-0/FIGURES/10>.
- [79] Y. Rangraz, M.M. Heravi, Recent advances in metal-free heteroatom-doped carbon heterogenous catalysts, *RSC Adv.* 11 (2021) 23725–23778. <https://doi.org/10.1039/d1ra03446d>.
- [80] Y. Gao, Q. Wang, G. Ji, A. Li, J. Niu, Doping strategy, properties and application of heteroatom-doped ordered mesoporous carbon, *RSC Adv.* 11 (2021) 5361–5383. <https://doi.org/10.1039/d0ra08993a>.
- [81] M. Seredych, T.J. Bandoz, Confined space reduced graphite oxide doped with sulfur as metal-free oxygen reduction catalyst, *Carbon N. Y.* 66 (2014) 227–233. <https://doi.org/10.1016/J.CARBON.2013.08.062>.
- [82] K. Preuss, A.M. Siwoniku, C.I. Bucur, M.M. Titirici, The Influence of Heteroatom Dopants Nitrogen, Boron, Sulfur, and Phosphorus on Carbon Electrocatalysts for the Oxygen Reduction Reaction, *Chempluschem*. 84 (2019) 457–464. <https://doi.org/10.1002/CPLU.201900083>.
- [83] S. Chen, F. Feng, Z.F. Ma, Lignin-derived nitrogen-doped porous ultrathin layered carbon as a high-rate anode material for sodium-ion batteries, *Compos. Commun.* 22 (2020) 100447. <https://doi.org/10.1016/J.COCO.2020.100447>.

- [84] C. Guo, Y. Li, Y. Xu, Q. Xiang, L. Sun, W. Zhang, W. Li, Y. Si, Z. Luo, A Highly Nanoporous Nitrogen-Doped Carbon Microfiber Derived from Bioresource as a New Kind of ORR Electrocatalyst, *Nanoscale Res. Lett.* 14 (2019) 22. <https://doi.org/10.1186/s11671-019-2854-9>.
- [85] A.B. Fuertes, M. Sevilla, Superior Capacitive Performance of Hydrochar-Based Porous Carbons in Aqueous Electrolytes, *ChemSusChem.* 8 (2015) 1049–1057. <https://doi.org/10.1002/cssc.201403267>.
- [86] F. Pan, J. Jin, X. Fu, Q. Liu, J. Zhang, Advanced oxygen reduction electrocatalyst based on nitrogen-doped graphene derived from edible sugar and urea, *ACS Appl. Mater. Interfaces.* 5 (2013) 11108–11114. <https://doi.org/10.1021/am403340f>.
- [87] C. Hu, Y. Zhou, R. Ma, Q. Liu, J. Wang, Reactive template synthesis of nitrogen-doped graphene-like carbon nanosheets derived from hydroxypropyl methylcellulose and dicyandiamide as efficient oxygen reduction electrocatalysts, *J. Power Sources.* 345 (2017) 120–130. <https://doi.org/10.1016/j.jpowsour.2017.01.124>.
- [88] Q. Li, D. Xu, X. Ou, F. Yan, Nitrogen-Doped Graphitic Porous Carbon Nanosheets Derived from In Situ Formed g-C<sub>3</sub>N<sub>4</sub> Templates for the Oxygen Reduction Reaction, *Chem. – An Asian J.* 12 (2017) 1816–1823. <https://doi.org/10.1002/ASIA.201700586>.
- [89] P. Gross, H.A. Höpfe, Biuret—A Crucial Reaction Intermediate for Understanding Urea Pyrolysis To Form Carbon Nitrides: Crystal-Structure Elucidation and In Situ Diffractometric, Vibrational and Thermal Characterisation, *Chem. – A Eur. J.* 26 (2020) 14366–14376. <https://doi.org/10.1002/CHEM.202001396>.
- [90] J. Lilloja, E. Kibena-Pöldsepp, A. Sarapuu, A. Kikas, V. Kisand, M. Käärik, M. Merisalu, A. Treshchalov, J. Leis, V. Sammelseg, Q. Wei, S. Holdcroft, K. Tammeveski, Nitrogen-doped carbide-derived carbon/carbon nanotube composites as cathode catalysts for anion exchange membrane fuel cell application, *Appl. Catal. B Environ.* 272 (2020) 119012. <https://doi.org/10.1016/j.apcatb.2020.119012>.
- [91] A.M. Bernhard, D. Peitz, M. Elsener, A. Wokaun, O. Kröcher, Hydrolysis and thermolysis of urea and its decomposition byproducts biuret, cyanuric acid and melamine over anatase TiO<sub>2</sub>, *Appl. Catal. B Environ.* 115–116 (2012) 129–137. <https://doi.org/10.1016/j.apcatb.2011.12.013>.
- [92] D. Guo, R. Shibuya, C. Akiba, S. Saji, T. Kondo, J. Nakamura, Active sites of nitrogen-doped carbon materials for oxygen reduction reaction clarified using model catalysts, *Science.* 351 (2016) 361–5. <https://doi.org/10.1126/science.aad0832>.
- [93] S. Gouse Peera, H.J. Kwon, T.G. Lee, A.M. Hussain, Heteroatom- and metalloid-doped carbon catalysts for oxygen reduction reaction: a mini-review, *Ionics* 2020 264. 26 (2020) 1563–1589. <https://doi.org/10.1007/S11581-020-03473-0>.
- [94] C.V. Rao, C.R. Cabrera, Y. Ishikawa, In search of the active site in nitrogen-doped carbon nanotube electrodes for the oxygen reduction reaction, *J. Phys. Chem. Lett.* 1 (2010) 2622–2627. <https://doi.org/10.1021/jz100971v>.
- [95] H. Miao, S. Li, Z. Wang, S. Sun, M. Kuang, Z. Liu, J. Yuan, Enhancing the pyridinic N content of Nitrogen-doped graphene and improving its catalytic activity for oxygen reduction reaction, *Int. J. Hydrogen Energy.* 42 (2017) 28298–28308. <https://doi.org/10.1016/j.ijhydene.2017.09.138>.

- [96] C. Hu, Q. Dai, L. Dai, Multifunctional carbon-based metal-free catalysts for advanced energy conversion and storage, *Cell Reports Phys. Sci.* 2 (2021) 100328. <https://doi.org/10.1016/J.XCRP.2021.100328>.
- [97] Y. Zhao, L. Yang, S. Chen, X. Wang, Y. Ma, Q. Wu, Y. Jiang, W. Qian, Z. Hu, Can boron and nitrogen co-doping improve oxygen reduction reaction activity of carbon nanotubes?, *J. Am. Chem. Soc.* 135 (2013) 1201–1204. [https://doi.org/10.1021/JA310566Z/SUPPL\\_FILE/JA310566Z\\_SI\\_001.PDF](https://doi.org/10.1021/JA310566Z/SUPPL_FILE/JA310566Z_SI_001.PDF).
- [98] S. Wang, E. Iyyamperumal, A. Roy, Y. Xue, D. Yu, L. Dai, S. Wang, E. Iyyamperumal, A. Roy, Y. Xue, D. Yu, L. Dai, Vertically Aligned BCN Nanotubes as Efficient Metal-Free Electrocatalysts for the Oxygen Reduction Reaction: A Synergetic Effect by Co-Doping with Boron and Nitrogen, *Angew. Chemie Int. Ed.* 50 (2011) 11756–11760. <http://doi.wiley.com/10.1002/anie.201105204> (accessed January 22, 2018).
- [99] Y. Su, Y. Zhang, X. Zhuang, S. Li, D. Wu, F. Zhang, X. Feng, Low-temperature synthesis of nitrogen/sulfur co-doped three-dimensional graphene frameworks as efficient metal-free electrocatalyst for oxygen reduction reaction, *Carbon N. Y.* 62 (2013) 296–301. <https://doi.org/10.1016/J.CARBON.2013.05.067>.
- [100] J. Liang, Y. Jiao, M. Jaroniec, S.Z. Qiao, Sulfur and Nitrogen Dual-Doped Mesoporous Graphene Electrocatalyst for Oxygen Reduction with Synergistically Enhanced Performance, *Angew. Chemie Int. Ed.* 51 (2012) 11496–11500. <https://doi.org/10.1002/anie.201206720>.
- [101] C. Deng, H. Zhong, X. Li, L. Yao, H. Zhang, A highly efficient electrocatalyst for oxygen reduction reaction: phosphorus and nitrogen co-doped hierarchically ordered porous carbon derived from an iron-functionalized polymer, *Nanoscale.* 8 (2016) 1580–1587. <https://doi.org/10.1039/C5NR06749A>.
- [102] C. You, L. Wang, Y. Huang, X. Jiang, X. Li, C. Wang, Y. Hua, X. Wang, S. Liao, High porosity nitrogen and phosphorous Co-doped carbon nanosheets as an efficient catalyst for oxygen reduction, *Int. J. Hydrogen Energy.* 43 (2018) 9749–9756. <https://doi.org/10.1016/J.IJHYDENE.2018.03.219>.
- [103] K. Qu, Y. Zheng, Y. Jiao, X. Zhang, S. Dai, S.-Z. Qiao, K. Qu, Y. Zheng, Y. Jiao, S. Dai, S.-Z. Qiao, X. Zhang, -Z S Qiao, Polydopamine-Inspired, Dual Heteroatom-Doped Carbon Nanotubes for Highly Efficient Overall Water Splitting, *Adv. Energy Mater.* 7 (2017) 1602068. <https://doi.org/10.1002/AENM.201602068>.
- [104] Y. Zhao, L. Yang, S. Chen, X. Wang, Y. Ma, Q. Wu, Y. Jiang, W. Qian, Z. Hu, Can Boron and Nitrogen Co-doping Improve Oxygen Reduction Reaction Activity of Carbon Nanotubes?, *J. Am. Chem. Soc.* 135 (2013) 1201–1204. <https://doi.org/10.1021/ja310566z>.
- [105] J. Ye, H. Zhao, W. Song, N. Wang, M. Kang, Z. Li, Enhanced electronic conductivity and sodium-ion adsorption in N/S co-doped ordered mesoporous carbon for high-performance sodium-ion battery anode, *J. Power Sources.* 412 (2019) 606–614. <https://doi.org/10.1016/J.JPOWSOUR.2018.12.002>.
- [106] Y. Zhang, F. Qi, Y. Liu, Fabrication of high B-doped ordered mesoporous carbon with 4-hydroxyphenylborate phenolic resin for supercapacitor electrode materials, *RSC Adv.* 10 (2020) 11210–11218. <https://doi.org/10.1039/D0RA00561D>.
- [107] J. Zhang, L. Dai, Nitrogen, Phosphorus, and Fluorine Tri-doped Graphene as a Multifunctional Catalyst for Self-Powered Electrochemical Water Splitting, *Angew. Chemie Int. Ed.* 55 (2016) 13296–13300. <https://onlinelibrary.wiley.com/doi/full/10.1002/anie.201607405> (accessed May 23, 2022).

- [108] M. Borghei, J. Lehtonen, L. Liu, O.J. Rojas, Advanced Biomass-Derived Electrocatalysts for the Oxygen Reduction Reaction, *Adv. Mater.* (2017) 1703691. <https://doi.org/10.1002/adma.201703691>.
- [109] F. Wang, D. Ouyang, Z. Zhou, S.J. Page, D. Liu, X. Zhao, Lignocellulosic biomass as sustainable feedstock and materials for power generation and energy storage, *J. Energy Chem.* 57 (2021) 247–280. <https://doi.org/10.1016/j.jechem.2020.08.060>.
- [110] A.T. Adeleye, A.A. Akande, C.K. Odoh, M. Philip, T.T. Fidelis, P.I. Amos, O.O. Banjoko, Efficient synthesis of bio-based activated carbon (AC) for catalytic systems: A green and sustainable approach, *J. Ind. Eng. Chem.* 96 (2021) 59–75. <https://doi.org/10.1016/J.IIEC.2021.01.044>.
- [111] R.I. Kosheleva, A.C. Mitropoulos, G.Z. Kyzas, Synthesis of activated carbon from food waste, *Environ. Chem. Lett.* 17 (2019) 429–438. <https://doi.org/10.1007/S10311-018-0817-5/FIGURES/4>.
- [112] W. Zhang, J. Yin, C. Wang, L. Zhao, W. Jian, K. Lu, H. Lin, X. Qiu, H.N. Alshareef, W. Zhang, L. Zhao, W. Jian, X. Qiu, J. Yin, H.N. Alshareef, H. Lin, C. Wang, K. Lu, Lignin Derived Porous Carbons: Synthesis Methods and Supercapacitor Applications, *Small Methods.* 5 (2021) 2100896. <https://doi.org/10.1002/SMTD.202100896>.
- [113] X. Wu, J. Jiang, C. Wang, J. Liu, Y. Pu, A. Ragauskas, S. Li, B. Yang, Lignin-derived electrochemical energy materials and systems, *Biofuels, Bioprod. Biorefining.* 14 (2020) 650–672. <https://doi.org/10.1002/bbb.2083>.
- [114] P. González-García, Activated carbon from lignocellulosics precursors: A review of the synthesis methods, characterization techniques and applications, *Renew. Sustain. Energy Rev.* 82 (2018) 1393–1414. <https://doi.org/10.1016/J.RSER.2017.04.117>.
- [115] Z. Zhu, Z. Xu, The rational design of biomass-derived carbon materials towards next-generation energy storage: A review, *Renew. Sustain. Energy Rev.* 134 (2020) 110308. <https://doi.org/10.1016/J.RSER.2020.110308>.
- [116] J. Deng, M. Li, Y. Wang, Biomass-derived carbon: Synthesis and applications in energy storage and conversion, *Green Chem.* 18 (2016) 4824–4854. <https://doi.org/10.1039/c6gc01172a>.
- [117] J. Wang, S. Kaskel, KOH activation of carbon-based materials for energy storage, *J. Mater. Chem.* 22 (2012) 23710–23725. <https://doi.org/10.1039/C2JM34066F>.
- [118] T. Zhang, W.P. Walawender, L.T. Fan, M. Fan, D. Daugaard, R.C. Brown, Preparation of activated carbon from forest and agricultural residues through CO<sub>2</sub> activation, *Chem. Eng. J.* 105 (2004) 53–59. <https://doi.org/10.1016/J.CEJ.2004.06.011>.
- [119] Y.T. Li, Y.T. Pi, L.M. Lu, S.H. Xu, T.Z. Ren, Hierarchical porous active carbon from fallen leaves by synergy of K<sub>2</sub>CO<sub>3</sub> and their supercapacitor performance, *J. Power Sources.* 299 (2015) 519–528. <https://doi.org/10.1016/J.JPOWSOUR.2015.09.039>.
- [120] I. Yang, M. Jung, M.S. Kim, D. Choi, J.C. Jung, Physical and chemical activation mechanisms of carbon materials based on the microdomain model, *J. Mater. Chem. A.* 9 (2021) 9815–9825. <https://doi.org/10.1039/D1TA00765C>.
- [121] M. Wu, R. Li, X. He, H. Zhang, W. Sui, M. Tan, Microwave-assisted preparation of peanut shell-based activated carbons and their use in electrochemical capacitors, *Carbon N. Y.* 86 (2015) 373. <https://doi.org/10.1016/J.CARBON.2015.02.012>.

- [122] K. Konno, Y. Oike, Y. Ohba, O. Sasaki, Y. Takiguchi, K. Onoe, T. Yamaguchi, Short-Time Preparation of NaOH-Activated Carbon from Sugar Cane Bagasse Using Microwave Plasma Heating, *Green Sustain. Chem.* 7 (2017) 259–269. <https://doi.org/10.4236/GSC.2017.74020>.
- [123] J.M.V. Nabais, P.J.M. Carrott, M.M.L.R. Carrott, J.A. Menéndez, Preparation and modification of activated carbon fibres by microwave heating, *Carbon N. Y.* 42 (2004) 1315–1320. <https://doi.org/10.1016/J.CARBON.2004.01.033>.
- [124] M. Gupta, N. Savla, C. Pandit, S. Pandit, P.K. Gupta, M. Pant, S. Khilari, Y. Kumar, D. Agarwal, R.R. Nair, D. Thomas, V.K. Thakur, Use of biomass-derived biochar in wastewater treatment and power production: A promising solution for a sustainable environment, *Sci. Total Environ.* 825 (2022) 153892. <https://doi.org/10.1016/J.SCITOTENV.2022.153892>.
- [125] Z. Hashmi, A.S. Jatoi, S. Nadeem, A. Anjum, S.M. Imam, H. Jangda, Comparative analysis of conventional to biomass-derived adsorbent for wastewater treatment: a review, *Biomass Convers. Biorefinery* 2022. 1 (2022) 1–32. <https://doi.org/10.1007/S13399-022-02443-Y>.
- [126] Y. Liu, J. Chen, B. Cui, P. Yin, C. Zhang, Design and Preparation of Biomass-Derived Carbon Materials for Supercapacitors: A Review, *C* 2018, Vol. 4, Page 53. 4 (2018) 53. <https://doi.org/10.3390/C4040053>.
- [127] Y. Huang, D. Wu, D. Cao, D. Cheng, Facile preparation of biomass-derived bifunctional electrocatalysts for oxygen reduction and evolution reactions, *Int. J. Hydrogen Energy.* 43 (2018) 8611–8622. <https://doi.org/10.1016/J.IJHYDENE.2018.03.136>.
- [128] X. Tang, D. Liu, Y.J. Wang, L. Cui, A. Ignaszak, Y. Yu, J. Zhang, Research advances in biomass-derived nanostructured carbons and their composite materials for electrochemical energy technologies, 2021.
- [129] W. Tang, Y. Zhang, Y. Zhong, T. Shen, X. Wang, X. Xia, J. Tu, Natural biomass-derived carbons for electrochemical energy storage, *Mater. Res. Bull.* 88 (2017) 234–241. <https://doi.org/10.1016/J.MATERRESBULL.2016.12.025>.
- [130] A. Pozio, M. Di Carli, A. Aurora, M. Falconieri, L. Della Seta, P.P. Prosini, Hard Carbons for Use as Electrodes in Li-S and Li-ion Batteries, *Nanomater.* 2022, Vol. 12, Page 1349. 12 (2022) 1349. <https://doi.org/10.3390/NANO12081349>.
- [131] M. Hao, R. Dun, Y. Su, L. He, F. Ning, X. Zhou, W. Li, In situ self-doped biomass-derived porous carbon as an excellent oxygen reduction electrocatalyst for fuel cells and metal–air batteries, *J. Mater. Chem. A.* 9 (2021) 14331–14343. <https://doi.org/10.1039/D1TA01417J>.
- [132] Q. Chen, X. Tan, Y. Liu, S. Liu, M. Li, Y. Gu, P. Zhang, S. Ye, Z. Yang, Y. Yang, Biomass-derived porous graphitic carbon materials for energy and environmental applications, *J. Mater. Chem. A.* 8 (2020) 5773–5811. <https://doi.org/10.1039/c9ta11618d>.
- [133] D. Wu, C. Zhu, Y. Shi, H. Jing, J. Hu, X. Song, D. Si, S. Liang, C. Hao, Biomass-Derived Multilayer-Graphene-Encapsulated Cobalt Nanoparticles as Efficient Electrocatalyst for Versatile Renewable Energy Applications, *ACS Sustain. Chem. Eng.* 7 (2019) 1137–1145. <https://doi.org/10.1021/acssuschemeng.8b04797>.
- [134] M. Nunes, I.M. Rocha, D.M. Fernandes, A.S. Mestre, C.N. Moura, A.P. Carvalho, M.F.R. Pereira, C. Freire, Sucrose-derived activated carbons: electron transfer properties and application as oxygen reduction electrocatalysts, *RSC Adv.* 5 (2015) 102919–102931. <https://doi.org/10.1039/C5RA20874B>.

- [135] B. Lu, J. Zhou, Y. Song, H. Wang, W. Xiao, D. Wang, Molten-salt treatment of waste biomass for preparation of carbon with enhanced capacitive properties and electrocatalytic activity towards oxygen reduction, *Faraday Discuss.* 190 (2016) 147–159. <https://doi.org/10.1039/C5FD00215J>.
- [136] Y. Hao, X. Zhang, Q. Yang, K. Chen, J. Guo, D. Zhou, L. Feng, Z. Slanina, Highly porous defective carbons derived from seaweed biomass as efficient electrocatalysts for oxygen reduction in both alkaline and acidic media, *Carbon N. Y.* 137 (2018) 93–103. <https://doi.org/10.1016/J.CARBON.2018.05.007>.
- [137] E. Guilminot, R. Gavillon, M. Chatenet, S. Berthon-Fabry, A. Rigacci, T. Budtova, New nanostructured carbons based on porous cellulose: Elaboration, pyrolysis and use as platinum nanoparticles substrate for oxygen reduction electrocatalysis, *J. Power Sources.* 185 (2008) 717–726. <https://doi.org/10.1016/j.jpowsour.2008.08.030>.
- [138] J. Rooke, C. de Matos Passos, M. Chatenet, R. Sescousse, T. Budtova, S. Berthon-Fabry, R. Mosdale, F. Maillard, Synthesis and Properties of Platinum Nanocatalyst Supported on Cellulose-Based Carbon Aerogel for Applications in PEMFCs, *J. Electrochem. Soc.* 158 (2011) B779. <https://doi.org/10.1149/1.3585744/XML>.
- [139] D. dan Ouyang, L. bing Hu, G. Wang, B. Dai, F. Yu, L. li Zhang, A review of biomass-derived graphene and graphene-like carbons for electrochemical energy storage and conversion, *New Carbon Mater.* 36 (2021) 350–372. [https://doi.org/10.1016/S1872-5805\(21\)60024-0](https://doi.org/10.1016/S1872-5805(21)60024-0).
- [140] J.E. Omoriyekomwan, A. Tahmasebi, J. Dou, R. Wang, J. Yu, A review on the recent advances in the production of carbon nanotubes and carbon nanofibers via microwave-assisted pyrolysis of biomass, *Fuel Process. Technol.* 214 (2021) 106686. <https://doi.org/10.1016/J.FUPROC.2020.106686>.
- [141] J.R. Zhao, J. Hu, J.F. Li, P. Chen, N-doped carbon nanotubes derived from waste biomass and its electrochemical performance, *Mater. Lett.* 261 (2020) 127146. <https://doi.org/10.1016/J.MATLET.2019.127146>.
- [142] Donald Sadoway: The missing link to renewable energy | TED Talk, (n.d.). [https://www.ted.com/talks/donald\\_sadoway\\_the\\_missing\\_link\\_to\\_renewable\\_energy/transcript?language=en#t-370191](https://www.ted.com/talks/donald_sadoway_the_missing_link_to_renewable_energy/transcript?language=en#t-370191) (accessed April 11, 2022).
- [143] B. Zhang, C. Wang, D. Liu, Y. Liu, X. Yu, L. Wang, Boosting ORR Electrocatalytic Performance of Metal-Free Mesoporous Biomass Carbon by Synergism of Huge Specific Surface Area and Ultrahigh Pyridinic Nitrogen Doping, *ACS Sustain. Chem. Eng.* 6 (2018) 13807–13812. <https://doi.org/10.1021/acssuschemeng.8b01876>.
- [144] K. Chatterjee, M. Ashokkumar, H. Gullapalli, Y. Gong, R. Vajtai, P. Thanikaivelan, P.M. Ajayan, Nitrogen-rich carbon nano-onions for oxygen reduction reaction, *Carbon N. Y.* 130 (2018) 645–651. <https://doi.org/10.1016/J.CARBON.2018.01.052>.
- [145] W. Yuan, Y. Feng, A. Xie, X. Zhang, F. Huang, S. Li, X. Zhang, Y. Shen, Nitrogen-doped nanoporous carbon derived from waste pomelo peel as a metal-free electrocatalyst for the oxygen reduction reaction, *Nanoscale.* 8 (2016) 8704–8711. <https://doi.org/10.1039/C6NR00764C>.
- [146] S. Wu, X. Xu, Y. Ren, X. Guo, H. Sun, G. Zhou, Recent research progresses in sustainable carbon-based electrocatalysts of oxygen reduction reaction, *Ionics (Kiel).* 28 (2022) 1017–1036. <https://doi.org/10.1007/S11581-021-04367-5/TABLES/3>.

- [147] M. Demir, A.A. Farghaly, M.J. Decuir, M.M. Collinson, R.B. Gupta, Supercapacitance and oxygen reduction characteristics of sulfur self-doped micro/mesoporous bio-carbon derived from lignin, *Mater. Chem. Phys.* 216 (2018) 508–516. <https://doi.org/10.1016/J.MATCHEMPHYS.2018.06.008>.
- [148] F. Qi, Z. Xia, W. Wei, H. Sun, S. Wang, G. Sun, Nitrogen/sulfur co-doping assisted chemical activation for synthesis of hierarchical porous carbon as an efficient electrode material for supercapacitors, *Electrochim. Acta.* 246 (2017) 59–67. <https://doi.org/10.1016/J.ELECTACTA.2017.05.192>.
- [149] P. Chen, L.-K.K. Wang, G. Wang, M.-R.R. Gao, J. Ge, W.-J.J. Yuan, Y.-H.H. Shen, A.-J.J. Xie, S.-H.H. Yu, Nitrogen-doped nanoporous carbon nanosheets derived from plant biomass: An efficient catalyst for oxygen reduction reaction, *Energy Environ. Sci.* 7 (2014) 4095–4103. <https://doi.org/10.1039/c4ee02531h>.
- [150] C. Guo, W. Liao, Z. Li, L. Sun, H. Ruan, Q. Wu, Q. Luo, J. Huang, C. Chen, Coprinus comatus-derived nitrogen-containing biocarbon electrocatalyst with the addition of self-generating graphene-like support for superior oxygen reduction reaction, *Sci. Bull.* 61 (2016) 948–958. <https://doi.org/10.1007/S11434-016-1088-9>.
- [151] J. Wang, H. Zhao, Y. Gao, D. Chen, C. Chen, M. Saccoccio, F. Ciucci, Ba<sub>0.5</sub>Sr<sub>0.5</sub>Co<sub>0.8</sub>Fe<sub>0.2</sub>O<sub>3-δ</sub> on N-doped mesoporous carbon derived from organic waste as a bi-functional oxygen catalyst, *Int. J. Hydrogen Energy.* 41 (2016) 10744–10754. <https://doi.org/10.1016/J.IJHYDENE.2016.04.049>.
- [152] Z. Liang, H. Zheng, R. Cao, Recent advances in Co-based electrocatalysts for the oxygen reduction reaction, *Sustain. Energy Fuels.* 4 (2020) 3848–3870. <https://doi.org/10.1039/D0SE00271B>.
- [153] Z. Shi, W. Yang, Y. Gu, T. Liao, Z. Sun, Z. Shi, W. Yang, Y. Gu, T. Liao, Z. Sun, Metal-Nitrogen-Doped Carbon Materials as Highly Efficient Catalysts: Progress and Rational Design, *Adv. Sci.* 7 (2020) 2001069. <https://doi.org/10.1002/ADVS.202001069>.
- [154] X. Hu, Y. Min, L.L. Ma, J.Y. Lu, H.C. Li, W.J. Liu, J.J. Chen, H.Q. Yu, Iron-nitrogen doped carbon with exclusive presence of Fe<sub>x</sub>N active sites as an efficient ORR electrocatalyst for Zn-air battery, *Appl. Catal. B Environ.* 268 (2020) 118405. <https://doi.org/10.1016/J.APCATB.2019.118405>.
- [155] R. Sibul, E. Kibena-Pöldsepp, S. Ratso, M. Kook, M.T. Sougrati, M. Käärik, M. Merisalu, J. Aruväli, P. Paiste, A. Treshchalov, J. Leis, V. Kisand, V. Sammelseg, S. Holdcroft, F. Jaouen, K. Tammeveski, Iron- and Nitrogen-Doped Graphene-Based Catalysts for Fuel Cell Applications, *ChemElectroChem.* 7 (2020) 1739–1747. <https://doi.org/10.1002/CELC.202000011>.
- [156] V.S. Bagotzky, M.R. Tarasevich, K.A. Radyushkina, O.A. Levina, S.I. Andrusyova, Electrocatalysis of the oxygen reduction process on metal chelates in acid electrolyte, *J. Power Sources.* 2 (1978) 233–240. [https://doi.org/10.1016/0378-7753\(78\)85014-9](https://doi.org/10.1016/0378-7753(78)85014-9).
- [157] S. Yang, Y. Yu, X. Gao, Z. Zhang, F. Wang, Recent advances in electrocatalysis with phthalocyanines, *Chem. Soc. Rev.* 50 (2021) 12985–13011. <https://doi.org/10.1039/D0CS01605E>.
- [158] D. Wang, X. Pan, P. Yang, R. Li, H. Xu, Y. Li, F. Meng, J. Zhang, M. An, Transition Metal and Nitrogen Co-Doped Carbon-based Electrocatalysts for the Oxygen Reduction Reaction: From Active Site Insights to the Rational Design of Precursors and Structures, *ChemSusChem.* 14 (2021) 33–55. <https://doi.org/10.1002/CSSC.202002137>.

- [159] M. Ladouceur, G. Lalande, D. Guay, J.P. Dodelet, L. Dignardbailey, M.L. Trudeau, R. Schulz, Pyrolyzed cobalt phthalocyanine as electrocatalyst for oxygen reduction, *J. Electrochem. Soc.* 140 (1993) 1974–1981. <https://doi.org/10.1149/1.2220748>.
- [160] Q. Jia, N. Ramaswamy, H. Hafiz, U. Tylus, K. Strickland, G. Wu, B. Barbiellini, A. Bansil, E.F. Holby, P. Zelenay, S. Mukerjee, Experimental Observation of Redox-Induced Fe-N Switching Behavior as a Determinant Role for Oxygen Reduction Activity, *ACS Nano*. 9 (2015) 12496–12505. [https://doi.org/10.1021/ACSNANO.5B05984/ASSET/IMAGES/LARGE/NN-2015-05984K\\_0006.JPEG](https://doi.org/10.1021/ACSNANO.5B05984/ASSET/IMAGES/LARGE/NN-2015-05984K_0006.JPEG).
- [161] Ballard to Offer World’s First PEM Fuel Cell Product Using Non Precious Metal Catalyst, (n.d.). <https://www.ballard.com/about-ballard/newsroom/news-releases/2017/09/13/ballard-to-offer-world-s-first-pem-fuel-cell-product-using-non-precious-metal-catalyst> (accessed May 25, 2022).
- [162] T. Tang, L. Ding, Z. Jiang, J.S. Hu, L.J. Wan, Advanced transition metal/nitrogen/carbon-based electrocatalysts for fuel cell applications, *Sci. China Chem.* 63 (2020) 1517–1542. <https://doi.org/10.1007/s11426-020-9835-8>.
- [163] D. Banham, S. Ye, K. Pei, J.I. Ozaki, T. Kishimoto, Y. Imashiro, A review of the stability and durability of non-precious metal catalysts for the oxygen reduction reaction in proton exchange membrane fuel cells, *J. Power Sources*. 285 (2015) 334–348. <https://doi.org/10.1016/J.JPOWSOUR.2015.03.047>.
- [164] R. Jasinski, Cobalt Phthalocyanine as a Fuel Cell Cathode, *J. Electrochem. Soc.* 112 (1965) 526. <https://doi.org/10.1149/1.2423590/XML>.
- [165] E. Antolini, Carbon supports for low-temperature fuel cell catalysts, *Appl. Catal. B Environ.* 88 (2009) 1–24. <https://doi.org/10.1016/j.apcatb.2008.09.030>.
- [166] Z. Zhang, S. Yang, M. Dou, H. Liu, L. Gu, F. Wang, Systematic study of transition-metal (Fe, Co, Ni, Cu) phthalocyanines as electrocatalysts for oxygen reduction and their evaluation by DFT, *RSC Adv.* 6 (2016) 67049–67056. <https://doi.org/10.1039/C6RA12426G>.
- [167] Z. Zhang, M. Dou, J. Ji, F. Wang, Phthalocyanine tethered iron phthalocyanine on graphitized carbon black as superior electrocatalyst for oxygen reduction reaction, *Nano Energy*. 34 (2017) 338–343. <https://doi.org/10.1016/j.nanoen.2017.02.042>.
- [168] M. Li, X. Bo, Y. Zhang, C. Han, L. Guo, Comparative study on the oxygen reduction reaction electrocatalytic activities of iron phthalocyanines supported on reduced graphene oxide, mesoporous carbon vesicle, and ordered mesoporous carbon, *J. Power Sources*. 264 (2014) 114–122.
- [169] A. Morozan, S. Campidelli, A. Filoramo, B. Jusselme, S. Palacin, Catalytic activity of cobalt and iron phthalocyanines or porphyrins supported on different carbon nanotubes towards oxygen reduction reaction, *Carbon N. Y.* 49 (2011) 4839–4847. <https://doi.org/10.1016/j.carbon.2011.07.004>.
- [170] I. Kruusenberg, N. Alexeyeva, K. Tammeveski, J. Kozlova, L. Matisen, V. Sammelselg, J. Solla-Gullón, J.M. Feliu, Effect of purification of carbon nanotubes on their electrocatalytic properties for oxygen reduction in acid solution, *Carbon N. Y.* 49 (2011) 4031–4039. <https://doi.org/10.1016/j.carbon.2011.05.048>.
- [171] W.S. Hummers, R.E. Offeman, Preparation of Graphitic Oxide, *J. Am. Chem. Soc.* 80 (1958) 1339–1339. <https://doi.org/10.1021/ja01539a017>.
- [172] A.J. Bard, L.R. Faulkner, *Electrochemical Methods: Fundamentals and Applications*, 2nd ed., Wiley, New York, 2001.

- [173] R.E. Davis, G.L. Horvath, C.W. Tobias, The solubility and diffusion coefficient of oxygen in potassium hydroxide solutions, *Electrochim. Acta.* 12 (1967) 287–297. <http://www.scopus.com/inward/record.url?eid=2-s2.0-0000971765&partnerID=40&md5=0057603faf73a71c9a47c0a14d1ebf4d>.
- [174] D.R. Lide, *CRC Handbook of Chemistry and Physics*, 82nd ed., CRC Press, Boca Ration, 2001. <https://doi.org/10.1021/ja906434c>.
- [175] D.J. Frisch, M.J.; Trucks, G.W.; Schlegel, H.B.; Scuseria, G.E.; Robb, M.A.; Cheeseman, J.R.; Scalmani, G.; Barone, V.; Mennucci, B.; Petersson, G.A.; Nakatsuji, H.; Caricato, M.; Li, X.; Hratchian, H.P.; Izmaylov, A.F.; Bloino, J.; Zheng, G.; Sonnenb, Gaussian 09, Revision E.01, (2009).
- [176] Chemcraft - Graphical program for visualization of quantum chemistry computations, (n.d.). <https://www.chemcraftprog.com/> (accessed December 29, 2020).
- [177] Y. Wang, M. Jiao, W. Song, Z. Wu, Doped fullerene as a metal-free electrocatalyst for oxygen reduction reaction: A first-principles study, *Carbon N. Y.* 114 (2017) 393–401. <https://doi.org/10.1016/j.carbon.2016.12.028>.
- [178] J.K. Nørskov, J. Rossmeisl, A. Logadottir, L. Lindqvist, J.R. Kitchin, T. Bligaard, H. Jónsson, Origin of the overpotential for oxygen reduction at a fuel-cell cathode, *J. Phys. Chem. B.* 108 (2004) 17886–17892. <https://pubs.acs.org/sharingguidelines> (accessed December 29, 2020).
- [179] NIST Chemistry WebBook, (n.d.). <https://webbook.nist.gov/chemistry/> (accessed December 29, 2020).
- [180] C. Jia, W. Ren, X. Chen, W. Yang, C. Zhao, (N, B) Dual Heteroatom-Doped Hierarchical Porous Carbon Framework for Efficient Electroreduction of Carbon Dioxide, *ACS Sustain. Chem. Eng.* 8 (2020) 6003–6010. <https://doi.org/10.1021/acssuschemeng.0c00739>.
- [181] E. Kukk, G. Snell, J.D. Bozek, W.T. Cheng, N. Berrah, Vibrational structure and partial rates of resonant Auger decay of the [Formula Presented] core excitations in nitric oxide, *Phys. Rev. A.* 63 (2001) 062702. <https://doi.org/10.1103/PhysRevA.63.062702>.
- [182] E. Kukk, K. Ueda, U. Hergenhausen, X.J. Liu, G. Prümper, H. Yoshida, Y. Tamenori, C. Makochehanwa, T. Tanaka, M. Kitajima, H. Tanaka, Violation of the Franck-Condon principle due to recoil effects in high energy molecular core-level photoionization, *Phys. Rev. Lett.* 95 (2005) 133001. <https://doi.org/10.1103/PHYSREVLETT.95.133001/FIGURES/4/MEDIUM>.
- [183] T. Weiss, V. Zielasek, M. Bäumer, Influence of Water on Chemical Vapor Deposition of Ni and Co thin films from ethanol solutions of acetylacetonate precursors, *Sci. Reports* 2015 51. 5 (2015) 1–13. <https://doi.org/10.1038/srep18194>.
- [184] J.D. Wiggins-Camacho, K.J. Stevenson, Effect of nitrogen concentration on capacitance, density of states, electronic conductivity, and morphology of N-doped carbon nanotube electrodes, *J. Phys. Chem. C.* 113 (2009) 19082–19090. <https://pubs.acs.org/doi/full/10.1021/jp907160v> (accessed July 6, 2020).
- [185] M. Rahsepar, M.R. Nobakht, H. Kim, M. Pakshir, Facile enhancement of the active catalytic sites of N-doped graphene as a high performance metal-free electrocatalyst for oxygen reduction reaction, *Appl. Surf. Sci.* 447 (2018) 182–190. <https://doi.org/10.1016/J.APSUSC.2018.03.227>.

- [186] J. Wu, Z. Yang, Q. Sun, X. Li, P. Strasser, R. Yang, Synthesis and electrocatalytic activity of phosphorus-doped carbon xerogel for oxygen reduction, *Electrochim. Acta.* 127 (2014) 53–60. <https://doi.org/10.1016/J.ELECTACTA.2014.02.016>.
- [187] T. Chen, J. Chen, K. Waki, An activity recoverable carbon nanotube based electrocatalysts: Rapid annealing effects and importance of defects, *Carbon N. Y.* 129 (2018) 119–127. <https://doi.org/10.1016/J.CARBON.2017.12.010>.
- [188] X. Lu, Z. Li, X. Yin, S. Wang, Y. Liu, Y. Wang, Controllable synthesis of three-dimensional nitrogen-doped graphene as a high performance electrocatalyst for oxygen reduction reaction, *Int. J. Hydrogen Energy.* 42 (2017) 17504–17513. <https://doi.org/10.1016/J.IJHYDENE.2017.02.090>.
- [189] X. Bai, Y. Shi, J. Guo, L. Gao, K. Wang, Y. Du, T. Ma, Catalytic activities enhanced by abundant structural defects and balanced N distribution of N-doped graphene in oxygen reduction reaction, *J. Power Sources.* 306 (2016) 85–91. <https://doi.org/10.1016/J.JPOWSOUR.2015.10.081>.
- [190] H.A.B.M.D. Weththasinha, Z. Yan, L. Gao, Y. Li, D. Pan, M. Zhang, X. Lv, W. Wei, J. Xie, Nitrogen doped lotus stem carbon as electrocatalyst comparable to Pt/C for oxygen reduction reaction in alkaline media, *Int. J. Hydrogen Energy.* 42 (2017) 20560–20567. <https://doi.org/10.1016/J.IJHYDENE.2017.06.011>.
- [191] X. Liu, H. Zhu, X. Yang, One-step synthesis of dopamine-derived micro/mesoporous nitrogen-doped carbon materials for highly efficient oxygen-reduction catalysts, *J. Power Sources.* 262 (2014) 414–420. <https://doi.org/10.1016/J.JPOWSOUR.2014.04.023>.
- [192] S.A. Wohlgemuth, R.J. White, M.G. Willinger, M.M. Titirici, M. Antonietti, A one-pot hydrothermal synthesis of sulfur and nitrogen doped carbon aerogels with enhanced electrocatalytic activity in the oxygen reduction reaction, *Green Chem.* 14 (2012) 1515–1523. <https://doi.org/10.1039/C2GC35309A>.
- [193] J. Dai, J. Yuan, P. Giannozzi, Gas adsorption on graphene doped with B, N, Al, and S: A theoretical study, *Appl. Phys. Lett.* 95 (2009) 232105. <https://doi.org/10.1063/1.3272008>.
- [194] I.A. Pašti, N.M. Gavrilov, A.S. Dobrota, M. Momčilović, M. Stojmenović, A. Topalov, D.M. Stanković, B. Babić, G. Ćirić-Marjanović, S. V. Mentus, The Effects of a Low-Level Boron, Phosphorus, and Nitrogen Doping on the Oxygen Reduction Activity of Ordered Mesoporous Carbons, *Electrocatalysis.* 6 (2015) 498–511. <https://doi.org/10.1007/S12678-015-0271-0/FIGURES/8>.
- [195] L. Yan, J. Yu, J. Houston, N. Flores, H. Luo, Biomass derived porous nitrogen doped carbon for electrochemical devices, *Green Energy Environ.* 2 (2017) 84–99. <https://doi.org/10.1016/J.GEE.2017.03.002>.
- [196] R.C. Bansal, M. Goyal, *Activated carbon adsorption*, 1st ed., CRC Press, 2005. <https://doi.org/10.1680/bwtse.63341.147>.
- [197] A. Ambrosi, C.K. Chua, N.M. Latiff, A.H. Loo, C.H.A. Wong, A.Y.S. Eng, A. Bonanni, M. Pumera, Graphene and its electrochemistry – an update, *Chem. Soc. Rev.* 45 (2016) 2458–2493. <https://doi.org/10.1039/C6CS00136J>.
- [198] S. Pylypenko, S. Mukherjee, T.S. Olson, P. Atanassov, Non-platinum oxygen reduction electrocatalysts based on pyrolyzed transition metal macrocycles, *Electrochim. Acta.* 53 (2008) 7875–7883. <https://doi.org/10.1016/j.electacta.2008.05.047>.

- [199] T.C. Nagaiah, S. Kundu, M. Bron, M. Muhler, W. Schuhmann, Nitrogen-doped carbon nanotubes as a cathode catalyst for the oxygen reduction reaction in alkaline medium, *Electrochem. Commun.* 12 (2010) 338–341. <https://doi.org/10.1016/j.elecom.2009.12.021>.
- [200] H.S. Oh, J.G. Oh, W.H. Lee, H.J. Kim, H. Kim, The influence of the structural properties of carbon on the oxygen reduction reaction of nitrogen modified carbon based catalysts, *Int. J. Hydrogen Energy.* 36 (2011) 8181–8186. <https://doi.org/10.1016/j.ijhydene.2011.04.139>.
- [201] J. Zhang, Q. Li, H. Wu, C. Zhang, K. Cheng, H. Zhou, M. Pan, S. Mu, Nitrogen-self-doped carbon with a porous graphene-like structure as a highly efficient catalyst for oxygen reduction, *J. Mater. Chem. A.* 3 (2015) 10851–10857. <https://doi.org/10.1039/C5TA00547G>.
- [202] M. Inagaki, M. Toyoda, Y. Soneda, T. Morishita, Nitrogen-doped carbon materials, *Carbon N. Y.* 132 (2018) 104–140. <https://doi.org/10.1016/J.CARBON.2018.02.024>.
- [203] L. Lai, J.R. Potts, D. Zhan, L. Wang, C.K. Poh, C. Tang, H. Gong, Z. Shen, J. Lin, R.S. Ruoff, Exploration of the active center structure of nitrogen-doped graphene-based catalysts for oxygen reduction reaction, *Energy Environ. Sci.* 5 (2012) 7936–7942. <https://doi.org/10.1039/c2ee21802j>.
- [204] N. Daems, X. Sheng, I.F.J. Vankelecom, P.P. Pescarmona, W.Y. Lee, C.S. Kim, H. Jónsson, H. Kuzmany, R. Pfeiffer, A. Barreiro, B. Büchner, T. Pichler, T. Seyller, K. Kobayashi, Metal-free doped carbon materials as electrocatalysts for the oxygen reduction reaction, *J. Mater. Chem. A.* 2 (2014) 4085–4110. <https://doi.org/10.1039/C3TA14043A>.
- [205] R. Celiešiūtė, R. Trusovas, G. Niaura, V. Švedas, G. Račiukaitis, Ž. Ruželė, R. Pauliukaite, Influence of the laser irradiation on the electrochemical and spectroscopic peculiarities of graphene-chitosan composite film, *Electrochim. Acta.* 132 (2014) 265–276. <https://doi.org/10.1016/J.ELECTACTA.2014.03.137>.
- [206] R. Trusovas, G. Račiukaitis, G. Niaura, J. Barkauskas, G. Valušis, R. Pauliukaite, Recent Advances in Laser Utilization in the Chemical Modification of Graphene Oxide and Its Applications, *Adv. Opt. Mater.* 4 (2016) 37–65. <https://doi.org/10.1002/adom.201500469>.
- [207] A.C. Ferrari, J. Robertson, Interpretation of Raman spectra of disordered and amorphous carbon, *Phys. Rev. B.* 61 (2000) 14095–14107. <https://doi.org/10.1103/PhysRevB.61.14095>.
- [208] A.C. Ferrari, J. Robertson, Resonant Raman spectroscopy of disordered, amorphous, and diamondlike carbon, 64 (2001) 075414. <https://doi.org/10.1103/PhysRevB.64.075414>.
- [209] C. Han, S. Wang, J. Wang, M. Li, J. Deng, H. Li, Y. Wang, Controlled synthesis of sustainable N-doped hollow core-mesoporous shell carbonaceous nanospheres from biomass, *Nano Res.* 7 (2014) 1809–1819. <https://doi.org/10.1007/s12274-014-0540-x>.
- [210] X. Wu, X. Yu, Z. Lin, J. Huang, L. Cao, B. Zhang, Y. Zhan, H. Meng, Y. Zhu, Y. Zhang, Nitrogen doped graphitic carbon ribbons from cellulose as non noble metal catalyst for oxygen reduction reaction, *Int. J. Hydrogen Energy.* 41 (2016) 14111–14122. <https://doi.org/10.1016/j.ijhydene.2016.05.275>.

- [211] C.W.B.B. Bezerra, L. Zhang, K. Lee, H. Liu, A.L.B.B. Marques, E.P. Marques, H. Wang, J. Zhang, A review of Fe–N/C and Co–N/C catalysts for the oxygen reduction reaction, *Electrochim. Acta.* 53 (2008) 4937–4951. <https://doi.org/10.1016/j.electacta.2008.02.012>.
- [212] Q. Liu, Y. Duan, Q. Zhao, F. Pan, B. Zhang, J. Zhang, Direct synthesis of nitrogen-doped carbon nanosheets with high surface area and excellent oxygen reduction performance, *Langmuir.* 30 (2014) 8238–8245. <https://doi.org/10.1021/la404995y>.
- [213] M. Wang, S. Wang, H. Yang, W. Ku, S. Yang, Z. Liu, G. Lu, Carbon-Based Electrocatalysts Derived From Biomass for Oxygen Reduction Reaction: A Minireview, *Front. Chem.* 8 (2020) 116. <https://doi.org/10.3389/fchem.2020.00116>.
- [214] L.X. Zuo, W.J. Wang, R. Bin Song, J.J. Lv, L.P. Jiang, J.J. Zhu, NaCl crystal tuning nitrogen self-doped porous graphitic carbon nanosheets for efficient oxygen reduction, *ACS Sustain. Chem. Eng.* 5 (2017) 10275–10282. <https://doi.org/10.1021/acssuschemeng.7b02291>.
- [215] J. Tang, Y. Wang, W. Zhao, R.J. Zeng, T. Liu, S. Zhou, Biomass-derived hierarchical honeycomb-like porous carbon tube catalyst for the metal-free oxygen reduction reaction, *J. Electroanal. Chem.* 847 (2019) 113230. <https://doi.org/10.1016/j.jelechem.2019.113230>.
- [216] H. Zheng, Y. Zhang, J. Long, R. Li, X. Gou, Nitrogen-Doped Porous Carbon Material Derived from Biomass of Beancurd as an Efficient Electrocatalyst for Oxygen Reduction and Zn-air Fuel Cell, *J. Electrochem. Soc.* 167 (2020) 084516. <https://iopscience.iop.org/article/10.1149/1945-7111/ab907f> (accessed June 29, 2020).
- [217] J. Zhao, Y. Liu, X. Quan, S. Chen, H. Yu, H. Zhao, Nitrogen-doped carbon with a high degree of graphitization derived from biomass as high-performance electrocatalyst for oxygen reduction reaction, *Appl. Surf. Sci.* 396 (2017) 986–993. <https://doi.org/10.1016/J.APSUSC.2016.11.073>.
- [218] Y. Zhang, Z. Gao, N. Song, J. He, X. Li, Graphene and its derivatives in lithium–sulfur batteries, *Mater. Today Energy.* 9 (2018) 319–335. <https://doi.org/10.1016/J.MTENER.2018.06.001>.
- [219] M. Yi, Z. Shen, A review on mechanical exfoliation for the scalable production of graphene, *J. Mater. Chem. A.* 3 (2015) 11700–11715. <https://doi.org/10.1039/c5ta00252d>.
- [220] B. Deng, Z. Liu, H. Peng, Toward Mass Production of CVD Graphene Films, *Adv. Mater.* 31 (2019). <https://doi.org/10.1002/adma.201800996>.
- [221] F. Ambroz, T.J. Macdonald, V. Martis, I.P. Parkin, F. Ambroz, T.J. Macdonald, I.P. Parkin, V. Martis, Evaluation of the BET Theory for the Characterization of Meso and Microporous MOFs, *Small Methods.* 2 (2018) 1800173. <https://doi.org/10.1002/SMTD.201800173>.
- [222] B. Huang, M. Xia, J. Qiu, Z. Xie, Biomass Derived Graphene-Like Carbons for Electrocatalytic Oxygen Reduction Reaction, *ChemNanoMat.* 5 (2019) 682–689. <https://doi.org/10.1002/cnma.201900009>.
- [223] Z. Wen, X. Wang, S. Mao, Z. Bo, H. Kim, S. Cui, G. Lu, X. Feng, J. Chen, Crumpled nitrogen-doped graphene nanosheets with ultrahigh pore volume for high-performance supercapacitor, *Adv. Mater.* 24 (2012) 5610–5616. <https://doi.org/10.1002/adma.201201920>.

- [224] D. Geng, Y.Y. Chen, Y.Y. Chen, Y. Li, R. Li, X. Sun, S. Ye, S. Knights, D.A. Saville, I.A. Aksay, High oxygen-reduction activity and durability of nitrogen-doped graphene, *Energy Environ. Sci.* 4 (2011) 760–764. <https://doi.org/10.1039/c0ee00326c>.
- [225] A. Ambrosi, C.K. Chua, A. Bonanni, M. Pumera, Electrochemistry of graphene and related materials, *Chem. Rev.* 114 (2014) 7150–7188. <https://doi.org/10.1021/cr500023c>.
- [226] K. Artyushkova, A. Serov, S. Rojas-Carbonell, P. Atanassov, Chemistry of Multitudinous Active Sites for Oxygen Reduction Reaction in Transition Metal-Nitrogen-Carbon Electrocatalysts, *J. Phys. Chem. C* 119 (2015) 25917–25928. <https://doi.org/10.1021/acs.jpcc.5b07653>.
- [227] K. Gao, B. Wang, L. Tao, B. V. Cuning, Z. Zhang, S. Wang, R.S. Ruoff, L. Qu, Efficient Metal-Free Electrocatalysts from N-Doped Carbon Nanomaterials: Mono-Doping and Co-Doping, *Adv. Mater.* 31 (2019) 1805121. <https://doi.org/10.1002/adma.201805121>.
- [228] Y. Tsujii, T. Akira, Y. Masahide, N. Yasunori, W. Yoshio, Xps studies of some chemically synthesized polypyrrole organic acceptor complexes, *Polym. J.* 20 (1988) 837–844. <https://doi.org/10.1295/polymj.20.845>.
- [229] R. Arrigo, M. Hävecker, S. Wrabetz, R. Blume, M. Lerch, J. McGregor, E.P.J. Parrott, J.A. Zeitler, L.F. Gladden, A. Knop-Gericke, R. Schlögl, D.S. Su, Tuning the acid/base properties of nanocarbons by functionalization via amination, *J. Am. Chem. Soc.* 132 (2010) 9616–9630. <https://doi.org/10.1021/ja910169v>.
- [230] Z. Chen, D. Higgins, Z. Chen, Nitrogen doped carbon nanotubes and their impact on the oxygen reduction reaction in fuel cells, *Carbon N. Y.* 48 (2010) 3057–3065. <https://doi.org/10.1016/J.CARBON.2010.04.038>.
- [231] E.J. Biddinger, U.S. Ozkan, Role of graphitic edge plane exposure in carbon nanostructures for oxygen reduction reaction, *J. Phys. Chem. C* 114 (2010) 15306–15314. <https://doi.org/10.1021/jp104074t>.
- [232] M. Cheng, R. Yang, L. Zhang, Z. Shi, W. Yang, D. Wang, G. Xie, D. Shi, G. Zhang, Restoration of graphene from graphene oxide by defect repair, *Carbon N. Y.* 50 (2012) 2581–2587. <https://doi.org/10.1016/J.CARBON.2012.02.016>.
- [233] F. Tuinstra, J.L. Koenig, Raman Spectrum of Graphite, *J. Chem. Phys.* 53 (1970) 1126–1130. <https://doi.org/10.1063/1.1674108>.
- [234] R. Trusovas, K. Ratautas, G. Račiukaitis, G. Niaura, Graphene layer formation in pinewood by nanosecond and picosecond laser irradiation, *Appl. Surf. Sci.* 471 (2019) 154–161. <https://doi.org/10.1016/j.apsusc.2018.12.005>.
- [235] Z.Z. Chen, D. Higgins, H. Tao, R.S. Hsu, Z.Z. Chen, Highly active nitrogen-doped carbon nanotubes for oxygen reduction reaction in fuel cell applications, *J. Phys. Chem. C* 113 (2009) 21008–21013. <https://doi.org/10.1021/jp908067v>.
- [236] M. Vikkisk, I. Kruusenberg, U. Joost, E. Shulga, I. Kink, K. Tammeveski, Electrocatalytic oxygen reduction on nitrogen-doped graphene in alkaline media, *Appl. Catal. B Environ.* 147 (2014) 369–376. <https://doi.org/10.1016/J.APCATB.2013.09.011>.
- [237] A. Sarapuu, E. Kibena-Pöldsepp, M. Borghei, K. Tammeveski, Electrocatalysis of oxygen reduction on heteroatom-doped nanocarbons and transition metal-nitrogen-carbon catalysts for alkaline membrane fuel cells, *J. Mater. Chem. A* 6 (2018) 776–804. <https://doi.org/10.1039/c7ta08690c>.

- [238] A.T. Masheter, L. Xiao, G.G. Wildgoose, A. Crossley, J.H. Jones, R.G. Compton, Voltammetric and X-ray photoelectron spectroscopic fingerprinting of carboxylic acid groups on the surface of carbon nanotubes via derivatisation with aryl nitro labels, *J. Mater. Chem.* 17 (2007) 3515–3524. <https://doi.org/10.1039/b705615j>.
- [239] G.G. Wildgoose, P. Abiman, R.G. Compton, Characterising chemical functionality on carbon surfaces, *J. Mater. Chem.* 19 (2009) 4875–4886. <https://doi.org/10.1039/b821027f>.
- [240] C. Domínguez, F.J. Pérez-Alonso, M.A. Salam, J.L. Gómez de la Fuente, S.A. Al-Thabaiti, S.N. Basahel, M.A. Peña, J.L.G. Fierro, S. Rojas, Effect of transition metal (M: Fe, Co or Mn) for the oxygen reduction reaction with non-precious metal catalysts in acid medium, *Int. J. Hydrogen Energy.* 39 (2014) 5309–5318. <https://doi.org/10.1016/j.ijhydene.2013.12.078>.
- [241] L. Ding, J. Qiao, X. Dai, J.J.J. Zhang, J.J.J. Zhang, B. Tian, Highly active electrocatalysts for oxygen reduction from carbon-supported copper-phthalocyanine synthesized by high temperature treatment, *Int. J. Hydrogen Energy.* 37 (2012) 14103–14113. <https://doi.org/10.1016/j.ijhydene.2012.07.046>.
- [242] Q. He, X. Yang, R. He, A. Bueno-López, H. Miller, X. Ren, W. Yang, B.E. Koel, Electrochemical and spectroscopic study of novel Cu and Fe-based catalysts for oxygen reduction in alkaline media, *J. Power Sources.* 213 (2012) 169–179. <https://doi.org/10.1016/j.jpowsour.2012.04.029>.
- [243] K. Vignarooban, J. Lin, A. Arvay, S. Kolli, I. Kruusenberg, K. Tammeveski, L. Munukutla, A.M. Kannan, Nano-electrocatalyst materials for low temperature fuel cells: A review, *Chinese J. Catal.* 36 (2015) 458–472. [https://doi.org/10.1016/S1872-2067\(14\)60175-3](https://doi.org/10.1016/S1872-2067(14)60175-3).
- [244] I. Kruusenberg, L. Matisen, K. Tammeveski, Oxygen electroreduction on multi-walled carbon nanotube supported metal phthalocyanines and porphyrins in alkaline media, *J. Nanosci. Nanotechnol.* 13 (2013) 621–627. <https://doi.org/10.1166/jnn.2013.6918>.
- [245] S. Ratso, I. Kruusenberg, M. Vikkisk, U. Joost, E. Shulga, I. Kink, T. Kallio, K. Tammeveski, Highly active nitrogen-doped few-layer graphene/carbon nanotube composite electrocatalyst for oxygen reduction reaction in alkaline media, *Carbon N. Y.* 73 (2014) 361–370. <https://doi.org/10.1016/j.carbon.2014.02.076>.
- [246] I. Kruusenberg, S. Ratso, M. Vikkisk, P. Kanninen, T. Kallio, A.M.A.M. Kannan, K. Tammeveski, Highly active nitrogen-doped nanocarbon electrocatalysts for alkaline direct methanol fuel cell, *J. Power Sources.* 281 (2015) 94–102. <https://doi.org/10.1016/j.jpowsour.2015.01.167>.
- [247] N. Sehlotho, T. Nyokong, Effects of ring substituents on electrocatalytic activity of manganese phthalocyanines towards the reduction of molecular oxygen, *J. Electroanal. Chem.* 595 (2006) 161–167. <https://doi.org/10.1016/j.jelechem.2006.07.011>.
- [248] J. Guo, H. He, D. Chu, R. Chen, OH<sup>-</sup> binding effects on metallophthalocyanine catalysts for O<sub>2</sub> reduction reaction in anion exchange membrane fuel cells, *Electrocatalysis.* 3 (2012) 252–264. <https://doi.org/10.1007/s12678-012-0106-1>.
- [249] I. Kruusenberg, L. Matisen, Q. Shah, A.M.M. Kannan, K. Tammeveski, Non-platinum cathode catalysts for alkaline membrane fuel cells, *Int. J. Hydrogen Energy.* 37 (2012) 4406–4412. <https://doi.org/10.1016/j.ijhydene.2011.11.143>.

- [250] Z.-H. Sheng, L. Shao, J.-J. Chen, W.-J. Bao, F.-B. Wang, X.-H. Xia, Catalyst-free synthesis of nitrogen-doped graphene via thermal annealing graphite oxide with melamine and its excellent electrocatalysis, *ACS Nano*. 5 (2011) 4350–4358. <https://doi.org/10.1021/nn103584t>.
- [251] K. Tammeveski, K. Kontturi, R.J. Nichols, R.J. Potter, D.J. Schiffrin, Surface redox catalysis for O<sub>2</sub> reduction on quinone-modified glassy carbon electrodes, *J. Electroanal. Chem.* 515 (2001) 101–112. [https://doi.org/10.1016/S0022-0728\(01\)00633-7](https://doi.org/10.1016/S0022-0728(01)00633-7).
- [252] I. Kruusenberg, J. Mondal, L. Matisen, V. Sammelselg, K. Tammeveski, Oxygen reduction on graphene-supported MN<sub>4</sub> macrocycles in alkaline media, *Electrochem. Commun.* 33 (2013) 18–22. <https://doi.org/10.1016/j.elecom.2013.04.005>.
- [253] F. Lima, G. V Fortunato, G. Maia, A remarkably simple characterization of glassy carbon-supported films of graphite, graphene oxide, and chemically converted graphene using Fe(CN)<sub>6</sub><sup>3-</sup>/Fe(CN)<sub>6</sub><sup>4-</sup> and O<sub>2</sub> as redox probes, *Rsc Adv.* 3 (2013) 9550–9560. <https://doi.org/10.1039/c3ra40412a>.
- [254] M.C.M. Alves, J.P. Dodelet, D. Guay, M. Ladouceur, G. Tourillon, Origin of the electrocatalytic properties for O<sub>2</sub> reduction of some heat-treated polyacrylonitrile and phthalocyanine cobalt compounds adsorbed on carbon black as probed by electrochemistry and X-ray absorption spectroscopy, *J. Phys. Chem.* 96 (1992) 10898–10905. <http://www.scopus.com/inward/record.url?eid=2-s2.0-30544451333&partnerID=40&md5=6fcbd10ada5034511497d893859b8be3>.
- [255] J. Zagal, M. Páez, A.A. Tanaka, J.R. dos Santos, C.A. Linkous, Electrocatalytic activity of metal phthalocyanines for oxygen reduction, *J. Electroanal. Chem.* 339 (1992) 13–30. [https://doi.org/10.1016/0022-0728\(92\)80442-7](https://doi.org/10.1016/0022-0728(92)80442-7).
- [256] S.I. Yamazaki, Y. Yamada, T. Ioroi, N. Fujiwara, Z. Siroma, K. Yasuda, Y. Miyazaki, Estimation of specific interaction between several Co porphyrins and carbon black: Its influence on the electrocatalytic O<sub>2</sub> reduction by the porphyrins, *J. Electroanal. Chem.* 576 (2005) 253–259. <https://doi.org/10.1016/j.jelechem.2004.10.022>.
- [257] J.H. Zagal, Metallophthalocyanines as catalysts in electrochemical reactions, *Coord. Chem. Rev.* 119 (1992) 89–136. [https://doi.org/10.1016/0010-8545\(92\)80031-L](https://doi.org/10.1016/0010-8545(92)80031-L).
- [258] Z. Mo, S. Liao, Y. Zheng, Z. Fu, Preparation of nitrogen-doped carbon nanotube arrays and their catalysis towards cathodic oxygen reduction in acidic and alkaline media, *Carbon N. Y.* 50 (2012) 2620–2627. <https://doi.org/10.1016/j.carbon.2012.02.021>.
- [259] S.L. Gojković, S. Gupta, R.F. Savinell, Heat-treated iron(III) tetramethoxyphenyl porphyrin supported on high-area carbon as an electrocatalyst for oxygen reduction - I. Characterization of the electrocatalyst, *J. Electrochem. Soc.* 145 (1998) 3493–3499. <http://www.scopus.com/inward/record.url?eid=2-s2.0-0032187134&partnerID=40&md5=abce5ffbc1c7d4f0c0bb11bb019b845>.
- [260] X. Qing, J. Shi, C. Ma, M. Fan, Z. Bai, Z. Chen, J. Qiao, J. Zhang, Simultaneous formation of nitrogen and sulfur-doped transition metal catalysts for oxygen reduction reaction through pyrolyzing carbon-supported copper phthalocyanine tetrasulfonic acid tetrasodium salt, *J. Power Sources.* 266 (2014) 88–98. <https://doi.org/10.1016/j.jpowsour.2014.04.136>.

- [261] I. Matanovic, K. Artyushkova, M.B. Strand, M.J. Dzara, S. Pylypenko, P. Atanassov, Core Level Shifts of Hydrogenated Pyridinic and Pyrrolic Nitrogen in the Nitrogen-Containing Graphene-Based Electrocatalysts: In-Plane vs Edge Defects, *J. Phys. Chem. C*. 120 (2016) 29225–29232. <https://doi.org/10.1021/acs.jpcc.6b09778>.
- [262] S. Kabir, K. Artyushkova, A. Serov, B. Kiefer, P. Atanassov, Binding energy shifts for nitrogen-containing graphene-based electrocatalysts – experiments and DFT calculations, *Surf. Interface Anal.* 48 (2016) 293–300. <https://doi.org/10.1002/SIA.5935>.
- [263] M. Xu, C. Li, H. Ren, L. Ding, K. Xu, J. Geng, Carbon-supported Co-phthalocyanine modified with pyridine, 2-acid pyridine and 2-methyl pyridine as novel cathode catalysts for alkaline PEM fuel cells, *J. Mol. Catal. A Chem.* 390 (2014) 69–75. <https://doi.org/10.1016/J.MOLCATA.2014.03.007>.
- [264] R. Zhang, Y. Peng, Z. Li, K. Li, J. Ma, Y. Liao, L. Zheng, X. Zuo, D. Xia, Oxygen electroreduction on heat-treated multi-walled carbon nanotubes supported iron polyphthalocyanine in acid media, *Electrochim. Acta.* 147 (2014) 343–351. <https://doi.org/10.1016/j.electacta.2014.09.064>.
- [265] K. Elouarzaki, R. Haddad, M. Holzinger, A. Le Goff, J. Thery, S. Cosnier, MWCNT-supported phthalocyanine cobalt as air-breathing cathodic catalyst in glucose/O<sub>2</sub> fuel cells, *J. Power Sources.* 255 (2014) 24–28. <https://doi.org/10.1016/J.JPOWSOUR.2013.12.109>.
- [266] D. Scherson, A.A. Tanaka, S.L. Gupta, D. Tryk, C. Fierro, R. Holze, E.B. Yeager, R.P. Lattimer, Transition metal macrocycles supported on high area carbon: Pyrolysis—mass spectrometry studies, *Electrochim. Acta.* 31 (1986) 1247–1258. [https://doi.org/10.1016/0013-4686\(86\)80144-X](https://doi.org/10.1016/0013-4686(86)80144-X).
- [267] J.H. Zagal, M.T.M. Koper, Reactivity Descriptors for the Activity of Molecular MN<sub>4</sub> Catalysts for the Oxygen Reduction Reaction, *Angew. Chemie Int. Ed.* 55 (2016) 14510–14521. <https://doi.org/10.1002/anie.201604311>.
- [268] J.H. Zagal, G.I. Cárdenas-Jirón, Reactivity of immobilized cobalt phthalocyanines for the electroreduction of molecular oxygen in terms of molecular hardness, *J. Electroanal. Chem.* 489 (2000) 96–100. [https://doi.org/10.1016/S0022-0728\(00\)00209-6](https://doi.org/10.1016/S0022-0728(00)00209-6).
- [269] J.H. Zagal, I. Ponce, D. Baez, R. Venegas, J. Pavez, M. Paez, M. Gulppi, A Possible Interpretation for the High Catalytic Activity of Heat-Treated Non-Precious Metal N<sub>x</sub>/C Catalysts for O<sub>2</sub> Reduction in Terms of Their Formal Potentials, *Electrochem. Solid-State Lett.* 15 (2012) B90. <https://doi.org/10.1149/2.032206esl>.
- [270] G.I. Cárdenas-Jirón, J.H. Zagal, Donor–acceptor intermolecular hardness on charge transfer reactions of substituted cobalt phthalocyanines, *J. Electroanal. Chem.* 497 (2001) 55–60. [https://doi.org/10.1016/S0022-0728\(00\)00434-4](https://doi.org/10.1016/S0022-0728(00)00434-4).
- [271] U. Tylus, Q. Jia, K. Strickland, N. Ramaswamy, A. Serov, P. Atanassov, S. Mukerjee, Elucidating oxygen reduction active sites in pyrolyzed metal-nitrogen coordinated non-precious-metal electrocatalyst systems, *J. Phys. Chem. C*. 118 (2014) 8999–9008. <https://doi.org/10.1021/jp500781v>.
- [272] J.H. Zagal, F. Javier Recio, C.A. Gutierrez, C. Zuñiga, M.A. Páez, C.A. Caro, Towards a unified way of comparing the electrocatalytic activity MN<sub>4</sub> macrocyclic metal catalysts for O<sub>2</sub> reduction on the basis of the reversible potential of the reaction, *Electrochem. Commun.* 41 (2014) 24–26. <https://doi.org/10.1016/j.elecom.2014.01.009>.

- [273] J. Masa, K. Ozoemena, W. Schuhmann, J.H. Zagal, Oxygen reduction reaction using  $N_4$ -metallomacrocyclic catalysts: fundamentals on rational catalyst design, *J. Porphyr. Phthalocyanines*. 16 (2012) 761–784. <https://doi.org/10.1142/S1088424612300091>.
- [274] E.A. González, M. Gulppi, M.A. Páez, J.H. Zagal, O<sub>2</sub> reduction on electrodes modified with nitrogen doped carbon nanotubes synthesized with different metal catalysts, *Diam. Relat. Mater.* 64 (2016) 119–129. <https://doi.org/10.1016/j.diamond.2016.02.003>.
- [275] C. Domínguez, F.J. Pérez-Alonso, M. Abdel Salam, S.A. Al-Thabaiti, A.Y. Obaid, A.A. Alshehri, J.L. Gómez de la Fuente, J.L.G. Fierro, S. Rojas, On the relationship between N content, textural properties and catalytic performance for the oxygen reduction reaction of N/CNT, *Appl. Catal. B Environ.* 162 (2015) 420–429. <https://doi.org/10.1016/j.apcatb.2014.07.002>.
- [276] Y. Cheng, H. Zhang, C. V Varanasi, J. Liu, Highly efficient oxygen reduction electrocatalysts based on winged carbon nanotubes, *Sci. Rep.* 3 (2013) 3195. <https://doi.org/10.1038/srep03195>.
- [277] Y. Jiang, Y. Xie, X. Jin, Q. Hu, L. Chen, L. Xu, J. Huang, Highly efficient iron phthalocyanine based porous carbon electrocatalysts for the oxygen reduction reaction, *RSC Adv.* 6 (2016) 78737–78742. <https://doi.org/10.1039/C6RA13106A>.
- [278] C. Li, Z. Han, Y. Yu, Y. Zhang, B. Dong, A. Kong, Y. Shan, Efficient oxygen electroreduction over ordered mesoporous Co–N-doped carbon derived from cobalt porphyrin, *RSC Adv.* 6 (2016) 15167–15174. <https://doi.org/10.1039/C5RA25862F>.
- [279] J.H. Zagal, F. Bedioui, *Electrochemistry of N<sub>4</sub> macrocyclic metal complexes: Volume 1: Energy*, second edition, Springer International Publishing, 2016. <https://doi.org/10.1007/978-3-319-31172-2>.
- [280] L. Osmieri, A.H.A. Monteverde Videla, M. Armandi, S. Specchia, Influence of different transition metals on the properties of Me–N–C (Me = Fe, Co, Cu, Zn) catalysts synthesized using SBA-15 as tubular nano-silica reactor for oxygen reduction reaction, *Int. J. Hydrogen Energy*. 41 (2016) 22570–22588. <https://doi.org/10.1016/j.ijhydene.2016.05.223>.

## Acknowledgements

First, I would like to thank my supervisors Dr. Jakob Kübarsepp and Dr. Ivar Kruusenberg, who has been next to me since the beginning of my scientific journey. I would like to thank my former supervisor Prof. Kaido Tammeveski from the University of Tartu, who first welcomed me in the laboratory back in 2014 and inspired me to continue the research on oxygen electroreduction on different electrocatalysts.

I would like to thank all the co-authors of the scientific publications this thesis is based on: Karl-Kalev Türk, Mairo Merisalu, Urmas Joost, Leonard Matisen, Väino Sammelselg, José H. Zagal, Eric Yu, Tanel Käämbre, Aleksandrs Volperts, Galina Dobele, Aivars Zhurinsh, Gediminas Niaura, Loreta Tamasauskaite-Tamasiunaite, Eugenijus Norkus, Karl Markus Villemson, Ragle Raudsepp, Krišjānis Šmits, Pangpang Wang, Anton V. Kuzmin, Andris Šutka, Bagrat A. Shainyan, Alexander Dyck, Mati Danilson, Mindaugas Andrulevičius.

All the people, who have spent a lot of time and nerves in order to help me with different problems and questions that have risen throughout the research that I have carried out. Especially I would like to thank Dr. Heiki Erikson, Dr. Sander Ratso and Dr. Kerli Liivand. You are the people who have helped me get over many obstacles that have been on the road and I can not even find the words to thank you all enough. But of course, all the people in our working group, whether from University of Tartu or National Institute of Chemical Physics and Biophysics, you have all been a great support and inspiration.

The research carried out within this PhD thesis was supported by many different funding sources: institutional research funding (IUT20-16 and IUT02-24, IUT2-25), the project TK117T of the Estonian Ministry of Education and Research, by the Estonian Research Council (Grant No. 9323, IN-DIGO, PSG312), by the EU through the European Regional Development Fund (TK141; TK134), by Fondecyt grant 1140199, by ERA.Net RUS Plus (HeDoCat), M-ERA.NET (WoBaCat), LZP-2018/1-019, project NETonia. This work was supported by the Smart specialisation scholarship for Kätlin Kaare and the Graduate School of Functional Materials and Technologies.

I would like to thank my family. Your support means a world to me.

I thank all my friends from the bottom of my heart, all these people who have been next to me throughout all this time and been cheering me up once the times get very tough.

And last but not least, two small helpers, who have seen all these endless hours that went by while putting together this thesis, sometimes being a bit of a distraction, but always the biggest cure for stress as well. I would like to give my thanks to Saatan and Käsilane. And yes, they are my cats.

## Abstract

### The electrochemical reduction of oxygen on noble metal free and biomass-based carbon nanomaterials

The oxygen reduction reaction is the main reaction taking place on the cathodes of fuel cells. Because of the sluggish kinetics of this reaction, up to date, platinum and platinum-based catalysts are mainly used as cathode catalysts in fuel cells. In this thesis, different carbon-based nanomaterials were studied as potential catalysts for the oxygen reduction reaction: metal free nitrogen- and sulfur-co-doped carbon composite, nitrogen-doped biomass based catalysts, and metal-nitrogen doped carbon nanotubes.

It is of utmost importance to find alternative catalyst materials that do not include precious metals and could promote the sustainable development goals set by the European Union. The two main paths that are research directions in the field are the following: transition metal-based catalysts on different carbon supports or heteroatom doped carbon nanomaterials that could serve as metal free catalysts. Non-metal electrocatalysts have some advantages (e.g. better stability, price) compared to the metal-based catalysts, but both paths are worth of research. This is shown by the number of growing research articles in this field.

All these materials studied within this thesis showed great potential to be employed in fuel cells, with the small-scale rotating disk electrode measurements showing that the oxygen reduction proceeded via 4-electron process or mixed 2+2 electron process (meaning that nearly all oxygen was converted to  $\text{OH}^-$ ). Although, the electrocatalytic activity of the studied materials was not better than of platinum catalyst, but for example, the Zn- and  $\text{Li}_2\text{Pc}$  based catalyst materials showed electrocatalytic activity comparable to the commonly employed transition metal-based catalyst (FePc). The activity of nitrogen-doped biomass-based catalyst materials was better than of the commercial nitrogen-doped graphene and not very far from platinum catalyst as well. Compared to the commercial Pt-based catalyst, the wood-based catalysts showed better stability and tolerance to methanol poisoning as well.

A variety of physical characterisation methods were employed to evaluate the structure and surface morphologies of the catalysts, as well as composition. In case of metal-free heteroatom-doped catalysts, the doping was successful in case of all different catalyst materials. The deconvolution X-ray photoelectron spectra showed that all the catalyst materials consisted of pyridinic-N and graphitic-N, which are both considered as being active towards the ORR.

As a result of this research, graphene-like carbon was synthesised from wood. Usually, graphene is prepared by employing different top-bottom or bottom-up methods and this research shows that it is possible to synthesise graphene-like carbon out of widely available biomass – wood. The TRL level in this work is 4 – technology is validated in lab.

Although all these catalysts showed high electrochemical activity towards the oxygen reduction reaction, the electrocatalytic properties could still be further tuned by trying out different activators, metal-macrocycles and the optimisation of synthesis parameters. The research carried out within this thesis paves a way for future research carried out on biomass-based and metal- and/or heteroatom-doped nanocarbon catalysts.

## Lühikokkuvõte

### Hapniku elektrokeemiline redutseerumine väärismetalli-vabadel ja biomassil põhinevatel süsiniku nanomaterjalidel

Vesinikkütuseelementide katoodil toimuv hapniku redutseerumisreaktsioon on tugeva hapniku-hapnik sideme tõttu väga aeglane protsess, mistõttu praegusel ajal kasutatakse katoodkatalüsaatoritena plaatina ja plaatinal põhinevaid katalüsaatormaterjale. Käesolevas doktoritöös uuriti erinevaid süsiniku nanomaterjale, mis oleksid potentsiaalsed hapniku redutseerumisreaktsiooni katalüsaatorid: lämmastiku ja väävliga kaasdopeeritud süsinikkomposiit, lämmastikuga dopeeritud biomassil põhinevad katalüsaatormaterjalid ning metallide ja lämmastikuga dopeeritud süsinikkanotorud.

Toetamaks Euroopa liidu jätkusuutlikkuse arengu eesmärke on oluline leida alternatiive väärismetallidele kütuseelementides. Peamiselt on siin kaks kandidaati: siirdemetallidel põhinevad katalüsaatormaterjalid erinevatel süsinikkandjatel või metallivabad heteroatomitega dopeeritud süsiniku nanomaterjalid. Mittemetallkatalüsaatoritel on võrreldes metallkatalüsaatoritega eeliseid (nt parem stabiilsus, hind), aga mõlemad harud on väärt uurimist, seda näitab ka vastavates valdkondades kasvavate teadusartiklite arv.

Doktoritöös uuritud materjalid omavad potentsiaali rakendamaks kütuseelementides: pöörleva ketaselektroodi meetodil tõestati, et hapniku redutseeriti pea täielikult hüdroksiidioonideks, mis on kütuseelemendi seisukohalt kõige olulisem. Elektrokatalüütiline aktiivsus ei olnud küll võrreldav kommertsiaalse plaatinakatalüsaatoriga, kuid näiteks tsink- ja dilitiumftalotsüaniinil põhinevate katalüsaatormaterjalide aktiivsus oli võrdväärne laialdaselt kasutatava raudftalotsüaniiniga. Lämmastikuga dopeeritud biomassil põhineva materjali aktiivsus oli oluliselt kõrgem kui kommertsiaalsel lämmastikuga dopeeritud grafeenil. Elektrokatalüütiline aktiivsus ei jäänud oluliselt alla ka plaatinakatalüsaatorile ning puidul põhineva katalüsaatormaterjali stabiilsus ja metanoolitaluvus oli oluliselt parem.

Materjalide struktuuri ja pinnamorfoloogia uurimiseks rakendati erinevaid füüsikalise karakteriseerimise meetodeid. Kõikide katalüsaatormaterjalide puhul oli dopeerimine heteroatomite ja/või metalliga edukas. Röntgenfotoelektron-spektritel lämmastiku piikide lahutamisel komponentideks leiti, et kõikides katalüsaatormaterjalides oli nii püridiinset kui ka grafiitset lämmastikku ning neid mõlemaid peetakse aktiivseteks hapniku redutseerumisreaktsioonil.

Käesoleva teadustöö tulemusena sünteesiti puidust grafeenilaadne süsinikmaterjal. Grafeeni toodetakse tavaliselt rakendades erinevaid alt-üles või ülevalt-alla meetodeid. Läbi viidud eksperimendid näitasid, et grafeenilaadset süsinikkanomaterjali saab toota ka laialdaselt levinud biomassist ehk puidust. Töö TVT on 4 – tehnoloogia on valideeritud laboris.

Kõikide töös sünteesitud katalüsaatormaterjalide elektrokatalüütiline aktiivsus hapniku redutseerumisreaktsiooni suhtes oli hea, kuid katalüsaatormaterjalide omadusi oleks võimalik veel modifitseerida varieerides aktivaatoreid, metall-makrotsükleid ja sünteesiparameetreid. Doktoritöös läbiviidud uurimistöö on oluline alustala tulevikus selles vallas tehtavatele edasistele eksperimentidele.



## Appendix 1

### Publication I

**K. Kaare**, I. Kruusenberg, M. Merisalu, L. Matisen, V. Sammelselg, K. Tammeveski, Electrocatalysis of oxygen reduction on multi-walled carbon nanotube supported copper and manganese phthalocyanines in alkaline media, *J. Solid State Electrochem.* 20 (2016) 921–929.



# Electrocatalysis of oxygen reduction on multi-walled carbon nanotube supported copper and manganese phthalocyanines in alkaline media

Kätlin Kaare<sup>1</sup> · Ivar Kruusenberg<sup>1</sup> · Mairo Merisalu<sup>2</sup> · Leonard Matisen<sup>2</sup> · Väino Sammelselg<sup>1,2</sup> · Kaido Tammeveski<sup>1</sup>

Received: 20 May 2015 / Revised: 20 July 2015 / Accepted: 22 July 2015 / Published online: 8 August 2015  
© Springer-Verlag Berlin Heidelberg 2015

**Abstract** Manganese phthalocyanine (MnPc) and copper phthalocyanine (CuPc)-modified electrodes were prepared using multi-walled carbon nanotubes (MWCNTs) as a support material. The catalyst materials were heat treated at four different temperatures to investigate the effect of pyrolysis on the oxygen reduction reaction (ORR) activity of these electrocatalysts. The MWCNT to metal phthalocyanine ratio was varied. Scanning electron microscopy (SEM) was employed to visualise the surface morphology of the electrodes and the x-ray photoelectron spectroscopic (XPS) study was carried out to analyse the surface composition of the most active catalyst materials. The ORR was studied in 0.1 M KOH solution employing the rotating disk electrode (RDE) method. Glassy carbon (GC) electrodes were modified with carbon nanotube-supported metal phthalocyanine catalysts using Tokuyama AS-4 ionomer. The RDE results revealed that the highest electrocatalytic activity for ORR was achieved upon heat treatment at 800 °C. CuPc-derived catalyst demonstrated lower catalytic activity as compared to the MnPc-derived counterpart, which is in good agreement with previous literature, whereas the activity of MnPc-based catalyst was higher than that reported earlier.

**Keywords** Oxygen reduction · Fuel cell · Electrocatalysis · Phthalocyanines · Carbon nanotubes

## Introduction

The electrochemical reduction of oxygen is one of the main reactions, which dominates the overall efficiency in both metal-air batteries and fuel cells [1, 2]. Although enormous work has been made to investigate the kinetics of the oxygen reduction reaction (ORR), it still remains one of the key issues in the fuel cell development and commercialisation. Sluggish ORR kinetics is caused mainly by the problems with O–O bond activation and dissociation. Poor kinetics of the ORR requires high loading of platinum for cathode catalyst, which leads to higher cost of the fuel cells. According to the research of the US Department of Energy, 56 % of the overall cost of the fuel cell stack comes from the platinum [3, 4]. Therefore, there is an enormous interest in developing non-noble metal catalysts for ORR. Among the other non-Pt catalyst materials, metal macrocyclic compounds such as phthalocyanines and porphyrins have attracted great attention as possible substitute to the noble metals. Metal-macrocyclic catalysts have been extensively studied since their discovery by Jasinski [5]. The ability of metal macrocyclic compounds to catalyse the ORR both in alkaline and acidic media has led to significant research activity of these materials [6–12]. Phthalocyanines and porphyrins containing transition metals as a central atom are considered as one of the most promising non-precious metal catalysts for ORR even though the promotion of the ORR depends on the type of metal and may display diverse electrocatalytic activity for different central metal atoms [13]. Metalloporphyrins and metallophthalocyanines have demonstrated extraordinary catalytic activity especially when they are adsorbed on the surface of nanocarbon supports such as

This paper is dedicated to Professor José H. Zagal on the occasion of his 65th birthday and in recognition of his contribution to electrochemistry.

✉ Kaido Tammeveski  
kaido@chem.ut.ee

<sup>1</sup> Institute of Chemistry, University of Tartu, Ravila 14a, 50411 Tartu, Estonia

<sup>2</sup> Institute of Physics, University of Tartu, Ravila 14c, 50411 Tartu, Estonia

carbon nanotubes (CNTs) [14–20]. To prepare state-of-the-art and stable carbon-supported metal-macrocyclic catalyst, a pyrolysis step under inert gas atmosphere is usually necessary [21]. It has been reported that transition metal macrocyclic-based catalysts have rather poor stability without the heat treatment [22]. Temperatures used for the pyrolysis usually vary from 550 to 950 °C and the right choice of temperature depends on the particular metal phthalocyanine or porphyrin [23, 24]. Despite the high research activity in the field of ORR electrocatalysis on metal-macrocyclic catalysts, there is still debate about the optimum temperature for the pyrolysis process and the formed catalytically active sites, which will promote the 4-electron reduction of oxygen [25, 26]. It has been shown that the structure of the metal macrocyclic compounds undergoes change during the pyrolysis step, contraction of interatomic distances will take place and metal-N<sub>x</sub> moieties will be integrated into the graphitic planes of the carbon support [27, 28]. It is generally accepted in the scientific community that metal-N<sub>x</sub> moieties are the active centres for ORR [29, 30]. There are also reports about the formation of metal catalyst particles on the surface of carbon materials with exceptional performance for the ORR [31, 32]. Reportedly, the ORR on transition metal macrocycle-modified carbon electrodes also depends on the solution pH. Seltho and Nyokong investigated the pH dependence of the ORR on Mn phthalocyanine complexes by varying the pH value of solution from 1 to 12 [33]. It was found that the ORR follows a 2-electron pathway in acidic media while the electron transfer number per O<sub>2</sub> molecule is four in alkaline media. Their results clearly pointed out the fact that the metallomacrocyclics, especially Mn phthalocyanine-based catalysts, may preferably be used in alkaline media rather than in acidic solutions. The biggest advantages of using these catalysts in alkaline media are improved material stability and faster ORR kinetics. Therefore, transition metal macrocyclics can be considered as suitable alternatives to Pt-based cathode catalysts in alkaline membrane fuel cells [34, 35].

The most frequently studied metallomacrocyclics are Fe and Co phthalocyanines because it has been reported that these metal phthalocyanines have the ability to promote the 4e<sup>-</sup> reduction of oxygen to water without the formation of peroxide intermediates [7, 19, 36]. There are numerous reports on the electrocatalytic properties of carbon materials modified with Co and Fe phthalocyanines and porphyrins and there is a continuously growing research activity in this area [37–39]. Whereas the ORR on Cu phthalocyanine (CuPc) and especially on Mn phthalocyanine (MnPc) modified carbon materials is rather poorly investigated compared to aforementioned other transition metal macrocyclic catalysts [21, 34, 40–47]. MnPc-based catalysts may reportedly have similar electrochemical behaviour to that of Fe phthalocyanine [41]. Most commonly used catalyst

preparation procedures of carbon-supported Cu and Mn phthalocyanines include also high-temperature treatment of the catalyst. At temperatures higher than 600 °C the structure of CuPc may decompose and form new surface species, expectedly Cu–N<sub>x</sub>–C moieties [45]. At the same time, pyrolysis at 900 °C will form metallic Cu clusters and as a result the electrochemical activity for ORR decreases and thereby preferable heat treatment temperature for carbon-supported CuPc catalysts is found to be around 800 °C [45]. Similar temperature dependence has been investigated for Mn phthalocyanine and pyrolysis at 800 °C has been found to be most appropriate also for MnPc [42]. However, the information about the carbon-supported Cu and Mn phthalocyanine catalyst preparation procedures and the ORR activity in alkaline media is rather controversial.

The purpose of this work is to compare the electrocatalytic activity of multi-walled carbon nanotubes modified with manganese and copper phthalocyanines for ORR in alkaline media. Our goal is to find optimum metallophthalocyanine to multi-walled carbon nanotube (MWCNT) mass ratio and pyrolysing conditions to achieve a higher ORR activity and stability of the electrocatalysts studied.

## Experimental

### Materials

Manganese(II) phthalocyanine (MnPc) and copper(II) phthalocyanine (CuPc) were purchased from Sigma-Aldrich. The multi-walled carbon nanotubes (MWCNTs, purity >95 %, diameter 30±10 nm, length 5–20 μm) used were purchased from NanoLab, Inc. (Brighton, MA, USA). Then, 5 wt% AS-4OH<sup>-</sup> ionomer solution (Tokuyama Corp.) was used in the preparation of catalyst ink in water. All the solutions were prepared with Milli-Q water (Millipore, Inc.).

### Preparation of MnPc/MWCNT and CuPc/MWCNT catalysts

In order to adsorb the metal macrocyclic compounds on the surface of MWCNTs, different ratios of MnPc or CuPc and MWCNTs (1:3, 1:1, 3:1) in 10-ml isopropanol were prepared and sonicated for 30 min followed by magnetic stirring for 1 h. The homogeneous mass was placed in a ceramic boat, dried at 100 °C, and pyrolysed at 400, 600, 800 or 1000 °C for 2 h in flowing argon atmosphere. The ratio of MnPc and CuPc to MWCNTs was varied from 25 to 75 %. The final loading of MnPc and CuPc on the MWCNTs was not ascertained.

## Scanning electron microscopy and x-ray photoelectron spectroscopy analysis

High-resolution scanning electron microscope (HR-SEM, Helios 600, FEI) was used to examine the surface morphology of the modified electrodes. The surface composition of the pyrolysed MnPc/MWCNT and CuPc/MWCNT catalysts was analysed using X-ray photoelectron spectroscopy (XPS). For the XPS studies, the catalyst materials dispersed in isopropanol ( $1 \text{ mg ml}^{-1}$ ) were deposited on a glassy carbon plate ( $1.1 \times 1.1 \text{ cm}$ ) and the solvent was allowed to evaporate in air. The XPS measurements were carried out with a SCIENTA SES-100 spectrometer using an unmonochromated Mg K $\alpha$  X-ray source (incident energy = 1253.6 eV), a take-off angle of  $90^\circ$  and a source power of 300 W. The pressure in the analysis chamber was below  $10^{-9}$  Torr. While collecting the survey scan, the following parameters were used: energy range = 1000 to 0 eV, pass energy = 200 eV, step size = 0.5 eV and for the high-resolution scan: energy range = 410 to 390 eV for the N1s region; 660 to 635 and 975 to 920 eV for the Mn2p and Cu2p regions, respectively, with pass energy = 200 eV and step size = 0.1 eV.

## Electrode preparation and electrochemical characterisation

For the rotating disk electrode (RDE) experiments a glassy carbon (GC) disk of geometric area ( $A$ ) of  $0.2 \text{ cm}^2$  was used as substrate material. GC disks (GC-20SS, Tokai Carbon) were pressed into a Teflon holder and then the electrodes were polished to a mirror finish with 1- and  $0.3\text{-}\mu\text{m}$  alumina slurries (Buehler). After alumina polishing, the electrodes were sonicated in water for 5 min. To obtain a uniform layer of electrocatalyst onto GC surface, the electrodes were modified with different catalysts using aqueous suspensions ( $1 \text{ mg ml}^{-1}$ ) containing 0.5 % AS-4OH $^-$  ionomer. All the suspensions were sonicated for 1 h. Then, a  $20\text{-}\mu\text{l}$  aliquot of the prepared catalyst suspension was pipetted onto the GC surface and was allowed to dry in air for 24 h.

The electrochemical measurements were made using the RDE technique employing an EDI101 rotator and a CTV101 speed control unit (Radiometer). Experiments were controlled with the General Purpose Electrochemical System (GPES) software and the potential was applied with an Autolab potentiostat/galvanostat PGSTAT30 (Eco Chemie B.V., The Netherlands). A Pt foil served as the counter electrode and a saturated calomel electrode (SCE) was used as a reference. All the potentials are referred to this electrode. Electrochemical experiments were carried out in 0.1 M KOH solution at room temperature ( $23 \pm 1^\circ\text{C}$ ). The solutions were saturated with Ar (99.999 %, AGA) or O $_2$  (99.999 %, AGA). A continuous flow of gases was maintained over the solution during the electrochemical measurements.

## Results and discussion

### SEM and XPS analysis of MnPc and CuPc modified MWCNT samples

HR-SEM images for MnPc/MWCNT and CuPc/MWCNT catalysts are presented in Fig. 1a, b, respectively. It can be seen that MnPc is much evenly dispersed on the surface of the MWCNTs and no bigger agglomeration of manganese metal particles neither carbon nanotubes is evident from the images. It is possible to find only barely visible small nanoparticles on the walls of the CNTs. At the same time CuPc/MWCNT sample surface is covered with larger Cu metal particles. Such an effect points to the complex nature of the catalyst on support surface.

Surface composition of the electrocatalysts was studied by X-ray photoelectron spectroscopy (XPS). Fig. 2a, b presents the XPS survey spectra of heat treated MnPc/MWCNT and CuPc/MWCNT samples, respectively. Both investigated catalysts were annealed at  $800^\circ\text{C}$ . Four XPS peaks were observed for both samples, which correspond to emission from C1s, satellite peak of the C1s spectrum, O1s and N1s. The O1s peak is related to the support material and is caused by various carbon-oxygen functionalities on the surface of carbon nanotubes. Identification of several functional groups from the O1s

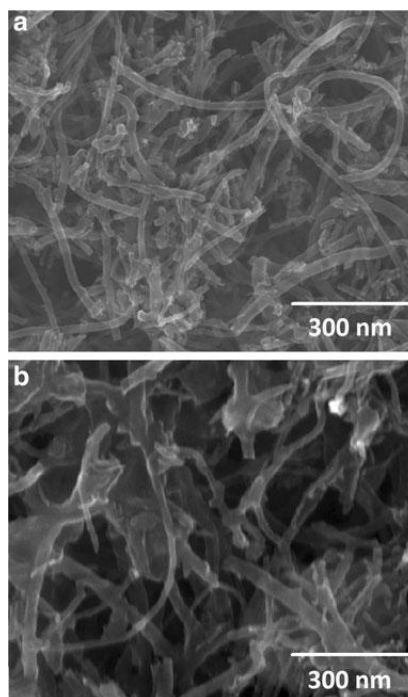


**Fig. 1** HR-SEM images of (a) MnPc/MWCNTs and (b) CuPc/MWCNTs on the GC electrode

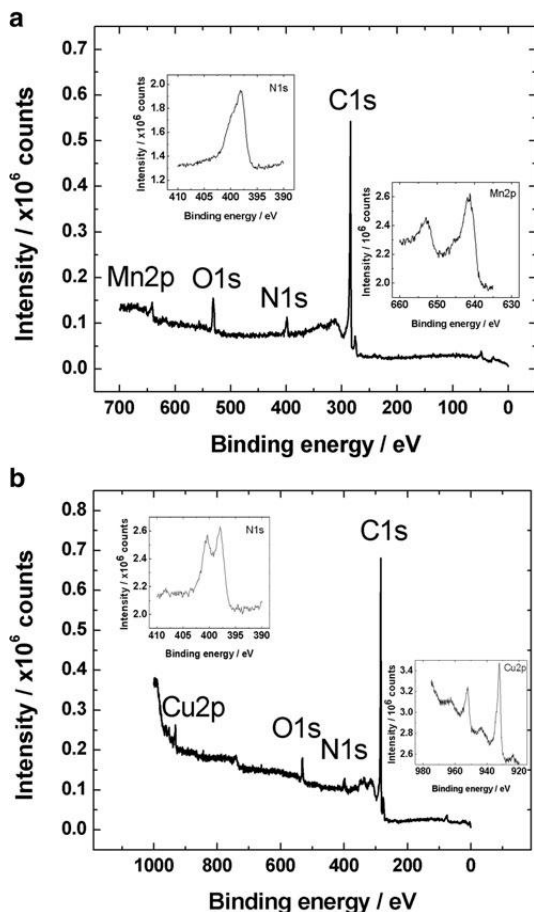


**Fig. 2** XPS survey spectra of (a) MnPc/MWCNT and (b) CuPc/MWCNT samples with inset spectra of N1s, Mn2p and Cu2p

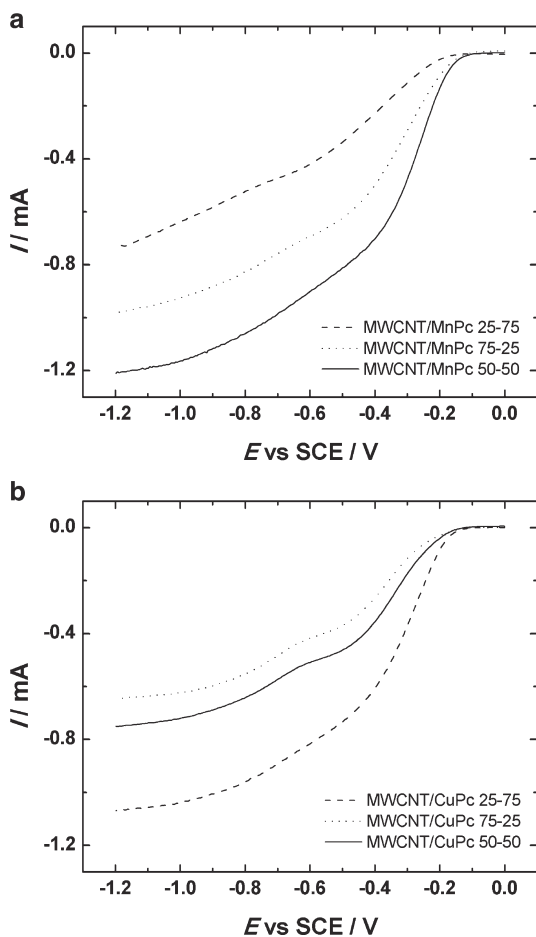
peak is complicated because of close binding energies, but different studies have demonstrated that quinone and carboxyl groups are present on the surface of MWCNTs [48, 49]. The N1s XPS core-level spectrum of MnPc/MWCNT is presented as inset in Fig. 2a. Three deconvoluted peaks are identified. Out of the others peak of pyridinic-N clearly emerges at 398.6 eV. Second hump at higher binding energy levels belongs to pyrrolic-N at around 400 eV and graphitic-N at around 401 eV. These results are in agreement with those obtained by Dominguez et al. [42]. The XPS core-level spectrum in the N1s region of CuPc/MWCNT samples in Fig. 2b shows clearly two peaks. The peak at 398.7 eV could be assigned to pyridinic-N but the N1s peak at higher binding energy at 401.3 eV corresponds to quaternary-N. It is clear that there is a contribution of pyrrolic-N and pyridine-N-oxide to these peaks as well but similarly to the O1s peak, it would be difficult to define the exact nature of these surface species

and the topic is still under the debate. Similar XPS results have been achieved also by Ding et al. [50]. In the inset of Fig. 2a, a wide XPS peak of Mn2p in the range of 640.9–641.6 eV is observable, which belongs to the different forms of manganese oxides and for Mn<sub>2p<sub>3/2</sub></sub>, which appears at around 640 eV. The small peak of Mn<sub>2p<sub>3/2</sub></sub> and wide peak of Mn<sub>2p<sub>1/2</sub></sub> are recognisable at 645 eV and at approximately 654 eV, respectively. From the Cu2p inset of Fig. 2b, one can observe XPS peak at 932.6 eV which belongs to Cu<sub>2p<sub>3/2</sub></sub> and arises most probably from decomposition of CuPc ring and reduction to Cu(I) during the pyrolysis [21]. Small hump at 934.6 eV can be attributed to the Cu(II)hydroxide formation by exposure to air. Wide peak in the range of 946–940 eV belongs to the Cu(II) satellite and peak at 952.2 eV to the Cu<sub>2p<sub>1/2</sub></sub>.

### Rotating disk electrode studies of O<sub>2</sub> reduction

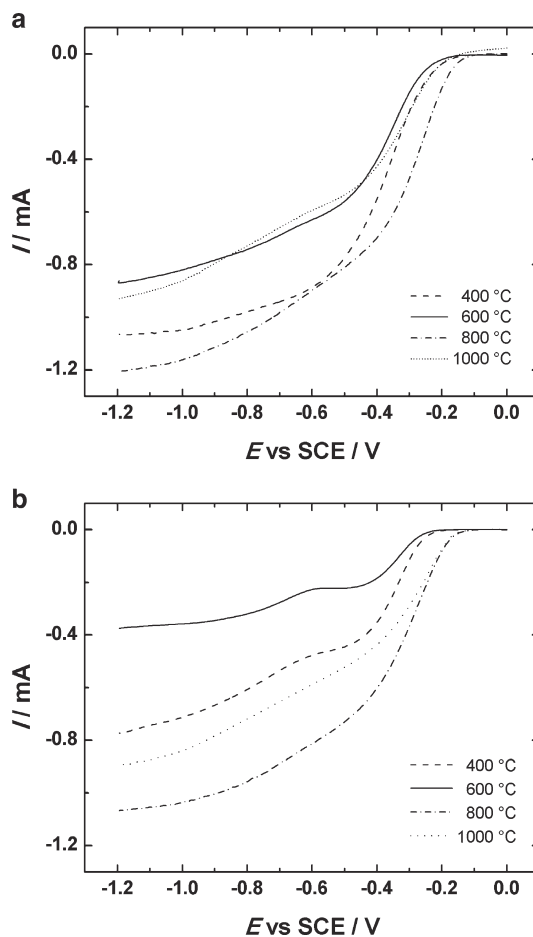
First, the metallophthalocyanine to MWCNT ratio was optimised for the pyrolysis process and the RDE experiments with metallophthalocyanine/MWCNT modified GC electrodes were carried out to investigate the effect of ratio differences on oxygen electroreduction. Figure 3a, b presents the RDE polarisation curves for oxygen reduction on GC electrodes modified with MnPc/MWCNT and CuPc/MWCNT catalysts, which were pyrolysed in different ratios and at 800 °C. These RDE experiments were performed in O<sub>2</sub>-saturated 0.1 M KOH solution at 1900 rpm. The RDE results obtained showed that in case of MnPc/MWCNT catalyst, the optimal ratio of MnPc to MWCNTs was 50:50 wt%, and for the CuPc/MWCNT material the best ratio was found to be 25 wt% of MWCNTs to 75 wt% of CuPc.

Figure 4 shows the comparative ORR polarisation curves of (a) MnPc/MWCNT and (b) CuPc/MWCNT catalysts heat treated at different temperatures. As shown in the Figure, the favourable pyrolysis temperature for both catalyst materials is 800 °C. The activity of the catalyst increases with the increase of heat treatment temperature to 800 °C noticeably. The half-wave potential of O<sub>2</sub> reduction shifts positive for more than 100 mV for both catalysts and for the CuPc/MWCNT material a similar shift is observed in case of the onset potential as well. The electrocatalytic activity of metallomacrocycles pyrolysed at this temperature is often attributed to the metal-nitrogen moieties and pyridinic nitrogen groups forming at 800 °C [35, 51]. The ORR activity of nitrogen surface groups is proved also by nitrogen doping of carbon nanomaterials [52, 53]. However, the further increase in temperature to 1000 °C will result in the decrease in the ORR activity. It has been proposed that the electrocatalytically active sites start to decompose into metallic Mn and Cu particles or metal carbides, which are less active catalysts in alkaline media as well the amount of electrocatalytically active pyridinic groups is decreasing at higher temperatures [50]. A set of the ORR



**Fig. 3** RDE voltammetry curves for oxygen reduction on (a) MnPc/MWCNT and (b) CuPc/MWCNT modified GC electrodes in  $O_2$ -saturated 0.1 M KOH.  $\nu=10 \text{ mV s}^{-1}$ ,  $\omega=1900 \text{ rpm}$ . The MWCNT to metallophthalocyanine ratio was varied (3:1, 1:1 and 1:3)

polarisation curves for both MnPc/MWCNT (50:50 weight ratio and heat treated at  $800^\circ\text{C}$ ) and CuPc/MWCNT (75:25 weight ratio and heat treated at  $800^\circ\text{C}$ ) catalysts are presented in Fig. 5a, b, respectively. The RDE data is presented for both catalyst materials having the highest ORR activity. As expected, the limiting currents in the hydrodynamic mode increase with the increasing rotation rate and the onset potential of the ORR on the same catalyst at different rotation rates is almost constant. Such a phenomenon shows that no catalyst material has left from the electrode and no essential changes take place with catalyst material during the electrochemical experiments. The onset potential of the ORR for MnPc/MWCNT catalyst material is  $-0.08 \text{ V}$  and for CuPc/MWCNT, it is ca.  $-0.11 \text{ V}$ , which are similar and even slightly better compared to the values achieved by the other working groups with MnPc and



**Fig. 4** Comparative RDE results of ORR measured at  $1900 \text{ rpm}$  on (a) MnPc/MWCNT and (b) CuPc/MWCNT catalysts heat treated at different temperatures.  $\nu=10 \text{ mV s}^{-1}$ ,  $\omega=1900 \text{ rpm}$

CuPc catalysts on Vulcan carbon XC-72R support [33, 34, 45]. The electrocatalytic activity of pyrolysed MnPc/MWCNT material is even somewhat better than that previously reported for CoPc/MWCNT and FePc/MWCNT [54]. For the CuPc/MWCNT catalyst (Fig. 5b), a small second reduction wave is observable, especially at higher rotation rates and it commences at higher negative potentials (ca.  $-0.65 \text{ V}$ ), which is common to the carbon materials in alkaline media and in agreement with previous reports [55]. The  $O_2$  reduction current in the potential range corresponding to the pre-wave is attributed to the oxygen-containing groups on the surface of undoped carbon materials, namely quinone-type functionalities [56]. Similar RDE results of  $O_2$  reduction have been obtained with GO-modified GC and for the non-pyrolysed metallophthalocyanine/GO electrodes recently [57, 58]. The high reduction current for both catalysts, especially for the

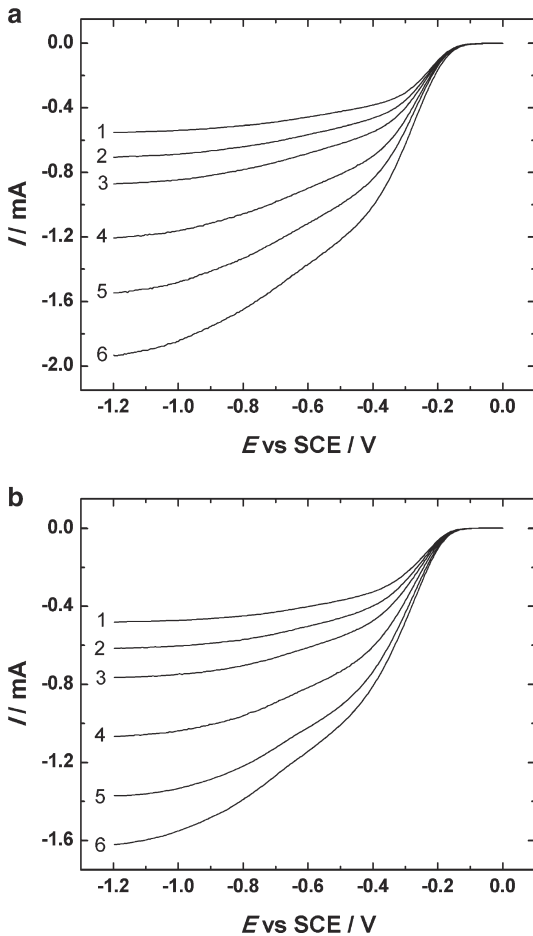


**Fig. 5** RDE voltammetry curves for oxygen reduction on (a) MnPc/MWCNT and (b) CuPc/MWCNT modified GC electrodes in  $O_2$  saturated 0.1 M KOH.  $\nu=10 \text{ mV s}^{-1}$ .  $\omega=(1) 360$ , (2) 610, (3) 960, (4) 1900, (5) 3100 and (6) 4600 rpm

MnPc/MWNT, was observed probably because of the generation of electrocatalytically active species, which usually form at temperatures from 700 to 950 °C. Ladouceur et al. have reported twice as high electrocatalytic activity of heat treated CoPc/XC-72, which was annealed at 800 °C, compared to the non-pyrolysed CoPc/XC-72 [59, 60].

The number of electrons transferred per  $O_2$  molecule ( $n$ ) was calculated from the Koutecky-Levich (K-L) equation [61]:

$$\frac{1}{I} = \frac{1}{I_k} + \frac{1}{I_d} = \frac{1}{nFAkc_{O_2}^b} + \frac{1}{0.62nFAD_{O_2}^{2/3}\nu^{-1/6}c_{O_2}^b\omega^{1/2}} \quad (1)$$

where  $I$  is the measured current,  $I_k$  and  $I_d$  are the kinetic and diffusion-limited currents, respectively,  $F$  is the Faraday

constant ( $96485 \text{ C mol}^{-1}$ ),  $A$  is the geometric surface area,  $\omega$  is the electrode rotation rate ( $\text{rad s}^{-1}$ ),  $k$  is the electrochemical rate constant for  $O_2$  reduction,  $D_{O_2}$  is the diffusion coefficient of oxygen ( $1.9 \times 10^{-5} \text{ cm}^2 \text{ s}^{-1}$ ) [62],  $c_{O_2}^b$  is the concentration of oxygen in the bulk ( $1.2 \times 10^{-6} \text{ mol cm}^{-3}$ ) [62] and  $\nu$  is the kinematic viscosity of the solution ( $0.01 \text{ cm}^2 \text{ s}^{-1}$ ) [63].

Figure 6a, b shows the K-L plots obtained from the RDE data on oxygen reduction on MnPc/MWCNT and CuPc/MWCNT, respectively, and at several rotation rates in 0.1 M KOH solution (data derived from the results presented in Fig. 5a, b). The intercepts of the extrapolated K-L lines were close to zero, which shows that the process of  $O_2$  reduction is almost entirely under diffusion control at high negative potentials, whereas at more positive potential, the process is under the mixed kinetics-diffusion control. The inset of Fig. 6a, b shows the  $n$  values calculated from the K-L equation at various potentials. For the MnPc/MWCNT catalyst at low overpotentials ( $E > -0.6 \text{ V}$ ) the  $n$

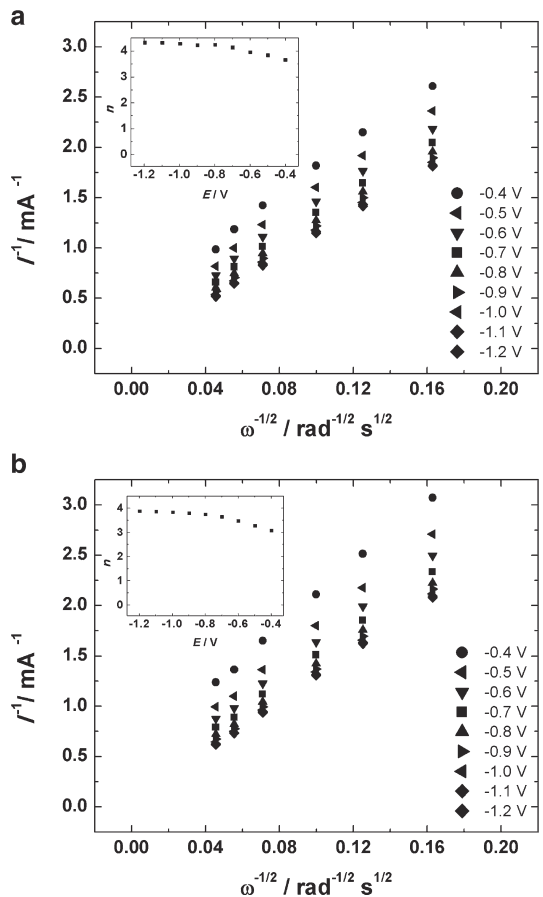


**Fig. 6** Koutecky-Levich plots for oxygen reduction on (a) MnPc/MWCNT and (b) CuPc/MWCNT electrodes in 0.1 M KOH at various potentials. The inset shows the potential dependence of  $n$

value is close to 3.5 and at more negative potential  $n$  reaches 4. This means that the ORR takes place as mixed  $2e^-$  and  $4e^-$  process at low overpotentials and both  $\text{HO}_2^-$  and  $\text{OH}^-$  are produced on the catalyst surface. It is obvious from these results that at more negative potential,  $n$  reaches 4 and it can be estimated that mostly  $\text{OH}^-$  ions are produced during the ORR process at the potentials more negative than  $-0.6$  V. This is in agreement with the previous studies in which the electroreduction of oxygen on MnPc/C catalysts was found to proceed primarily via a 4-electron pathway in alkaline media [33, 64]. Inset of Fig. 6b corresponds to CuPc/MWCNT and one can see a similar tendency as it was observed for the MnPc/MWCNT catalyst only that  $n$  reaches 4 at more negative potentials ( $E < -0.8$  V).

Figure 7 presents the comparative RDE results of  $\text{O}_2$  reduction obtained for GC electrodes modified with the most active catalyst materials studied (MnPc/MWCNT 50:50 weight ratio and heat treated at  $800^\circ\text{C}$  and CuPc/MWCNT 75:25 weight ratio and heat treated at  $800^\circ\text{C}$ ). The RDE voltammetry curve for  $\text{O}_2$  reduction on pure MWCNT-modified GC electrodes has been added for comparison purposes. As shown in Fig. 7, the onset potential of  $\text{O}_2$  reduction on unmodified MWCNTs is substantially more negative than that of MnPc- or CuPc-modified MWCNTs. Especially for MnPc/MWCNT material, the onset potential of which shifted positive for more than 0.1 V and the reduction current values at 1900 rpm were almost 0.8 mA higher as compared to unmodified MWCNTs. CuPc/MWCNT modified GC electrodes differ only slightly from MnPc/MWCNT modified electrodes, having marginally negatively shifted onset potential and current values only 0.15 mA lower at 1900 rpm. All this indicates that the ORR activity is entirely determined by the catalytically active sites formed by pyrolysis of the attached metallophthalocyanines on the surface of MWCNTs. However, there are visible differences in catalytic activity between

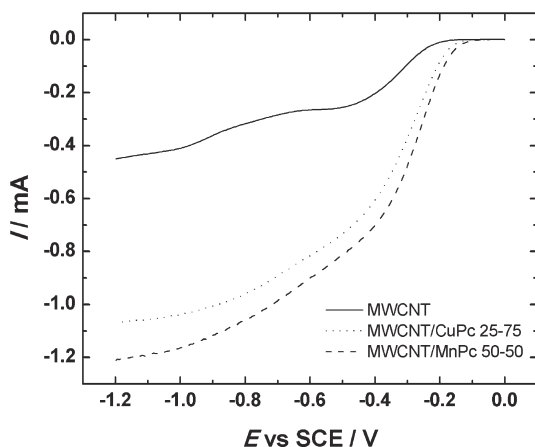


**Fig. 7** RDE voltammetry curves for oxygen reduction on different catalyst material modified GC electrodes in  $\text{O}_2$ -saturated 0.1 M KOH.  $v = 10 \text{ mV s}^{-1}$ ,  $\omega = 1900 \text{ rpm}$

MnPc/MWCNT and CuPc/MWCNT catalysts, which could be explained by the difference in the central metal atom of metallophthalocyanine and existence of better  $\pi$ - $\pi$  interactions between metallophthalocyanine and MWCNTs [65]. The interaction of MnPc/MWCNT with oxygen is more favourable compared to that of CuPc/MWCNT because the energy differences of the central metal d-orbitals. It was reported by Zagal that a high electrocatalytic activity of metallophthalocyanines is expected in conditions where the relative energies of the central metal d-orbitals in metallophthalocyanine is with similar energy to the catalysed species. Thus highest electrocatalytic activity for ORR is expected for the metallophthalocyanines containing a central metal ion that can reversibly bind both  $\text{HO}^-$  and oxygen [38].

Tafel analysis is used to give a deeper insight into the kinetics of oxygen electroreduction. The adsorption of oxygen species on MnPc/MWCNT and CuPc/MWCNT catalysts can be regarded as one of the most important steps in the overall ORR process. It has been reported that on Pt-based catalysts, the adsorption of oxygen can follow either Temkin or Langmuir isotherm. The Temkin and Langmuir isotherms represent the conditions on Pt surface, where the oxygen species are reflected by the linear appearance of the low and high current density regions of the Tafel plot, respectively. The Tafel slope associated to the Temkin conditions is  $-60 \text{ mV dec}^{-1}$  and Langmuir conditions is  $-120 \text{ mV dec}^{-1}$  [66]. However, somewhat different Tafel slope values have been reported for the Pt/CNT catalysts in alkaline solutions as well [67]. Fig. 8 presents the results of Tafel analysis for catalyst materials shown in Fig. 7 (MnPc/MWCNT 50:50 weight ratio and heat treated at  $800^\circ\text{C}$  and CuPc/MWCNT 75:25 weight ratio and heat treated at  $800^\circ\text{C}$ ). The Tafel slope values for MnPc/MWCNT

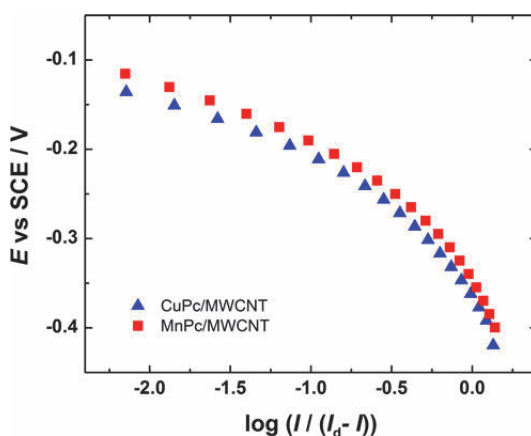


**Fig. 8** Tafel plots for oxygen reduction on MnPc/MWCNT and CuPc/MWCNT catalysts in 0.1 M KOH. Data derived from Fig. 7

catalyst at low and high current densities were found to be  $-65$  and  $-140$  mV dec $^{-1}$ , respectively, which is slightly lower than that reported in the literature for Vulcan XC-72 supported MnPc [34]. The slope values for CuPc/MWCNT catalyst are  $-50$  and  $-126$  mV dec $^{-1}$  at low and high overpotentials, respectively. Similar slopes have been found for the other metallomacrocyclic-modified nanocarbon catalysts [21].

On the basis of the results of the RDE experiments for catalyst materials heated at different temperatures, it can be concluded that the samples prepared at  $800$  °C showed the best activity towards the ORR. It has been proposed that the achieved electrocatalytic activity could be assigned to the pyridinic-type nitrogen formed at the temperatures as high as  $800$  °C [68]. It is also proven that the catalytic activity for the cathodic ORR cannot be related only to central metal, thus hereby to Mn or Cu, because it is well known that central metal atoms are playing minor role in the ORR in alkaline solutions [69]. Even if the metal nanoparticles on carbon supports are sometimes reported not to be related to the activity of the catalyst and nitrogen not being a part of the catalytically active site for ORR, these two species together can form highly active catalyst centre for oxygen electroreduction as also demonstrated in this study. The importance of MnPc and CuPc based catalysts as cathode materials for ORR has been highly recognised [34, 70] and the results obtained in the present work give further insight into their electrocatalytic properties.

## Conclusions

Current work has shown that MWCNT-supported manganese and copper phthalocyanines exhibit high electrocatalytic activity for ORR in alkaline media. Mn and Co phthalocyanines were supported on carbon nanotubes in different mass ratios employing a simple adsorption method. These catalyst materials were heat treated at four different temperatures from  $400$  to  $1000$  °C. The XPS results showed decomposition of the phthalocyanine ring because of the heat treatment and the formation of different electrocatalytically active metallic and nitrogen surface groups. The ORR kinetics was studied by the RDE method in  $0.1$  M KOH and it was found that the electrocatalytic activity of these metal phthalocyanine-based catalysts depend strongly on the heat treatment temperature. The best ORR performance was obtained with heat treatment of MWCNT-supported MnPc at  $800$  °C. Because of the high catalytic activity of MnPc/MWCNT material, it is expected to be a very promising candidate to be used as alternative cathode catalyst to noble-metals in anion-exchange membrane fuel cells.

**Acknowledgments** This research was financially supported by institutional research funding (IUT20-16 and IUT02-24) and by the project TK117T of the Estonian Ministry of Education and Research and by the Estonian Research Council (Grant No. 9323).

## References

- Zhang L, Zhang JJ, Wilkinson DP, Wang HJ (2006) *J Power Sources* 156:171–182
- Gong K, Du F, Xia Z, Durstock M, Dai L (2009) *Science* 323:760–764
- James B, Kalinoski J (2009) DOE-EERE fuel cell technologies program-2009 DOE hydrogen program review
- Nie Y, Li L, Wei Z (2015) *Chem Soc Rev* 44:2168–2201
- Jasinski R (1964) *Nature* 201:1212–1213
- Baranton S, Coutanceau C, Roux C, Hahn F, Léger JM (2005) *J Electroanal Chem* 577:223–234
- Claude E, Addou T, Latour JM, Aldebert P (1997) *J Appl Electrochem* 28:57–64
- Lalande G, Faubert G, Côté R, Guay D, Dodelet JP, Weng LT, Bertrand P (1996) *J Power Sources* 61:227–237
- Li X, Popov BN, Kawahara T, Yanagi H (2011) *J Power Sources* 196:1717–1722
- Kalvelage H, Mecklenburg A, Kunz U, Hoffmann U (2000) *Chem Eng Technol* 23:803–807
- Bambagioni V, Bianchini C, Filippi J, Lavacchi A, Oberhauser W, Marchionni A, Moneti S, Vizza F, Psaro R, Dal Santo V, Gallo A, Recchia S, Sordelli L (2011) *J Power Sources* 196:2519–2529
- Yuan Y, Ahmed J, Kim S (2011) *J Power Sources* 196:1103–1106
- Lu Y, Reddy RG (2007) *Electrochim Acta* 52:2562–2569
- Mamuru SA, Ozoemena KI (2010) *Electroanalysis* 22:985–994
- Zhang W, Shaikh AU, Tsui EY, Swager TM (2009) *Chem Mater* 21:3234–3241
- Schilling T, Okunola A, Masa J, Schuhmann W, Bron M (2010) *Electrochim Acta* 55:7597–7602
- Okunola A, Kowalewska B, Bron M, Kulesza PJ, Schuhmann W (2009) *Electrochim Acta* 54:1954–1960
- Xu Z, Li H, Cao G, Zhang Q, Li K, Zhao X (2011) *J Mol Catal A Chem* 335:89–96
- Morozan A, Campidelli S, Filoramo A, Jusselme B, Palacin S (2011) *Carbon* 49:4839–4847
- Kim SK, Jeon S (2012) *Electrochim Commun* 22:141–144
- He Q, Yang X, He R, Bueno-López A, Miller H, Ren X, Yang W, Koel BE (2012) *J Power Sources* 213:169–179
- Wiesener K (1986) *Electrochim Acta* 31:1073–1078
- Lee K, Ishihara A, Mitsushima S, Kamiya N, Ota KI (2004) *Electrochim Acta* 49:3479–3485
- Meng H, Larouche N, Lefèvre M, Jaouen F, Stansfield B, Dodelet JP (2010) *Electrochim Acta* 55:6450–6461
- Scherson DA, Gupta SL, Fierro C, Yeager EB, Kordesch ME, Eldridge J, Hoffman RW, Blue J (1983) *Electrochim Acta* 28:1205–1209
- van Veen JAR, Colijn HA, van Baar JF (1988) *Electrochim Acta* 33:801–804
- Lefèvre M, Dodelet JP, Bertrand P (2002) *J Phys Chem B* 106:8705–8713
- Bouwkamp-Wijnoltz AL, Visscher W, Van Veen JAR, Boellaard E, Van der Kraan AM, Tang SC (2002) *J Phys Chem B* 106:12993–13001
- Vasudevan P, Santosh, Mann N, Tyagi S (1990) *Transit Metal Chem* 15:81–90
- Van Veen JAR, Van Baar JF, Kroese KJ (1981) *J Chem Soc Faraday Trans 1: Phys Chem Condens Phases* 77:2827–2843
- Biloul A, Contamin O, Savy M, Scarbeck G, Riga J, Verbist J (1994) *J Electroanal Chem* 379:321–328
- Biloul A, Contamin O, Scarbeck G, Savy M, Palys B, Riga J, Verbist J (1994) *J Electroanal Chem* 365:239–246
- Sehltho N, Nyokong T (2006) *J Electroanal Chem* 595:161–167
- Guo J, He H, Chu D, Chen R (2012) *Electrocatalysis* 3:252–264

35. Vignarooban K, Lin J, Arvay A, Kolli S, Kruusenberg I, Tammeveski K, Munukutla L, Kannan AM (2015) *Chin J Catal* 36:458–472
36. Yu EH, Cheng S, Logan BE, Scott K (2009) *J Appl Electrochem* 39:705–711
37. Chen R, Li H, Chu D, Wang G (2009) *J Phys Chem C* 113:20689–20697
38. Zagal JH (1992) *Coord Chem Rev* 119:89–136
39. Zhang S, Zhang H, Hua X, Chen S (2015) *J Mater Chem A* 3: 10013–10019
40. Orellana W (2012) *Chem Phys Lett* 541:81–84
41. Zagal JH, Javier Recio F, Gutierrez CA, Zuñiga C, Páez MA, Caro CA (2014) *Electrochem Commun* 41:24–26
42. Domínguez C, Pérez-Alonso FJ, Abdel Salam M, Gómez De La Fuente JL, Al-Thabaiti SA, Basahel SN, Peña MA, Fierro JLG, Rojas S (2014) *Int J Hydrogen Energy* 39:5309–5318
43. Zhang Q, Zhu T, Qing X, Qiao J, Sun S (2015) *RSC Adv* 5:50344–50352
44. Reis RM, Valim RB, Rocha RS, Lima AS, Castro PS, Bertotti M, Lanza MRV (2014) *Electrochim Acta* 139:1–6
45. Ding L, Xin Q, Dai X, Zhang J, Qiao J (2013) *Ionics* 19:1415–1422
46. Vallejos-Burgos F, Utsumi S, Hattori Y, Garcia X, Gordon AL, Kanoh H, Kaneko K, Radovic LR (2012) *Fuel* 99:106–117
47. Guo J, Zhou J, Chu D, Chen R (2013) *J Phys Chem C* 117:4006–4017
48. Masheter AT, Xiao L, Wildgoose GG, Crossley A, Jones JH, Compton RG (2007) *J Mater Chem* 17:3515–3524
49. Wildgoose GG, Abiman P, Compton RG (2009) *J Mater Chem* 19: 4875–4886
50. Ding L, Qiao J, Dai X, Zhang J, Zhang J, Tian B (2012) *Int J Hydrogen Energy* 37:14103–14113
51. Kruusenberg I, Matisen L, Tammeveski K (2013) *J Nanosci Nanotechnol* 13:621–627
52. Ratso S, Kruusenberg I, Vikkisk M, Joost U, Shulga E, Kink I, Kallio T, Tammeveski K (2014) *Carbon* 73:361–370
53. Kruusenberg I, Ratso S, Vikkisk M, Kanninen P, Kallio T, Kannan AM, Tammeveski K (2015) *J Power Sources* 281:94–102
54. Kruusenberg I, Matisen L, Shah Q, Kannan AM, Tammeveski K (2012) *Int J Hydrogen Energy* 37:4406–4412
55. Sheng Z-H, Shao L, Chen J-J, Bao W-J, Wang F-B, Xia X-H (2011) *ACS Nano* 5:4350–4358
56. Tammeveski K, Kontturi K, Nichols RJ, Potter RJ, Schiffrin DJ (2001) *J Electroanal Chem* 515:101–112
57. Kruusenberg I, Mondal J, Matisen L, Sammelselg V, Tammeveski K (2013) *Electrochem Commun* 33:18–22
58. Lima F, Fortunato GV, Maia G (2013) *RSC Adv* 3:9550–9560
59. Alves MCM, Dodelet JP, Guay D, Ladouceur M, Tourillon G (1992) *J Phys Chem* 96:10898–10905
60. Ladouceur M, Lalonde G, Guay D, Dodelet JP, Dignardbailey L, Trudeau ML, Schulz R (1993) *J Electrochem Soc* 140:1974–1981
61. Bard AJ, Faulkner LR (2001) *Electrochemical methods: fundamentals and applications*, 2nd edn. Wiley, New York
62. Davis RE, Horvath GL, Tobias CW (1967) *Electrochim Acta* 12: 287–297
63. Lide DR (2001) *CRC Handbook of Chemistry and Physics*, 82nd edn. CRC Press, Boca Raton
64. Zagal J, Paez M, Tanaka AA, Dossantos JR, Linkous CA (1992) *J Electroanal Chem* 339:13–30
65. Yamazaki SI, Yamada Y, Ioroi T, Fujiwara N, Siroma Z, Yasuda K, Miyazaki Y (2005) *J Electroanal Chem* 576:253–259
66. Sepa DB, Vojnovic MV, Damjanovic A (1980) *Electrochim Acta* 25:1491–1496
67. Alexeyeva N, Tammeveski K, Lopez Cudero A, Solla-Gullon J, Feliu JM (2010) *Electrochim Acta* 55:794–803
68. Mo Z, Liao S, Zheng Y, Fu Z (2012) *Carbon* 50:2620–2627
69. Gojković SL, Gupta S, Savinell RF (1998) *J Electrochem Soc* 145: 3493–3499
70. Qing L, Shi J, Ma C, Fan M, Bai Z, Chen Z, Qiao J, Zhang J (2014) *J Power Sources* 266:88–98



## Appendix 2

### Publication II

K.-K. Türk, **K. Kaare**, I. Kruusenberg, M. Merisalu, U. Joost, L. Matisen, V. Sammelseg, J.H. Zagal, K. Tammeveski, Oxygen Electroreduction on Zinc and Dilithium Phthalocyanine Modified Multiwalled Carbon Nanotubes in Alkaline Media, *J. Electrochem. Soc.* 164 (2017) H338–H344.





## Oxygen Electroreduction on Zinc and Dilithium Phthalocyanine Modified Multiwalled Carbon Nanotubes in Alkaline Media

Karl-Kalev Türk,<sup>a</sup> Kätlin Kaare,<sup>a</sup> Ivar Krusenberg,<sup>a</sup> Mairo Merisalu,<sup>a,b</sup> Urmas Joost,<sup>b</sup> Leonard Matisen,<sup>b</sup> Väino Sammelselg,<sup>a,b,\*</sup> José H. Zagal,<sup>c,\*</sup> and Kaido Tammeveski<sup>a,\*,z</sup>

<sup>a</sup>Institute of Chemistry, University of Tartu, 50411 Tartu, Estonia

<sup>b</sup>Institute of Physics, University of Tartu, 50411 Tartu, Estonia

<sup>c</sup>Departamento de Química de los Materiales, Laboratorio de Electrocatálisis, Universidad de Santiago de Chile, Sucursal Matucana, Santiago 9170022, Chile

Dilithium and zinc phthalocyanine derived catalysts supported on multiwalled carbon nanotubes (MWCNTs) have been studied as non-precious metal catalysts for oxygen electroreduction. The electrocatalysts were prepared by simple pyrolysis by varying the pyrolysis temperature and metal phthalocyanine-to-MWCNT ratio. The surface morphology of the catalyst materials was characterized by scanning electron microscopy (SEM) and surface composition by X-ray photoelectron spectroscopy (XPS). The rotating disk electrode (RDE) method was used to determine the electrocatalytic activity of these materials in 0.1 M KOH solution. The oxygen reduction reaction (ORR) activities achieved are comparable to well-studied Fe and Co phthalocyanine based catalysts in alkaline media, showing the great potential of non-redox-active metal phthalocyanine-derived catalysts as cathode materials for metal-air batteries and fuel cells. The number of electrons transferred per O<sub>2</sub> molecule was determined by the Koutecky-Levich analysis, which indicated that at high negative potentials the ORR process followed a four-electron pathway. The O<sub>2</sub> reduction results obtained in this study show clearly the important role of non-redox-active metal ion in the formation of active sites for ORR on pyrolyzed and carbon supported Li and Zn metallomacrocylic compounds.

© 2017 The Electrochemical Society. [DOI: 10.1149/2.0821706jes] All rights reserved.

Manuscript submitted November 15, 2016; revised manuscript received February 20, 2017. Published March 31, 2017.

The increasing need for clean energy and the uncertainty of the fossil fuel prices are the main reasons for the continuous research interest in fuel cells as an alternative power source for automotive applications.<sup>1-4</sup> Low-temperature fuel cells such as proton-exchange membrane fuel cells (PEMFCs) and anion-exchange membrane fuel cells (AEMFCs) are one of the best solutions due to the low working temperature and high efficiency. The main drawback, which is hindering the commercialization of this technology, is the high cost of the fuel cell cathode. So far mostly the Pt and Pt-alloy nanoparticles supported on high-area carbon materials have been employed as cathode catalysts for oxygen reduction reaction (ORR), but the utilization of Pt-based materials will lead to multiple problems. Scarcity, high cost of Pt metal, sensitivity to CO and poor stability are some of the reasons, which are hampering the wide commercialization of the low-temperature fuel cell technology.<sup>5,6</sup> For these reasons there has been an enormous research interest for many years in finding an active Pt-free catalyst for ORR.<sup>7-10</sup>

Metallophthalocyanines (MPc) have been widely studied as fuel cell catalysts for more than a half century since the first report on their ORR electrocatalytic activity by Jasinski.<sup>11</sup> These metallomacrocylic compounds both in acidic and alkaline environment are considered among the most promising candidates for non-noble metal catalyst in terms of the ORR activity.<sup>12-23</sup> However, intact MPcs lack the long-term stability required for fuel-cell operation. Nevertheless, it is important to indicate that some MN<sub>4</sub> macrocylic compounds have an ability to reduce O<sub>2</sub> via four-electron pathway.<sup>24-26</sup> It has been stated that for iron and manganese phthalocyanines a 4-electron O<sub>2</sub> reduction pathway is favored, while for the Ni, Co and Cu phthalocyanines mostly 2-electron reduction occurs.<sup>24,25</sup> For fuel cell applications the 4-electron O<sub>2</sub> reduction pathway to H<sub>2</sub>O predominates. In contrast, the 2-electron reduction of oxygen is an unwanted process since hydrogen peroxide as the product of this reaction is harmful to catalyst and to the membrane and also delivers less energy than the 4-electron reduction. Previous studies have shown that transition metal macrocycle-based catalysts are more active in alkaline solution than in acidic media and therefore it is obvious that the ORR mechanism on these catalysts is pH dependent.<sup>20,25,27</sup> Even though the pH-dependence is obvious, the exact reaction sites responsible for the ORR electrocatalytic activity and the reaction mechanisms on these catalyst materials are still under

debate. The transition metal ion in the center of the Pc ring has been considered the main factor for enhanced ORR kinetics.<sup>24</sup> Therefore by varying the central metal and modifying ligand it is possible to enhance the electrocatalytic activity of MN<sub>4</sub> macrocycles.<sup>28</sup> It has been also suggested that the presence of transition metals in pyrolysis is needed to prepare catalytically active sites, but it is not completely clarified if the metal is an important component of the catalyst or its attendance is necessary to synthesize the active site.<sup>29</sup>

Besides that, it has been proposed that the electrocatalytic activity for ORR is related to the central metal ion M(III)/(II) redox potential.<sup>25</sup> It has been reported that the more positive is the redox potential the higher catalytic activity.<sup>25</sup> This explanation is not suitable for Li and Zn phthalocyanines studied in this work, since these central metal ions do not exhibit this kind of redox transition. Selvaraj et al. studied dilithium phthalocyanine (Li<sub>2</sub>Pc) for ORR catalyst in non-aqueous Li-O<sub>2</sub> cells.<sup>30</sup> They concluded that Li<sub>2</sub>Pc is a good catalyst for that application and it is due to the electronic interactions between Pc ring and O<sub>2</sub> molecule. Similarly to Li<sub>2</sub>Pc only a few studies have been made using Zn phthalocyanine (ZnPc) as catalyst material.<sup>31-34</sup> ZnPc complexes have been also studied for other applications, including gas sensing.<sup>35,36</sup>

In recent years there have been many studies where transition metal macrocylic compounds have been mixed with novel carbon-based support materials such as carbon nanotubes,<sup>37-40</sup> graphene,<sup>41-43</sup> reduced graphene oxide,<sup>44,45</sup> carbon nanotube/graphene composites<sup>46</sup> and mesoporous carbon<sup>47,48</sup> for electrocatalytic applications. Multiwalled carbon nanotubes (MWCNTs) are excellent support material for MPc due to their large surface area, good electrical conductivity and enhanced mass transport.<sup>5,49</sup> Studies have shown that using MWCNTs as support material improves the catalyst durability.<sup>50</sup> The results obtained indicate that pyrolysis in the temperature range from 700 to 1000 °C in inert atmosphere destroys the macrocycle structure but increases the catalyst activity and stability.<sup>17</sup> Different studies have shown that the optimal pyrolysis temperature for ORR electrocatalyst depends on the used MN<sub>4</sub> macrocycle type and carbon support and it is usually around 800 or 900 °C.<sup>29,51</sup>

In this work a simple procedure is used to prepare pyrolyzed catalysts of ZnPc and Li<sub>2</sub>Pc supported on MWCNTs to study the electrocatalytic activity of these materials toward the ORR in alkaline media. To our knowledge the literature on the application of ZnPc and Li<sub>2</sub>Pc for electrocatalysis is rather scarce. This motivated us to thoroughly investigate the ZnPc and Li<sub>2</sub>Pc derived catalysts to shed light on their electrocatalytic properties. The main aim is to find out the best

\*Electrochemical Society Member.

<sup>z</sup>E-mail: kaido@chem.ut.ee

MPC-to-MWCNT mass ratio and the optimum pyrolysis temperature for ORR electrocatalysis and potential catalyst material suitable for AEMFC application. We do believe that this study is contributing to a better understanding of the role of different metal ions in MPC ring for the preparation of active electrocatalyst materials for ORR.

### Experimental

**Materials and chemicals.**—Zinc phthalocyanine (ZnPc) and dilithiumpthalocyanine (Li<sub>2</sub>Pc) were purchased from Sigma-Aldrich and used as provided. Multiwalled carbon nanotubes (MWCNTs) with length of 5–20 μm, diameter of 30 ± 10 nm and purity >95% were bought from NanoLab, Inc. (Brighton, MA, USA). The as-received MWCNTs were heat-treated in concentrated nitric and sulfuric acid mixture (1:1, v/v) under reflux condition at 55°C for 2 h and then at 80°C for 3 h.<sup>52</sup> After that the MWCNTs were washed with Milli-Q water (Millipore, Inc.). The final product was dried in vacuo for 15 h. 5 wt% AS-4 OH<sup>-</sup> ionomer solution (Tokuyama Corp., Japan) was used in electrode preparation.

**Preparation of MWCNT/ZnPc and MWCNT/Li<sub>2</sub>Pc catalysts.**—To prepare the MWCNT/ZnPc and MWCNT/Li<sub>2</sub>Pc catalysts, mixtures of different MWCNT-to-MPC ratio (3:1, 1:1 and 1:3) were sonicated in isopropanol for 1 h to achieve uniform dispersions. Then the mixture was dried in a vacuum oven at 40°C and placed in a quartz boat. Afterwards the catalyst powder was pyrolyzed at different temperatures (400–1000°C) for 2 h in N<sub>2</sub> atmosphere. Finally the furnace was cooled down to room temperature and the catalyst powder was collected.

**Surface characterization of MWCNT/MPC catalysts by SEM and XPS.**—The surface morphology of MWCNT/ZnPc and MWCNT/Li<sub>2</sub>Pc catalysts was examined by a high-resolution scanning electron microscope (HR-SEM, Helios 600, FEI). X-ray photoelectron spectroscopy (XPS) was used for analyzing the surface composition of MWCNT/ZnPc and MWCNT/Li<sub>2</sub>Pc catalysts. For the XPS analysis the catalyst materials dispersed in isopropanol (4 mg mL<sup>-1</sup>) were deposited on a glassy carbon plate (1.1 × 1.1 cm) and the solvent was allowed to evaporate in air. XPS measurements were carried out with a SCIENITA SES-100 spectrometer using an unmonochromated Mg K<sub>α</sub> X-ray source (incident energy = 1253.6 eV), a take-off angle of 90° and a source power of 300W. The pressure in the analysis chamber was below 10<sup>-9</sup> Torr. For collecting the survey spectra the following parameters were used: energy range = 1050 to 0 eV, pass energy = 200 eV, step size = 0.5 eV and for the high-resolution scan: energy range = 410 to 390 eV for the N 1s, 60 to 50 eV for the Li 1s and 1030 to 1015 eV for the Zn 2p region, respectively, with pass energy = 200 eV and step size = 0.1 eV.

**Electrode preparation and electrochemical characterization.**—A glassy carbon (GC) disk of geometric area (A) of 0.2 cm<sup>2</sup> was used as substrate material to perform the rotating disk electrode (RDE) measurements. GC disks (GC-20SS, Tokai Carbon) were cut from rods and pressed into a Teflon holder and polished to a mirror finish with 1 and 0.3 μm alumina slurries (Buehler). Before carrying out the RDE experiments the electrodes were sonicated in isopropyl alcohol and also in Milli-Q water for 5 min. The electrodes were coated with catalyst material by using the catalyst ink suspension in isopropanol (4 mg mL<sup>-1</sup>). All the suspensions contained 0.25% of AS-4 OH<sup>-</sup> ionomer (Tokuyama Corp., Japan). An aliquot of catalyst suspension was pipetted onto the GC surface and was allowed to dry in air for 12 h. The catalyst loading of 0.4 mg cm<sup>-2</sup> was employed for electrochemical testing.

The RDE measurements were carried out using an EDI101 rotator and a CTV101 speed control unit (Radiometer). The electrode rotation rates (ω) were as follows: 360, 610, 960, 1900, 3100 and 4600 rpm. General Purpose Electrochemical System (GPES) software was used to control the electrochemical experiments and the potential was applied by an Autolab potentiostat/galvanostat PGSTAT30

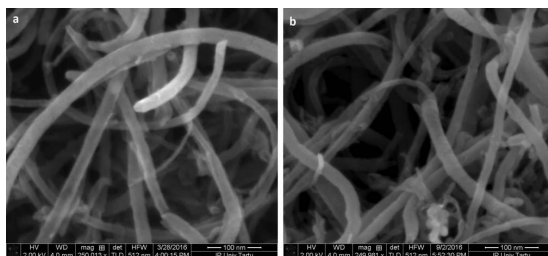


**Figure 1.** HR-SEM images of (a) MWCNT/ZnPc and (b) MWCNT/Li<sub>2</sub>Pc modified GC electrodes.

(Metrohm-Autolab, The Netherlands). The counter electrode was Pt foil and reference electrode was saturated calomel electrode (SCE). All the potentials are referred to SCE. A potential scan rate (v) of 10 mV s<sup>-1</sup> was used for oxygen reduction measurements. The electrolyte was 0.1 M KOH solution and used for electrochemical measurements at room temperature (23 ± 1°C). Ar (99.999%) or O<sub>2</sub> (99.999%) gases by AGA were used to saturate the electrolyte solution. A continuous gas flow was maintained over the solutions during all electrochemical experiments.

### Results and Discussion

**Physical characterization of MWCNT/ZnPc and MWCNT/Li<sub>2</sub>Pc catalysts.**—The surface morphology of MWCNT/ZnPc and MWCNT/Li<sub>2</sub>Pc catalysts with mass ratio of 3:1 and 1:1, respectively, deposited on a GC disk was studied by high-resolution scanning electron microscopy. The HR-SEM images of these samples are presented in Figures 1a and 1b. In Figure 1a it can be seen that there are non-agglomerated carbon nanotubes on the sample surface and there is no evidence of the formation of large amount of ZnPc particles. Figure 1b presents the HR-SEM image of MWCNT/Li<sub>2</sub>Pc catalyst, which is very similar to the MWCNT/ZnPc material. For both catalysts it can be seen that MWCNTs are quite well dispersed and there are some solid residues of phthalocyanines on the MWCNT surface.

The surface composition of the catalyst powders was studied by X-ray photoelectron spectroscopy (XPS). Figures 2a and 2b presents the XPS wide-scan spectra of MWCNT/ZnPc (75–25) and MWCNT/Li<sub>2</sub>Pc (50–50) catalysts, respectively. Both materials were pyrolyzed at 800°C. It is possible to separate four peaks in the overview spectra of the studied materials, which can be assigned to emission from C 1s, N 1s, O 1s and Zn 2p or Li 1s. High-resolution XPS spectra in the N 1s region show four peaks that correspond to pyridinic-N (398 eV), pyrrolic-N (400 eV), quaternary-N (401 eV) and pyridine-N-oxide (403 eV). The XPS analysis of N-containing carbon nanomaterials has been dealt with in a greater detail by Atanassov workgroup.<sup>53,54</sup> Total nitrogen content was 2.8 at% and 3.2 at% for MWCNT/ZnPc and MWCNT/Li<sub>2</sub>Pc catalysts, respectively. Different forms of nitrogen as determined by XPS analysis are listed in Table 1.

Two of these forms of nitrogen, pyridinic-N and quaternary-N, have been previously proposed as active sites for ORR in alkaline conditions.<sup>55,56</sup> The origin of these N 1s peaks is usually attributed to decomposition of the MN<sub>4</sub> macrocyclic complexes at high temperature, since it is the only source of nitrogen. The O 1s peak is the result of various carbon-oxygen functionalities on the MWCNT surface.<sup>57</sup> In the inset of Figure 2a high-resolution spectrum in the Zn 2p region can be observed and the XPS peak can be assigned to Zn metal or ZnO (≈1022 eV) in total content of 0.7 at%. For MWCNT/Li<sub>2</sub>Pc catalyst the XPS analysis shows different states of Li species (≈55–56 eV) in content of 3.4 at% in the studied sample. It can be concluded that the XPS peak with binding energy of 55.6 eV belongs to Li in Li<sub>2</sub>O form. Peak with binding energy 55.1 eV can be attributed to pure Li metal. As the appearance of the pure zinc and lithium particles on the surface of the carbon support is rather unlikely then we propose hereby that the particles of these metals may be located between the

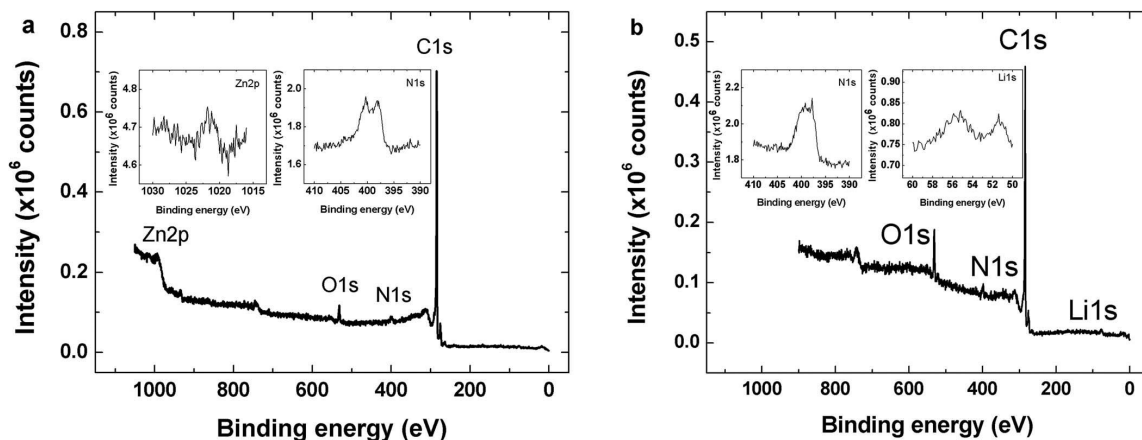


**Figure 2.** XPS survey spectra of the catalyst materials (a) MWCNT/ZnPc (75–25) and (b) MWCNT/Li<sub>2</sub>Pc (50–50) with inset spectra of N1s and Zn2p and Li1s, respectively. Catalysts were pyrolyzed at 800°C.

**Table I.** Relative content of nitrogen forms in the MWCNT/MPc catalysts pyrolyzed at 800°C.

Catalyst	Pyridinic-N	Pyrrhic-N	Quaternary-N	Pyridine-N-oxide
MWCNT/ZnPc (75–25)	40	31	14	15
MWCNT/Li <sub>2</sub> Pc (50–50)	56	31	12	1

MWCNTs or incorporated into the plane of graphitic carbon structure and connected additionally to the nitrogen species. In the literature it is reported that the presence of transition metals during the pyrolysis is necessary for synthesizing a highly active catalyst probably serving as templates to form MN<sub>4</sub> moieties but it is not clear what is its exact role of transition metals in the formation of the active sites for ORR in case of the non-redox-active metals.<sup>29</sup>

To give a better overview of the optimization of heat-treatment temperature of the catalysts, the XPS results of MWCNT/MPc

materials pyrolyzed at different temperatures are presented in Figures S1 and S2 (Tables S1 and S2) to highlight the relation between pyrolysis temperature, surface composition and electrocatalytic activity (see Supplementary Material).

**Rotating disk electrode studies of O<sub>2</sub> reduction.**—RDE measurements were carried out for evaluating the electrocatalytic activity of MWCNT/ZnPc and MWCNT/Li<sub>2</sub>Pc catalysts toward the ORR in alkaline solution. Figures 3a and 3b shows the RDE polarization curves for oxygen reduction on MWCNT/ZnPc and MWCNT/Li<sub>2</sub>Pc modified GC electrodes, respectively, where the MPc-to-MWCNTs mass ratio was varied as follows: 75–25, 50–50, and 25–75. The ORR polarization curve of the unmodified MWCNTs is shown for comparison purposes. All these MWCNT/MPc catalysts are pyrolyzed at 800°C and the RDE polarization curves were obtained at the same rotation rate ( $\omega = 1900$  rpm). It can be seen in Figure 3a that the most active catalyst for ORR is MWCNT/ZnPc with a mass ratio of 75–25. The ORR onset potential ( $E_{\text{onset}}$ ) of this catalyst is  $-0.07$  V, which is almost 100 mV more positive than the second best catalyst with MWCNT-to-ZnPc ratio of 50–50. The half-wave potential ( $E_{1/2}$ )

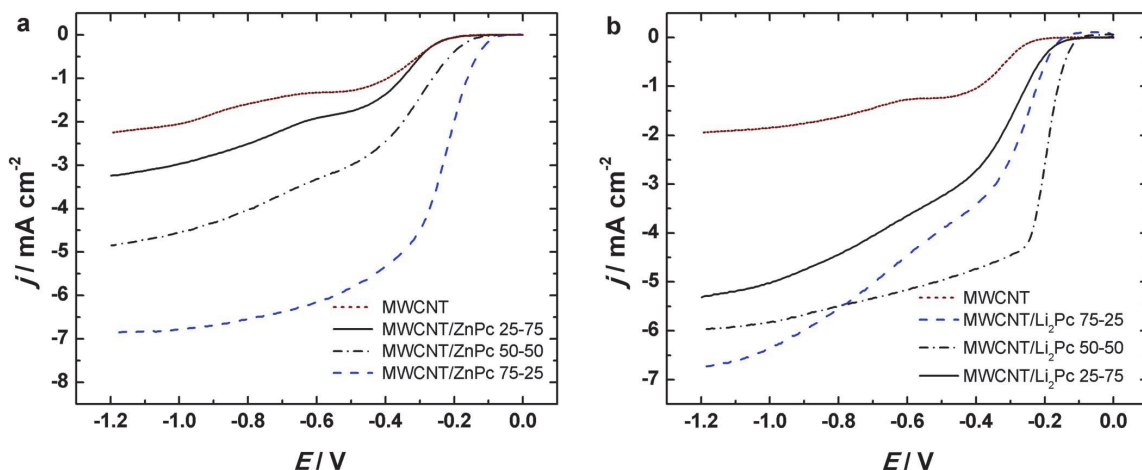


**Figure 3.** Comparative RDE polarization curves for oxygen reduction on (a) MWCNT/ZnPc and (b) MWCNT/Li<sub>2</sub>Pc modified GC electrodes in O<sub>2</sub>-saturated 0.1 M KOH.  $\nu = 10$  mV s<sup>-1</sup>,  $\omega = 1900$  rpm. The MWCNT-to-MPc ratio was varied (75–25, 50–50 and 25–75). Catalysts were pyrolyzed at 800°C.

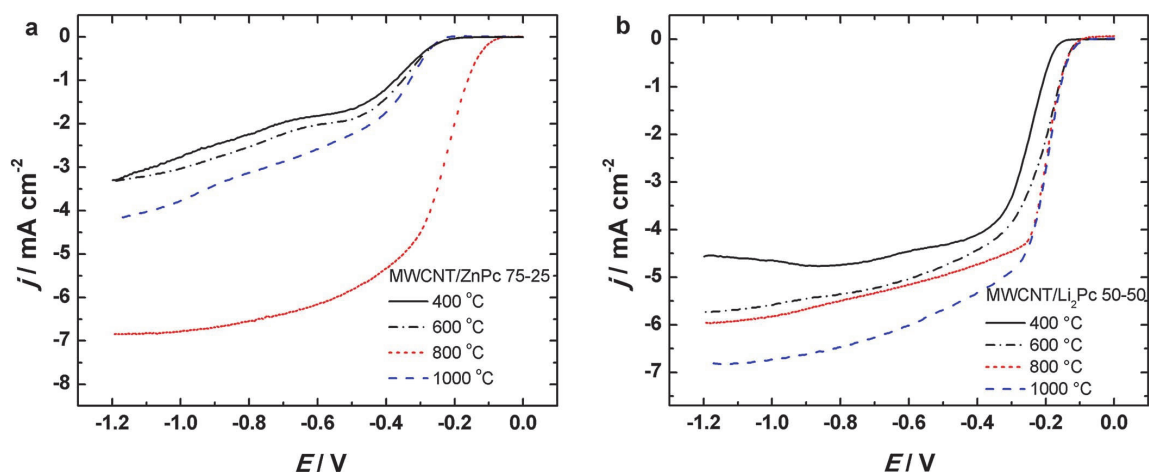


**Figure 4.** RDE polarization curves for oxygen reduction on (a) MWCNT/ZnPc (75–25) and (b) MWCNT/Li<sub>2</sub>Pc (50–50) modified GC electrodes in O<sub>2</sub>-saturated 0.1 M KOH.  $v = 10 \text{ mV s}^{-1}$ ,  $\omega = 1900 \text{ rpm}$ . The catalysts were heat-treated at different temperatures (400–1000 °C).

on this catalyst material is rather positive (approximately  $-0.25 \text{ V}$ ). The electrocatalytic activity for ORR increases in the following order: unmodified MWCNTs followed by MWCNT/ZnPc with ratio of 25–75, 50–50, and 75–25 indicating the fact that only minor amounts of ZnPc are needed to increase the electrocatalytic activity of the carbon based catalyst materials. When looking at the overall ORR activity, it can be concluded that by modifying carbon nanotubes with ZnPc has definitely a positive effect on the electrocatalytic properties.

Similarly to MWCNT/ZnPc catalysts, pyrolyzed MWCNT/Li<sub>2</sub>Pc materials were studied for ORR in alkaline media by varying MWCNT-to-Li<sub>2</sub>Pc mass ratio at a pyrolysis temperature of 800 °C. The ORR polarization curves for MWCNT/Li<sub>2</sub>Pc catalysts in 0.1 M KOH solution at 1900 rpm are shown in Figure 3b. For MWCNT/Li<sub>2</sub>Pc catalyst the best weight ratio for ORR electrocatalysis was found to be for MWCNT-to-Li<sub>2</sub>Pc ratio of 50–50, followed by mass ratio of 75–25, 25–75 and lastly unmodified MWCNTs. Although the MWCNT/Li<sub>2</sub>Pc catalyst material with 75–25 mass ratio shows slightly higher reduction current density, the  $E_{1/2}$  and ORR onset potential values still lower than that observed for 50–50 proportion catalyst. The  $E_{\text{onset}}$  for the most active catalyst is ca.  $-0.1 \text{ V}$  and  $E_{1/2}$  approximately  $-0.2 \text{ V}$ . When comparing with the most active MWCNT/ZnPc catalyst, it has slightly more negative  $E_{\text{onset}}$ , however the  $E_{1/2}$  value is 0.05 V higher.

For both types of catalysts the temperature of pyrolysis was optimized for the catalyst mass ratio of MWCNT-to-ZnPc (75–25) and MWCNT-to-Li<sub>2</sub>Pc (50–50) and the electroreduction of O<sub>2</sub> was studied in alkaline media. The electrocatalysts were prepared by varying the catalyst pyrolysis temperature at 400, 600, 800 or 1000 °C for 2 h in N<sub>2</sub> atmosphere. The ORR polarization curves, which were recorded in 0.1 M KOH solution at 1900 rpm are shown in Figures 4a and 4b for MWCNT/ZnPc and MWCNT/Li<sub>2</sub>Pc catalysts, respectively.

The RDE results showed that the optimum annealing temperature for MWCNT/ZnPc catalyst was 800 °C. It can be seen that there is a remarkable increase in the ORR activity for material which is pyrolyzed at 800 °C as compared to the catalysts heat-treated at other temperatures.

The ORR onset potential for this catalyst is 120 mV more positive as compared to the MWCNT/ZnPc catalyst pyrolyzed at other temperatures. Also the reduction current density is significantly higher than on other catalysts. This is in clear agreement with previous ORR studies reported on another MPc modified carbon nanotube catalyst materials.<sup>39,45,57</sup> An increased electrocatalytic activity of the pyrolyzed

materials was explained by Yeager et al., who reported that upon heat-treatment the M-N<sub>x</sub> moieties could act as more active sites for ORR as compared to untreated M-N<sub>4</sub> species.<sup>58</sup> Zagal<sup>26,59–61</sup> and Mukerjee<sup>62,63</sup> have proposed that the increase in electrocatalytic activity with pyrolysis of MN<sub>4</sub> complexes can be mainly attributed to an increase in the electron-withdrawing character of the environment around the MN<sub>4</sub> moiety, which is revealed by substantial shift in the M(III)/II redox signals to more positive values of the pyrolyzed materials compared to the intact MN<sub>4</sub> complexes. Essentially, this means that more positive redox potentials favor the electrocatalytic activity for ORR.<sup>25,26,28,59–63</sup> In this work, since the different complexes do not exhibit any visible redox activity on the metal center or any other redox couple associated to active sites the higher ORR activity of pyrolyzed catalysts cannot be attributed to shifts in the redox potentials or it is possible that these changes are not visible in cyclic voltammograms. However, Zn and Li are both known to be able to coordinate with electron pairs and form coordination complexes. It is likely that this type of interaction can also take place between Zn, Li and N-species on the surface of catalyst and thereby form the electrocatalytically active sites. One of the reasons for the improved ORR activity is apparently the formation of different active nitrogen surface species.<sup>64</sup> Four types of nitrogen doped into carbon have been identified: graphitic-N (quaternary-N), pyridinic-N, pyrrolic-N, and pyridine-N-oxide. Among these, pyridinic-N and graphitic-N are typically considered as the active groups for ORR in alkaline media, while pyrrolic-N and pyridine-N-oxide are considered to be inactive.<sup>10,65,66</sup> However, since there has not yet been demonstrated a way to obtain only a single type of nitrogen species on a catalyst, it is rather hard to precisely determine a contribution to the ORR activity of different nitrogen groups separately and thereby there has been a large controversy in the literature about this issue.

For the MWCNT/Li<sub>2</sub>Pc catalysts the electrocatalytic activity for ORR on 600, 800 and 1000 °C pyrolyzed materials does not change very much with different heat-treatment temperature as all the materials have same  $E_{\text{onset}}$  value. The ORR activity in terms of the  $E_{1/2}$  values is also rather similar for MWCNT/Li<sub>2</sub>Pc materials heat-treated between 600 and 1000 °C. The exception is the catalyst pyrolyzed at 400 °C. However, the material pyrolyzed at 1000 °C shows the highest reduction current density. The influence of the pyrolysis temperature on the electrocatalytic properties of MWCNT/Li<sub>2</sub>Pc catalysts studied in this work is in accordance with the literature, whereas a similar effect on heat-treatment has been observed before.<sup>67</sup> It is well known

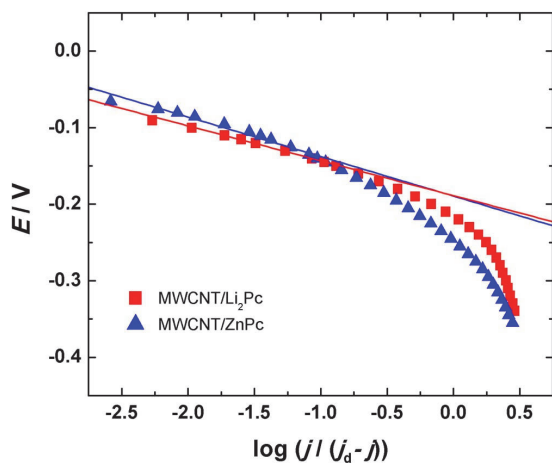


**Figure 5.** Tafel plots for oxygen reduction on MWCNT/ZnPC (75–25, 800°C) and MWCNT/Li<sub>2</sub>Pc (50–50, 1000°C) catalysts in 0.1 M KOH.

that the heat-treatment of nitrogen surface groups containing catalyst at higher temperature than 800°C will lead to the increase of the number of quaternary nitrogen groups on the carbon surface as well an increase of the amount of graphitized carbon, which in turn will lead to the higher electrical conductivity of the catalyst materials.<sup>68</sup> The higher ORR current values at more negative potentials are also visible in Figure 4b for MWCNT/Li<sub>2</sub>Pc catalyst pyrolyzed at 1000°C.

Tafel analysis was used to study the kinetics of oxygen electroreduction on these novel catalyst materials. Tafel plots of the most active MWCNT/ZnPC (75–25 and 800°C) and MWCNT/Li<sub>2</sub>Pc (50–50 and 1000°C) materials are shown in Figure 5.

Redox catalysts like for example FePc have typical Tafel slopes in the range from 30 to 40 mV dec<sup>-1</sup>.<sup>26</sup> This is usually caused by the fact that the catalytic process involves a fast M<sup>+n</sup>/M<sup>+(n-1)</sup> electron transfer process involving the metal center previous to the rate-determining step. For most redox catalysts the onset currents are observed at potentials close to the M(III)OH/(II) redox transition which is pH dependent in a wide pH range.<sup>26</sup> This in turn shows also that the surface concentration of M(II) active sites are under Nernstian potential control at low ORR overpotentials and thereby potential-dependent.<sup>26,62</sup> However, in

the present case we do not detect any redox signals attributed to the catalysts in the potential region where catalytic currents are observed. However we observe that the slope values at low current densities are -45 and -52 mV dec<sup>-1</sup> for MWCNT/Li<sub>2</sub>Pc and MWCNT/ZnPC catalysts, respectively. Tafel slopes close to -40 mV dec<sup>-1</sup> have been observed also for the iron and cobalt phthalocyanines with the redox active metal center catalysts.<sup>69</sup>

Figures 6a and 6b illustrate a set of ORR polarization curves for the most active MWCNT/ZnPC and MWCNT/Li<sub>2</sub>Pc catalysts. For both catalysts it is evident that the  $E_{\text{onset}}$  is the same at different rotation rates and we observe that the catalyst is stable and does not flake off from the electrode substrate or undergo changes during the experiment. The  $E_{\text{onset}}$  is approximately -0.07 V for MWCNT/ZnPC catalyst and ca. -0.1 V for MWCNT/Li<sub>2</sub>Pc at  $j = 25 \mu\text{A cm}^{-2}$ . It has been proposed, that active MPc catalysts have central metal ions that have nearly half-filled *d*-orbitals, such as Fe, Co or Mn.<sup>26,28,70</sup> In the case of Li<sub>2</sub>Pc and ZnPC, we are looking at *s*-block metal ions and an ion, which has full *d*-block of electrons. The ORR activity of these catalysts can be thereby mainly explained by the formation of different forms of active nitrogen species by the pyrolysis of the mixture and act as active sites for ORR.<sup>38</sup>

The number of electrons transferred per O<sub>2</sub> molecule (*n*) was estimated by the Koutecky–Levich (K–L) equation using the experimental RDE data:<sup>71</sup>

$$\frac{1}{j} = \frac{1}{j_k} + \frac{1}{j_D} = -\frac{1}{nFkc_{\text{O}_2}^b} - \frac{1}{0.62nFD_{\text{O}_2}^{2/3}\nu^{-1/6}c_{\text{O}_2}^b\omega^{1/2}} \quad [1]$$

where *j* is the experimentally measured current density at a specific potential *E*, *j<sub>k</sub>* is the kinetically controlled current density at *E* and *j<sub>D</sub>* is the diffusion-limited current density, *F* is the Faraday constant (96,485 C mol<sup>-1</sup>),  $\omega$  is the electrode rotation rate (rad s<sup>-1</sup>), *k* is the electrochemical rate constant for ORR (cm s<sup>-1</sup>) for the specific potential *E*, *D<sub>O<sub>2</sub></sub>* is the diffusion coefficient of O<sub>2</sub> ( $1.9 \times 10^{-5}$  cm<sup>2</sup> s<sup>-1</sup>),<sup>72</sup>  $c_{\text{O}_2}^b$  is the concentration of O<sub>2</sub> ( $1.2 \times 10^{-6}$  mol cm<sup>-3</sup>),<sup>72</sup> and  $\nu$  is the kinematic viscosity of the solution (0.01 cm<sup>2</sup> s<sup>-1</sup>).<sup>73</sup>

Figures 7a and 7b present the K-L plots obtained from the RDE data for MWCNT/ZnPC and MWCNT/Li<sub>2</sub>Pc catalysts in 0.1 M KOH solution. The K-L lines are parallel and the intercepts are close to zero at high negative potentials in both plots, which indicates that the process of oxygen reduction is limited by mass-transfer at higher overpotentials. The number of electrons transferred per O<sub>2</sub> molecule as a function of the electrode potential for the MWCNT/ZnPC catalyst is given as an inset to Figure 7a. It indicates that over the range of potentials studied the ORR process overwhelmingly proceeds via a 4-

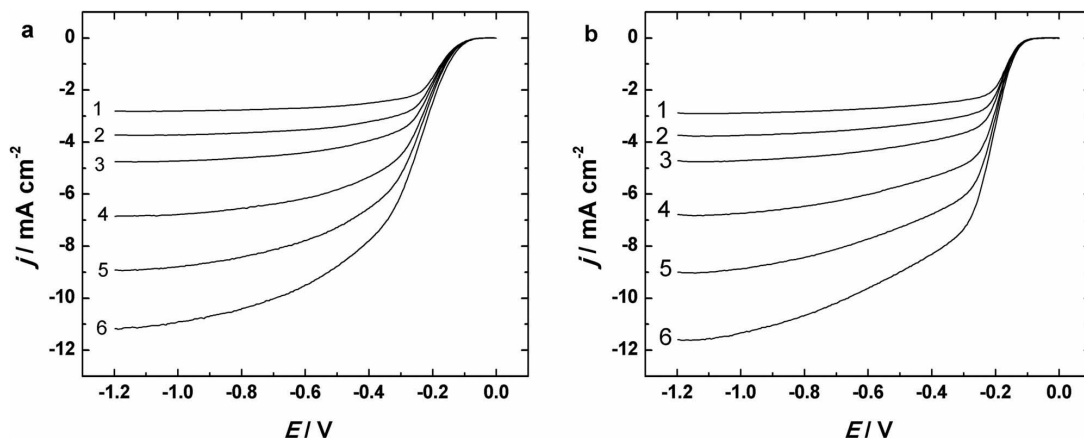


**Figure 6.** RDE voltammetry curves for oxygen reduction on (a) MWCNT/ZnPC (75–25, 800°C) and (b) MWCNT/Li<sub>2</sub>Pc (50–50, 1000°C) modified GC electrode in O<sub>2</sub>-saturated 0.1 M KOH.  $\nu = 10 \text{ mV s}^{-1}$ ,  $\omega =$  (1) 360, (2) 610, (3) 960, (4) 1900, (5) 3100 and (6) 4600 rpm.

electron pathway. A similar trend is observed for the MWCNT/Li<sub>2</sub>Pc catalyst (inset to Figure 7b).

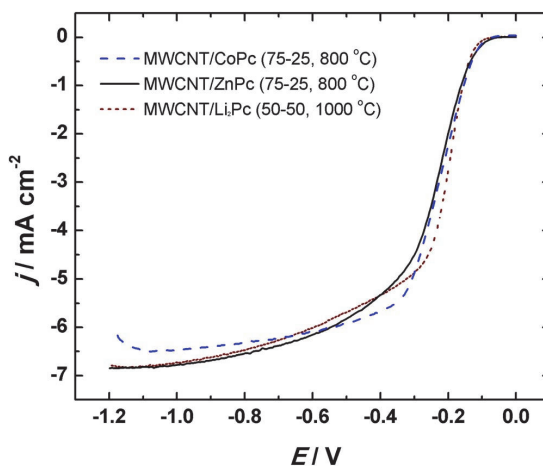
Both of the catalysts studied are rather unique as they exhibit the desirable 4-electron oxygen reduction to H<sub>2</sub>O and a comparable ORR activity to that of other MPc-based catalysts.<sup>20,74,75</sup> Osmieri et al. have studied the influence of transition metals, including ZnPc, on the electrocatalytic properties of pyrolyzed catalysts synthesized with SBA-15.<sup>76</sup> For Zn-N-C catalyst they have reported an  $E_{\text{onset}}$  of  $-0.14$  V vs. SCE (converted from RHE to SCE) while for MWCNT/ZnPc it is more positive,  $-0.07$  V at similar rotation speeds (900 rpm for Zn-N-CNT and 960 rpm for MWCNT/ZnPc). Moreover, the value of  $E_{1/2}$  for Zn-N-C is slightly more negative being  $-0.24$  V vs.  $-0.238$  V for the MWCNT/ZnPc catalyst. Also taking into account that catalyst loadings are different, Zn-N-C loading of  $0.637$  mg cm<sup>-2</sup> in the work by Osmieri et al.<sup>76</sup> vs. MWCNT/ZnPc loading of  $0.4$  mg cm<sup>-2</sup> in this work, it can be concluded that the MWCNT/ZnPc catalyst exhibits improved electrocatalytic activity. Morozan et al.<sup>20</sup> have studied Co- and Fe-phthalocyanines and porphyrins supported on MWCNTs and have achieved similar results in terms of  $E_{\text{onset}}$  and limiting current densities as compared to MWCNT/Li<sub>2</sub>Pc and MWCNT/ZnPc catalysts studied in the present work.

Figure 8 presents a comparison of oxygen reduction polarization curves with CoPc supported on MWCNTs (MWCNT-to-CoPc ratio 3:1; pyrolyzed at 800°C) that we have previously tested in same conditions as Li and Zn phthalocyanine based catalysts. We can see that ZnPc and Li<sub>2</sub>Pc modified catalysts exhibit similar performance to the state-of-the-art CoPc-based catalyst in alkaline media.

As the general aim of the fuel cell and metal-air batteries related research is to find a suitable catalyst for cathode, the report on a 4e<sup>-</sup> reduction of O<sub>2</sub> is of utmost importance. Hydrogen peroxide produced by 2e<sup>-</sup> oxygen reduction process is harmful to fuel cell membrane as well to the metal-air batteries and thereby unwanted. Further, the 2-electron reduction of O<sub>2</sub> delivers less energy than the full 4-electron reduction. These ZnPc and Li<sub>2</sub>Pc based catalysts could be used for low-temperature fuel cell and metal-air battery applications. In the next stage of work these catalysts will be tested as cathode materials in AEMFCs.

## Conclusions

In this work unique dilithium and zinc phthalocyanine derived materials were prepared as electrocatalysts for ORR using multiwalled carbon nanotubes as a support material. It was found that these novel catalyst materials exhibit comparable ORR activity in alkaline media to the state-of-the-art metallophthalocyanine-based catalysts. The RDE data analysis shows that a 4-electron reduction of O<sub>2</sub> to wa-



**Figure 8.** RDE polarization curves for oxygen reduction on the most active MWCNT/ZnPc, MWCNT/Li<sub>2</sub>Pc and MWCNT/CoPc modified GC electrodes in O<sub>2</sub>-saturated 0.1 M KOH.  $v = 10$  mV s<sup>-1</sup>,  $\omega = 1900$  rpm. Catalyst loadings are  $0.4$  mg cm<sup>-2</sup> for all the MWCNT/MPc catalysts.

ter occurs in a wide potential range, which is the favorable reaction pathway for fuel cell applications. The results obtained give further insights for better understanding the role of non-redox-active metal ion in phthalocyanine ring for ORR electrocatalysis. The previously suggested interpretations based on the redox transition on the central metal ion in the electrocatalytic process are not suitable for these metal macrocycle derived catalysts and new reaction schemes need to be proposed. However, the Tafel slopes close to  $-60$  mV dec<sup>-1</sup> for electrodes containing ZnPc suggest that the first process is a fast one-electron transfer step followed by a slow chemical step. Electrodes having Li<sub>2</sub>Pc show Tafel slopes close to  $-40$  mV dec<sup>-1</sup>, which could suggest that the rate-determining step is a second one-electron transfer preceded by fast one-electron transfer step. It is not yet clear, which active redox species is involved in the first step but it is very unlikely that involves the metal center (Li or Zn) and it is also not clear why these redox signals of the hypothetical non-metal redox centers are not visible by cyclic voltammetry. The importance of surface nitrogen species formed by pyrolysis of MWCNT/MPc materials toward ORR is highlighted.

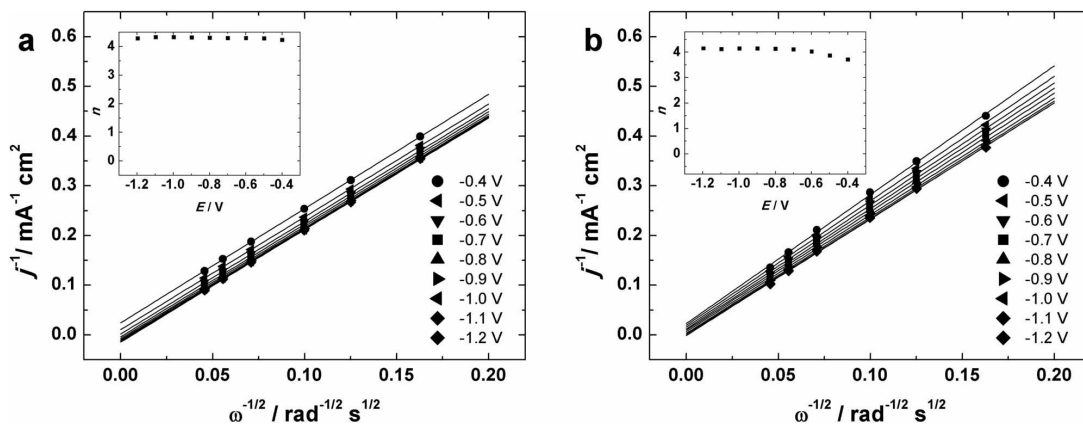


**Figure 7.** K-L plots for O<sub>2</sub> reduction on (a) MWCNT/ZnPc (75–25, 800°C) and (b) MWCNT/Li<sub>2</sub>Pc (50–50, 1000°C) catalysts in 0.1 M KOH at various potentials. The inset shows the potential dependence of  $n$ .

### Acknowledgments

This research was financially supported by institutional research funding (IUT20-16, IUT2-25 and IUT2-24) of the Estonian Ministry of Education and Research and by the Estonian Research Council (INDIGO project). This research was also supported by the EU through the European Regional Development Fund (TK141 “Advanced materials and high-technology devices for energy recuperation systems”) and by Fondecyt grant 1140199.

### References

- J. K. Dombrovskis and A. E. C. Palmqvist, *Fuel Cells*, **16**, 4 (2016).
- F. Jaouen, E. Proietti, M. Lefevre, R. Chenitz, J. -P. Dodelet, G. Wu, H. T. Chung, C. M. Johnston, and P. Zelenay, *Energy Environ. Sci.*, **4**, 114 (2011).
- Z. Chen, D. Higgins, A. Yu, L. Zhang, and J. Zhang, *Energy Environ. Sci.*, **4**, 3167 (2011).
- K. N. Wood, R. O'Hayre, and S. Pylypenko, *Energy Environ. Sci.*, **7**, 1212 (2014).
- Y. Y. Shao, G. P. Yin, and Y. Z. Gao, *J. Power Sources*, **171**, 558 (2007).
- Y. Y. Shao, G. P. Yin, Z. B. Wang, and Y. Z. Gao, *J. Power Sources*, **167**, 235 (2007).
- L. M. Rivera Gavidia, G. Garcia, D. Anaya, A. Querejeta, F. Alcaide, and E. Pastor, *Appl. Catal. B: Environ.*, **184**, 12 (2016).
- X. X. Zhang, W. P. Ouyang, D. R. Zeng, Y. F. Zhan, F. Y. Xie, W. H. Zhang, J. Chen, and H. Meng, *Catal. Today*, **264**, 206 (2016).
- F. Roncaroli, E. S. Dal Molin, F. A. Viva, M. M. Bruno, and E. B. Halac, *Electrochim. Acta*, **174**, 66 (2015).
- K. P. Gong, F. Du, Z. H. Xia, M. Durstock, and L. M. Dai, *Science*, **323**, 760 (2009).
- R. J. Jasinski, *Nature*, **201**, 1212 (1964).
- Y. Y. Liu, X. P. Yue, K. X. Li, J. L. Qiao, D. P. Wilkinson, and J. J. Zhang, *Coord. Chem. Rev.*, **315**, 153 (2016).
- A. Abbaspour and E. Mirahmadi, *Electrochim. Acta*, **105**, 92 (2013).
- Y. Y. Jiang, Y. Z. Lu, X. Y. Lv, D. X. Han, Q. X. Zhang, L. Niu, and W. Chen, *ACS Catal.*, **3**, 1263 (2013).
- S. M. Zhang, H. Y. Zhang, X. Hua, and S. L. Chen, *J. Mater. Chem. A*, **3**, 10013 (2015).
- L. Ding, X. F. Dai, R. Lin, H. J. Wang, and J. L. Qiao, *J. Electrochem. Soc.*, **159**, F577 (2012).
- S. Maldonado and K. J. Stevenson, *J. Phys. Chem. B*, **108**, 11375 (2004).
- L. Ding, Q. Xin, X. J. Zhou, J. L. Qiao, H. Li, and H. J. Wang, *J. Appl. Electrochem.*, **43**, 43 (2013).
- R. M. Reis, R. B. Valim, R. S. Rocha, A. S. Lima, P. S. Castro, M. Bertotti, and M. R. V. Lanza, *Electrochim. Acta*, **139**, 1 (2014).
- A. Morozan, S. Campidelli, A. Filoramo, B. Jusselme, and S. Palacin, *Carbon*, **49**, 4839 (2011).
- X. X. Wang, B. Wang, J. Zhong, F. P. Zhao, N. Han, W. J. Huang, M. Zeng, J. Fan, and Y. G. Li, *Nano Res.*, **9**, 1497 (2016).
- V. Mani, R. Devasanathipathy, S. M. Chen, J. A. Gu, and S. T. Huang, *Renew. Energy*, **74**, 867 (2015).
- O. O. Fashedemi and K. I. Ozoemena, *RSC Adv.*, **5**, 22869 (2015).
- K. Vignarooban, J. Lin, A. Arvay, S. Kolli, I. Kruusenberg, K. Tammeveski, L. Munukutla, and A. M. Kannan, *Chinese J. Catal.*, **36**, 458 (2015).
- J. H. Zagal, F. J. Recio, C. A. Gutierrez, C. Zufiga, M. A. Paez, and C. A. Caro, *Electrochem. Commun.*, **41**, 24 (2014).
- J. H. Zagal and M. T. M. Koper, *Angew. Chem. Int. Ed.*, **55**, 14510 (2016).
- G. V. Zhutavaeva, V. A. Bogdanovskaya, E. S. Davydova, L. P. Kazanskii, and M. R. Tarasevich, *J. Solid State Electrochem.*, **18**, 1319 (2014).
- J. Masa, K. Ozoemena, W. Schuhmann, and J. H. Zagal, *J. Porphyrins Phthalocyanines*, **16**, 761 (2012).
- C. Dominguez, F. J. Perez-Alonso, M. A. Salam, J. L. G. de la Fuente, S. A. Al-Thabaiti, S. N. Basahel, M. A. Pena, J. L. G. Fierro, and S. Rojas, *Int. J. Hydrogen Energy*, **39**, 5309 (2014).
- C. Selvaraj, N. Munichandraiah, and L. G. Scanlon, *J. Porphyrins Phthalocyanines*, **16**, 255 (2012).
- Z. J. Liu, Q. Q. Jiang, R. L. Zhang, R. M. Gao, and J. S. Zhao, *Electrochim. Acta*, **187**, 81 (2016).
- E. Ermis, Y. Cimen, F. Dumludag, A. R. Ozkaya, B. Salih, and O. Bekaroglu, *Polyhedron*, **49**, 129 (2013).
- T. Zhu, X. Qing, P. Xu, Y. Song, and J. Qiao, *ECS Trans.*, **66**, 105 (2015).
- Ü. E. Özen, E. Doğan, M. Özer, Ö. Bekaroglu, and A. R. Özkaya, *J. Electrochem. Soc.*, **163**, A2001 (2016).
- X. H. Liang, Z. M. Chen, H. Wu, L. X. Guo, C. Y. He, B. Wang, and Y. Q. Wu, *Carbon*, **80**, 268 (2014).
- R. Saini, A. Mahajan, R. K. Bedi, D. K. Aswal, and A. K. Debnath, *Sens. Actuators B Chem.*, **198**, 164 (2014).
- R. Cao, R. Thapa, H. Kim, X. Xu, M. G. Kim, Q. Li, N. Park, M. L. Liu, and J. Cho, *Nat. Commun.*, **4**, 2076 (2013).
- R. Zhang, Y. X. Peng, Z. P. Li, K. Li, J. Ma, Y. Liao, L. R. Zheng, X. Zuo, and D. G. Xia, *Electrochim. Acta*, **147**, 343 (2014).
- K. Elouarzaki, R. Haddad, M. Holzinger, A. Le Goff, J. Thery, and S. Cosnier, *J. Power Sources*, **255**, 24 (2014).
- K. Kaare, I. Kruusenberg, M. Merisalu, L. Matisen, V. Sammelselg, and K. Tammeveski, *J. Solid State Electrochem.*, **20**, 921 (2016).
- E. Yoo and H. S. Zhou, *J. Power Sources*, **244**, 429 (2013).
- L. L. Cui, G. J. Lv, and X. Q. He, *J. Power Sources*, **282**, 9 (2015).
- H. J. Choi, N. A. Kumar, and J. B. Baek, *Nanoscale*, **7**, 6991 (2015).
- D. Liu and Y. T. Long, *ACS Appl. Mater. Interfaces*, **7**, 24063 (2015).
- I. Kruusenberg, J. Mondal, L. Matisen, V. Sammelselg, and K. Tammeveski, *Electrochem. Commun.*, **33**, 18 (2013).
- K. K. Türk, I. Kruusenberg, J. Mondal, P. Rauwel, J. Kozlova, L. Matisen, V. Sammelselg, and K. Tammeveski, *J. Electroanal. Chem.*, **756**, 69 (2015).
- J. K. Dombrovskis, H. Y. Jeong, K. Fossum, O. Terasaki, and A. E. C. Palmqvist, *Chem. Mater.*, **25**, 856 (2013).
- J. Y. Cheon, C. Ahn, D. J. You, C. Pak, S. H. Hur, J. Kim, and S. H. Joo, *J. Mater. Chem. A*, **1**, 1270 (2013).
- E. Antolini, *Appl. Catal. B Environ.*, **88**, 1 (2009).
- J. Deng, P. J. Ren, D. H. Deng, L. Yu, F. Yang, and X. H. Bao, *Energy Environ. Sci.*, **7**, 1919 (2014).
- Q. G. He, X. F. Yang, X. M. Ren, B. E. Koel, N. Ramaswamy, S. Mukerjee, and R. Kostecki, *J. Power Sources*, **196**, 7404 (2011).
- I. Kruusenberg, M. Marandi, V. Sammelselg, and K. Tammeveski, *Electrochem. Solid State Lett.*, **12**, F31 (2009).
- I. Matanovic, K. Artyushkova, M. B. Strand, M. J. Dzara, S. Pylypenko, and P. Atanassov, *J. Phys. Chem. C*, **120**, 29225 (2016).
- S. Kabir, K. Artyushkova, A. Serov, B. Kiefer, and P. Atanassov, *Surf. Interface Anal.*, **48**, 293 (2016).
- M. Xu, C. Li, H. Q. Ren, L. L. Ding, K. Xu, and J. J. Geng, *J. Mol. Catal. A Chem.*, **390**, 69 (2014).
- R. Zhang, Y. Peng, Z. Li, K. Li, J. Ma, Y. Liao, L. Zheng, X. Zuo, and D. Xia, *Electrochim. Acta*, **147**, 343 (2014).
- I. Kruusenberg, N. Alexeyeva, K. Tammeveski, J. Kozlova, L. Matisen, V. Sammelselg, J. Solla-Gullon, and J. M. Feliu, *Carbon*, **49**, 4031 (2011).
- D. Scherson, A. A. Tanaka, S. L. Gupta, D. Tryk, C. Fierro, R. Holze, E. B. Yeager, and R. P. Lattimer, *Electrochim. Acta*, **31**, 1247 (1986).
- J. H. Zagal and G. I. Cárdenas-Jirón, *J. Electroanal. Chem.*, **489**, 96 (2000).
- J. H. Zagal, I. Ponce, D. Baez, R. Venegas, J. Pavez, M. Paez, and M. Gulppi, *Electrochem. Solid State Lett.*, **15**, B90 (2012).
- G. I. Cárdenas-Jirón and J. H. Zagal, *J. Electroanal. Chem.*, **497**, 55 (2001).
- Q. Jia, N. Ramaswamy, H. Hafiz, U. Tylus, K. Strickland, G. Wu, B. Barbillini, A. Bansil, E. F. Holby, P. Zelenay, and S. Mukerjee, *ACS Nano*, **9**, 12496 (2015).
- U. Tylus, Q. Jia, K. Strickland, N. Ramaswamy, A. Serov, P. Atanassov, and S. Mukerjee, *J. Phys. Chem. C*, **118**, 8999 (2014).
- E. A. Gonzalez, M. Gulppi, M. A. Paez, and J. H. Zagal, *Diam. Relat. Mater.*, **64**, 119 (2016).
- C. Domínguez, F. J. Pérez-Alonso, M. Abdel Salam, S. A. Al-Thabaiti, A. Y. Obaid, A. A. Alshehri, J. L. Gómez de la Fuente, J. L. G. Fierro, and S. Rojas, *Appl. Catal. B: Environ.*, **162**, 420 (2015).
- Y. Cheng, H. Zhang, C. V. Varanasi, and J. Liu, *Sci. Rep.*, **3**, 3195 (2013).
- Y. Jiang, Y. Xie, X. Jin, Q. Hu, L. Chen, L. Xu, and J. Huang, *RSC Adv.*, **6**, 78737 (2016).
- C. Li, Z. Han, Y. Yu, Y. Zhang, B. Dong, A. Kong, and Y. Shan, *RSC Adv.*, **6**, 15167 (2016).
- V. Bambagioni, C. Bianchini, J. Filippi, A. Lavacchi, W. Oberhauser, A. Marchionni, S. Moneti, F. Vizza, R. Psaro, V. Dal Santo, A. Gallo, S. Recchia, and L. Sordelli, *J. Power Sources*, **196**, 2519 (2011).
- J. H. Zagal and F. Bedioui, *Electrochemistry of N4 Macrocyclic Metal Complexes*, Volume 1: Energy, Second Edition, (2016).
- A. J. Bard and L. R. Faulkner, *Electrochemical Methods: Fundamentals and Applications*, 2nd Edition, John Wiley & Sons, New York (2001).
- R. E. Davis, G. L. Horvath, and C. W. Tobias, *Electrochim. Acta*, **12**, 287 (1967).
- D. R. Lide, *CRC Handbook of Chemistry and Physics, 82nd Edition*, CRC Press, Boca Raton (2001).
- I. Kruusenberg, L. Matisen, and K. Tammeveski, *J. Nanosci. Nanotechnol.*, **13**, 621 (2013).
- I. Kruusenberg, L. Matisen, Q. Shah, A. M. Kannan, and K. Tammeveski, *Int. J. Hydrogen Energy*, **37**, 4406 (2012).
- L. Osmieri, A. H. A. Monteverde Videla, M. Armandi, and S. Specchia, *Int. J. Hydrogen Energy*, **41**, 22570 (2016).



## Appendix 3

### Publication III

K.M. Villemson, **K. Kaare**, R. Raudsepp, T. Käämbre, K. Šmits, P. Wang, A. V. Kuzmin, A. Šutka, B.A. Shainyan, I. Kruusenberg, Identification of Active Sites for Oxygen Reduction Reaction on Nitrogen- and Sulfur-Codoped Carbon Catalysts, *J. Phys. Chem. C.* 123 (2019) 16065–16074.



# Identification of Active Sites for Oxygen Reduction Reaction on Nitrogen- and Sulfur-Codoped Carbon Catalysts

Karl Markus Villemson,<sup>†</sup> Kätlin Kaare,<sup>‡</sup> Ragle Raudsepp,<sup>‡</sup> Tanel Käämbre,<sup>§</sup> Krišjānis Šmits,<sup>||</sup> Pangpang Wang,<sup>⊥</sup> Anton V. Kuzmin,<sup>#</sup> Andris Sutka,<sup>||</sup> Bagrat A. Shainyan,<sup>#</sup> and Ivar Kruusenberg<sup>\*,‡,⊥</sup>

<sup>†</sup>Institute of Chemistry, University of Tartu, Ravila 14a, 50411 Tartu, Estonia

<sup>‡</sup>National Institute of Chemical Physics and Biophysics, Akadeemia tee 23, 12618 Tallinn, Estonia

<sup>§</sup>Institute of Physics, University of Tartu, Wilhelm Ostwald Street 1, 50411 Tartu, Estonia

<sup>||</sup>Institute of Solid State Physics, University of Latvia, Kengaraga 8, 1063 Riga, Latvia

<sup>⊥</sup>Nanomaterials Laboratory, Institute of Systems, Information Technologies and Nanotechnologies, 819-0388 Fukuoka, Japan

<sup>#</sup>Siberian Branch of Russian Academy of Sciences, A. E. Favorsky Irkutsk Institute of Chemistry, 1 Favorsky Street, 664033 Irkutsk, Russian Federation

<sup>\*</sup>Research Laboratory of Functional Materials Technologies, Faculty of Materials Science and Applied Chemistry, Riga Technical University, P. Valdena 3/7, 1048 Riga, Latvia

**ABSTRACT:** Nitrogen- and sulfur-codoped carbon catalysts were prepared as electrocatalytic materials for the oxygen reduction reaction (ORR). Herein, we propose a novel and effective one-pot synthetic approach to prepare a NS-doped carbon catalyst by using the mixture of graphene oxide and multi-walled carbon nanotubes as a carbon support. Successful NS-doping of carbon and formation of the catalytically active sites were confirmed by X-ray photoelectron spectroscopy and with energy dispersion spectroscopy. The ORR activity of NS-codoped carbon was investigated by using a rotating disc electrode method. The NS-doped carbon shows superior ORR performance in alkaline media, and the electrocatalytic mechanism for the reduction of oxygen was well explained by density functional theory calculations of graphene sheets.



## 1. INTRODUCTION

One of the main obstacles to develop and commercialize energy converting and storing systems such as fuel cells and metal–air batteries is the slow reaction kinetics of the oxygen reduction reaction (ORR). At present, Pt-based catalysts are mainly used in order to lower the activation energy and accelerate the ORR. In view of high cost and poor durability of Pt-based catalysts, it is estimated that almost half of the fuel cell cost comes from the noble metal catalyst.<sup>1,2</sup> Starting from the 1960s, scientists have been trying to find the alternative to Pt-based catalysts in fuel cells. Many of these studies have demonstrated that metal-free carbon nanomaterials doped with heteroatoms are one of the promising materials because of their low cost, long-term stability, good endurance to fuel impurities, and prominent catalytic activity for the ORR. Carbon nanomaterials such as graphene, graphene oxide (GO), carbon nanotubes (CNTs), mesoporous carbon, and so forth serve as an excellent catalyst support because of their large specific area and superb electrical conductivity. Nevertheless, carbon materials alone are not active enough to catalyze ORR. One of the possibilities to increase their activity is to dope heteroatoms into the carbon network. Mainly, N, P, S, and B are used as dopants because of their reasonable atomic size compared with the carbon atom.<sup>3–15</sup> Because all of

these dopants mentioned have different number of valence electrons compared to the carbon, they change electron-donor properties of the material and create active sites for oxygen adsorption. Because of the synergistic effect of codoping, it is shown to be more effective than doping with one heteroatom.<sup>16,17</sup> Zhang et al. and Qui et al. have both demonstrated increased activity in codoped N/S carbon materials compared with the solely doped N or S carbon framework.<sup>18,19</sup>

As a result of doping, the atomic charge density and spin density are changed; charge redistribution facilitates the O<sub>2</sub> chemisorption on the carbon material surface, weakens the O–O bonding, and as a result promotes the ORR process.<sup>20</sup> Different carbon materials, such as ordered mesoporous carbon,<sup>21</sup> carbon dots,<sup>22</sup> carbon nanofiber networks,<sup>23</sup> graphene with carbon nanospheres,<sup>24</sup> and mesoporous graphene<sup>25</sup> have been doped with nitrogen and sulfur in earlier works. Physical and chemical properties of graphene will make it the best possible candidate for catalyst formation. However, the problems related to restacking of graphene layers

Received: January 5, 2019

Revised: May 17, 2019

Published: May 25, 2019

and agglomeration are making it difficult to use graphene as an electrocatalyst alone.<sup>26</sup> Restacking causes decrease in the surface area, as it gets similar to graphite and this in turn also lowers the conductivity of the material.<sup>27</sup> It has been reported that adding carbon black to graphene reduces the agglomeration of graphene sheets and, as a result, the electrochemical properties get better.<sup>28</sup> Thereby, to avoid graphene restacking, it is utmost important to add some material to it, which could act as a spacer between the graphene layers and thus contribute to overall surface area and conductivity of the catalyst material.<sup>26</sup> CNTs are widely used spacers for graphene.<sup>4,26,29</sup> Adding CNTs to graphene has a positive effect on the electrochemical activity, as CNTs will create enough space for transport of reactants and also increase the electron transfer rate because CNTs act as circuits between graphene layers.<sup>29</sup> Using spacers for graphene and doping with heteroatoms have both a synergistic effect that contributes to achieving better electrochemical activity for the ORR.

In this work, we demonstrate increased catalytic activity of facile, single-step codoped N and S carbon nanomaterials. N-doping was chosen because of a large variety and availability of nitrogen-containing compounds as well as proven enhanced catalytic activity after nitrogen doping. S-doping has also shown to enhance ORR, but because the electronegativity of sulfur is rather similar to that of the carbon, its catalytic effect is determined by the change in spin density in carbon atoms.<sup>30–33</sup> On top of the electrochemical analysis and physical characterization, density functional theory (DFT) calculations of graphene sheets doped with sulfur atom and nitrogen atoms of three types (pyrolic, pyridinic, and graphitic) were performed to support the experimental results and interpretations and to gain an insight into the structure and properties of the principal intermediates of ORR.

## 2. EXPERIMENTAL SECTION

**2.1. Materials and Catalysts Preparation.** The GO material used in this work was synthesized from graphite powder by a modified Hummers' method.<sup>3,34</sup> Multi-walled CNTs (NanoLab) used in this work were acid-treated before their usage via a published procedure.<sup>35</sup> Vulcan XC 72R was bought from Fuel Cell Store.

GO and MWCNTs were weighed and added into the vial so that the amount of GO would correspond to the weight of the nanotubes. To improve the material's properties, the mixture of GO and MWCNTs was doped in the presence of N and S precursor: *o*-methylisourea bisulfate (oMUS). oMUS was purchased from Sigma-Aldrich. To prepare the N- and S-codoped carbon catalyst, the first step was to ultrasonically blend GO and MWCNTs and surfactant polyvinylpyrrolidone in isopropanol (Honeywell).

Then, the N and S precursor with mass ratio 1 [1:1 MWCNT/reduced graphene oxide (rGO)]/5 (oMUS) was added, and dispersion was sonicated for 1 h to achieve a homogeneous mixture and dried in vacuum at 65 °C. For heteroatom doping, the pyrolysis process is also needed, as the precursor decomposes at high temperatures and the doping also takes place simultaneously. The material was then collected into a quartz boat and pyrolyzed in a flowing nitrogen atmosphere at 800 °C for 2 h. After that, the furnace was slowly cooled to room temperature and the products were collected and weighed. After blending, the catalysts were dried in vacuum at 75 °C. The catalyst prepared in the presence of oMUS is designated as C/oMUS.

**2.2. Physical Characterization.** The X-ray photoelectron spectroscopy (XPS) measurements were performed using a Scienta SES100 hemispherical analyzer (operated at 200 eV pass energy) and non-monochromated Mg K $\alpha$  incident exciting radiation from an XR-4 twin anode X-ray source (Thermo VG Scientific), with an overall spectral resolution of approximately 0.6 eV. The XPS sample was made by pressing the obtained flaky sample material into a metallic indium ingot.

A high-resolution elemental mapping analysis of the C/oMUS was conducted on spherical aberration-corrected scanning transmission electron microscopy (STEM, JEM-ARM200CF, JEOL, Japan) with energy dispersion spectroscopy (EDS) under an accelerating voltage of 200 kV. For the STEM-EDS observation, the suspension of the C/oMUS powder dispersed into ethanol was dropped onto a 200 mesh copper TEM grid containing a 20 nm thick amorphous carbon supporting film. Transmission electron microscopy images were obtained using Tecnai G2 F20 (FEI). A fast Fourier transform (FFT) analysis was made using a DigitalMicrograph (Gatan).

**2.3. Electrode Preparation and Electrochemical Characterization.** ORR polarization curves were measured using the rotating disk electrode (RDE) method. The experiments were undertaken using six different rotation rates ( $\omega$ ), from 4600 to 360 rpm. Pine AFMSRCE (Pine, USA) rotator and speed controlling unit were used for the RDE measurements. The software used for controlling the experiments was Nova 2.1.2 (Metrohm Autolab P.V., The Netherlands), and the potential was applied with a potentiostat/galvanostat Autolab PGSTAT 128N (Metrohm Autolab P.V., The Netherlands). All of the electrochemical tests were carried out by using three electrodes. The Pt foil was used as a counter electrode, saturated calomel electrode (SCE) as a reference electrode, and catalyst-coated glassy carbon (GC) electrode as a working electrode. All of the potentials in this work are referred to the SCE electrode. Electrochemical measurements were performed in 0.1 M KOH solution at room temperature ( $23 \pm 1$  °C). The solution was saturated with O<sub>2</sub> (6.0) to study ORR, and for measuring background, the solution was saturated with Ar (5.0). A continuous flow of gases was maintained over the solution during the measurement.

GC electrodes were polished to a mirror finish with 1 and 0.3  $\mu\text{m}$  alumina slurries (Buehler) before the catalyst coating. To clean the electrodes from polishing debris, sonication in both 2-propanol and Milli-Q water for 5 min was undertaken. The C/oMUS catalyst suspension in isopropanol (4 mg mL<sup>-1</sup>) containing 0.25% Tokuyama OH<sup>-</sup> ionomer AS-4 (Tokuyama Corporation, Japan) was prepared for the modification of electrodes. The suspensions were then homogenized via sonication for 1 h prior to modifying the electrodes. After that, 20  $\mu\text{L}$  of the suspension was pipetted onto the GC surface in 5  $\mu\text{L}$  fractions to cover the surface of GC uniformly and was allowed to dry in an oven at 50 °C for 12 h. The electrode loading used was 400  $\mu\text{g cm}^{-2}$ .

**2.4. Theoretical Calculations.** Theoretical calculations were performed at the DFT level using Becke's three-parameter exchange potential and Lee–Yang–Parr correlation functional. All calculations were performed with full geometry optimization using 6-31+G(d) basis set or 6-311G(d) basis set for frequency calculations, utilizing Gaussian09 program suite<sup>36</sup> and visualized with ChemCraft program.<sup>37</sup> Because the process under investigation occurs in oxidative conditions,

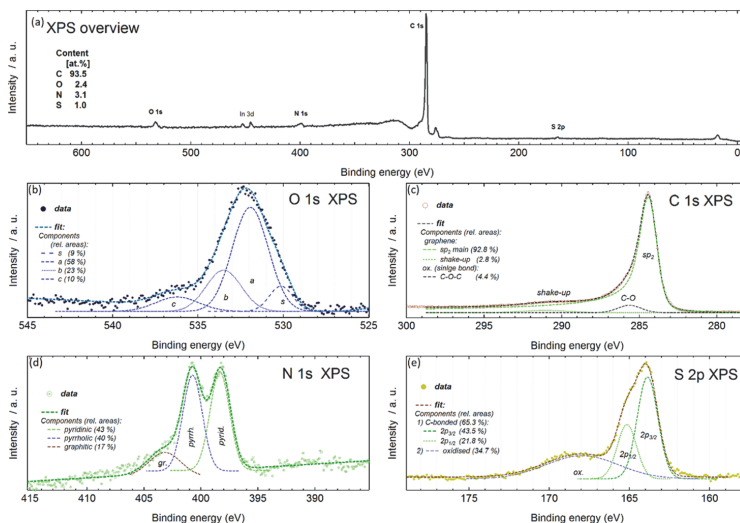


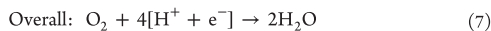
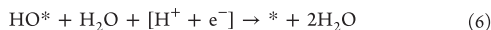
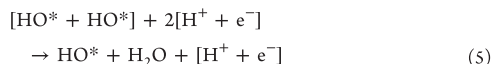
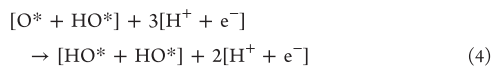
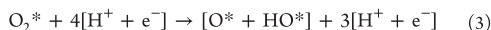
**Figure 1.** (a) Overview XPS spectrum of 1:5 C/O/MUS; high-resolution spectra of (b) O 1s, (c) C 1s, (d) N 1s, and (e) S 2p.

various oxidized forms were computed and the most energetically favorable one (pyridine N-oxide) was used in further calculations. The next step was to calculate the N,S,O-doped graphene with O<sub>2</sub> in different positions, and again, the most energetically favorable form was chosen.

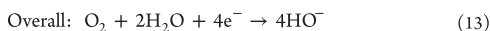
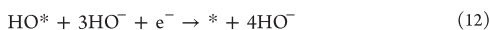
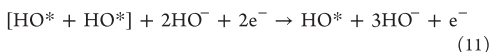
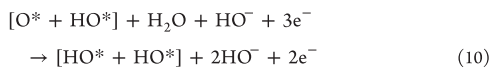
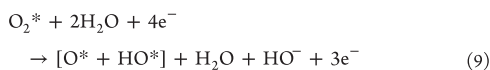
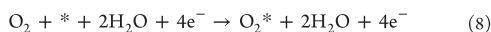
To study the stability of the various O<sub>2</sub> adsorbates along with O<sub>2</sub> protonated species involved in the ORR on the N,S-doped GO, the adsorption energy ( $E_{\text{ads}}$ ) was evaluated as follows

$$E_{\text{ads}} = E_{\text{adsorbate/GrO-NS}} - E_{\text{adsorbate}} - E_{\text{GrO-NS}} \quad (1)$$

where  $E_{\text{adsorbate/GrO-NS}}$ ,  $E_{\text{adsorbate}}$  and  $E_{\text{GrO-NS}}$  are gas-phase total energies of the adsorbate together with GrO-NS, the isolated adsorbate, and GrO-NS, respectively. A negative value of  $E_{\text{ads}}$  indicates the exothermic adsorption process. The four-electron ORR mechanisms were investigated on the GrO-NS in the present study. In the acidic medium, each ORR step is defined as follows ( $*$  = GrO-NS)<sup>38</sup>



In the alkaline medium, each ORR step is defined as follows



Finally, the energy diagrams of ORR were estimated in accordance with the method proposed by Nørskov et al.<sup>39</sup> using eq 14

$$\Delta G = \Delta E + \Delta \text{ZPE} - T\Delta S + \Delta G_{\text{U}} + \Delta G_{\text{pH}} \quad (14)$$

where  $\Delta E$  is the energy difference between the products and the reactants (eqs 2–13),  $\Delta \text{ZPE}$  and  $\Delta S$  are the zero-point correction to the total energy and correction to the entropy, respectively,  $T$  is the temperature (298.15 K);  $\Delta G_{\text{U}} = -neU$ , where  $n$ ,  $e$ , and  $U$  denote the number of electrons in the reaction, the electron charge, and electrode overpotential with respect to the standard hydrogen electrode, respectively; and  $\Delta G_{\text{pH}} = k_{\text{B}}T \ln 10 \times \text{pH}$ , where  $k_{\text{B}}$  is the Boltzmann constant. In the present study,  $\text{pH} = 0$  ( $\Delta G_{\text{pH}} = 0$ ) and  $\text{pH} = 13$  ( $\Delta G_{\text{pH}} = 0.77$  eV) were assumed for acidic medium and alkaline medium, respectively. The free energy of H<sub>2</sub>O in bulk water was calculated in the gas phase under a pressure of 0.035 bar (the equilibrium vapor pressure of H<sub>2</sub>O at 298.15 K). The total and free energy of  $[\text{H}^+ + \text{e}^-]$  in the solution, according to a computational hydrogen electrode model, was estimated as the energy of 1/2H<sub>2</sub> under standard conditions. The free energy of HO<sup>-</sup> was obtained from the reaction in equilibrium in the water solution,  $\text{H}^+ + \text{HO}^- = \text{H}_2\text{O}$ . The entropies of the molecules in the gas phase were taken from the NIST

database.<sup>40</sup> The ZPE corrections of all species excluding GrO-NS were obtained from vibrational frequencies.

Note that we omit here the consideration of graphene S-oxidized forms in view of a rather low oxygen content (2.4 at. %, see Section 3.1) because this issue deserves special analysis and will be the subject of a separate study.

### 3. RESULTS AND DISCUSSION

**3.1. Physical Characterization of the N- and S-Codoped MWCNT/rGO Composite.** The surface chemical composition was studied using XPS. Fitting was performed using the SPANCF curve-fitting macropackage as presented in previous studies.<sup>41,42</sup> Figure 1a displays an overview spectrum; close-up views of the O 1s, N 1s, C 1s, and S 2p regions are shown in Figure 1b–e. The overview spectrum (Figure 1a) shows a dominating carbon content (93.5 at. %), as well as small quantities of oxygen (2.4 at. %), nitrogen (3.1 at. %), and sulfur (1.0 at. %), also a trace signal from the indium metal substrate. This confirms that N and S have been successfully incorporated into the carbon framework and oMUS can be used as a precursor for N and S codoping. The O 1s spectra (Figure 1b) have a broad [full width at half-maximum (fwhm)  $\sim 3.5$  eV] peak with a maximum at 531.9 eV, which suggests dominant C–O single bonds. The asymmetry of the high binding energy flank decreasing more slowly might accommodate a minor contribution of doubly bound carbon, although the asymmetry in the O 1s XPS might have several origins (proximity to a carboxyl radical, as an example).<sup>43</sup> The C 1s spectra (Figure 1c) have a dominant peak with the maximum at 284.3 eV (fwhm approximately 1.4 eV) and an asymmetric shape, characteristic of  $sp^2$ -bonded carbon, viz., in (nonoxidized) graphene. Therefore, to avoid overestimating contributions from any oxidized components, the C 1s spectrum was primarily fitted with an asymmetric Doniach–Sunjic line profile suitable for core XPS peaks of samples of metallic character. Second, two minor contributions were introduced, which relate to the shake-up (i.e., kinetic energy loss) feature related to the graphene itself and is a broad feature centered approximately 6 eV above the main graphene C 1s peak on the binding energy scale and, more significantly, a minor contribution (at the level of 4–5% of the total C 1s intensity), which can relate to carbon single bonded to oxygen. The N 1s spectra (Figure 1d) show two well-separated peaks at 398.3 eV and at 400.7 eV, which correspond to pyridinic N and pyrrolic N, respectively, and have very similar spectral weight (of the N 1s spectral area, the peak areas indicate 43% pyridinic and 40% pyrrolic nitrogen positions). The remaining broader spectral feature with its maximum toward higher binding energy with a maximum at approximately 403.2 eV indicates 17% graphitic nitrogen content. All three configurations of nitrogen (pyridinic N, pyrrolic N, and graphitic N) are recognized as active species for the ORR.<sup>44</sup> The S 2p spectra (Figure 1e) with the leading  $2p_{3/2}$  peak at 163.9 eV correspond to C–S–C bonds, and a more diffuse broader feature at higher binding energies centered just below 168 eV binding energy, which corresponds to sulfur oxides, which occur at the edges of the carbon network.<sup>45</sup>

TEM images show that the samples consist of typical multilayer CNTs and graphene/GO layers (Figure 2a). High-resolution TEM images from areas in Figure 2a and typical hexagonal FFT images originating from two-layer GO are shown in Figure 2b. All over the sample, one layer or

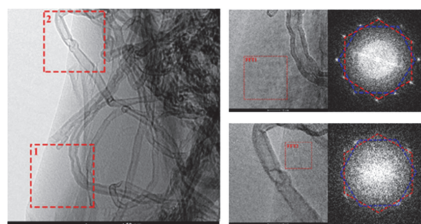


Figure 2. TEM image of the 1:5 C/oMUS catalyst material.

multilayer GO agglomerations together with CNT were observed.

Figure 3 shows the elemental mapping in the 1:5 C/oMUS observed by STEM–EDS. Nitrogen can be clearly found with

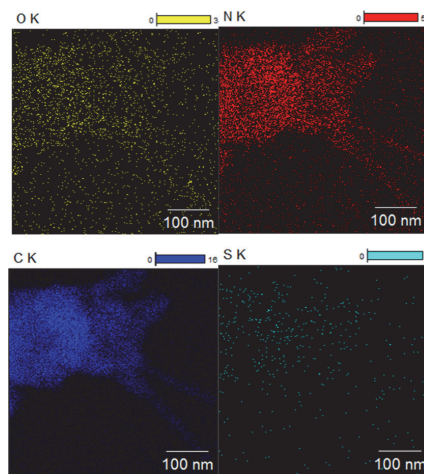


Figure 3. Elemental mapping images of oxygen, nitrogen, carbon, and sulfur in the 1:5 C/oMUS catalyst material.

the same distribution as the carbon, which means the nitrogen was successfully doped into the carbon. The existence of sulfur was also confirmed, but the distribution of which was not such clear because of its content was lower than that of the nitrogen. The high-resolution elemental mapping results are consistent with the XPS, and it can provide the microdistribution of the doping elements, which is helpful to understand the mechanism of the high catalyst efficiency.

**3.2. ORR Studies in 0.1 M KOH.** The ORR was studied on C/oMUS-modified GC electrodes in 0.1 M KOH solution at room temperature using the RDE setup. At first, the ratio of C and oMUS was varied. The results in 0.1 M KOH at a rotating speed of 1900 rpm are shown in Figure 4. The best ratio was 1:5. The differences between ratios of 1:5 and 1:2.5 are not significant but increasing the precursor dose has an influence on ORR onset and half-wave potential. However, one can also see from Figure 4 that the overdosing of the doping precursor has a strong effect on the electrocatalytic activity. Both the onset and half-wave potential of the 1:7.5 C/oMUS are shifted to much more negative potentials, and the performance of the electrocatalyst drops drastically. This phenomenon could be caused by the minor and hardly

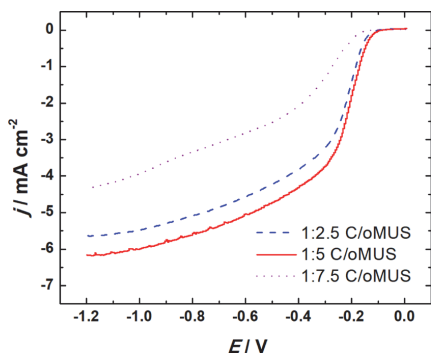


Figure 4. RDE voltammetry curves for ORR on modified GC electrodes in  $O_2$ -saturated 0.1 M KOH.  $\nu = 10 \text{ mV s}^{-1}$ ,  $\omega = 1900 \text{ rpm}$ .

recognizable change in the catalyst structure and porosity which is reportedly related to the change of the doping agent concentration.<sup>46</sup> Apparently, the change in the doping agent to carbon ratio can also hamper the electrocatalytic activity of graphene type materials by unwanted change in the graphene lattice structure which in turn will result in reduced number of edge defects and active sites.<sup>47</sup> A higher doping agent to carbon ratio creates more defects to the  $sp^2$ -carbon network and thereby reduces electrical conductivity of the carbon network.<sup>48</sup>

To evaluate the effect of pyrolysis temperature, the 1:5 C/oMUS was also pyrolyzed at different temperatures, as it can be seen from Figure 5. The best electrochemical activity was

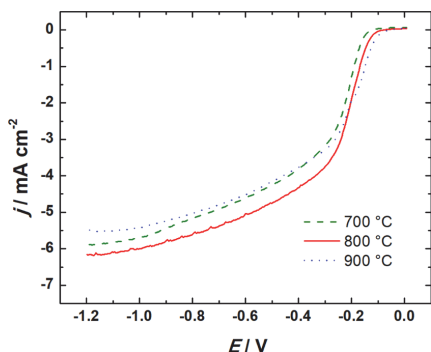


Figure 5. RDE voltammetry curves for ORR on modified GC electrodes pyrolyzed at different temperatures in  $O_2$ -saturated 0.1 M KOH.  $\nu = 10 \text{ mV s}^{-1}$ ,  $\omega = 1900 \text{ rpm}$ .

achieved when the pyrolysis was carried out at 800 °C. For the catalyst heat treated at 900 °C, the onset and half-wave potentials are even a bit better, but the limiting current values decrease notably at more negative potentials. This could be attributed to carbon reconstruction to heal the defects and damaging of topological defect active sites which can occur at 900 °C and above.<sup>49</sup> Previous studies have shown that the low pyrolysis temperature can result in lower limiting current densities as well poor conductivity of the material, whereas if the heating temperature is too high, then the amount of structural defects can be few and limiting current densities of

the catalyst can again be suppressed.<sup>50,51</sup> Therefore, we can assume that the pyrolysis of carbon in the presence of oMUS at 800 °C can provide right amount of defects and exposed edges for the ORR, which however is rather speculative as an exact reason for the catalytic change and the chemical nature and the amount of active sites for the ORR on this type of catalysts are still under debate. It is also proposed that heteroatom doping of carbon materials below 800 °C can result from the lower carbonization degree of the catalyst, whereas higher temperatures may result from the higher decomposition degree of the heteroatom species leading to lower electrocatalytic activity.<sup>52,53</sup> It is worth noting that pyrolysis at different temperatures can also tailor the contents of the different N configurations (graphitic N, pyridinic N, and pyrrolic N) in C/oMUS catalysts. Specially, the pyridinic N content, which is confirmed to be one of the key factors, to be related to the activity of the ORR.<sup>54</sup>

The ORR results for the 1:5 C/oMUS catalyst material are shown in Figure 6a. The onset potential for this material is  $-0.08 \text{ V}$ , and the catalytic current is increasing with increasing rotation speed, indicating that the process is under diffusion control. The Koutecky–Levich (K–L) plots were also constructed (Figure 6b) using the  $O_2$  reduction reaction polarization data shown in Figure 6a. This was done using the K–L equation<sup>55</sup>

$$\frac{1}{j} = \frac{1}{j_k} + \frac{1}{j_d} = -\frac{1}{nFkc_{O_2}^b} - \frac{1}{0.62nFD_{O_2}^{2/3}\nu^{-1/6}c_{O_2}^b\omega^{1/2}} \quad (15)$$

where  $j$  is the current density measured experimentally,  $j_k$  and  $j_d$  are the kinetic and diffusion limited current densities, respectively,  $k$  is the electrochemical rate constant for  $O_2$  reduction,  $c_{O_2}^b$  is the concentration of oxygen in the bulk ( $1.2 \times 10^{-6} \text{ mol cm}^{-3}$ ),<sup>56</sup>  $F$  is the Faraday constant ( $96485 \text{ C mol}^{-1}$ ),  $D_{O_2}$  is the diffusion coefficient of  $O_2$  in 0.1 M KOH ( $1.9 \times 10^{-5} \text{ cm}^2 \text{ s}^{-1}$ ),<sup>56</sup>  $\nu$  is the kinematic viscosity of the solution ( $0.01 \text{ cm}^2 \text{ s}^{-1}$ ), and  $\omega$  is the rotation rate of the electrode ( $\text{rad s}^{-1}$ ).<sup>57</sup> The K–L plots are linear, and extrapolating them to y-axis, the intercept is near zero, indicating that in the studied potential range, the reduction process is diffusion limited. The number of electrons transferred per  $O_2$  molecules ( $n$ ) was also calculated. At higher negative potentials, the number of electrons transferred per  $O_2$  molecule is 4; at more positive potential, it drops a bit. The limiting current density for 1900 rpm was  $-6.16 \text{ mA cm}^{-2}$  (Figure 6a). This is very similar to the expected value obtained from the K–L eq 15 which was  $-6.21 \text{ mA cm}^{-2}$ .

The enhanced ORR performance was achieved because of N- and S-codoping. As the difference of electronegativity between carbon (2.55) and nitrogen (3.04) is quite large, this created favorable sites for  $O_2$  surface adsorption.<sup>20</sup> The bonding of oxygen is weakened, and a four-electron reduction process is happening at the electrode. As the electronegativity between carbon (2.55) and sulfur (2.58) is quite similar, it could mean that doping with S has no effect on the ORR. However, two lone pairs of electrons on sulfur can have effect on the interaction with  $O_2$ , it can easily donate electron, and as a result, four-electron reduction may happen. Sulfur due to its large atomic radius (110 ppm) can also cause defects in the carbon structure, which creates a charge difference what facilitates the  $O_2$  chemisorption.<sup>58,59</sup>

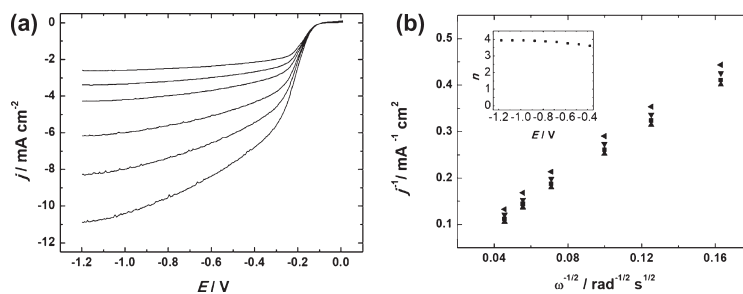


**Figure 6.** (a) RDE polarization curves for oxygen reduction on GC electrodes modified with 1:5 C/oMUS in  $O_2$  saturated 0.1 M KOH.  $\nu = 10 \text{ mV s}^{-1}$ ,  $\omega =$  (1) 360, (2) 610, (3) 960, (4) 1900, (5) 3100, and (6) 4600 rpm; (b) K–L plots for oxygen reduction on the 1:5 C/oMUS electrode in 0.1 M KOH at various potentials. The inset figure shows the changes of  $n$  values in studied potential range.

Although there are reports that the introduction of N doping can effectively improve the ORR catalytic activity of carbon, the identity and role of the electrocatalytically active center are still controversial as its contribution to catalytic activity is not well defined. Pyridinic N modifies the band structure of carbon, raising the density of p states near the Fermi level and lowering the work function. However, pyridinic N alone is not an effective promoter for ORR activity of carbon, as evidenced by the sluggish ORR activity beforehand. At the same time, the relative electronegativity of graphitic N reduces the electron density on the adjacent C nuclei, which helps electron transfer from the adjacent C to N atoms, and N back donates electrons to adjacent C p orbitals.<sup>60,61</sup> Figure 7 compares the RDE

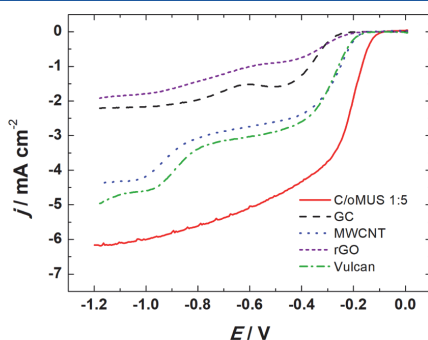


**Figure 7.** RDE voltammetry curves for ORR on unmodified GC, MWCNTs, rGO, Vulcan carbon, and C/oMUS 1:5 modified GC electrodes in  $O_2$ -saturated 0.1 M KOH.  $\nu = 10 \text{ mV s}^{-1}$ ,  $\omega = 1900 \text{ rpm}$ .

results for the NS-doped nanocarbon material along with GC, undoped MWCNTs, rGO, and Vulcan carbon to better express the activity trends of the NS-doping. The ORR onset potential for C/oMUS is about 80 mV higher than that of the MWCNTs and close to 150 mV higher than that for the GC. Rather low limiting current densities of the rGO are most probably caused by the restacking and ionomer related effects. One can also see that C/oMUS has lost the two-wave polarization curve structure typical to the carbon catalysts in alkaline media. Thereby, it is evident that the ORR reaction pathway and mechanism have changed because of NS-doping of the carbon.

For the easy comparison of C/oMUS 1:5 with other similar heteroatom-doped catalysts, the mass activity was also

calculated. The most often used potential for determining the mass activity of a catalyst is  $-0.2 \text{ V}$ . The mass activity of 1:5 C/oMUS at  $-0.2 \text{ V}$  is  $4.89 \text{ A g}^{-1}$ . This is noticeably better than other doped carbon materials, for example, the ones investigated by Pašti et al. which had mass activities from 0.5 to  $3.5 \text{ A g}^{-1}$ .<sup>62</sup>

As the durability and methanol tolerance of the catalyst material are some of the key parameters of an electrocatalyst, chronoamperometry was conducted with the most active electrocatalyst. The measurement was carried out for 20 h in  $O_2$ -saturated 0.1 M KOH. The constant voltage was set at 0.45 V versus SCE by using the stationary electrode. At first, the current density drops, but then it stabilizes. The catalyst material is relatively stable during the whole experiment. To verify the methanol tolerance of the catalyst material, the 3 M MeOH was also added to the solution while carrying out the chronoamperometry measurements. The 3 M MeOH was added at exactly 10 h and as it can be seen from Figure 8, there

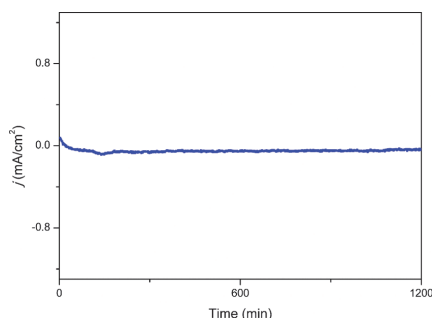


**Figure 8.** Chronoamperometric response of 1:5 C/oMUS at  $-0.45 \text{ V}$  (vs SCE) in  $O_2$ -saturated 0.1 M KOH.

is no noticeable drop of the current density. Zhang et al. have also conducted chronoamperometry measurements on nitrogen-doped rGO, where  $\text{Co}_3\text{O}_4$  nanoparticles were also anchored on the heteroatom-doped carbon material.<sup>63</sup> However, their results showed that the addition of 3 M methanol had clear effect to the ORR activity as the current density dropped and did not reach the initial state till the end of the experiment.

**3.3. DFT Calculations.** For DFT calculations, a graphene sheet of  $\text{C}_{54}\text{H}_{18}$  **1a** was chosen and doped with nitrogen and

sulfur atoms to give structure **1b** which correlates in composition with the XPS data (Figure 9). Because the

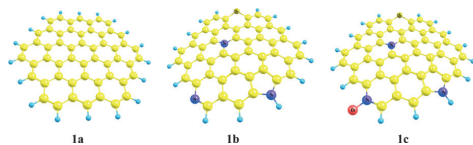


**Figure 9.** Nondoped  $C_{54}H_{18}$  (**1a**), N,S-doped  $C_{49}H_{15}N_3S$  (**1b**), and oxidized N,S-doped  $C_{49}H_{15}N_3SO$  (**1c**) graphene sheets.

catalyst used in the experiment was partially oxidized (rGO), we have tested various C-oxidized isomers of the epoxide and pyridine N-oxide structures. The pyridine N-oxide form of the rGO-N,S **1c** corresponds to the global minimum, with the energy of formation of  $\sim 0.87$  eV. Therefore, structure **1c** was chosen for ORR simulation.

On the next step, we tested structure **1c** to find the most favorable active site for adsorption of oxygen using as a criterion the Mulliken positive charges on the carbon atoms. Structure **2a** in Figure 10, in which the  $O_2$  molecule is adsorbed over the  $C_\alpha-C_\beta$  bond at the graphitic nitrogen atom, is most energetically favorable ( $E_{\text{ads}} = -1.14$  eV) and corresponds to the global minimum among other local minima. The O–O distance in structure **2a** increases by 0.263 Å with respect to that in free  $O_2$  molecule and equals to 1.478 Å.

Protonation of the O–O moiety in  $O_2^*$  **2a** by  $[H^+ + e^-]$  occurs with rupture of the O–O bond with the formation of the adduct  $[O^* HO^*]$  (**3**), thus excluding the two-electron ORR pathway. The O–O bond breaking was also found to occur when the cationic or anionic form of **3** was protonated. Adduct **3** is characterized by  $E_{\text{ads}} = -1.41$  eV, which is 0.27 eV

lower than that of  $O_2^*$  (**2a**). Further protonation of **3** with  $[H^+ + e^-]$  in direction to  $O^*$  or  $HO^*$  results in the formation of diol  $[HO^* HO^*]$  **4** with a small exothermic effect,  $E_{\text{ads}} = -0.01$  eV with respect to **3**. Third, the  $[H^+ + e^-]$  transfer to **4** produces the molecule of water and adduct  $HO^*$ , **5**, which is the most stable species in the series **2–5** ( $E_{\text{ads}} = -1.51$  eV).

According to eqs 2–14, the free-energy diagrams were drawn for reduction of  $O_2$  on rGO-N,S **1c** at different electrode overpotentials  $U$  in acidic and alkaline media (Figure 11). As follows from the diagram, in both media, the adsorption of oxygen on the surface of the catalyst expectedly gives rise to the increase of the free energy by 0.81 eV because of the entropy losses upon adsorption. The development of the ORR in the acidic medium gradually decreases the free energy down to  $U = 0.85$  V, when the free energies of the intermediates  $3[H^+ + e^-] + O^* + HO^*$  and  $2[H^+ + e^-] + 2HO^*$  become equal. Further increase of overpotential to  $U = 1.23$  V (corresponding to the equilibrium in the system  $2H_2 + O_2 \rightleftharpoons 2H_2O$ ) results in that all intermediates lie in the diagram above the initial or final level of the system, so that all oxygen species are ablated from the surface of the catalyst. If to exclude from consideration the step of molecular oxygen adsorption on the active site of the catalyst, the rate-determining step in the acidic medium for overpotentials  $U > 0.85$  V is the second protonation step leading to the formation of diol  $2HO^*$ .

In the alkaline medium, at small negative overpotentials, the reduction of  $O_2^*$  ORR proceeds in a barrierless fashion with monotonous free-energy decrease. At overpotential  $U = 0.0$  V, the free energy of intermediate  $HO^*$  is lower than that of the product of the reaction ( $-0.04$  eV) and, hence, the final step of ORR will be rate-determining. This trend is retained for positive overpotentials in alkaline media, up to the equilibrium overpotential ( $0 \text{ V} < U < 0.46 \text{ V}$ ). However, when overpotential leading to equilibrium in the system ( $U = 0.46$

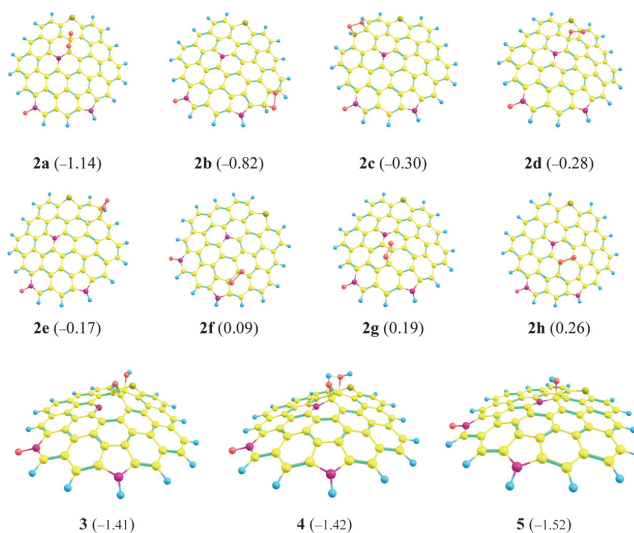


**Figure 10.** Structures of  $O_2^*$  (**2a–h**), reduced forms  $[O^* HO^*]$  (**3**),  $[HO^* HO^*]$  (**4**), and  $HO^*$  (**5**) adsorbed on rGO-N,S (**1c**, Figure 9). In brackets:  $E_{\text{ads}}$  (eV) with respect to nonreacting molecules:  $O_2$ ,  $OOH$ ,  $H_2O_2$ , and  $OH$ . Yellow—carbon, blue—hydrogen, red—oxygen, magenta—nitrogen, and olive—sulfur.

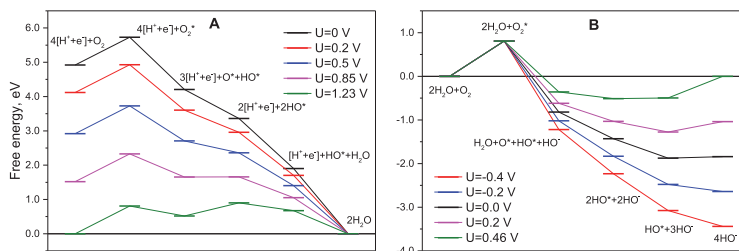


**Figure 11.** Free-energy diagrams for the reduction of  $\text{O}_2$  on rGO-NS 1c at different electrode overpotentials  $U$  in acidic (A) and alkaline (B) media.

V) is applied, the most favorable structure is the one corresponding to intermediate  $2\text{HO}^*$ , whose free energy is equal to  $(-0.51 \text{ eV})$ .

However, in a real system, the free-energy increase in the step of adsorption must be much smaller, or the free energy may even decrease. The point is that oxygen is supplied to the cathode either in the dissolved form or through porous membranes, in other words, in the form in which it already interacts with other species. This, in turn, means that the entropy losses will be much smaller than those calculated for adsorption of pure gaseous molecular oxygen on the catalyst and may be even outweighed by the energy gain because of adsorption.

#### 4. CONCLUSIONS

A novel and effective approach has been used to prepare the nitrogen- and sulfur-codoped carbon catalyst for the ORR. The NS-doped carbon catalyst was synthesized by using the heat treatment of the mixture of GO and multi-walled CNTs together with  $\alpha\text{MUS}$ . This NS-codoped catalyst provides a valuable template to explore the heteroatom codoping effects toward ORR. As it is almost impossible to detect the exact catalytic site and the reaction mechanism for the ORR on the NS-codoped carbon catalyst by using only electrochemical and physical characterization methods, then DFT calculations were carried out. DFT simulations on graphene doped with nitrogen and sulfur atoms were chosen according to the XPS data and ORR test results. It was found that the  $C_\alpha$  and  $C_\beta$  carbon atoms at the graphitic nitrogen located close to the sulfur atom, correspond to the global minimum, and are thereby energetically most favorable  $(-1.14 \text{ eV})$  for the oxygen electroreduction. It is also clear from the current results that the NS-codoped catalysts are interesting candidates for various practical applications such as metal–air batteries and fuel cells and thereby the reaction mechanisms of these catalysts are worth of further study.

#### AUTHOR INFORMATION

##### Corresponding Author

\*E-mail: [ivar.kruusenberg@kbfi.ee](mailto:ivar.kruusenberg@kbfi.ee). Phone: +372-5036963.

##### ORCID

Andris Šutka: 0000-0002-5739-0164

Bagrat A. Shainyan: 0000-0002-4296-7899

Ivar Kruusenberg: 0000-0002-8199-9324

##### Notes

The authors declare no competing financial interest.

#### ACKNOWLEDGMENTS

This research was financially supported by ERA.Net RUS Plus funding mechanism (Project HeDoCat) and by the European Regional Development Fund project TK134.

#### REFERENCES

- (1) Sealy, C. The Problem with Platinum. *Mater. Today* **2008**, *11*, 65–68.
- (2) Ferreira, P. J.; la O', G. J.; Shao-Horn, Y.; Morgan, D.; Makharia, R.; Kocha, S.; Gasteiger, H. A. Instability of Pt/C Electrocatalysts in Proton Exchange Membrane Fuel Cells. *J. Electrochem. Soc.* **2005**, *152*, A2256.
- (3) Ratso, S.; Kruusenberg, I.; Joost, U.; Saar, R.; Tammeveski, K. Enhanced Oxygen Reduction Reaction Activity of Nitrogen-Doped Graphene/Multi-Walled Carbon Nanotube Catalysts in Alkaline Media. *Int. J. Hydrogen Energy* **2016**, *41*, 22510–22519.
- (4) Ratso, S.; Kruusenberg, I.; Vikkisk, M.; Joost, U.; Shulga, E.; Kink, I.; Kallio, T.; Tammeveski, K. Highly Active Nitrogen-Doped Few-Layer Graphene/Carbon Nanotube Composite Electrocatalyst for Oxygen Reduction Reaction in Alkaline Media. *Carbon* **2014**, *73*, 361–370.
- (5) Vikkisk, M.; Kruusenberg, I.; Ratso, S.; Joost, U.; Shulga, E.; Kink, I.; Rauwel, P.; Tammeveski, K. Enhanced Electrocatalytic Activity of Nitrogen-Doped Multi-Walled Carbon Nanotubes towards the Oxygen Reduction Reaction in Alkaline Media. *RSC Adv.* **2015**, *5*, 59495–59505.
- (6) Inamdar, S.; Choi, H.-S.; Wang, P.; Song, M. Y.; Yu, J.-S. Sulfur-Containing Carbon by Flame Synthesis as Efficient Metal-Free Electrocatalyst for Oxygen Reduction Reaction. *Electrochem. Commun.* **2013**, *30*, 9–12.
- (7) Klingele, M.; Pham, C.; Vuyuru, K. R.; Britton, B.; Holdcroft, S.; Fischer, A.; Thiele, S. Sulfur Doped Reduced Graphene Oxide as Metal-Free Catalyst for the Oxygen Reduction Reaction in Anion and Proton Exchange Fuel Cells. *Electrochem. Commun.* **2017**, *77*, 71–75.
- (8) Choi, C. H.; Chung, M. W.; Park, S. H.; Woo, S. I. Additional Doping of Phosphorus and/or Sulfur into Nitrogen-Doped Carbon for Efficient Oxygen Reduction Reaction in Acidic Media. *Phys. Chem. Chem. Phys.* **2013**, *15*, 1802–1805.
- (9) Biddinger, E. J.; von Deak, D.; Ozkan, U. S. Nitrogen-Containing Carbon Nanostructures as Oxygen-Reduction Catalysts. *Top. Catal.* **2009**, *52*, 1566–1574.
- (10) Chen, P.; Wang, L.-K.; Wang, G.; Gao, M.-R.; Ge, J.; Yuan, W.-J.; Shen, Y.-H.; Xie, A.-J.; Yu, S.-H. Nitrogen-Doped Nanoporous Carbon Nanosheets Derived from Plant Biomass: An Efficient Catalyst for Oxygen Reduction Reaction. *Energy Environ. Sci.* **2014**, *7*, 4095–4103.
- (11) Guo, Q.; Zhao, D.; Liu, S.; Chen, S.; Hanif, M.; Hou, H. Free-Standing Nitrogen-Doped Carbon Nanotubes at Electrospun Carbon Nanofibers Composite as an Efficient Electrocatalyst for Oxygen Reduction. *Electrochim. Acta* **2014**, *138*, 318–324.
- (12) Wong, W. Y.; Daud, W. R. W.; Mohamad, A. B.; Kadhum, A. A. H.; Majlan, E. H.; Loh, K. S. Nitrogen-Containing Carbon Nanotubes

as Cathodic Catalysts for Proton Exchange Membrane Fuel Cells. *Diam. Relat. Mater.* **2012**, *22*, 12–22.

(13) Sheng, Z.-H.; Gao, H.-L.; Bao, W.-J.; Wang, F.-B.; Xia, X.-H. Synthesis of Boron Doped Graphene for Oxygen Reduction Reaction in Fuel Cells. *J. Mater. Chem.* **2012**, *22*, 390–395.

(14) Wang, L.; Dong, H.; Guo, Z.; Zhang, L.; Hou, T.; Li, Y. Potential Application of Novel Boron-Doped Graphene Nanoribbon as Oxygen Reduction Reaction Catalyst. *J. Phys. Chem. C* **2016**, *120*, 17427–17434.

(15) Yang, L.; Jiang, S.; Zhao, Y.; Zhu, L.; Chen, S.; Wang, X.; Wu, Q.; Ma, J.; Ma, Y.; Hu, Z. Boron-Doped Carbon Nanotubes as Metal-Free Electrocatalysts for the Oxygen Reduction Reaction. *Angew. Chem. Int. Ed.* **2011**, *50*, 7132–7135.

(16) Han, C.; Bo, X.; Zhang, Y.; Li, M.; Guo, L. One-Pot Synthesis of Nitrogen and Sulfur Co-Doped Onion-like Mesoporous Carbon Vesicle as an Efficient Metal-Free Catalyst for Oxygen Reduction Reaction in Alkaline Solution. *J. Power Sources* **2014**, *272*, 267–276.

(17) Higgins, D. C.; Hoque, M. A.; Hassan, F.; Choi, J.-Y.; Kim, B.; Chen, Z. Oxygen Reduction on Graphene-Carbon Nanotube Composites Doped Sequentially with Nitrogen and Sulfur. *ACS Catal.* **2014**, *4*, 2734–2740.

(18) Zhang, H.; Liu, X.; He, G.; Zhang, X.; Bao, S.; Hu, W. Bioinspired Synthesis of Nitrogen/Sulfur Co-Doped Graphene as an Efficient Electrocatalyst for Oxygen Reduction Reaction. *J. Power Sources* **2015**, *279*, 252–258.

(19) Qiu, Y.; Huo, J.; Jia, F.; Shanks, B. H.; Li, W. N- and S-Doped Mesoporous Carbon as Metal-Free Cathode Catalysts for Direct Biorenewable Alcohol Fuel Cells. *J. Mater. Chem. A* **2016**, *4*, 83–95.

(20) Zhang, J.; Dai, L. Heteroatom-Doped Graphitic Carbon Catalysts for Efficient Electrocatalysis of Oxygen Reduction Reaction. *ACS Catal.* **2015**, *5*, 7244–7253.

(21) Hua, Y.; Jiang, T.; Wang, K.; Wu, M.; Song, S.; Wang, Y.; Tsiakaras, P. Efficient Pt-Free Electrocatalyst for Oxygen Reduction Reaction: Highly Ordered Mesoporous N and S Co-Doped Carbon with Saccharin as Single-Source Molecular Precursor. *Appl. Catal., B* **2016**, *194*, 202–208.

(22) Li, L.; Yu, B.; You, T. Nitrogen and Sulfur Co-Doped Carbon Dots for Highly Selective and Sensitive Detection of Hg (II) Ions. *Biosens. Bioelectron.* **2015**, *74*, 263–269.

(23) Liu, T.; Guo, Y.-F.; Yan, Y.-M.; Wang, F.; Deng, C.; Rooney, D.; Sun, K.-N. CoO Nanoparticles Embedded in Three-Dimensional Nitrogen/Sulfur Co-Doped Carbon Nanofiber Networks as a Bifunctional Catalyst for Oxygen Reduction/Evolution Reactions. *Carbon* **2016**, *106*, 84–92.

(24) Wu, M.; Wang, J.; Wu, Z.; Xin, H. L.; Wang, D. Synergistic Enhancement of Nitrogen and Sulfur Co-Doped Graphene with Carbon Nanosphere Insertion for the Electrocatalytic Oxygen Reduction Reaction. *J. Mater. Chem. A* **2015**, *3*, 7727–7731.

(25) Liang, J.; Jiao, Y.; Jaroniec, M.; Qiao, S. Z. Sulfur and Nitrogen Dual-Doped Mesoporous Graphene Electrocatalyst for Oxygen Reduction with Synergistically Enhanced Performance. *Angew. Chem. Int. Ed.* **2012**, *51*, 11496–11500.

(26) Wang, Y.; Wu, Y.; Huang, Y.; Zhang, F.; Yang, X.; Ma, Y.; Chen, Y. Preventing Graphene Sheets from Restacking for High-Capacitance Performance. *J. Phys. Chem. C* **2011**, *115*, 23192–23197.

(27) Wang, X.; Zhi, L.; Müllen, K. Transparent, Conductive Graphene Electrodes for Dye-Sensitized Solar Cells. *Nano Lett.* **2008**, *8*, 323–327.

(28) Yan, J.; Wei, T.; Shao, B.; Ma, F.; Fan, Z.; Zhang, M.; Zheng, C.; Shang, Y.; Qian, W.; Wei, F. Electrochemical Properties of Graphene Nanosheet/Carbon Black Composites as Electrodes for Supercapacitors. *Carbon* **2010**, *48*, 1731–1737.

(29) Choi, C. H.; Chung, M. W.; Kwon, H. C.; Chung, J. H.; Woo, S. I. Nitrogen-Doped Graphene/Carbon Nanotube Self-Assembly for Efficient Oxygen Reduction Reaction in Acid Media. *Appl. Catal., B* **2014**, *144*, 760–766.

(30) Sun, Y.; Wu, J.; Tian, J.; Jin, C.; Yang, R. Sulfur-Doped Carbon Spheres as Efficient Metal-Free Electrocatalysts for Oxygen Reduction Reaction. *Electrochim. Acta* **2015**, *178*, 806–812.

(31) Yang, Z.; Yao, Z.; Li, G.; Fang, G.; Nie, H.; Liu, Z.; Zhou, X.; Chen, X. a.; Huang, S.; Chen, X.; et al. Sulfur-Doped Graphene as an Efficient Metal-Free Cathode Catalyst for Oxygen Reduction. *ACS Nano* **2012**, *6*, 205–211.

(32) Yang, S.; Zhi, L.; Tang, K.; Feng, X.; Maier, J.; Müllen, K. Efficient Synthesis of Heteroatom (N or S)-Doped Graphene Based on Ultrathin Graphene Oxide-Porous Silica Sheets for Oxygen Reduction Reactions. *Adv. Funct. Mater.* **2012**, *22*, 3634–3640.

(33) Jeon, I.-Y.; Zhang, S.; Zhang, L.; Choi, H.-J.; Seo, J.-M.; Xia, Z.; Dai, L.; Baek, J.-B. Edge-Selectively Sulfurized Graphene Nanoplatelets as Efficient Metal-Free Electrocatalysts for Oxygen Reduction Reaction: The Electron Spin Effect. *Adv. Mater.* **2013**, *25*, 6138–6145.

(34) Hummers, W. S.; Offeman, R. E. Preparation of Graphitic Oxide. *J. Am. Chem. Soc.* **1958**, *80*, 1339.

(35) Kruusenberg, I.; Marandi, M.; Sammelselg, V.; Tammeveski, K. Hydrodynamic Deposition of Carbon Nanotubes onto HOPG: The Reduction of Oxygen on CNT/HOPG Electrodes in Alkaline Solution. *Electrochem. Solid-State Lett.* **2009**, *12*, F31–F34.

(36) Frisch, M. J.; Trucks, W.; Schlegel, H. B.; Scuseria, G. E.; Robb, M. A.; Cheeseman, J. R.; Scalmani, G.; Barone, V.; Mennucci, B.; Petersson, G. A.; et al. *Gaussian 09*, Revision E. 01; Gaussian, Inc.: Wallingford, CT, 2009.

(37) Zhurko, G. A. *ChemCraft*.

(38) Wang, Y.; Jiao, M.; Song, W.; Wu, Z. Doped Fullerene as a Metal-Free Electrocatalyst for Oxygen Reduction Reaction: A First-Principles Study. *Carbon* **2017**, *114*, 393–401.

(39) Nørskov, J. K.; Rossmeisl, J.; Logadottir, A.; Lindqvist, L.; Kitchin, J. R.; Bligaard, T.; Jónsson, H. Origin of the Overpotential for Oxygen Reduction at a Fuel-Cell Cathode. *J. Phys. Chem. B* **2004**, *108*, 17886–17892.

(40) NIST. Chemistry WebBook (Accessed 4 April 2019).

(41) Kukkk, E.; Snell, G.; Bozek, J. D.; Cheng, W. T.; Berrah, N. Vibrational Structure and Partial Rates of Resonant Auger Decay of the [Formula Presented] Core Excitations in Nitric Oxide. *Phys. Rev. A: At., Mol., Opt. Phys.* **2001**, *63*, 062702.

(42) Kukkk, E.; Ueda, K.; Hergenbahn, U.; Liu, X. J.; Prümper, G.; Yoshida, H.; Tamenori, Y.; Makochekanwa, C.; Tanaka, T.; Kitajima, M.; et al. Violation of the Franck-Condon Principle Due to Recoil Effects in High Energy Molecular Core-Level Photoionization. *Phys. Rev. Lett.* **2005**, *95*, 133001.

(43) Weiss, T.; Zielasek, V.; Bäumer, M. Influence of Water on Chemical Vapor Deposition of Ni and Co Thin Films from Ethanol Solutions of Acetylacetonate Precursors. *Sci. Rep.* **2015**, *5*, 18194.

(44) Chen, J.; Zhang, H.; Liu, P.; Li, Y.; Li, G.; An, T.; Zhao, H. Thiourea Sole Doping Reagent Approach for Controllable N, S Co-Doping of Pre-Synthesized Large-Sized Carbon Nanospheres as Electrocatalyst for Oxygen Reduction Reaction. *Carbon* **2015**, *92*, 339–347.

(45) Su, Y.; Zhang, Y.; Zhuang, X.; Li, S.; Wu, D.; Zhang, F.; Feng, X. Low-Temperature Synthesis of Nitrogen/Sulfur Co-Doped Three-Dimensional Graphene Frameworks as Efficient Metal-Free Electrocatalyst for Oxygen Reduction Reaction. *Carbon* **2013**, *62*, 296–301.

(46) Wiggins-Camacho, J. D.; Stevenson, K. J. Effect of Nitrogen Concentration on Capacitance, Density of States, Electronic Conductivity, and Morphology of N-Doped Carbon Nanotube Electrodes. *J. Phys. Chem. C* **2009**, *113*, 19082–19090.

(47) Rahsepar, M.; Nobakht, M. R.; Kim, H.; Pakshir, M. Facile Enhancement of the Active Catalytic Sites of N-Doped Graphene as a High Performance Metal-Free Electrocatalyst for Oxygen Reduction Reaction. *Appl. Surf. Sci.* **2018**, *447*, 182–190.

(48) Wu, J.; Yang, Z.; Sun, Q.; Li, X.; Strasser, P.; Yang, R. Synthesis and Electrocatalytic Activity of Phosphorus-Doped Carbon Xerogel for Oxygen Reduction. *Electrochim. Acta* **2014**, *127*, 53–60.

(49) Chen, T.; Chen, J.; Waki, K. An Activity Recoverable Carbon Nanotube Based Electrocatalysts: Rapid Annealing Effects and Importance of Defects. *Carbon* **2018**, *129*, 119–127.

(50) Lu, X.; Li, Z.; Yin, X.; Wang, S.; Liu, Y.; Wang, Y. Controllable Synthesis of Three-Dimensional Nitrogen-Doped Graphene as a High

Performance Electrocatalyst for Oxygen Reduction Reaction. *Int. J. Hydrogen Energy* **2017**, *42*, 17504–17513.

(51) Bai, X.; Shi, Y.; Guo, J.; Gao, L.; Wang, K.; Du, Y.; Ma, T. Catalytic Activities Enhanced by Abundant Structural Defects and Balanced N Distribution of N-Doped Graphene in Oxygen Reduction Reaction. *J. Power Sources* **2016**, *306*, 85–91.

(52) Weththasinha, H. A. B. M. D.; Yan, Z.; Gao, L.; Li, Y.; Pan, D.; Zhang, M.; Lv, X.; Wei, W.; Xie, J. Nitrogen Doped Lotus Stem Carbon as Electrocatalyst Comparable to Pt/C for Oxygen Reduction Reaction in Alkaline Media. *Int. J. Hydrogen Energy* **2017**, *42*, 20560–20567.

(53) Liu, X.; Zhu, H.; Yang, X. One-Step Synthesis of Dopamine-Derived Micro/Mesoporous Nitrogen-Doped Carbon Materials for Highly Efficient Oxygen-Reduction Catalysts. *J. Power Sources* **2014**, *262*, 414–420.

(54) Miao, H.; Li, S.; Wang, Z.; Sun, S.; Kuang, M.; Liu, Z.; Yuan, J. Enhancing the Pyridinic N Content of Nitrogen-Doped Graphene and Improving Its Catalytic Activity for Oxygen Reduction Reaction. *Int. J. Hydrogen Energy* **2017**, *42*, 28298–28308.

(55) Bard, A. J.; Faulkner, L. R. *Electrochemical Methods: Fundamentals and Applications*, 2nd ed.; Wiley: New York, 2001.

(56) Davis, R. E.; Horvath, G. L.; Tobias, C. W. The Solubility and Diffusion Coefficient of Oxygen in Potassium Hydroxide Solutions. *Electrochim. Acta* **1967**, *12*, 287–297.

(57) Lide, D. R. *CRC Handbook of Chemistry and Physics*, 82nd ed.; CRC Press: Boca Ration, 2001.

(58) Wohlgemuth, S.-A.; White, R. J.; Willinger, M.-G.; Titirici, M.-M.; Antonietti, M. A One-Pot Hydrothermal Synthesis of Sulfur and Nitrogen Doped Carbon Aerogels with Enhanced Electrocatalytic Activity in the Oxygen Reduction Reaction. *Green Chem.* **2012**, *14*, 1515.

(59) Dai, J.; Yuan, J.; Giannozzi, P. Gas Adsorption on Graphene Doped with B, N, Al, and S: A Theoretical Study. *Appl. Phys. Lett.* **2009**, *95*, 232105.

(60) Geng, D.; Chen, Y.; Chen, Y.; Li, Y.; Li, R.; Sun, X.; Ye, S.; Knights, S. High Oxygen-Reduction Activity and Durability of Nitrogen-Doped Graphene. *Energy Environ. Sci.* **2011**, *4*, 760–764.

(61) Wang, L.; Yang, C.; Dou, S.; Wang, S.; Zhang, J.; Gao, X.; Ma, J.; Yu, Y. Nitrogen-Doped Hierarchically Porous Carbon Networks: Synthesis and Applications in Lithium-Ion Battery, Sodium-Ion Battery and Zinc-Air Battery. *Electrochim. Acta* **2016**, *219*, 592–603.

(62) Pašti, I. A.; Gavrilov, N. M.; Dobrota, A. S.; Momčilović, M.; Stojmenović, M.; Topalov, A.; Stanković, D. M.; Babić, B.; Cirić-Marjanović, G.; Mentus, S. V. The Effects of a Low-Level Boron, Phosphorus, and Nitrogen Doping on the Oxygen Reduction Activity of Ordered Mesoporous Carbons. *Electrocatalysis* **2015**, *6*, 498–511.

(63) Zhang, T.; He, C.; Sun, F.; Ding, Y.; Wang, M.; Peng, L.; Wang, J.; Lin, Y. Co<sub>3</sub>O<sub>4</sub> Nanoparticles Anchored on Nitrogen-Doped Reduced Graphene Oxide as a Multifunctional Catalyst for H<sub>2</sub>O<sub>2</sub> Reduction, Oxygen Reduction and Evolution Reaction. *Sci. Rep.* **2017**, *7*, 43638.

## Appendix 4

### Publication IV

**K. Kaare**, E. Yu, A. Volperts, G. Dobele, A. Zhurinsh, A. Dyck, G. Niaura, L. Tamasauskaite-Tamasiunaite, E. Norkus, M. Andrulevičius, M. Danilson, I. Kruusenberg, Highly Active Wood-Derived Nitrogen-Doped Carbon Catalyst for the Oxygen Reduction Reaction, *ACS Omega*. 5 (2020) 23578–23587.



# Highly Active Wood-Derived Nitrogen-Doped Carbon Catalyst for the Oxygen Reduction Reaction

Kätlin Kaare, Eric Yu, Aleksandrs Volperts, Galina Dobele, Aivars Zhurinsh, Alexander Dyck, Gediminas Niaura, Loreta Tamasauskaite-Tamasiunaite, Eugenijus Norkus, Mindaugas Andrulevičius, Mati Danilson, and Ivar Kruusenberg\*

Cite This: *ACS Omega* 2020, 5, 23578–23587

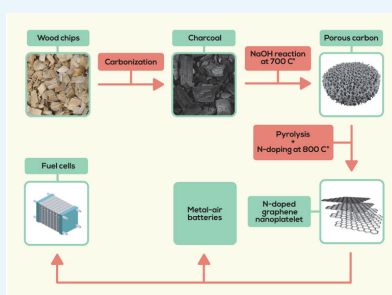
Read Online

ACCESS |

Metrics & More

Article Recommendations

**ABSTRACT:** In this recent decade, great interest has risen to develop metal-free and cheap, biomass-derived electrocatalysts for oxygen reduction reaction (ORR). Herein, we report a facile strategy to synthesize an electrochemically active nanocarbon material from the renewable and biological resource, wood biomass. The ORR activity of the catalyst material was investigated in 0.1 M KOH solution by employing the rotating disc electrode method. Scanning electron microscopy, transmission electron microscopy, X-ray photoelectron spectroscopy, and Raman spectroscopy were employed to obtain more information about the catalyst material's morphology and composition. The material exhibits outstanding electrocatalytic activity with low onset potential and high current density, similar to that of a commercial Pt/C catalyst in an alkaline medium. The results clearly ascertain that wooden biomass can be easily transformed into novel carbon nanostructures with superior ORR activity and possibility to be used in fuel cells and metal–air batteries.



## INTRODUCTION

The number of studies dedicated to renewable energy conversion and storage devices, such as batteries, fuel cells, and photovoltaic systems has gained utmost importance as pollution levels caused by large scale consumption of fossil fuels have continued to rise year by year.<sup>1</sup> The fuel cell is considered one of the most significant modern breakthroughs in the energy section because of its high efficiency,<sup>2</sup> grid independency, and longer operating times in comparison to the battery technologies.<sup>3</sup> Despite the many research efforts made to improve performance, efficiency, and durability, large-scale commercialization of fuel cells still remains problematic.<sup>4,5</sup> One major concern is the high price of widely used platinum-based catalysts.<sup>6</sup> These catalysts also suffer from poisoning due to carbon monoxide which may be present in the supply gas.<sup>7,8</sup> Therefore, it is crucial to develop cheaper, platinum-free materials that exhibit similar electrochemical activity and higher stability than current commonly used noble metal-based nanocatalysts.<sup>3</sup> Since the oxygen reduction reaction (ORR) at the fuel cell cathode has very slow kinetics because of strong O=O bonds,<sup>9</sup> accelerating this reaction becomes a question of optimizing reaction rates using different metals. One possibility is to use transition metal-based and/or heteroatom-doped catalyst materials.<sup>10,11</sup> For example, metallo-macrocycles<sup>12–15</sup> and transition metal chlorides<sup>16–18</sup> incorporated into modified carbon materials have been

intensively studied. The option of using heteroatoms for doping nanostructured  $sp^2$  carbons is especially attractive because, for example, if the nitrogen is in pyridinic form, its  $\pi$  electrons can be donated to electron-poor reactions, such as the ORR.<sup>19</sup> On the other side, the improved ORR activity of heteroatom-doped carbon materials is also directly linked to the charge redistribution.<sup>20</sup> For example, adding nitrogen dopants that have higher electronegativity will generate positive charge density on carbon atoms and the  $O_2$  chemisorption will change, which in turn will also effectively weaken the O–O bond and thereby promote the ORR.<sup>21</sup> Most commonly used heteroatoms for carbon doping are nitrogen,<sup>20,22</sup> boron,<sup>23,24</sup> sulfur,<sup>25,26</sup> and phosphorus.<sup>27,28</sup> Special focus has lately been directed to nitrogen-doped carbon as ORR catalysts, as interest in this topic has grown considerably.<sup>29</sup> This is mainly because nitrogen-doped carbon materials have shown good activity towards the ORR in alkaline media compared to commercial Pt/C catalysts.<sup>30,31</sup> Nitrogen-doped carbon catalysts are most commonly prepared

Received: April 29, 2020

Accepted: August 13, 2020

Published: September 11, 2020



via pyrolysis method, by mixing nitrogen precursors and carbon, then heating above 700 °C to achieve high electrocatalytic activity.<sup>20,32</sup> A N-doped catalyst material may contain different forms of nitrogen: pyridinic-N, pyrrolic-N, graphitic-N (or quaternary-N), and pyridinic-N-oxide.<sup>33,34</sup> For pyridinic-N, each N atom that is located at the edge is bonded to two C atoms and is a member of a heterocyclic aromatic ring, donating one p-electron to the  $\pi$  system. Pyrrolic-N refers to N atoms that are incorporated into the five-member heterocyclic ring where each N atom is bonded to two C atoms and donates two p-electrons to the  $\pi$  system. In the case of graphitic-N, the N atoms replace the C atoms in the graphene plane. Pyridine-N-oxide binds to two C atoms and to one O atom, so the binding energy has a +5 eV shift in the positive direction. However, there is still a debate over the active sites on these materials that promote the ORR.<sup>20,35,36</sup> Rao et al. report the pyridinic-N to be responsible for enhanced ORR activity,<sup>35</sup> while others claim that graphitic-N is the major contributor.<sup>34</sup>

The most common carbon materials used for N-doping include carbon nanotubes,<sup>37,38</sup> carbide-derived carbon,<sup>39</sup> carbon blacks,<sup>40,41</sup> MOFs,<sup>42</sup> and graphene.<sup>43–45</sup> Presently, graphene is one of the most popular candidates because of its high conductivity and attractive thermal and mechanical properties.<sup>46</sup> Among the previously mentioned support materials, biomass-derived carbon has lately been achieving enormous interest.<sup>47–53</sup> Lignin-rich wood mass has been reported to be an extraordinary precursor for high surface area carbon synthesis.<sup>54</sup> Lignin plays a crucial role in this high surface area nanocarbon formation as it constitutes up to 35 wt % of the dry mass of wood.<sup>55</sup> However, for the preparation of the nitrogen-doped carbon catalyst, additional treatment with nitrogen-containing precursors is needed since lignin naturally lacks nitrogen functionalities.<sup>56</sup> Borghei et al. have reported good ORR activity for wood-based nitrogen-doped carbon.<sup>57</sup> The main problem with wood-derived doped carbon catalysts is the heterogeneity of the final material.<sup>55</sup> To form nitrogen-doped carbon nanomaterials with a desirable structure, optimized activation and pyrolysis procedures as well as a compatible nitrogen source and structure-directing agent are needed.<sup>58,59</sup> Different nitrogen sources have been used for synthesizing nitrogen-doped carbons, such as urea or melamine,<sup>60,61</sup> but the previous work has shown that dicyandiamide (DCDA) may give better doping effects towards the ORR.<sup>60</sup>

As the world is still mostly dependent on fossil fuels, the conversion of biomass into carbon has received an enormous interest lately.<sup>53,57,62</sup> Most of the by-products of the wood industry are traditionally simply burnt,<sup>62</sup> so there is a great need to find more efficient ways for valorizing different by-products from wood. This could also help to substitute most fossil-based carbon nanomaterials that are used as a catalyst carrier in energy conversion systems with greener and cheaper biomass-based materials that also possess good electrocatalytic activity. Besides wood-based precursors, other animal- or plant-based precursors could be used, such as chitosan,<sup>30,63</sup> dandelion seeds,<sup>64</sup> fresh beancurd,<sup>65</sup> etc. Herein, we present an easy procedure to synthesize a highly active catalyst material with the widely available alder wood char as the biological waste and DCDA as the nitrogen precursor. The obtained N-doped carbon is used as an electrocatalyst for the ORR in alkaline media, and the activity of this kind of biological waste-

based catalyst is comparable to expensive commercial Pt/C materials.

## RESULTS AND DISCUSSION

The samples were studied using nitrogen adsorption at 77 K, and the isotherms are presented in Figure 1. It can be seen that

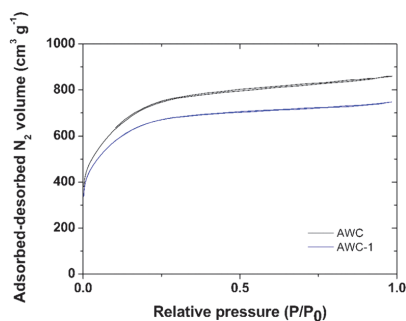


Figure 1. Isotherms of nitrogen sorption at 77 K of wood-derived N-doped carbon before (AWC) and after secondary pyrolysis (AWC-1).

both samples are highly microporous since the isotherms belong to type I.<sup>66</sup> The BET surface area changed negligibly after the second pyrolysis from 2435 to 2245 m<sup>2</sup> g<sup>-1</sup>, but the total volume of pores ( $V_{\text{total}}$ ) and the average pore diameter value ( $L$ ) increased (Table 1).

Table 1. Porosity of Wood-Derived N-Doped Carbon Before (AWC) and After Secondary Pyrolysis (AWC-1)

samples	$S_{\text{BET}}$ , m <sup>2</sup> g <sup>-1</sup>	$S_{\text{DEF}}$ , m <sup>2</sup>	$V_{\text{total}}$ , cm <sup>3</sup> g <sup>-1</sup>	$V_{\text{micp}}(\text{DR})$ , cm <sup>3</sup> g <sup>-1</sup>	$L$ , nm
AWC	2435	1763	1.27	0.86	1.36
AWC-1 (after second pyrolysis)	2245	1594	1.34	0.82	1.63

The morphology of the catalyst material AWC-1 was further studied with SEM. AWC-1 exhibits an irregular granular structure: it consists of mostly amorphous carbon with a rough surface structure (Figure 2a,c), but at the same time, some parts of the catalyst show the typical structure of nanoplatelets (Figure 2b).

The microstructure of the prepared N-doped wood-based catalyst material was further investigated with TEM and is shown in Figure 3a–c. Figure 3b shows the material consists of graphitic lattice fringes (this likely correlates to the platelets seen from the SEM images as well) and areas of amorphous carbon that has a porous structure (Figure 3c,d). Thickness of the 10x layered catalyst particle is 3.55 nm, and the interlayer spacing between two layers is ~0.35 nm. Likewise, the interlayer spacing of few layered graphene is also close to 0.35 nm, revealing that some parts of the catalyst possess a graphene-like structure.<sup>67</sup> It could also be seen from the SEM images that the material contains some nanoplatelets, and this is further confirmed by TEM microphotos as well.

Surface composition of the catalyst material AWC-1 was studied using XPS. From the XPS survey spectra, peaks of C 1s, O 1s, N 1s can be detected. The high-resolution XPS spectra of C 1s and N 1s are presented in Figure 4a,b, respectively. The C 1s peak mostly consists of sp<sup>2</sup> hybridized

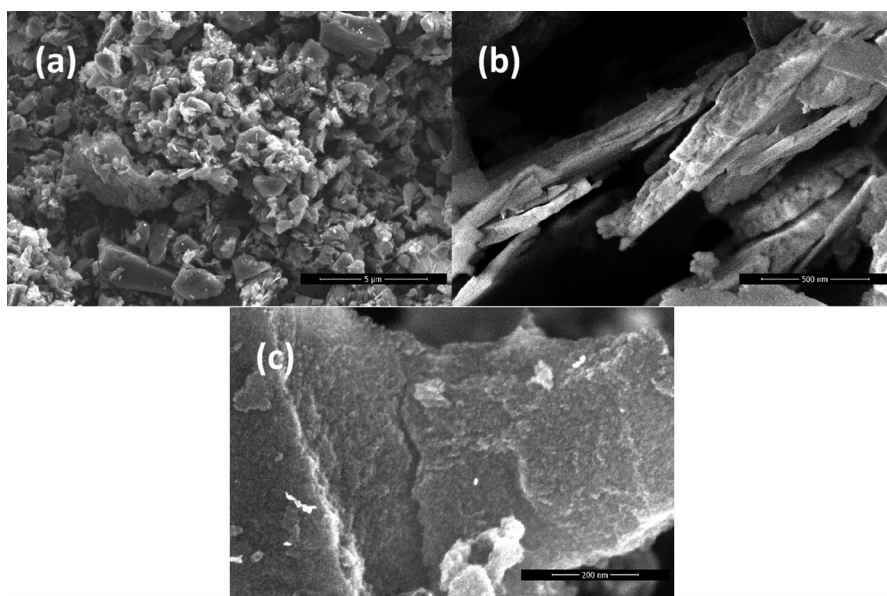


Figure 2. (a–c) SEM images of wood-derived N-doped carbon AWC-1.

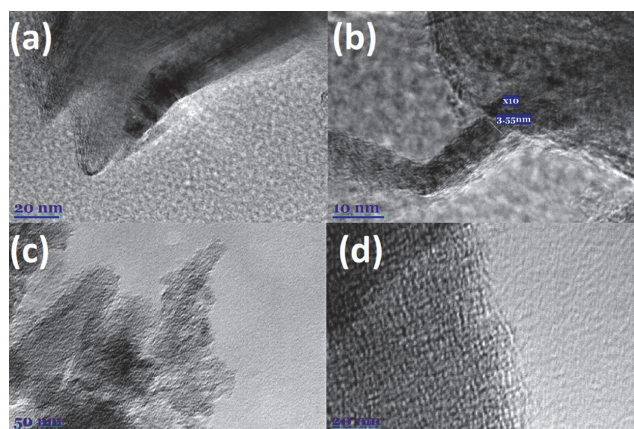


Figure 3. (a–d) TEM microphotographs of wood-derived nitrogen-doped carbon AWC-1.

carbon atoms.<sup>68</sup> The nitrogen content in the catalyst material AWC-1 is quite low (1.56 wt %), and therefore, the intensity of the N 1s peak is also rather low, but it can be deconvoluted into different nitrogen species. It is widely believed that the electrochemical activity is related to different nitrogen surface types rather than the overall nitrogen content;<sup>69,70</sup> the N 1s peak was fitted and four peaks can be identified: pyridinic-N (398.3 eV), pyrrolic-N (399.7 eV), graphitic-N (400.8 eV), and N–O (402.3 eV).<sup>71,72</sup> Most nitrogen was in the pyridinic form (59%) followed by the graphitic form (53%). The amount of pyrrolic-N and N–O was 21 and 23%, respectively. Lai et al. have shown that pyridinic-N lowers the onset potential of the ORR<sup>73</sup> and graphitic-N acts as an active center for the ORR, which in turn helps to achieve higher diffusion

limiting current density; meanwhile, other nitrogen species, such as pyrrolic-N and N–O have no significant effect on the activity of the ORR on N-doped carbon materials.<sup>73,74</sup>

Raman spectroscopy is able to provide rich information on the structure and disorder of carbon networks in carbon-based materials.<sup>63,75,76</sup> Figure 5 shows a 532 nm excited Raman spectrum of N-doped alder wood char-based catalyst materials before (AWC sample) and after (AWC-1 sample) secondary pyrolysis and ball-milling in the spectral region of 400–3200  $\text{cm}^{-1}$ . Two intense bands near 1345 and 1594  $\text{cm}^{-1}$  belong to characteristic D and G modes of the carbon network.<sup>75–77</sup> The  $E_{2g}$  symmetry G band is associated with the in-plane relative motion of carbon atom pairs in  $sp^2$  hybridization.<sup>76</sup> This mode is always allowed in carbon-based materials. The  $A_{1g}$  symmetry

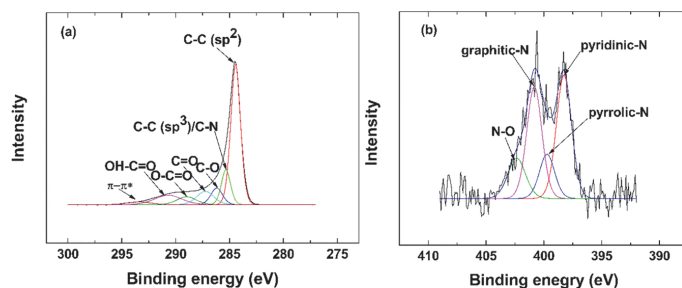


Figure 4. (a) Deconvoluted C 1s spectra and (b) deconvoluted N 1s spectra of the catalyst material AWC-1.

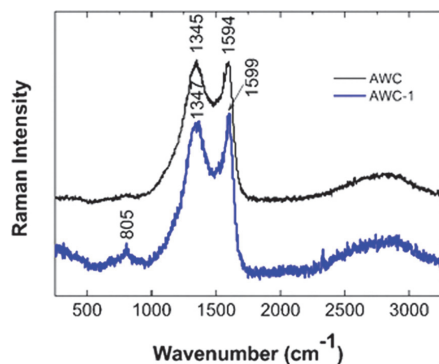


Figure 5. Raman spectra of wood-derived N-doped carbon before (AWC) and after secondary pyrolysis (AWC-1). The excitation wavelength is 532 nm (0.6 mW).

D mode arises from breathing vibrations of aromatic rings; thus, presence of defects is required for this mode activation.<sup>63,75–77</sup> Parameters of these bands were estimated by fitting the experimental contour with four Gaussian–Lorentzian form components in the frequency region of 900–1800  $\text{cm}^{-1}$ . The widths of D and G bands of the sample AWC determined as full width at half maximum (FWHM) were found to be 204 and 79  $\text{cm}^{-1}$ , respectively. Such high width of the bands and high relative integrated intensity ratio of D and G bands ( $A(D)/A(G) \approx 3.6$ ) indicate considerable disorder in

the carbon network of the studied material. It should be noted that the FWHM value of the G band for undoped pristine graphene was found to be 15  $\text{cm}^{-1}$ .<sup>78</sup> Secondary pyrolysis (AWC-1) results in a considerable decrease in the ratio of integrated intensities ( $A(D)/A(G) = 2.2$ ) and a slight decrease in the width of the D band (FWHM = 196  $\text{cm}^{-1}$ ). Considering the peak intensity ratio for D and G bands, we found that  $I(D)/I(G)$  decreases from 1.02 to 0.93 upon the secondary pyrolysis of the sample AWC. The high difference in integrated and peak intensity ratios is related with the difference in width of D and G bands (FWHM of the G band is considerably lower). However, both integrated and peak intensity ratios decrease after the secondary pyrolysis of the AWC sample. These spectral changes indicate a slight decrease in the number of graphene layer defects for the sample treated with additional pyrolysis.<sup>69</sup> The  $I(D)/I(G)$  ratio probes the density of point-like defects related to modifications in the carbon lattice because of the destruction of  $\text{sp}^2$  hybridization.<sup>75</sup> Formation of oxygen-containing functionalities results in the development of  $\text{sp}^3$  defect sites.<sup>75</sup> The observed slight decrease in the  $I(D)/I(G)$  ratio might be related to the high temperature-induced deoxygenation of the carbon lattice and recovery of the graphene  $\text{sp}^2$  structure.

The ORR activity of the previously prepared N-doped wood-based carbon material was studied on GC electrodes in 0.1 M KOH solution by using the RDE method. The results of the RDE experiment are shown in Figure 6a. To evaluate the ORR activity of the catalyst material, the onset potential ( $E_{\text{onset}}$ ) is an important criterion; for N-doped wood-based carbon (AWC-1), the  $E_{\text{onset}}$  is approximately at 0.92 V vs RHE.

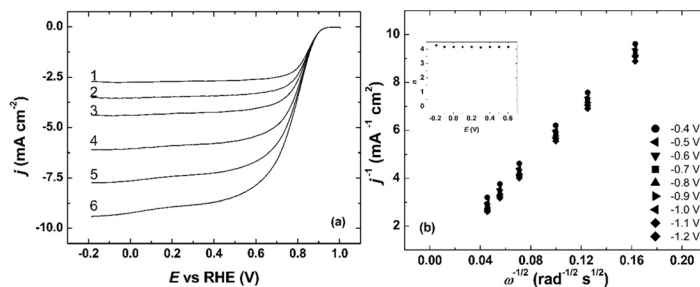
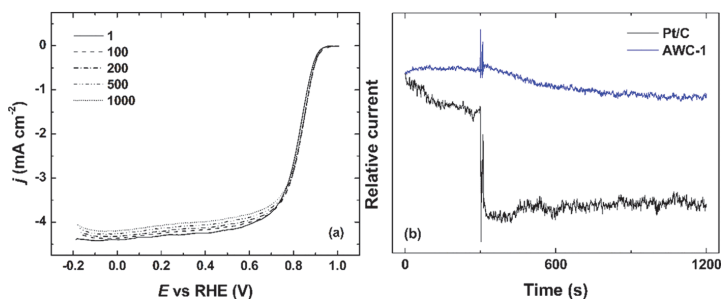


Figure 6. (a) RDE polarization curves for oxygen reduction on GC electrodes modified with a N-doped wood-based catalyst (AWC-1) in  $\text{O}_2$ -saturated 0.1 M KOH.  $\nu = 10 \text{ mV s}^{-1}$ .  $\omega =$  (1) 360, (2) 610, (3) 960, (4) 1900, (5) 3100, and (6) 4600 rpm. (b) K–L plots for oxygen reduction on a N-doped wood-based electrode in 0.1 M KOH at various potentials. The inset figure shows the changes of  $n$  values in the studied potential range.



**Figure 7.** (a) Stability of GC electrodes modified with AWC-1 during 1000 cycles.  $\omega = 960$  rpm. (b) Chronoamperometric responses of the catalyst material AWC-1 at 0.6 V with the addition of 3 M methanol.

One can also see from Figure 6a that despite increasing the rotation rate, the onset potential remains the same, indicating at least the short-term stability of the catalyst. Similar tendencies have been previously observed by Hu et al., who studied nitrogen-doped hydroxypropyl methylcellulose for the ORR in the alkaline media.<sup>79</sup> Even though the electrocatalytic activity of their catalyst was similar to the catalyst presented in the current work, it is important to note that the catalyst loading used by Hu et al. was higher than used herein. Han et al. have also synthesized N-doped hollow-core, mesoporous nanospheres with the BET surface area of  $770 \text{ m}^2 \text{ g}^{-1}$  and 4.4–6.7% nitrogen content but also with a higher catalyst loading.<sup>80</sup> Therefore, it is evident that the electrocatalytic ORR activity presented in the current work is comparable or even higher than the ones reported for similar catalyst materials. The Koutecký-Levich (K-L) plots were also constructed using the  $\text{O}_2$  reduction reaction polarization data shown in Figure 6a. This was done using the K-L equation:<sup>81</sup>

$$\frac{1}{j} = \frac{1}{j_k} + \frac{1}{j_d} = -\frac{1}{nFkc_{\text{O}_2}^b} - \frac{1}{0.62FkD_{\text{O}_2}^{2/3}\nu^{-1/6}c_{\text{O}_2}^b\omega^{1/2}} \quad (1)$$

where  $j$  is the experimentally measured current density from which the background current has been subtracted,  $j_k$  and  $j_d$  are the kinetic and diffusion limited current densities, respectively,  $k$  is the electrochemical rate constant for  $\text{O}_2$  reduction,  $c_{\text{O}_2}^b$  is the concentration of oxygen in the bulk ( $1.2 \times 10^{-6} \text{ mol cm}^{-3}$ ),<sup>82</sup>  $F$  is the Faraday constant ( $96,485 \text{ C mol}^{-1}$ )  $D_{\text{O}_2}$  is the diffusion coefficient of  $\text{O}_2$  in 0.1 M KOH ( $1.9 \times 10^{-5} \text{ cm}^2 \text{ s}^{-1}$ ),<sup>82</sup>  $\nu$  is the kinematic viscosity of the solution ( $0.01 \text{ cm}^2 \text{ s}^{-1}$ ),<sup>82</sup> and  $\omega$  is the rotation rate of the electrode ( $\text{rad s}^{-1}$ ).<sup>83</sup> Figure 6b shows the K-L plots retrieved from the ORR polarization curves at different rotation speeds in 0.1 M KOH. The K-L lines are approximately linear, and the intercepts of the extrapolated lines are close to zero, indicating that the oxygen reduction process happening on the electrode is diffusion limited within the potential range studied. The number of electrons transferred per  $\text{O}_2$  molecule ( $n$ ) was also calculated at various potentials using the K-L equation (the inset of Figure 6b). This value of  $n$  is close to four in the potential range studied, which indicates that oxygen is directly reduced to water. However, it is impossible to determine via K-L analysis if this is a direct four-electron reduction of oxygen or reduction via the  $\text{HO}_2^-$  intermediate ( $2 \text{ e}^- + 2 \text{ e}^-$  reduction) pathway.

Stability is also an important factor for fuel cell or metal–air battery applications. Stability test results for the N-doped wood-based catalyst during 1000 potential cycles between 1 and  $-0.2$  V are shown in Figure 7a. The onset and half-wave potentials did not change much during the 1000 potential cycles in alkaline media. However, a slight change in diffusion current values can be observed, meaning that the catalyst morphology on the electrode changes with no effect on the active sites. Another potential and more likely cause of this could be that a small amount of the catalyst material detaches from the electrode during stability tests. Methanol tolerance tests comparing as-prepared catalyst AWC-1 and commercial Pt/C were carried out to further study the catalyst durability for potential application in direct methanol fuel cells. As seen from Figure 7b, the addition of methanol at 300 s causes a sharp current loss in the case of commercial Pt/C; the relative current drops to  $\sim 30\%$ . Current drop after injection of methanol for AWC-1 is not as huge; the value of relative current decreases a bit, but stabilizes and shows no significant change.

The comparison of oxygen reduction polarization curves in 0.1 M KOH solution is shown in Figure 8. The RDE

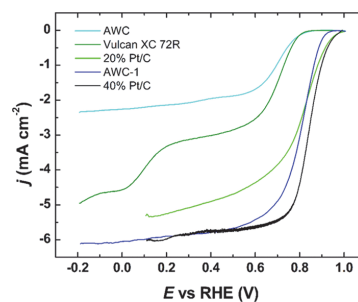


**Figure 8.** RDE voltammetry curves for oxygen reduction on GC electrodes modified with different catalyst materials in  $\text{O}_2$ -saturated 0.1 M KOH.  $\nu = 10 \text{ mV s}^{-1}$ ,  $\omega = 1900$  rpm.

polarization curves for AWC, Vulcan XC 72R, and commercial 20% and 40% Pt/C catalyst materials have been added for comparison purposes. The onset potential and half-wave potential for the N-doped wood-based catalyst is much more positive compared to AWC and the most commonly used catalyst support, Vulcan XC 72R. The slight negative shift of the onset potential is observable in comparison with 20% Pt/C

but at the same time, the diffusion-limited current density is reaching much higher values compared to the commercial 20% platinum catalyst. Wu et al. have synthesized nitrogen-doped graphitic carbon nanoribbons<sup>84</sup> exhibiting higher onset potential than presented hereby but with a 2.3 mg cm<sup>-2</sup> catalyst loading, which is five times higher than the loading of current catalyst material AWC-1. Wu et al. have also been using ferrous chloride in their catalyst preparation process, which may have a great impact to the electrocatalytic activity. There are many research articles about the conversion of biomass into carbon,<sup>30,53,57,64,65,85</sup> and some of these materials show even better electrochemical activity towards the ORR than the material studied herein, but the goal of this work was to use a precursor that is widely available in Europe.

The above-described electrocatalytic properties of the synthesized N-doped wood-derived carbon catalysts may be due to an extremely high surface area and enlarged pore volume of the catalyst, increasing during the secondary pyrolysis step. Other factors include the high percentage of pyridinic-N in the nitrogen-doped material. A synergy of all these properties should be responsible for the remarkable ORR activity of the novel wood-derived electrocatalyst. Overall, this trailblazing work shows the development of highly effective, cheap, and electrochemically active nanocarbon materials for energy storage and conversion applications using wooden biomass as a renewable and biological resource of carbon.

Tafel plots (from the data shown in Figure 8) comparing 20% Pt/C and AWC-1 are shown in Figure 9. At low current

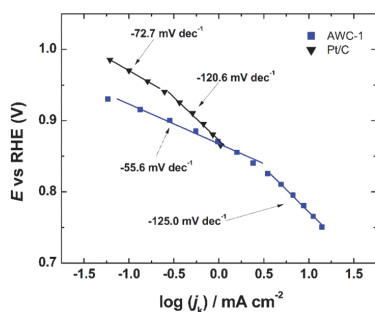


Figure 9. Tafel plots with the linear fits used for the determination of the Tafel slopes.

densities the slope value for 20% Pt/C is  $-72.7 \text{ mV dec}^{-1}$  and for AWC-1  $-55.6 \text{ mV dec}^{-1}$ . At higher overpotentials the corresponding values are  $-120.6 \text{ mV dec}^{-1}$  and  $-125.0 \text{ mV dec}^{-1}$ , respectively.

## CONCLUSIONS

The nitrogen-doped wood-derived carbon catalyst was synthesized using alder wood char as the carbon source. Compared to the most commonly used commercial carbon XC 72R, wood-derived N-doped carbon AWC-1 exhibits remarkably improved electrocatalytic ORR activity. AWC-1 shows an onset potential of 0.92 V vs RHE and a half-wave potential of 0.85 V vs RHE in an alkaline medium in addition to improved stability compared to commercial Pt/C. The synthesized wood-derived N-doped carbon is a promising alternative to state-of-the-art precious metal-based catalysts and may be an excellent catalyst carrier for many other applications. The

superiority of wood-derived catalysts is demonstrated with ORR activity comparable to a commercial 20% Pt/C catalyst in 0.1 M KOH solution. Such electrocatalytic activity in alkaline media can be explained by the synergistic effect of a high surface area and pore volume and high pyridinic nitrogen content. Thus, this work proposes a facile synthetic strategy to design highly active multifunctional wooden biomass-based materials toward different energy storage and conversion applications.

## EXPERIMENTAL SECTION

### Preparation of N-Doped Wood-Based Catalyst.

Commercial alder charcoal made by SIA Fille 2000 (Latvia) was the precursor with an 82% nonvolatile carbon content. Charcoal was refined in a planetary mill Pulverizette Classic 5 (Fitsch, Germany) using zirconia mortar and beads to reach a fraction of  $\sim 10 \text{ m}^{-6}$  and then impregnated with a 50% NaOH (Chempur, Piekary Slaskie, Poland) solution. The mass ratio of activator to carbonizate was 3 to 1. The obtained mixture was activated in an Ar flow ( $100 \text{ L h}^{-1}$ ) at  $700 \text{ }^\circ\text{C}$  for 120 min (Nabertherm 40 L muffle oven, Lilienthal, Germany). The product was washed with deionized water, 10% HCl (Lachner, Neratovice, Czech Republic), and water again until the filtrate pH reached 5. AC was dried overnight at  $105 \text{ }^\circ\text{C}$ . Ash content was 0.1–0.2%. The process is described in details elsewhere.<sup>86</sup>

The activated sample was further doped with nitrogen using dicyandiamide (DCDA; Sigma–Aldrich, Germany) solution in dimethylformamide (DMF; Lachner, Czech Republic) with a mass ratio of AC/DCDA = 1:20. DMF was later removed in a rotary evaporator. Doping was carried out at  $800 \text{ }^\circ\text{C}$  for 1 h in an argon atmosphere; the sample obtained is denoted as AWC. The sample was later ball-milled using zirconia beads and secondary pyrolysis was performed in the tube furnace at  $800 \text{ }^\circ\text{C}$  in a flowing nitrogen atmosphere. The resulting final catalyst material is denoted as AWC-1.

**Physical Characterization.** The porous structure of the AC was evaluated from  $\text{N}_2$  sorption/desorption isotherms determined in a sorptometer Quantachrome NOVA 4000 (Boynton Beach, FL, U.S.A.) by means of NovaWin 11.03 software. Degassing was performed at  $300 \text{ }^\circ\text{C}$  for 2 h. The results were assessed using the theories of Brunauer–Emmet–Teller (BET, in a  $P/P_0$  range of 0.05–0.35), Dubinin–Radushkevich (DR, in a  $P/P_0$  range of  $10^{-5}$ –0.35), and quenched solid density functional theory (QSDFT, in a whole  $P/P_0$  range).

The morphology of the prepared catalyst was characterized using an SEM-focused ion beam instrument (Helios Nanolab 650). The shape and size of the catalyst particles were further examined using a Tecnai G2 F20 X-TWIN transmission electron microscope equipped with an EDAX spectrometer and an r-TEM detector. For microscopic examinations, 10 mg of the sample was first sonicated in 1 mL of ethanol for 1 h and then deposited on a Cu grid covered with a continuous carbon film.

For performing X-ray photoelectron spectroscopy (XPS), a Kratos Axis Ultra DLD X-ray photoelectron spectrometer with monochromatic Al  $K\alpha$  radiation ( $h\nu = 1486.6 \text{ eV}$ ) was used. The pass energy values used for the survey and high-resolution spectra were 160 and 20 eV, respectively. The energy scale of the system was calibrated with respect to Au 4f7/2, Ag 3d5/2, and Cu 2p3/2 peak positions. Vision 2.2.10 software was used for the peak deconvolution and atomic concentration calculation procedures. All spectra fitting procedures were

performed using symmetrical peaks and a 70:30 Gauss–Lorentz function ratio unless stated otherwise in the text. Raman spectra were recorded using an inVia Raman (Renishaw, U.K.) spectrometer equipped with a thermoelectrically cooled ( $-70\text{ }^{\circ}\text{C}$ ) CCD camera and microscope. Raman spectra were excited with 532 nm radiation with diode-pumped solid state (DPSS) laser (Renishaw, UK). The 20x/0.40 NA objective lens and 1800 lines/mm grating were used to record the Raman spectra. The accumulation time was set to 40 s. To avoid damage of the sample, the laser power at the sample was restricted to 0.6 mW. The Raman frequencies were calibrated using the polystyrene standard. Parameters of the bands were determined by fitting the experimental spectra with Gaussian–Lorentzian shape components using GRAMS/A1 8.0 (Thermo Scientific) software.

**Electrochemical Characterization.** To perform rotating disc electrode (RDE) measurements, glassy carbon discs (GCs) with a geometric area ( $A$ ) of  $0.2\text{ cm}^2$  were used as the substrate material. First, the electrodes were polished using 1 and  $0.3\text{ }\mu\text{m}$  aluminium oxide ( $\text{Al}_2\text{O}_3$ ; Buehler) paste. After polishing, the electrodes were sonicated for 5 min in isopropanol (Sigma–Aldrich) and Milli-Q water. The catalyst ink with a concentration of  $4\text{ mg mL}^{-1}$  in isopropanol was prepared using 0.25% of AS-04  $\text{OH}^-$  ionomer (Tokuyama Corp., Japan). The electrodes were evenly covered with the catalyst material by drop coating  $20\text{ }\mu\text{L}$  of previously prepared catalyst ink. The loading of the catalyst material on the GC electrode was  $400\text{ }\mu\text{g cm}^{-2}$ . After coating, the electrodes were dried in the oven at  $60\text{ }^{\circ}\text{C}$ . The electrochemical measurements were carried out using the RDE method. A Pine AFMSRCE (Pine, USA) rotator and speed controlling unit were used for the RDE measurements. The software used for controlling the experiments was Nova 2.1.2 (Metrohm Autolab P.V., The Netherlands), and the potential was applied with a potentiostat/galvanostat Autolab PGSTAT 128 N (Metrohm Autolab P.V., The Netherlands). All electrochemical tests were carried out in a three-electrode cell using Pt foil as the counter electrode and a saturated calomel electrode (SCE) as the reference electrode. As all potentials in this work were measured vs SCE, the potentials were calculated in the reversible hydrogen electrode (RHE) scale using the Nernst equation:

$$E_{\text{RHE}} = E_{\text{SCE}} + 0.059\text{pH} + E_{\text{SCE}}^0 \quad (2)$$

where  $E_{\text{SCE}}$  is the experimentally measured potential vs SCE, and  $E_{\text{SCE}}^0 = 0.242\text{ V}$  at  $25\text{ }^{\circ}\text{C}$ . All the potential values in the text are stated against RHE, unless noted otherwise. Electrochemical measurements were performed in  $0.1\text{ M KOH}$  solution at room temperature ( $23 \pm 1\text{ }^{\circ}\text{C}$ ). For studying the ORR, the solution was saturated with  $\text{O}_2$  (6.0), and for measuring the background, the solution was saturated with  $\text{N}_2$  (5.0). A continuous flow of gases was maintained over the solution during the measurement. The RDE for 1000 potential cycles at a scan rate of  $100\text{ mV s}^{-1}$  was applied to test the stability of the catalyst material. The rotation rate was set to 960 rpm during stability tests. Linear-sweep voltammograms (LSVs) were recorded after every 100 cycles at a scan rate of  $10\text{ mV s}^{-1}$ . To further study the stability of the prepared catalyst material, methanol tolerance tests were also conducted at  $0.6\text{ V}$  in  $\text{O}_2$ -saturated  $0.1\text{ M KOH}$ . To perform the methanol tolerance test, the rotation speed was set to 1900 rpm and  $3\text{ M MeOH}$  was added at 300 s.

## AUTHOR INFORMATION

### Corresponding Author

Ivar Kruusenberg – National Institute of Chemical Physics and Biophysics, 10213 Tallinn, Estonia; [orcid.org/0000-0002-8199-9324](https://orcid.org/0000-0002-8199-9324); Phone: +372 503 6963; Email: [ivar.kruusenberg@kbfi.ee](mailto:ivar.kruusenberg@kbfi.ee)

### Authors

Kätlin Kaare – Institute of Chemistry, University of Tartu, 50411 Tartu, Estonia; National Institute of Chemical Physics and Biophysics, 10213 Tallinn, Estonia

Eric Yu – Department of Chemical and Biomolecular Engineering, University of California at Berkeley, Berkeley 94720, California, United States of America

Aleksandrs Volpert – Latvian State Institute of Wood Chemistry, Riga LV-1006, Latvia

Galina Dobele – Latvian State Institute of Wood Chemistry, Riga LV-1006, Latvia

Aivars Zhurinh – Latvian State Institute of Wood Chemistry, Riga LV-1006, Latvia

Alexander Dyck – DLR Institute of Networked Energy Systems, Urban and Residential Technologies, 26129 Oldenburg, Germany; [orcid.org/0000-0002-5010-8226](https://orcid.org/0000-0002-5010-8226)

Gediminas Niaura – State Research Institute Center for Physical Sciences and Technology, LT-02300 Vilnius, Lithuania

Loreta Tamasauskaitė-Tamasiunaite – State Research Institute Center for Physical Sciences and Technology, LT-02300 Vilnius, Lithuania

Eugenijus Norkus – State Research Institute Center for Physical Sciences and Technology, LT-02300 Vilnius, Lithuania

Mindaugas Andrulevičius – Institute of Materials Science of Kaunas University of Technology, Kaunas LT-51423, Lithuania

Mati Danilson – Laboratory of Optoelectronic Materials Physics, Department of Materials and Environmental Technology, Tallinn University of Technology, 19086 Tallinn, Estonia

Complete contact information is available at: <https://pubs.acs.org/10.1021/acsomega.0c01974>

### Notes

The authors declare no competing financial interest.

## ACKNOWLEDGMENTS

This research was financially supported by the M-ERA.NET project “Wood-based Carbon Catalysts for Low-temperature Fuel Cells (WoBaCat),” ERA.Net RUS Plus project “Novel Heteroatom-doped Nanocarbon Catalyst for Fuel Cell and Metal-air Battery Applications (HeDoCat),” and L2P-2018/1-0194 project “Nanostructured Nitrogenated Carbon Materials as Promoters in Energy Harvesting and Storage Technologies (NN-CARMA).” The funding for the research stays at the DLR-Institute of Networked Energy Systems e.V. (Germany) from the Federal Ministry of Education, and Research in the framework of the project NETonia is greatly appreciated. This work was also supported by the European Union through the European Regional Development Fund, Project TK134 EQUITANT.

## REFERENCES

(1) Martins, F.; Felgueiras, C.; Smitkova, M.; Caetano, N. Analysis of Fossil Fuel Energy Consumption and Environmental Impacts in European Countries. *Energies* **2019**, *12*, 964.

- (2) Borup, R.; Meyers, J.; Pivovar, B.; Kim, Y. S.; Mukundan, R.; Garland, N.; Myers, D.; Wilson, M.; Garzon, F.; Wood, D.; Zelenay, P.; More, K.; Stroh, K.; Zawodzinski, T.; Boncella, J.; McGrath, J. E.; Inaba, M.; Miyatake, K.; Hori, M.; Ota, K.; Ogumi, Z.; Miyata, S.; Nishikata, A.; Siroma, Z.; Uchimoto, Y.; Yasuda, K.; Kimijima, K. I.; Iwashita, N. Scientific Aspects of Polymer Electrolyte Fuel Cell Durability and Degradation. *Chem. Rev.* **2007**, *107*, 3904–3951.
- (3) Gröger, O.; Gasteiger, H. A.; Suchsland, J.-P. Review—Electromobility: Batteries or Fuel Cells? *J. Electrochem. Soc.* **2015**, *162*, A2605–A2622.
- (4) Debe, M. K. Electrocatalyst Approaches and Challenges for Automotive Fuel Cells. *Nature* **2012**, *486*, 43–51.
- (5) Volkovich, Y. M.; Sosenkin, V. E.; Bagotsky, V. S. Structural and Wetting Properties of Fuel Cell Components. *J. Power Sources* **2010**, *195*, 5429–5441.
- (6) Chen, Z.; Higgins, D.; Yu, A.; Zhang, L.; Zhang, J. A Review on Non-Precious Metal Electrocatalysts for PEM Fuel Cells. *Energy Environ. Sci.* **2011**, *4*, 3167–3192.
- (7) Bagotzky, V. S.; Osetrova, N. V.; Skundin, A. M. Fuel Cells: State-of-the-Art and Major Scientific and Engineering Problems. *Russ. J. Electrochem.* **2003**, *39*, 919–934.
- (8) Cheng, X.; Shi, Z.; Glass, N.; Zhang, L.; Zhang, J.; Song, D.; Liu, Z.-S.; Wang, H.; Shen, J. A Review of PEM Hydrogen Fuel Cell Contamination: Impacts, Mechanisms, and Mitigation. *J. Power Sources* **2007**, *165*, 739–756.
- (9) Gewirth, A. A.; Thorum, M. S. Electroreduction of Dioxygen for Fuel-Cell Applications: Materials and Challenges. *Inorg. Chem.* **2010**, *49*, 3557–3566.
- (10) Dombrovskis, J. K.; Palmqvist, A. E. C. Recent Progress in Synthesis, Characterization and Evaluation of Non-Precious Metal Catalysts for the Oxygen Reduction Reaction. *Fuel Cells* **2016**, *16*, 4–22.
- (11) Zheng, Y.; Jiao, Y.; Jaroniec, M.; Jin, Y.; Qiao, S. Z. Nanostructured Metal-Free Electrochemical Catalysts for Highly Efficient Oxygen Reduction. *Small* **2012**, *8*, 3550–3566.
- (12) Jasinski, R. A New Fuel Cell Cathode Catalyst. *Nature* **1964**, *201*, 1212–1213.
- (13) Choi, H.-J.; Ashok Kumar, N.; Baek, J.-B. Graphene Supported Non-Precious Metal-Macrocycle Catalysts for Oxygen Reduction Reaction in Fuel Cells. *Nanoscale* **2015**, *7*, 6991–6998.
- (14) Kobayashi, M.; Niwa, H.; Saito, M.; Harada, Y.; Oshima, M.; Ofuchi, H.; Terakura, K.; Ikeda, T.; Koshigoe, Y.; Ozaki, J.; Miyata, S. Indirect Contribution of Transition Metal towards Oxygen Reduction Reaction Activity in Iron Phthalocyanine-Based Carbon Catalysts for Polymer Electrolyte Fuel Cells. *Electrochim. Acta* **2012**, *74*, 254–259.
- (15) Ding, L.; Dai, X.; Lin, R.; Wang, H.; Qiao, J. Electrochemical Performance of Carbon-Supported Co-Phthalocyanine Modified with Co-Added Metals (M = Fe, Co, Ni, V) for Oxygen Reduction Reaction. *J. Electrochem. Soc.* **2012**, *159*, F577–F584.
- (16) Kruusenberg, I.; Ramani, D.; Ratso, S.; Joost, U.; Saar, R.; Rauwel, P.; Kannan, A. M.; Tammeveski, K. Cobalt-Nitrogen Co-Doped Carbon Nanotube Cathode Catalyst for Alkaline Membrane Fuel Cells. *ChemElectroChem* **2016**, *3*, 1455–1465.
- (17) Si, Y.-J.; Xiong, Z.-P.; Chen, C.-G.; Liu, P.; Wu, H.-J. A Non-Precious Metal Catalyst for Oxygen Reduction Prepared by Heat-Treating a Mechanical Mixture of Carbon Black, Melamine and Cobalt Chloride. *Chin. Chem. Lett.* **2013**, *24*, 1109–1111.
- (18) Mutyalu, S.; Mathiyarasu, J.; Mulchandani, A. Methanol Tolerant, High Performance, Noble Metal Free Electrocatalyst Developed from Polyaniline and Ferric Chloride for the Oxygen Reduction Reaction. *RSC Adv.* **2015**, *5*, 92648–92655.
- (19) Zhao, Y.; Yang, L.; Chen, S.; Wang, X.; Ma, Y.; Wu, Q.; Jiang, Y.; Qian, W.; Hu, Z. Can Boron and Nitrogen Co-Doping Improve Oxygen Reduction Reaction Activity of Carbon Nanotubes? *J. Am. Chem. Soc.* **2013**, *135*, 1201–1204.
- (20) Wong, W. Y.; Daud, W. R. W.; Mohamad, A. B.; Kadhum, A. A. H.; Loh, K. S.; Majlan, E. H. Recent Progress in Nitrogen-Doped Carbon and Its Composites as Electrocatalysts for Fuel Cell Applications. *Int. J. Hydrogen Energy* **2013**, *38*, 9370–9386.
- (21) Tang, C.; Zhang, Q. Nanocarbon for Oxygen Reduction Electrocatalysis: Dopants, Edges, and Defects. *Adv. Mater.* **2017**, *29*, 1604103.
- (22) Gao, F.; Zhao, G.-L.; Yang, S. Catalytic Reactions on the Open-Edge Sites of Nitrogen-Doped Carbon Nanotubes as Cathode Catalyst for Hydrogen Fuel Cells. *ACS Catal.* **2014**, *4*, 1267–1273.
- (23) Van Tam, T.; Kang, S. G.; Babu, K. F.; Oh, E.-S.; Lee, S. G.; Choi, W. M. Synthesis of B-Doped Graphene Quantum Dots as a Metal-Free Electrocatalyst for the Oxygen Reduction Reaction. *J. Mater. Chem. A* **2017**, *5*, 10537–10543.
- (24) Su, J.; Cao, X.; Wu, J.; Jin, C.; Tian, J.-H.; Yang, R. One-Pot Synthesis of Boron-Doped Ordered Mesoporous Carbons as Efficient Electrocatalysts for the Oxygen Reduction Reaction. *RSC Adv.* **2016**, *6*, 24728–24737.
- (25) Bandosz, T. J.; Ren, T.-Z. Porous Carbon Modified with Sulfur in Energy Related Applications. *Carbon* **2017**, *118*, S61–S77.
- (26) El-Sawy, A. M.; Mosa, I. M.; Su, D.; Guild, C. J.; Khalid, S.; Joesten, R.; Rusling, J. F.; Suib, S. L. Controlling the Active Sites of Sulfur-Doped Carbon Nanotube-Graphene Nanolobes for Highly Efficient Oxygen Evolution and Reduction Catalysis. *Adv. Energy Mater.* **2016**, *6*, 1501966.
- (27) Li, R.; Wei, Z.; Gou, X.; Xu, W. Phosphorus-Doped Graphene Nanosheets as Efficient Metal-Free Oxygen Reduction Electrocatalysts. *RSC Adv.* **2013**, *3*, 9978–9984.
- (28) Zhu, Y.-P.; Liu, Y.; Liu, Y.-P.; Ren, T.-Z.; Chen, T.; Yuan, Z.-Y. Direct Synthesis of Phosphorus-Doped Mesoporous Carbon Materials for Efficient Electrocatalytic Oxygen Reduction. *ChemCatChem* **2015**, *7*, 2903–2909.
- (29) Masa, J.; Xia, W.; Muhler, M.; Schuhmann, W. On the Role of Metals in Nitrogen-Doped Carbon Electrocatalysts for Oxygen Reduction. *Angew. Chem. Int. Ed.* **2015**, *54*, 10102–10120.
- (30) Liu, Q.; Duan, Y.; Zhao, Q.; Pan, F.; Zhang, B.; Zhang, J. Direct Synthesis of Nitrogen-Doped Carbon Nanosheets with High Surface Area and Excellent Oxygen Reduction Performance. *Langmuir* **2014**, *30*, 8238–8245.
- (31) Zhang, L.; Niu, J.; Dai, L.; Xia, Z. Effect of Microstructure of Nitrogen-Doped Graphene on Oxygen Reduction Activity in Fuel Cells. *Langmuir* **2012**, *28*, 7542–7550.
- (32) Lin, Z.; Waller, G.; Liu, Y.; Liu, M.; Wong, C.-P. Facile Synthesis of Nitrogen-Doped Graphene via Pyrolysis of Graphene Oxide and Urea, and Its Electrocatalytic Activity toward the Oxygen-Reduction Reaction. *Adv. Energy Mater.* **2012**, *2*, 884–888.
- (33) Liu, H.; Liu, Y.; Zhu, D. Chemical Doping of Graphene. *J. Mater. Chem.* **2011**, *21*, 3335–3345.
- (34) Yang, Z.; Nie, H.; Chen, X.; Chen, X.; Huang, S. Recent Progress in Doped Carbon Nanomaterials as Effective Cathode Catalysts for Fuel Cell Oxygen Reduction Reaction. *J. Power Sources* **2013**, *236*, 238–249.
- (35) Rao, C. V.; Cabrera, C. R.; Ishikawa, Y. In Search of the Active Site in Nitrogen-Doped Carbon Nanotube Electrodes for the Oxygen Reduction Reaction. *J. Phys. Chem. Lett.* **2010**, *1*, 2622–2627.
- (36) Guo, D.; Shibuya, R.; Akiba, C.; Saji, S.; Kondo, T.; Nakamura, J. Active Sites of Nitrogen-Doped Carbon Materials for Oxygen Reduction Reaction Clarified Using Model Catalysts. *Science* **2016**, *351*, 361–365.
- (37) Gong, K.; Du, F.; Xia, Z.; Durstock, M.; Dai, L. Nitrogen-Doped Carbon Nanotube Arrays with High Electrocatalytic Activity for Oxygen Reduction. *Science* **2009**, *323*, 760–764.
- (38) Jana, D.; Sun, C.-L.; Chen, L.-C.; Chen, K.-H. Effect of Chemical Doping of Boron and Nitrogen on the Electronic, Optical, and Electrochemical Properties of Carbon Nanotubes. *Prog. Mater. Sci.* **2013**, *58*, 565–635.
- (39) Ratso, S.; Kruusenberg, I.; Käärik, M.; Kook, M.; Saar, R.; Pärs, M.; Leis, J.; Tammeveski, K. Highly Efficient Nitrogen-Doped Carbide-Derived Carbon Materials for Oxygen Reduction Reaction in Alkaline Media. *Carbon* **2017**, *113*, 159–169.
- (40) Jayabharathi, C.; Venkatesh Kumar, P.; Rao, M. S.; Mathiyarasu, J.; Phani, K. L. N. Nitrogen-Doped Carbon Black as Methanol

Tolerant Electrocatalyst for Oxygen Reduction Reaction in Direct Methanol Fuel Cells. *Electrochim. Acta* **2012**, *74*, 171–175.

(41) Liu, J.; Song, P.; Ruan, M.; Xu, W. Catalytic Properties of Graphitic and Pyridinic Nitrogen Doped on Carbon Black for Oxygen Reduction Reaction. *Chin. J. Catal.* **2016**, *37*, 1119–1126.

(42) Xia, B. Y.; Yan, Y.; Li, N.; Wu, H. B.; Lou, X. W.; Wang, X. A Metal-Organic Framework-Derived Bifunctional Oxygen Electrocatalyst. *Nat. Energy* **2016**, *1*, 15006.

(43) Zhang, L.; Xia, Z. Mechanisms of Oxygen Reduction Reaction on Nitrogen-Doped Graphene for Fuel Cells. *J. Phys. Chem. C* **2011**, *115*, 11170–11176.

(44) Geng, D.; Chen, Y.; Chen, Y.; Li, Y.; Li, R.; Sun, X.; Ye, S.; Knights, S. High Oxygen-Reduction Activity and Durability of Nitrogen-Doped Graphene. *Energy Environ. Sci.* **2011**, *4*, 760–764.

(45) Wang, H.; Maiyalagan, T.; Wang, X. Review on Recent Progress in Nitrogen-Doped Graphene: Synthesis, Characterization, and Its Potential Applications. *ACS Catal.* **2012**, *2*, 781–794.

(46) Fasolino, A.; Los, J. H.; Katsnelson, M. I. Intrinsic Ripples in Graphene. *Nat. Mater.* **2007**, *6*, 858–861.

(47) De, S.; Balu, A. M.; van der Waal, J. C.; Luque, R. Biomass-Derived Porous Carbon Materials: Synthesis and Catalytic Applications. *ChemCatChem* **2015**, *7*, 1608–1629.

(48) Ou, J.; Zhang, Y.; Chen, L.; Zhao, Q.; Meng, Y.; Guo, Y.; Xiao, D. Nitrogen-Rich Porous Carbon Derived from Biomass as a High Performance Anode Material for Lithium Ion Batteries. *J. Mater. Chem. A* **2015**, *3*, 6534–6541.

(49) Gao, S.; Li, X.; Li, L.; Wei, X. A Versatile Biomass Derived Carbon Material for Oxygen Reduction Reaction, Supercapacitors and Oil/Water Separation. *Nano Energy* **2017**, *33*, 334–342.

(50) Gao, Z.; Zhang, Y.; Song, N.; Li, X. Biomass-Derived Renewable Carbon Materials for Electrochemical Energy Storage. *Mater. Res. Lett.* **2017**, *5*, 69–88.

(51) Dobelev, G.; Vervikishko, D.; Volperts, A.; Bogdanovich, N.; Shkolnikov, E. Characterization of the Pore Structure of Nanoporous Activated Carbons Produced from Wood Waste. *Holzforschung* **2013**, *67*, 587–594.

(52) Dobelev, G.; Volperts, A.; Zhurinsk, A.; Vervikishko, D.; Shkolnikov, E.; Ozolinsh, J. Wood Based Activated Carbons for Supercapacitor Electrodes with Sulfuric Acid Electrolyte. *Holzforschung* **2017**, *71*, 591–598.

(53) Wang, M.; Wang, S.; Yang, H.; Ku, W.; Yang, S.; Liu, Z.; Lu, G. Carbon-Based Electrocatalysts Derived from Biomass for Oxygen Reduction Reaction: A Minireview. *Front. Chem.* **2020**, *8*, 116.

(54) Suhas; Carrott, P. J. M.; Ribeiro Carrott, M. M. L. Lignin - from Natural Adsorbent to Activated Carbon: A Review. *Bioresour. Technol.* **2007**, *98*, 2301–2312.

(55) Yan, L.; Yu, J.; Houston, J.; Flores, N.; Luo, H. Biomass Derived Porous Nitrogen Doped Carbon for Electrochemical Devices. *Green Energy Environ.* **2017**, *2*, 84–99.

(56) Ma, Z.; Zhang, H.; Yang, Z.; Ji, G.; Yu, B.; Liu, X.; Liu, Z. Mesoporous Nitrogen-Doped Carbons with High Nitrogen Contents and Ultrahigh Surface Areas: Synthesis and Applications in Catalysis. *Green Chem.* **2016**, *18*, 1976–1982.

(57) Borghei, M.; Lehtonen, J.; Liu, L.; Rojas, O. J. Advanced Biomass-Derived Electrocatalysts for the Oxygen Reduction Reaction. *Adv. Mater.* **2018**, *30*, 1703691.

(58) Liu, J.; Zhang, T.; Wang, Z.; Dawson, G.; Chen, W. Simple Pyrolysis of Urea into Graphitic Carbon Nitride with Recyclable Adsorption and Photocatalytic Activity. *J. Mater. Chem.* **2011**, *21*, 14398.

(59) Guilminot, E.; Gavillon, R.; Chatenet, M.; Berthon-Fabry, S.; Rigacci, A.; Budtova, T. New Nanostructured Carbons Based on Porous Cellulose: Elaboration, Pyrolysis and Use as Platinum Nanoparticles Substrate for Oxygen Reduction Electrocatalysis. *J. Power Sources* **2008**, *185*, 717–726.

(60) Vikkisk, M.; Kruusenberg, I.; Joost, U.; Shulga, E.; Kink, I.; Tammeveski, K. Electrocatalytic Oxygen Reduction on Nitrogen-Doped Graphene in Alkaline Media. *Appl. Catal., B* **2014**, *147*, 369–376.

(61) Ratso, S.; Kruusenberg, I.; Vikkisk, M.; Joost, U.; Shulga, E.; Kink, I.; Kallio, T.; Tammeveski, K. Highly Active Nitrogen-Doped Few-Layer Graphene/Carbon Nanotube Composite Electrocatalyst for Oxygen Reduction Reaction in Alkaline Media. *Carbon* **2014**, *73*, 361–370.

(62) Deng, J.; Li, M.; Wang, Y. Biomass-Derived Carbon: Synthesis and Applications in Energy Storage and Conversion. *Green Chem.* **2016**, *18*, 4824–4854.

(63) Celiešiūtė, R.; Trusovas, R.; Niaura, G.; Švedas, V.; Račiukaitis, G.; Ruželė, Ž.; Pauliukaite, R. Influence of the Laser Irradiation on the Electrochemical and Spectroscopic Peculiarities of Graphene-Chitosan Composite Film. *Electrochim. Acta* **2014**, *132*, 265–276.

(64) Tang, J.; Wang, Y.; Zhao, W.; Zeng, R. J.; Liu, T.; Zhou, S. Biomass-Derived Hierarchical Honeycomb-like Porous Carbon Tube Catalyst for the Metal-Free Oxygen Reduction Reaction. *J. Electroanal. Chem.* **2019**, *847*, 113230.

(65) Zheng, H.; Zhang, Y.; Long, J.; Li, R.; Gou, X. Nitrogen-Doped Porous Carbon Material Derived from Biomass of Beancurd as an Efficient Electrocatalyst for Oxygen Reduction and Zn-Air Fuel Cell. *J. Electrochem. Soc.* **2020**, *167*, No. 084516.

(66) Bansal, R. C.; Goyal, M. *Activated Carbon Adsorption*; 1st ed.; CRC Press: 2005.

(67) Ambrosi, A.; Chua, C. K.; Latiff, N. M.; Loo, A. H.; Wong, C. H. A.; Eng, A. Y. S.; Bonanni, A.; Pumerma, M. Graphene and Its Electrochemistry – an Update. *Chem. Soc. Rev.* **2016**, *45*, 2458–2493.

(68) Pylypenko, S.; Mukherjee, S.; Olson, T. S.; Atanassov, P. Non-Platinum Oxygen Reduction Electrocatalysts Based on Pyrolyzed Transition Metal Macrocycles. *Electrochim. Acta* **2008**, *53*, 7875–7883.

(69) Nagaiah, T. C.; Kundu, S.; Bron, M.; Muhler, M.; Schuhmann, W. Nitrogen-Doped Carbon Nanotubes as a Cathode Catalyst for the Oxygen Reduction Reaction in Alkaline Medium. *Electrochem. Commun.* **2010**, *12*, 338–341.

(70) Oh, H.-S.; Oh, J.-G.; Lee, W. H.; Kim, H.-J.; Kim, H. The Influence of the Structural Properties of Carbon on the Oxygen Reduction Reaction of Nitrogen Modified Carbon Based Catalysts. *Int. J. Hydrogen Energy* **2011**, *36*, 8181–8186.

(71) Zhang, J.; Li, Q.; Wu, H.; Zhang, C.; Cheng, K.; Zhou, H.; Pan, M.; Mu, S. Nitrogen-Self-Doped Carbon with a Porous Graphene-like Structure as a Highly Efficient Catalyst for Oxygen Reduction. *J. Mater. Chem. A* **2015**, *3*, 10851–10857.

(72) Inagaki, M.; Toyoda, M.; Soneda, Y.; Morishita, T. Nitrogen-Doped Carbon Materials. *Carbon* **2018**, *132*, 104–140.

(73) Lai, L.; Potts, J. R.; Zhan, D.; Wang, L.; Poh, C. K.; Tang, C.; Gong, H.; Shen, Z.; Lin, J.; Ruoff, R. S. Exploration of the Active Center Structure of Nitrogen-Doped Graphene-Based Catalysts for Oxygen Reduction Reaction. *Energy Environ. Sci.* **2012**, *5*, 7936–7942.

(74) Daems, N.; Sheng, X.; Vankelecom, I. F. J.; Pescarmona, P. P. Metal-Free Doped Carbon Materials as Electrocatalysts for the Oxygen Reduction Reaction. *J. Mater. Chem. A* **2014**, *2*, 4085–4110.

(75) Trusovas, R.; Račiukaitis, G.; Niaura, G.; Barkauskas, J.; Valušis, G.; Pauliukaite, R. Recent Advances in Laser Utilization in the Chemical Modification of Graphene Oxide and Its Applications. *Adv. Opt. Mater.* **2016**, *4*, 37–65.

(76) Ferrari, A. C.; Robertson, J. Interpretation of Raman Spectra of Disordered and Amorphous Carbon. *Phys. Rev. B* **2000**, *61*, 14095–14107.

(77) Ferrari, A. C.; Robertson, J. Resonant Raman Spectroscopy of Disordered, Amorphous, and Diamondlike Carbon. *Phys. Rev. B* **2001**, *64*, No. 075414.

(78) Ribeiro-Soares, J.; Oliveros, M. E.; Garin, C.; David, M. V.; Martins, L. G. P.; Almeida, C. A.; Martins-Ferreira, E. H.; Takai, K.; Enoki, T.; Magalhães-Paniago, R.; Malachias, A.; Jorio, A.; Archanjo, B. S.; Achete, C. A.; Cangaço, L. G. Structural Analysis of Polycrystalline Graphene Systems by Raman Spectroscopy. *Carbon* **2015**, *95*, 646–652.

(79) Hu, C.; Zhou, Y.; Ma, R.; Liu, Q.; Wang, J. Reactive Template Synthesis of Nitrogen-Doped Graphene-like Carbon Nanosheets Derived from Hydroxypropyl Methylcellulose and Dicyandiamide as

Efficient Oxygen Reduction Electrocatalysts. *J. Power Sources* **2017**, *345*, 120–130.

(80) Han, C.; Wang, S.; Wang, J.; Li, M.; Deng, J.; Li, H.; Wang, Y. Controlled Synthesis of Sustainable N-Doped Hollow Core-Mesoporous Shell Carbonaceous Nanospheres from Biomass. *Nano Res.* **2014**, *7*, 1809–1819.

(81) Bard, A. J.; Faulkner, L. R. *Electrochemical Methods: Fundamentals and Applications*; 2nd ed.; Wiley: New York, 2001.

(82) Davis, R. E.; Horvath, G. L.; Tobias, C. W. The Solubility and Diffusion Coefficient of Oxygen in Potassium Hydroxide Solutions. *Electrochim. Acta* **1967**, *12*, 287–297.

(83) Lide, D. R. *CRC Handbook of Chemistry and Physics*; 82nd ed.; CRC Press: Boca Ration, 2001.

(84) Wu, X.; Yu, X.; Lin, Z.; Huang, J.; Cao, L.; Zhang, B.; Zhan, Y.; Meng, H.; Zhu, Y.; Zhang, Y. Nitrogen Doped Graphitic Carbon Ribbons from Cellulose as Non Noble Metal Catalyst for Oxygen Reduction Reaction. *Int. J. Hydrogen Energy* **2016**, *41*, 14111–14122.

(85) Zhao, J.; Liu, Y.; Quan, X.; Chen, S.; Yu, H.; Zhao, H. Nitrogen-Doped Carbon with a High Degree of Graphitization Derived from Biomass as High-Performance Electrocatalyst for Oxygen Reduction Reaction. *Appl. Surf. Sci.* **2017**, *396*, 986–993.

(86) Dobeles, G.; Dizhbite, T.; Gil, M. V.; Volperts, A.; Centeno, T. A. Production of Nanoporous Carbons from Wood Processing Wastes and Their Use in Supercapacitors and CO<sub>2</sub> Capture. *Biomass Bioenergy* **2012**, *46*, 145–154.

## Appendix 5

### Publication V

**K. Kaare**, E. Yu, T. Käämbre, A. Volperts, G. Dobele, A. Zhurinsh, G. Niaura, L. Tamasauskaite-Tamasiunaite, E. Norkus, I. Kruusenberg, Biomass-derived Graphene-like Catalyst Material for Oxygen Reduction Reaction, *ChemNanoMat*. 7 (2021) 307–313.



# Biomass-derived Graphene-like Catalyst Material for Oxygen Reduction Reaction

Kätlin Kaare,<sup>[a, f]</sup> Eric Yu,<sup>[b]</sup> Tanel Käämbre,<sup>[c]</sup> Aleksandrs Volperts,<sup>[d]</sup> Galina Dobele,<sup>[d]</sup> Aivars Zhurins,<sup>[d]</sup> Gediminas Niaura,<sup>[e]</sup> Loreta TamasauskaiteTamasunaite,<sup>[e]</sup> Eugenijus Norkus,<sup>[e]</sup> and Ivar Kruusenberg<sup>\*[f]</sup>

**Abstract:** A novel and sustainable method was established to prepare a nitrogen doped graphene-like material from a renewable, secondary raw material with potential application in the catalysis of oxygen reduction reaction (ORR). Alder wood char was used as a precursor material for producing a sustainable graphene-like carbon catalyst for the ORR. Alder wood char was first activated (AWC) and then doped with nitrogen (N-AWC). The graphene-like structure was confirmed using transmission electron microscopy (TEM) and Raman spectroscopy. Electrochemical characterization was carried out in 0.1 M KOH, showing that in alkaline media the

ORR activity of the N-doped wood char-based graphene-like material is superior compared to non-sustainable commercial N-doped graphene. The onset potential of the ORR on N-AWC was shifted to positive direction by 75 mV in comparison to the commercially available nitrogen-doped graphene and the half-wave potential was shifted even by 239 mV. This renewable biomass-derived graphene-like carbon catalyst shows a great potential alternative to current synthetic graphite, graphene nanoplatelets and graphene materials in areas such as fuel cells and batteries.

## Introduction

Graphene is a two-dimensional (2D) allotrope of carbon and has many attractive properties, such as a high electrical conductivity and good thermal, optical, and mechanical properties.<sup>[1,2]</sup> These traits make graphene a versatile material with applications in areas such as field effect transistors (FETs), transparent conductive films (TCFs) and sensors.<sup>[1,3]</sup> It is also widely used in energy storage devices, such as in fuel cells,<sup>[4,5]</sup> supercapacitors<sup>[6,7]</sup> and metal-air batteries.<sup>[8–10]</sup> Traditionally, the synthesis methods of graphene include mechanical exfoliation from graphite (so called Scotch tape method)<sup>[11]</sup> and chemical

vapor deposition (CVD). These methods produce single- and few-layer graphene<sup>[12]</sup> but are impractical for producing graphene on a large scale. For that reason, the most widely used method for production is the chemical reduction of graphite oxide to synthesize reduced graphene oxide (rGO) sheets.<sup>[13]</sup>

In recent years, the conversion of biomass into valuable carbon nanomaterials has been a topic of great interest. Currently, global production of agricultural lignocellulosic waste is around ~200 billion per year.<sup>[14]</sup> Agricultural residues consist mostly of cellulose, hemicellulose and lignin. Thus, converting biomass to carbon structures is an alternative way of producing carbonaceous materials, such as graphene.<sup>[15–21]</sup> Different types of biomass has been used to produce carbon nanomaterials, such as biological precursors<sup>[16,22,23]</sup> as well as lignocellulosic precursors.<sup>[24,25]</sup> These renewable resources are ideal candidates to produce nanomaterials in a more sustainable way. Commonly the methods involve a first activation of biomass to achieve the porous structure and then the further doping of carbon materials with heteroatoms, such as nitrogen, which improves the conductivity and catalytic activity of these materials.<sup>[26,27]</sup> The conversion of biomass to carbon nanostructures paves the way for a new avenue of nanomaterial synthesis and could potentially solve scale-up issues with traditional methods of graphene production.

In this report we demonstrate a two-step synthesis method of producing nitrogen-doped graphene-like material from biomass that shows better electrochemical activity towards the ORR than commercially produced nitrogen-doped graphene.

[a] K. Kaare  
Institute of Chemistry  
University of Tartu  
Ravila 14a, 50411 Tartu (Estonia)

[b] E. Yu  
Department of Chemical and Biomolecular Engineering  
University of California  
Berkeley, Gilman Hall, 94720 Berkeley, California (USA)

[c] Dr. T. Käämbre  
Institute of Physics  
University of Tartu  
W. Ostwaldi Str 1, 50411 Tartu (Estonia)

[d] Dr. A. Volperts, Dr. G. Dobele, Dr. A. Zhurins  
Latvian State Institute of Wood Chemistry  
Dzerbenes street 27, Riga LV-1006 (Latvia)

[e] Dr. G. Niaura, Dr. L. TamasauskaiteTamasunaite, Dr. E. Norkus  
State research institute Center for Physical Sciences and Technology  
Savanorių ave. 231, LT-02300 Vilnius (Lithuania)

[f] K. Kaare, Dr. I. Kruusenberg  
National Institute of Chemical Physics and Biophysics  
Akadeemia tee 23, 10213 Tallinn (Estonia)  
E-mail: ivar.kruusenberg@kbfi.ee

Supporting information for this article is available on the WWW under <https://doi.org/10.1002/cnma.202000615>

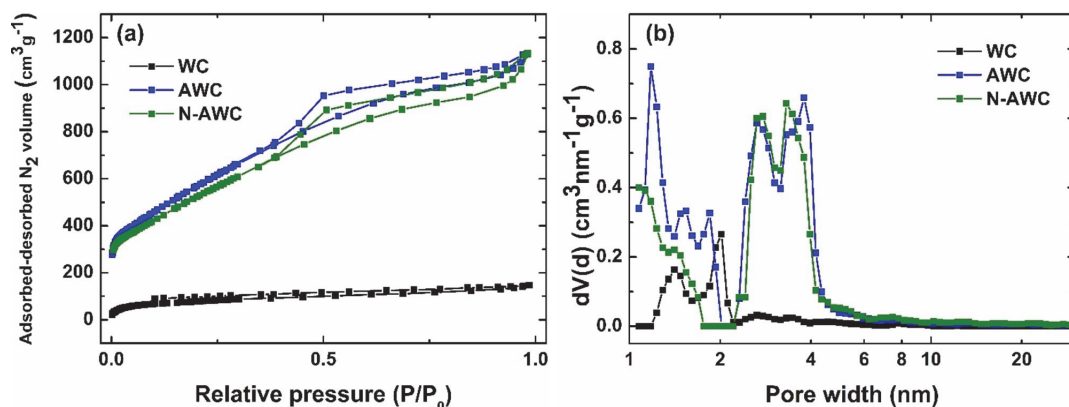
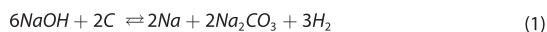


Figure 1. (a) N<sub>2</sub> adsorption-desorption isotherms for WC, AWC and N-AWC, and (b) pore distribution for WC, AWC, N-AWC.

## Results and Discussion

### Physical characterization of the catalyst material

The textural properties of the pristine, activated and doped wood-based materials were studied using N<sub>2</sub> physisorption, with the isotherms shown in Figure 1a and the pore size distributions calculated according to the quenched solid density functional theory (QSDFT) shown in Figure 1b. The surface areas calculated according to the Brunauer-Emmett-Teller (BET) theory as well as the QSDFT are presented in Table 1 ( $S_{BET}$  and  $S_{DFT}$ ). As it can be seen, prior to activation, the wood-char (WC) material has a rather low surface area, which the activation successfully increases by an order of magnitude. It has been reported that the activation mechanism carried out with NaOH takes place as follows:<sup>[26]</sup>



The thermal reaction between NaOH and C releases many gaseous substances.<sup>[17,18,20]</sup> After activation the porous carbon structure gives the dicyandiamide (DCDA) derived nitrogen species a lot of surface to react with during the doping process and determines the final specific surface area (SSA) of the material, as it does not decrease significantly during the doping. The total ( $V_{\text{total}}$ ) and micropore volumes ( $V_{\text{micro(DR)}}$ , calculated according to the Dubinin-Radushkevich theory) as well as the average pore diameter ( $L$ ) in Table 1 also show that the activation was very successful in introducing micro-mesoporos-

ity to the catalyst material. The microporosity is somewhat decreased during the doping process due to a closure of some of the micropores as the carbon becomes more ordered during heating.

The microstructure of the N-AWC was studied using TEM shown in Figure 2a,b. The morphology of typical wavy and wrinkled layered graphene can be seen in Figure 2a. The appearance of this N-doped graphene has also been recorded by previous researchers.<sup>[21,23,29,30]</sup> The space between two layers is 0.34 nm (Figure 2b) which matches the distance between two layers in graphene-like materials.<sup>[31]</sup> It has been found that in case of biomass the usage of activator promotes the rearrangement of the carbon atoms to form a graphene-like structure.<sup>[17,18,20]</sup> The additional SEM measurement that also confirms the graphene-like structure of the N-AWC can be found on Figure S1.

The surface elemental composition was studied using X-ray photoelectron spectroscopy (XPS). From the overview spectrum (Figure 3a), it is possible to distinguish between oxygen, nitrogen, and carbon peaks. Owing to limited statistics, particularly for the N 1s peak in the overview, their relative content (in at. %) given in the legend was verified using comparison of the corresponding region spectra, in all cases normalized to acquisition time, instrument transmission function, photoionization cross section and estimated escape depth at their respective kinetic energies. Compared to the literature, the overall surface N content in the N-AWC material is rather low.<sup>[32-34]</sup> The C 1s main peak can be seen near 284.5 eV and this corresponds to carbon in sp<sup>2</sup> hybridization (Figure 3b)<sup>[32]</sup> with

Table 1. Textural properties of wood-based catalysts as determined by BET and QSDFT analysis.

Material	$S_{BET}$ m <sup>2</sup> g <sup>-1</sup>	$S_{DFT}$ m <sup>2</sup> g <sup>-1</sup>	$V_{\text{total}}$ cm <sup>3</sup> g <sup>-1</sup>	$V_{\text{micro(DR)}}$ cm <sup>3</sup> g <sup>-1</sup>	$L$ , nm
WC	280	180	0.20	0.11	2.02
AWC	2088	1419	1.61	0.44	2.26
N-AWC	1924	1383	1.60	0.35	2.31

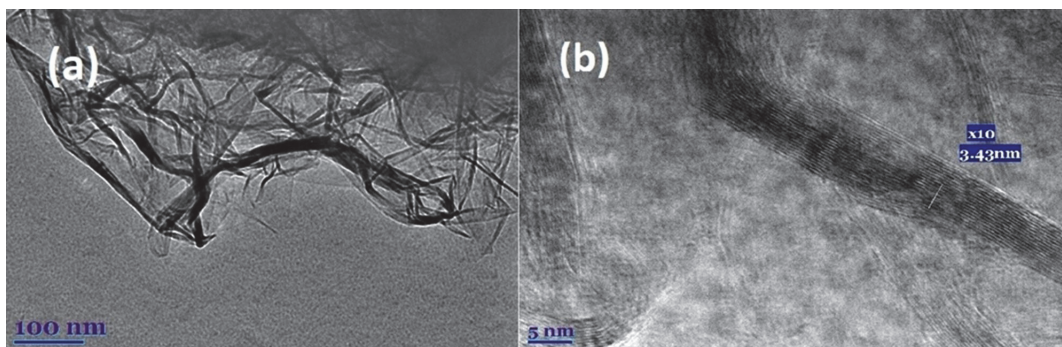


Figure 2. TEM photos of the N-doped graphene-like wood-based (N-AWC) catalyst material.

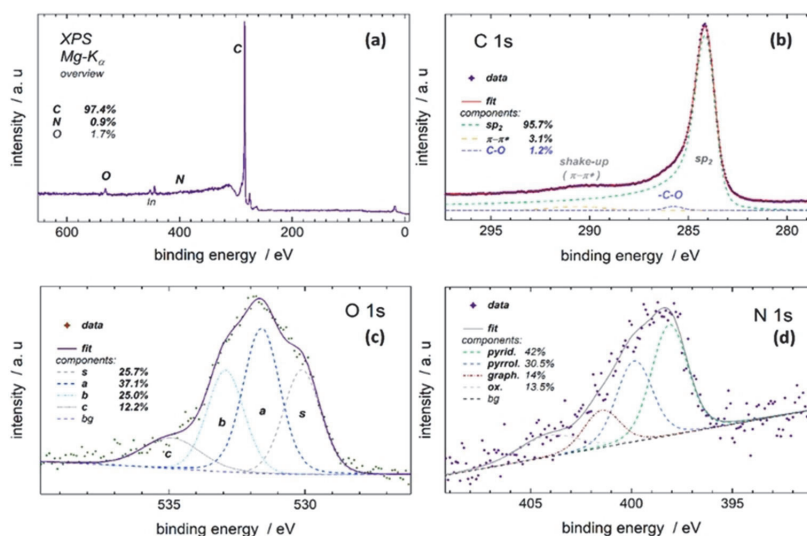


Figure 3. (a) XPS survey, (b) C 1s and (c) O 1s and (d) N 1s spectra of N-doped alder wood char catalyst material.

the characteristic asymmetric (Doniach-Sunjić) line shape of metallic (graphene) specimen, which accounts for 95.7% of C 1s intensity, the remaining contributions being from valence shake-up centered around 290 eV (3.1%) and a minor component at 285.8 eV typical of singly bonded (C–O) oxygen. The O 1s region (Figure 3c) was fitted assuming a minimum number of equal width (FWHM) Gaussians after subtracting a Tougaard background, which yielded components at 530.1 eV, 531.6 eV, 532.9 eV and 535 eV. The indium peak is also evident as the sample was pressed into metallic indium ingot during measurement and having slightly short of 100% coverage has implications on interpreting the O 1s spectrum (Figure 3c), while its visibility in the spectrum owes largely due to the relatively high photoionization cross section of the In 3d level; the In:O atomic content ratio from XPS is less than 1:6, which

implies that in the O 1s spectrum (Figure 3c), the lowest binding energy component at 530.1 eV can only be attributed to indium substrate surface oxide when assuming fully oxidized indium within XPS probe depth, which is not fully plausible, the other possible contribution being here from quinone moiety in the sample.<sup>[35,36]</sup> The component peak a at 531.6 eV lies in the range of both doubly bound carbon as well as surface hydroxyl groups. A contribution also from the latter in the C 1s is plausible since in the C 1s spectrum, no C=O feature (around 288.5 eV) can be identified, though this could be engulfed in the onset of the C 1s shake-up features of the overly abundant sp<sup>2</sup> carbon. The component peak b at 532.9 eV gives a measure of singly bound carbon (C–O). However, theories around ORR activity on N-doped carbon materials is still controversial. Some groups have discovered the high nitrogen content on the

surface as the key factor in achieving high electrochemical activity.<sup>[37–39]</sup> Others have found no correlation between higher content of nitrogen and enhanced electrochemical activity.<sup>[40–42]</sup> To examine the structure of the N dopants, the N 1s peak was deconvoluted (Figure 3d) using equal width gaussian line shapes for the 3 lower binding energy lines, and relaxing the width constraint on the N–O species somewhat less uniquely defined possible nearest neighbour configurations. The most abundant component was pyridinic-N at 398.2 eV binding energy (42%), followed by pyrrolic-N at 400.2 eV (30.5%), graphitic-N at 402.4 eV (14%) and N–O at 405 eV (13.5%). Both theoretical calculations<sup>[43]</sup> and experiments with catalysts containing almost only pyridinic nitrogen<sup>[44]</sup> have shown that pyridinic-N is the most active nitrogen moiety. As almost half of the nitrogen in N–AWC was in pyridinic form, the effect is significant even though the overall nitrogen content might be low.

Raman spectroscopy was used to study molecular structure of the synthesized carbon catalyst. Figure 4 compares activated and N-doped alder wood char-based (N–AWC) catalyst material, similarly prepared sample without the N-doping (AWC), and the wood-char (WC) material. For characterizing carbon materials, three main bands can be used: D, G, and 2D. The corresponding wavenumbers (for 532-nm excited spectrum) are near 1350, 1580, and 2695  $\text{cm}^{-1}$ , respectively.

In addition, low intensity shoulder near 1619  $\text{cm}^{-1}$  belongs to D' mode. D and D' modes are associated with defects that

are present in materials as well as  $\text{sp}^3$  hybridized carbons.<sup>[45]</sup> G band corresponds to  $\text{sp}^2$  hybridized carbon (C–C and N–C).<sup>[46,47]</sup> The Raman spectrum of pristine WC sample before activation shows broad D and G bands near 1362 and 1595  $\text{cm}^{-1}$ , respectively. The characteristic 2D band of graphene-like material near 2695  $\text{cm}^{-1}$  is not visible; instead, the broad feature, composed of several bands appears in the high frequency region. The D and G bands are broad. The width of G band determined as full width at half maximum (FWHM(G)) was found to be 78.3  $\text{cm}^{-1}$ . Thus, the observed Raman spectrum of WC material indicates a highly disordered carbon network.<sup>[48,49]</sup> Considerable changes in the Raman spectra were observed after activation (AWC sample) and N-doping (N–AWC sample) procedures (Figure 4). The observed spectra resemble a graphene-like material with a well-defined 2D band near 2695  $\text{cm}^{-1}$  and relatively narrow G and D bands near 1580 and 1347  $\text{cm}^{-1}$ , respectively.<sup>[48,49]</sup> The ratio  $I_D/I_G$  is used to characterize defects or irregularities in carbon materials. The smaller the ratio, the less defects are present in carbon material.<sup>[45]</sup> For our alder wood char synthesized material, TEM images showed a graphene-like structure. Further analysis of Raman spectra (Figure 4) shows a D band intensity lower than G band for both N–AWC and AWC materials, resulting in a  $I_D/I_G$  ratio of 0.43 and 0.36, for N-doped and undoped samples, respectively. In addition, the FWHM(G) was found to be slightly higher for N-doped sample (FWHM(G)=30.0  $\text{cm}^{-1}$ ) in comparison to the sample without the N-doping (FWHM(G)=27.5  $\text{cm}^{-1}$ ). Thus, both studied parameters indicate that N-doping induces slight disordering in the graphene plane. Finally, the broad feature near 1450–1500  $\text{cm}^{-1}$  is visible after fitting the experimental contour with Lorentzian-Gaussian form components. The relative intensity of this band is highest in the case of pristine WC material. This band can serve as an indicator of amorphization of the carbon.<sup>[48,49]</sup> One can see that intensity of this band is higher in the case of N-doped sample comparing with AWC.

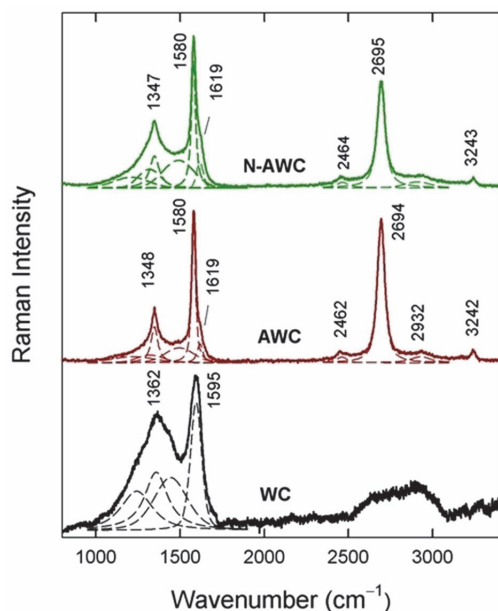


**Figure 4.** Raman spectra of activated and N-doped alder wood char-based catalyst (N–AWC), similarly prepared sample without N-doping (AWC), and wood-char (WC) material. The fitted Lorentzian-Gaussian form components are also shown. The excitation wavelength is 532 nm (0.6 mW).

#### Electrochemical characterization in alkaline media

To investigate electrochemical properties of graphene-like catalyst material, ORR experiments were carried out using rotating disc electrode (RDE) method in 0.1 M KOH solution by using glassy carbon (GC) as a substrate. The ORR polarization curves are shown on Figure 5a. The wood-based graphene-like material has an onset potential ( $E_{\text{onset}}$ ) of  $-0.085$  V and half-wave potential ( $E_{1/2}$ ) of  $-0.215$  V.  $E_{\text{onset}}$  in this work is defined as the potential value at 0.1  $\text{mA cm}^{-2}$ . The Koutecky-Levich (K–L) plot and electrons transferred per  $\text{O}_2$  molecule ( $n$ ) are shown in Figure 5b. K–L plots are calculated using K–L equation shown below from the ORR polarization data in Figure 5a:<sup>[50]</sup>

$$\frac{1}{j} = \frac{1}{j_k} + \frac{1}{j_d} = -\frac{1}{nFkC_{\text{O}_2}^b} - \frac{1}{0.62nFD_{\text{O}_2}^{2/3} \nu^{-1/6} C_{\text{O}_2}^b \omega^{1/2}} \quad (2)$$

where,  $j$  is the ORR current density measured experimentally (background has been subtracted),  $j_k$  and  $j_d$  are the kinetic and diffusion limited current densities, respectively,  $F$  is the Faraday

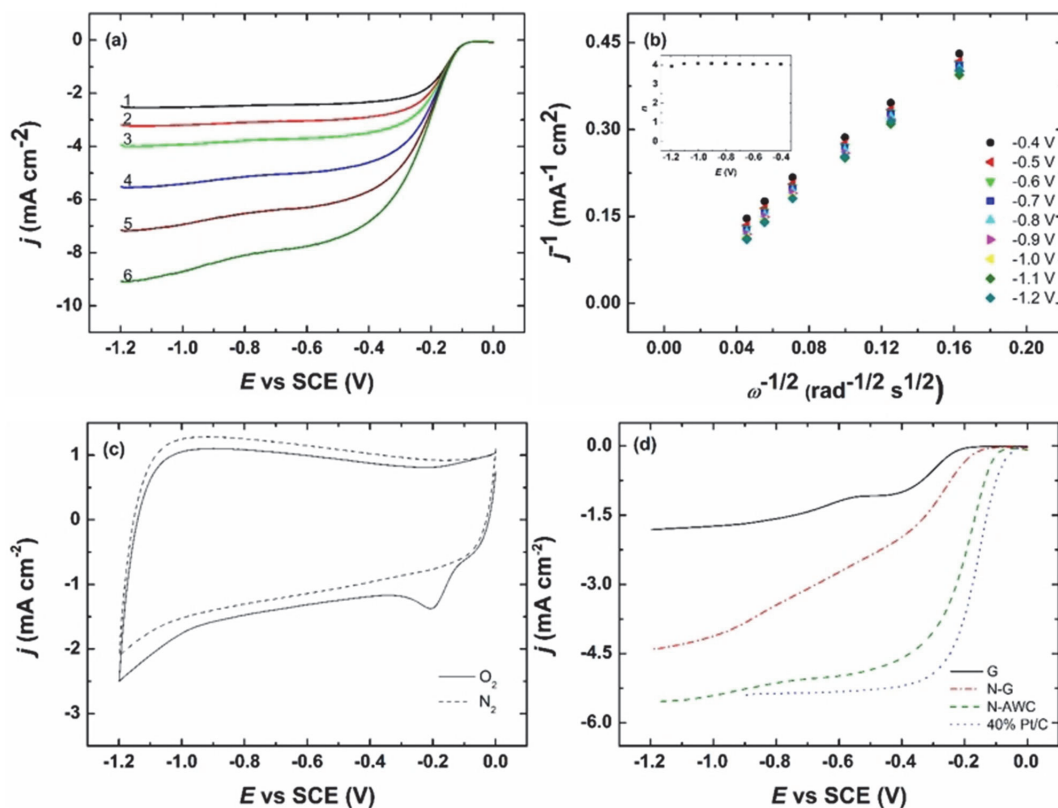


**Figure 5.** (a) RDE polarization curves of GC electrodes modified with N-doped alder wood char-based catalyst material in  $O_2$  saturated 0.1 M KOH.  $\nu = 10 \text{ mVs}^{-1}$ ,  $\omega = (1) 360, (2) 610, (3) 960, (4) 1900, (5) 3100$  and  $(6) 4600$  rpm. (b) Koutecky-Levich plots derived from the experimental data shown in Figure 5a. The inset shows the potential dependence of  $n$ . (c) CV in  $O_2$  or  $N_2$  saturated 0.1 M KOH. (d) comparison of polarization curves for oxygen reduction on N-doped alder wood char-based catalyst and commercial materials.

constant ( $96,485 \text{ Cmol}^{-1}$ ),  $k$  is the heterogenous rate constant for  $O_2$  reduction,  $\omega$  is the electrode rotation rate ( $\text{rad s}^{-1[51]}$ ),  $D_{O_2}$  is the diffusion coefficient of oxygen ( $1.9 \times 10^{-5} \text{ cm}^2 \text{ s}^{-1[52]}$ ),  $C_{O_2}^0$  is the oxygen concentration ( $1.2 \times 10^{-6} \text{ mol cm}^{-3[52]}$ ) in 0.1 M KOH, and  $\nu$  is the kinematic viscosity of the solution ( $0.01 \text{ cm}^2 \text{ s}^{-1}$ ).

The RDE polarization curves were measured at various rotation speeds between 360 rpm to 4600 rpm, shown in Figure 5a. The current density increases with the rotation speed due to shorter diffusion distance. The  $E_{\text{onset}}$  shows no significant change during the RDE measurements, indicating that the catalyst material is not detaching from the electrode over the period of testing. The K–L plot (Figure 5b) indicates that the process is almost entirely diffusion limited (data derived by the results shown on Figure 5a), as the intercept is close to zero. The number of electrons transferred per  $O_2$  molecule ( $n$ ) is 4 in the studied potential range, indicating that the process proceeds via 4-electron pathway (inset of Figure 5b). Figure 5c compares the cyclic voltammetry (CV) curves recorded in  $O_2$ -

saturated or in  $N_2$ -saturated 0.1 M KOH at  $10 \text{ mVs}^{-1}$ , respectively. Compared to CV curve recorded in  $N_2$ -saturated electrolyte, the sample N–AWC shows noticeable cathodic ORR peak around  $-0.2 \text{ V}$  in the  $O_2$ -saturated 0.1 M KOH. The comparison with undoped graphene (G) and commercial nitrogen-doped graphene (N–G) is shown on Figure 5d. The  $E_{\text{onset}}$  and  $E_{1/2}$  values for commercial N–G are  $-0.155 \text{ V}$  and  $-0.454 \text{ V}$ , respectively. The N-doped biomass-based catalyst material's onset and half-wave potentials are both significantly more positive than those of commercial material ( $-0.085 \text{ V}$  and  $-0.215 \text{ V}$ , respectively). The catalyst material contains different N-groups, with the most abundant N-group being pyridinic-N. The question which nitrogen group is contributing most to ORR activity is still a topic of extensive debate. It has been found that the pyridinic-N is the one mainly responsible in achieving high electrocatalytic activity.<sup>[42,53–55]</sup> Lai *et al.* have shown that pyridinic-N lowers the onset potential for ORR polarization curve.<sup>[42]</sup>

Compared to a commercial 40% Pt/C catalyst, the values of  $E_{\text{onset}}$  and  $E_{1/2}$  are somewhat more negative in case of N–AWC

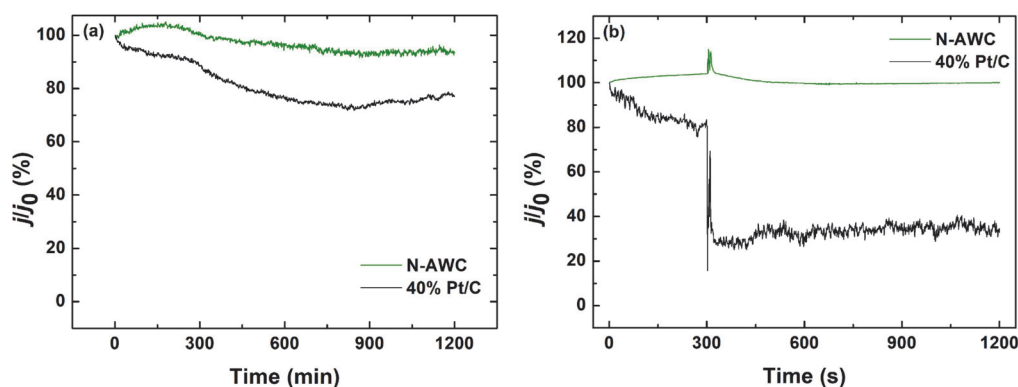


**Figure 6.** (a) Chronoamperometric responses for 20 h for the N-AWC and commercial 40% Pt/C at  $-0.4$  V,  $\omega = 610$  rpm, (b) Chronoamperometric responses for the N-AWC and commercial 40% Pt/C to methanol (added at 300 s) at  $-0.4$  V,  $\omega = 1900$  rpm.

(Figure 5d), but the goal in this work was rather to show that it is also possible to synthesize sustainable biomass-based N-doped graphene-like material, that has a higher ORR activity than the commercial N-doped material. The further modification of N-AWC with platinum could give even better results, but this is out of the scope of the work carried out within this article, as the goal was to synthesize metal-free carbon catalyst.

To further investigate the activity and stability of the as-prepared catalyst material, chronoamperometry and methanol tolerance testing was carried out at  $-0.4$  V. The chronoamperometric responses of commercial 40% Pt/C and N-AWC can be seen on Figure 6a. The current drop for commercial platinum catalyst after 1200 minutes was around 23%, but for the catalyst material synthesized from alder wood char, the current loss was not so notorious, as the relative current density was about 93% after 1200 minutes. This clearly demonstrates the better durability of the biomass-based material in comparison to the state-of-the-art Pt/C catalyst. Methanol tolerance test result can be seen on Figure 6b, where methanol was added at 300 seconds. The relative current density for 40% Pt/C decreases drastically, and stabilizes at around 35%, but in case of N-AWC there is just a slight change after the injection of methanol and relative current density remains at around 100%. These results indicate good stability and methanol tolerance of the N-doped alder wood char-based catalyst in alkaline conditions.

Biomass-based carbon materials are also widely used in supercapacitors.<sup>[24]</sup> All biomass consists mostly of carbon and the main components of biomass are also the same: cellulose, hemicellulose and lignin.<sup>[56]</sup> The conversion of biomass may include many steps including an additional pre-treatment step, but our two-step approach has potential to be integrated in larger scale synthesis.

## Conclusion

In this work, alder wood char was used as a precursor material to synthesize a sustainable graphene-like carbon nanomaterial catalyst. The electrochemical activity towards the ORR was studied in 0.1 M KOH solution by employing rotating disc electrode method. The results showed that compared to commercial non-sustainable nitrogen-doped graphene, the material synthesized herein shows better activity towards the ORR. The stability compared to commercial Pt/C catalyst was also significantly better.

## Acknowledgements

This research was financially supported by M-ERA.NET project "Wood-based Carbon Catalysts for Low-temperature Fuel Cells" (WoBaCat), by LZP-2018/1-0194 project "Nanostructured Nitrogenated Carbon Materials as Promoters in Energy Harvesting and Storage Technologies (NN-CARMA), by ERA.Net RUS Plus funding mechanism (Project HeDoCat), by the European Regional Development Fund project TK134 EQUITANT and by the Estonian Research Council PSG312. The maintenance of XPS is carried out thanks to the financial assistance from ERDF TK141.

## Conflict of Interest

The authors declare no conflict of interest.

**Keywords:** sustainable catalyst · oxygen reduction reaction · fuel cells · electrocatalysis · metal-free catalyst

[1] Y. Zhu, S. Murali, W. Cai, X. Li, J. W. Suk, J. R. Potts, R. S. Ruoff, *Adv. Mater.* 2010, 22, 3906–3924.

- [2] S. Park, R. S. Ruoff, *Nat. Nanotechnol.* **2009**, *4*, 217–224.
- [3] X. Huang, Z. Yin, S. Wu, X. Qi, Q. He, Q. Zhang, Q. Yan, F. Boey, H. Zhang, *Small* **2011**, *7*, 1876–1902.
- [4] M. Liu, R. Zhang, W. Chen, *Chem. Rev.* **2014**, *114*, 5117–5160.
- [5] S. Ramakrishnan, M. Karuppanan, M. Vinothkannan, K. Ramachandran, O. J. Kwon, D. J. Yoo, *ACS Appl. Mater. Interfaces* **2019**, *11*, 12504–12515.
- [6] Y. Huang, J. Liang, Y. Chen, *Small* **2012**, *8*, 1805–1834.
- [7] Y. Zhu, S. Murali, M. D. Stoller, K. J. Ganesh, W. Cai, P. J. Ferreira, A. Pirkle, R. M. Wallace, K. A. Cychosz, M. Thommes, D. Su, E. A. Stach, R. S. Ruoff, *Science* **2011**, *332*, 1537–1541.
- [8] D. U. Lee, H. W. Park, D. Higgins, L. Nazar, Z. Chen, *J. Electrochem. Soc.* **2013**, *160*, F910–F915.
- [9] Z. Chen, D. Higgins, Z. Chen, D. U. Lee, *J. Mater. Chem. A* **2013**, *1*, 2639–2645.
- [10] S. Ramakrishnan, J. Balamurugan, M. Vinothkannan, A. R. Kim, S. Sengodan, D. J. Yoo, *Appl. Catal. B* **2020**, *279*, 119381.
- [11] M. Yi, Z. Shen, *J. Mater. Chem. A* **2015**, *3*, 11700–11715.
- [12] B. Deng, Z. Liu, H. Peng, *Adv. Mater.* **2019**, *31*, DOI 10.1002/adma.201800996.
- [13] C. K. Chua, M. Pumeria, *Chem. Soc. Rev.* **2014**, *43*, 291–312.
- [14] J. K. Saini, R. Saini, L. Tewari, *3 Biotech* **2015**, *5*, 337–353.
- [15] M. Borghei, J. Lehtonen, L. Liu, O. J. Rojas, *Adv. Mater.* **2017**, 1703691.
- [16] A. Primo, P. Atienzar, E. Sanchez, J. M. Delgado, H. Garcia, *Chem. Commun.* **2012**, *48*, 9254–9256.
- [17] J. Zhang, Y. Sun, J. Zhu, Z. Kou, P. Hu, L. Liu, S. Li, S. Mu, Y. Huang, *Nano Energy* **2018**, *52*, 307–314.
- [18] J. Zhang, C. Zhang, Y. Zhao, I. S. Amiin, H. Zhou, X. Liu, Y. Tang, S. Mu, *Appl. Catal. B* **2017**, *211*, 148–156.
- [19] J. Zhu, Y. Huang, W. Mei, C. Zhao, C. Zhang, J. Zhang, I. S. Amiin, S. Mu, *Angew. Chem. Int. Ed.* **2019**, *58*, 3859–3864.
- [20] J. Zhang, H. Zhou, X. Liu, J. Zhang, T. Peng, J. Yang, Y. Huang, S. Mu, *J. Mater. Chem. A* **2016**, *4*, 15870–15879.
- [21] B. Huang, M. Xia, J. Qiu, Z. Xie, *ChemNanoMat* **2019**, *5*, 682–689.
- [22] B. Huang, Y. Liu, Q. Guo, Y. Fang, M. M. Titirici, X. Wang, Z. Xie, *Carbon* **2020**, *156*, 179–186.
- [23] F. Pan, J. Jin, X. Fu, Q. Liu, J. Zhang, *ACS Appl. Mater. Interfaces* **2013**, *5*, 11108–11114.
- [24] P. Thomas, C. W. Lai, M. R. Bin Johan, *J. Anal. Appl. Pyrolysis* **2019**, *140*, 54–85.
- [25] Y. Liu, B. Huang, X. Lin, Z. Xie, *J. Mater. Chem. A* **2017**, *5*, 13009–13018.
- [26] H. Wang, T. Maiyalagan, X. Wang, *ACS Catal.* **2012**, *2*, 781–794.
- [27] C. Sathiskumar, S. Ramakrishnan, M. Vinothkannan, A. Rhan Kim, S. Karthikeyan, D. J. Yoo, *Nanomaterials* **2019**, *10*, 76.
- [28] A. L. Cazetta, A. M. M. Vargas, E. M. Nogami, M. H. Kunita, M. R. Guilherme, A. C. Martins, T. L. Silva, J. C. G. Moraes, V. C. Almeida, *Chem. Eng. J.* **2011**, *174*, 117–125.
- [29] Z. Wen, X. Wang, S. Mao, Z. Bo, H. Kim, S. Cui, G. Lu, X. Feng, J. Chen, *Adv. Mater.* **2012**, *24*, 5610–5616.
- [30] D. Geng, Y. Y. Chen, Y. Y. Chen, Y. Li, R. Li, X. Sun, S. Ye, S. Knights, D. A. Saville, I. A. Aksay, *Energy Environ. Sci.* **2011**, *4*, 760–764.
- [31] A. Ambrosi, C. K. Chua, A. Bonanni, M. Pumeria, *Chem. Rev.* **2014**, *114*, 7150–7188.
- [32] K. Artyushkova, A. Serov, S. Rojas-Carbonell, P. Atanassov, *J. Phys. Chem. C* **2015**, *119*, 25917–25928.
- [33] N. Daems, X. Sheng, I. F. J. Vankelecom, P. P. Pescarmona, W. Y. Lee, C. S. Kim, H. Jónsson, H. Kuzmany, R. Pfeiffer, A. Barreiro, B. Büchner, T. Pichler, T. Seyller, K. Kobayashi, *J. Mater. Chem. A* **2014**, *2*, 4085–4110.
- [34] K. Gao, B. Wang, L. Tao, B. V. Cunnig, Z. Zhang, S. Wang, R. S. Ruoff, L. Qu, *Adv. Mater.* **2019**, *31*, 1805121.
- [35] Y. Tsujii, T. Akira, Y. Masahide, N. Yasunori, W. Yoshio, *Polym. J.* **1988**, *20*, 837–844.
- [36] R. Arrigo, M. Hävecker, S. Wrabetz, R. Blume, M. Lerch, J. McGregor, E. P. J. Parrott, J. A. Zeiter, L. F. Gladden, A. Knop-Gericke, R. Schlögl, D. S. Su, *J. Am. Chem. Soc.* **2010**, *132*, 9616–9630.
- [37] Z. Chen, D. Higgins, Z. Chen, *Carbon* **2010**, *48*, 3057–3065.
- [38] C. V. Rao, C. R. Cabrera, Y. Ishikawa, *J. Phys. Chem. Lett.* **2010**, *1*, 2622–2627.
- [39] H. S. Oh, J. G. Oh, W. H. Lee, H. J. Kim, H. Kim, *Int. J. Hydrogen Energy* **2011**, *36*, 8181–8186.
- [40] E. J. Biddinger, U. S. Ozkan, *J. Phys. Chem. C* **2010**, *114*, 15306–15314.
- [41] T. C. Nagaiah, S. Kundu, M. Bron, M. Muhler, W. Schuhmann, *Electrochem. Commun.* **2010**, *12*, 338–341.
- [42] L. Lai, J. R. Potts, D. Zhan, L. Wang, C. K. Poh, C. Tang, H. Gong, Z. Shen, J. Lin, R. S. Ruoff, *Energy Environ. Sci.* **2012**, *5*, 7936–7942.
- [43] J. D. Wiggins-Camacho, K. J. Stevenson, *J. Phys. Chem. C* **2009**, *113*, 19082–19090.
- [44] D. Guo, R. Shibuya, C. Akiba, S. Saji, T. Kondo, J. Nakamura, *Science* **2016**, *351*, 361–5.
- [45] M. Cheng, R. Yang, L. Zhang, Z. Shi, W. Yang, D. Wang, G. Xie, D. Shi, G. Zhang, *Carbon* **2012**, *50*, 2581–2587.
- [46] F. Tuinstra, J. L. Koenig, *J. Chem. Phys.* **1970**, *53*, 1126–1130.
- [47] C. Han, S. Wang, J. Wang, M. Li, J. Deng, H. Li, Y. Wang, *Nano Res.* **2014**, *7*, 1809–1819.
- [48] A. C. Ferrari, J. Robertson, *Phys. Rev. B* **2001**, *64*, 075414.
- [49] R. Trusovas, K. Ratautas, G. Račiukaitis, G. Niaura, *Appl. Surf. Sci.* **2019**, *471*, 154–161.
- [50] A. J. Bard, L. R. Faulkner, *Electrochemical Methods: Fundamentals and Applications*, Wiley, New York, **2001**.
- [51] D. R. Lide, *CRC Handbook of Chemistry and Physics*, CRC Press, Boca Ration, **2001**.
- [52] R. E. Davis, G. L. Horvath, C. W. Tobias, *Electrochim. Acta* **1967**, *12*, 287–297.
- [53] Z. Chen, D. Higgins, H. Tao, R. S. Hsu, Z. Chen, *J. Phys. Chem. C* **2009**, *113*, 21008–21013.
- [54] M. Vikkisk, I. Kruusenberg, U. Joost, E. Shulga, I. Kink, K. Tammeveski, *Appl. Catal. B* **2014**, *147*, 369–376.
- [55] A. Sarapuu, E. Kibena-Pöldsepp, M. Borghei, K. Tammeveski, *J. Mater. Chem. A* **2018**, *6*, 776–804.
- [56] P. Kaur, G. Verma, S. S. Sekhon, *Prog. Mater. Sci.* **2019**, *102*, 1–71.

Manuscript received: November 27, 2020  
 Revised manuscript received: January 15, 2021  
 Accepted manuscript online: January 28, 2021  
 Version of record online: February 11, 2021

# Curriculum vitae

## Personal data

Name: Kätlin Kaare  
Date of birth: 09.03.1994  
E-mail: katlin.kaare@kbfi.ee

## Education

2018–... Tallinn University of Technology, PhD in Mechanical Engineering  
2016–2018 University of Tartu, MSc in Chemistry (*cum laude*)  
2013–2016 University of Tartu, BSc in Chemistry  
2010–2013 Väike-Maarja Gymnasium

## Professional employment

2018–... National Institute of Chemical Physics and Biophysics, Junior Researcher

## Honours and awards

- 2018, Rickard Kruusberg Scholarship
- 2017, Ants and Maria Silvere and Sigfried Pant Scholarship

## Field of Research

- Natural Sciences and Engineering
- Chemistry and Chemical Technology
- CERCS classification: P401 Electrochemistry

## Defended theses

- 2018, Electrochemical reduction of oxygen on wood-based N-doped catalyst materials, MSc, supervisors Kaido Tammeveski and Ivar Kruusenberg, University of Tartu, Faculty of Science and Technology, Institute of Chemistry
- 2016, Electrochemical reduction of oxygen on multi-walled carbon nanotubes modified with metallo-phthalocyanines, BSc, supervisors Kaido Tammeveski and Ivar Kruusenberg, University of Tartu, Faculty of Science and Technology, Institute of Chemistry

## Scientific work

### Publications

1. Kaare, K; Yu, Eric; Käämbre, T; Volperts, A; Dobele, G; Zhurinsh, A; Niaura, G; Tamasauskaite-Tamasiunaite, L; Norkus, E; Kruusenberg, I. (2021). ChemNanoMat, 7. DOI: 10.1002/cnma.202000615.
2. Kaare, K; Yu, E; Volperts, A; Dobele, G; Zhurinsh, A; Dyck, A; Niaura, G; Tamasauskaite-Tamasiunaite, L; Norkus, E; Andrulevicius, M; Danilson, M; Kruusenberg, I. (2020). ACS Omega, 5 (37), 23578–23587. DOI: 10.1021/acsomega.0c01974.
3. Volperts, A; Plavniece, A; Dobele, G; Zhurinsh, A; Kruusenberg, I; Kaare, K; Locs, J; Tamasauskaite-Tamasiunaite, L; Norkus, E. (2019). Renewable Energy, 141, 40–45. DOI: 10.1016/j.renene.2019.04.002.
4. Villemson, K. M.; Kaare, K; Raudsepp, R; Käämbre, T; Smits, K; Wang, P; Kuzmin, A. V.; Šutka, A; Shainyan, B. A.; Kruusenberg, I. (2019). The Journal of Physical Chemistry C, 123 (26), 16065–16074. DOI: 10.1021/acs.jpcc.9b00117.

5. Türk, K.K.; Kaare, K.; Kruusenberg, I.; Merisalu, M.; Joost, U.; Matisen, L.; Sammelseg, V.; Zagal, J.H.; Tammeveski, K. (2017). *Journal of The Electrochemical Society*, 164 (6), H338–H344. DOI: 10.1149/2.0821706jes.
6. Kaare, K.; Kruusenberg, I.; Merisalu, M.; Matisen, L.; Sammelseg, V.; Tammeveski, K. (2016). *Journal of Solid State Electrochemistry*, 20 (4), 921–929. DOI: 10.1007/s10008-015-2990-9.

#### **Conference Presentations**

1. K. Kaare, I. Kruusenberg, A. Volperts, A. Zhurinsh, G. Dobele, Lignin-based N-doped Carbon Nanomaterials for the ORR, in ECS 241st meeting, May 2022.

## Elulookirjeldus

### Isikuandmed

Nimi: Kätlin Kaare  
Sünniaeg: 09.03.1994  
E-post: katlin.kaare@kbfi.ee

### Hariduskäik

2018–... Tallinna Tehnikaülikool, PhD Mehhanotehnika  
2016–2018 Tartu Ülikool, MSc Keemia  
2013–2016 Tartu Ülikool, BSc Keemia  
2010–2013 Väike-Maarja Gümnaasium, keskkharidus

### Teenistuskäik

2018–... Keemilise ja bioloogilise füüsika instituut, nooremteadur

### Autasud

- 2018, Rickard Kruusbergi nimeline stipendium "Seikle õpingute läbi!"
- 2017, Ants ja Maria Silvere ning Sigfried Panti stipendium

### Teadustöö põhisuunad

- Loodusteadused ja tehnika
- Keemia ja keemiatehnika
- CERCS klassifikaator: P401 Elektrokeemia

### Kaitstud lõputööd

- 2018, Hapniku elektrokeemiline redutseerumine puidul põhinevatel N-dopeeritud katalüsaatormaterjalidel, MSc, juhendajad Kaido Tammeveski ja Ivar Kruusenberg, Tartu Ülikool, Loodus- ja täppisteaduste valdkond, keemia instituut
- 2016, Hapniku elektrokeemiline redutseerumine metall-ftalotsüaniinidega modifitseeritud mitmeseinalistel süsinikanotorudel, BSc, juhendajad Kaido Tammeveski ja Ivar Kruusenberg, Tartu Ülikool, Loodus- ja täppisteaduste valdkond, keemia instituut

### Teadustegevus

Teadusartiklite ja konverentsiettekanete loetelu on toodud inglisekeelse elulookirjelduse juures.

ISSN 2585-6901 (PDF)  
ISBN 978-9949-83-878-3 (PDF)